Wave-based numerical methods for damage identification in components and structures

Submitted March 2021, in partial fulfillment of
the conditions for the award of the degree **PhD**.

Konstantinos Sfoungaris
4272682

Supervised by Dimitrios Chronopoulos; Savvas Triantafyllou

Faculty of Engineering
University of Nottingham

Signature ___________________

Date ______ / ______ / ______

Abstract

Components and structures accumulate damage during operation, which degrades their load bearing capacity and is prone to causing catastrophic failure. The demand for fuel efficiency and reduction of pollutant emissions has shifted the design of many structures, predominantly aerospace, to incorporate more composite materials. Composite materials are especially susceptible to critical failure due to operation-induced and accidental damage modes, that have adverse impact on the material strength. Timely detection and identification of damage is important in ensuring structural integrity and safety. Continuous and reliable condition monitoring of components is even more important in lightweight structures that have lower loadbearing redundancy.

Recent advances in sensors and signal processing, along with the availability of computational power, have rendered model-based monitoring and damage identification solutions attractive. Computational models for wave simulation remain, however, too heavy for conventional use. Robust and efficient modelling of certain damage modes, such as cracks, introduces additional complexities in numerical models for solids. Computational cost for inverse schemes, where multiple solutions for the unknown and sought damage parameters are required, even becomes prohibitive.

This work introduces mesh-independent modelling of damage through XFEM, in wave analysis. The behaviour of damage is investigated with the developed method, and validated by established explicit Finite Element models. A signal processing methodology with wavelet transform is also implemented to further investigate the feasibility of wave scattering as means of damage identification, with a view over available wave actuation and measurement methods.

The proposed methodology can achieve significant model reduction calculating wave scattering. Furthermore, identification of cracks is feasible, provided multiple wavemodes can be identified and measured.

Contents

List of Figures

Chapter 1

Introduction

Non-Destructive Testing techniques for Structural Health Monitoring have remained relevant in both Industry and Research in the last decades. The introduction of novel materials to accommodate for the demand of increased performance and decreased cost, the ageing and the elusive end-of-life-cycle behaviour of structures, a number of cases of spectacular structural failure—that shatter our perceived establishment of strength and safety standards-, along with the introduction and maturing of technologies along the gamut from sensors to data processing to analysis and modelling , have rendered SHM a candidate major pillar in Engineering sciences, along with Design and Analysis. Researching the possibilities of SHM and developing its features is an open quest, and the question to which extent might SHM come to complement the other pillars of Engineering is open.

Structural Health Monitoring is "the process of implementing a damage identification strategy for aerospace, civil and mechanical engineering" [1]. Non-Destructive Testing is the measurement of a material, component or structure's property whilst maintaining its structural integrity and functionality. Non-Destructive Evaluation and Non-Destructive Inspection are alternative terms used in the same context in the Literature. Taking the letter of the definition, SHM will necessarily incorporate NDT techniques. The distinction between the two is that SHM refers to a continuous process of informed application of Non-Destructive Techniques—among others—towards the assessment of the monitored

---

[1] Definition given by Worden et al. (2007) and a very popular one in Literature

object's condition. An integral SHM system might involve several NDT techniques to collect data regarding local damage, flaws and failure at different scales: an aircraft's SHM system involves several —scheduled or exigent—ultrasound checks for flaws, while also logging data from accelerometers and strain gauges mounted on its components. In this thesis, the terms SHM and NDT are both used depending on context, as though the techniques developed fall within the NDT technique spectrum, their development is done with mindfulness of integrated SHM systems.

1.1 Motivation

There exist both negative and positive reinforcing causes to implement NDT and SHM; negative, in the sense that one wishes to deter some consequence from not perusing, and positive in the sense that one aspires to somehow do better by perusing. The lack of monitoring may result in unpredicted catastrophic failure, with the subsequent toll. Implementing monitoring, on the other hand, may be advantageous in reducing downtime and implementing lightweight solutions in vehicles. Furthermore, the introduction of new technologies have rendered monitoring solutions attractive in comparison with other possibilities such as overdesigning and damage mitigation.

1.1.1 Cost of inspection and the greater cost of the lack thereof

Failure of structures is a cause for fear. The humane perception even more tends to focus on fearing spectacular catastrophic events. People have been found to be more afraid of dying due to a plane crash, rather than a car accident or heart attack, even though the two latter causes are several times more likely Shaver (2015). Engineering science has been focusing on improving safety and has done so, by learning from the collective mistakes of people who have built something that failed. Lives and fortunes have been lost due to failure. For one part, personal responsibility is key: driving carefully does help limit car accidents, and looking after one's health mitigates the risk of heart failure. It is among the engineer's responsibilities to learn from the mistakes of others, and a contemporary engineer carries experience from centuries of successes and failures of the art's practice. Considering the current morality and contemporary ethics, "killing the architect's son" [2] is not an acceptable repercussion and will definitely not undo any damage.

The very recent collapse of Ponte Morandi in Genoa, Italy, came to remind us of the grim consequences of failure. Several causes have been identified: hanging cables had had their cross section reduced; furthermore, a landslide is reported to have caused the collapse of one of the bridge's stays. An analysis conducted in 2017 noted a discrepancy of the order of 10% in the bridge's base eigenfrequencies from the ideal pristine state. Finally, the bridge was traversing its 51st year out of a projected 50-year life cycle. The referenced information, details and references can be found in the wikipedia page.

In 1988, Flight 243 of Aloha Airlines suffered catastrophic failure. The negative pressure that the fuselage experiences in high altitudes caused critical crack propagation. Cracks had been formed due to fatigue, around the windows, and exacerbated due to corrosion. It is one of the staple handbook case studies of fatigue-induced fracture. It is a common design consideration in aircraft fuselages, ship hulls, that openings should avoid sharp corners, as they cause stress concentrations. This is a problem examined by Fracture Mechanics and some further elaboration will be done in Chapter 2.

The cost of lack of inspection is indeed potentially vast. The approach of monitoring and inspections, however, is not without costs either. A trade off exists between overdesigning a structure (introduce higher safety factors) to reduce the risk of failure due to damage, and reduce the safety factors while introducing monitoring. The cost of inspection for commercial aircraft amounts to about 30% of their life cycle (Kessler et al., 2002). This is shifted to as much as 85% regarding defence assets (Derriso et al., 2016). Furthermore, 70% of the inspection expenses are incurred by airframe inspection.

Infrastructure is nowadays mounted with multiple sensors, to allow condition monitoring. Monitoring is accounted for in the cost. This can be considered as creating a precedent on the cost partition, with stakeholders finding that the cost of the lack of monitoring is

---

[2] "*If a builder builds a house for someone, and does not construct it properly, and the house which he built falls in and kills its owner, then that builder shall be put to death. If it kills the son of the owner, the son of that builder shall be put to death.*", from the Code of Hammurabi (Johns, 1903)

greater than the cost of the lack thereof.

1.1.2 Lightweight designs call for continuous monitoring

Recent decades have seen a consistent increase in usage of Glass/Carbon Fibre Reinforced Polymers (GFRP,CFRP), colloquially referred to as composites. The most desirable property they exhibit is their high stiffness to weight ratio; their absolute values for stiffness are still comparable to steel. Their strength and tolerance of extreme environmental conditions are also advantages.

Two driving forces can be identified for the increasing adoption of composite materials: performance and efficiency. Those both are compounded as on principle, lighter vehicles deliver more useful power. The distinction remains however, as the respective design philosophies exist: namely, performance design in aerospace, performance automotive and other sports applications such as sailing. Performance designs have pioneered the incorporation of composites and paved the way to everyday applications in fuel efficiency.

The introduction of composites has introduced new challenges in the analysis and design. Composites exhibit anisotropy in both stiffness and strength. Furthermore, their structure and properties can be tailored to fit the application. Consequent to their structure, their failure modes are complex and a lot of research has been invested in identifying and modelling them. Concerns for complex modes of failure, such as Barely Visible Impact Damage (BVID) that affects compressive strength of parts, require continuous inspection. Fatigue damage is also unpredictable and relative overdesign is required, with the introduction of large Safety Factors to counter the uncertainty of material strength.

The integration of SHM in the design of a part's or structure's life cycle opens the possibility of lighter, more efficient designs. The mission of SHM is to predict flaws in a timely manner and allow decisions to be made, regarding interventions, repairs and decommissioning. The design of an SHM system should therefore account for it's object structure's purpose and operation and allow informed decisions to be made. It is important to develop accurate and efficient NDT techniques that will address the challenges.

1.1.3 Smart structures are driving the development of SHM systems

The science and technology of structures is increasingly escaping the bounds of materials research and incorporates knowledge from different fields. Nowadays, reseach is more convergent, and boundaries between fields dimmer. Advances in different fields: sensor technlogies (Pramanik and Arockiarajan, 2019; Meyer et al., 2019), networks, data transfer and computer science (Wu and Jahanshahi, 2020; Bao et al., 2019), nanotechnology, tend to change the role of the material and the structural component, from a passive shell or support element to an active entity, capable of extracting information with respect to its environment's or its own condition, adapting to external stimuli and exercising control. The approach of SHM, i.e. continuous condition monitoring and assessment, is highly commensurate with the quest to incorporate sensing capabilities in materials. Interrogation and data acquisition are becoming an integral part of the structure, thus rendering the deployment of SHM systems feasible. Smart materials may have integrated SHM as an end goal, or their sensing capabilities might come as an auspicious side effect. Embedding ferromagnetic microwires in the polymer matrix affects the material's electromagnetic properties and makes stress sensing possible through coupling effects with microwaves (Qin and Peng, 2013). Piezoelectrics embedded in materials can act as vibration controls, energy harvesters and actuators and sensors for vibration and wave-based monitoring (Ji and Yun, 2020). The approach of incorporating SHM systems from the design and manufacturing stage of a component has been gaining ground (Tuloup et al., 2019; Meyer et al., 2019).

1.2 Background

SHM and NDT is an avidly multidisciplinary field, implementing diverse techniques for the structure interrogation, measurement acquisition, data processing and fusion, signal processing, analysis and inference. Novel technologies in equipment offer possibilities for accurate measurements, while mathematical and modelling tools make the processing of large quantities of data feasible.

This section surveys the state-of-the-art in NDT and SHM. The review is conducted by thematic: available modelling techniques; materials, behaviour and laws; NDT and SHM techniques based on dynamics: vibration and waves; finally, miscellaneous NDT and SHM techniques such as thermography and radiography.

Conclusions are drawn such that the scope and the projected impact of this thesis can be outlined.

1.2.1 Fundamentals of modelling in engineering

Science endeavours to understand the world through a process of creating models. The models' predictions are tested against data collected from nature—i.e. against reality-, and assessed on their meritful interpretation. A successful model in physics is one that interprets the most data with the least determinable parameters. To that end, the most successful to-date model is perhaps Einsten's General Relativity. GR has succeeded in predicting the elliptical orbit of planets, gravitational waves, and various instances of gravitational lensing around massive objects. With respect to the planetary motion, several theories have been tested through the ages: the epicycle theory (e.g. Ptolemy) postulated that celestial bodies had to be moving in cycles, as that was considered the divine shape; should the bodies aberrate from a perfect circular trajectory, they would be moving in a superposition of cycles [3]. The fact that the Earth was placed in the centre only made things more complicated. Eventually Newton introduced his laws that explained the motion of all bodies, using only one universal gravitational constant, which is what is used in most engineering applications, as structures that significantly warp space-time are not feasible from the economic-technical standpoint.

In engineering applications the interest is focused from making accurate predictions with the least possible parameters, to making predictions within a confidence interval with parameters that are feasible to measure. Physical models are consistently use during a

---

[3] The idea of circular superposition also governs Fourier's decomposition of functions into sinusoidal series, but, as with many other contraptions contemporary to Ptolemy's, such as Heron's steam engine, the implications of such ideas had not been thoroughly contemplated.

structure's conceptualization. Constructing an accurate physical model of an existent structure is significantly more complicated, when degradation and uncertainties are introduced. It is therefore advantageous to use generalized trainable models, that can make projections of the structure's response, if given sufficient data.

Physical models

Physical models in engineering applications are often derived from simple assumptions. Their scope is to simulate phenomena within a certain scope, surpassing which, transcends applicability. To that end, common phenomena are formulated as differential equations, e.g.: Maxwell's equations for electromagnetic fields, heat equation, Navier-Stokes equations for fluids.

The aforementioned methods refer to the assumption of continuum mechanics. Particle methods, peridynamics and molecular dynamics are other methods of simulation that do not adhere to the continuum assumptions, opting for particle interaction laws instead. They are accurate albeit difficult to calibrate and computationally very costly.

Computational models for NDT and SHM involve solid mechanics almost exclusively, although occasional acoustic, thermal and electromagnetic phenomena are considered in specific applications.

The dynamic equilibrium equation for a continuous solid body Ω reads

$$\nabla \cdot \boldsymbol{\sigma} + \mathbf{b} = \rho \ddot{\mathbf{u}} \tag{1.1}$$

where $\boldsymbol{\sigma}$ is the stress tensor, $\mathbf{b}$ some body force, ρ the material density and $\ddot{\mathbf{u}}$ the second derivative of displacement with respect to time, i.e. the acceleration of the infinitessimal. The dot operation between the nabla a quantity denotes the divergence, and decreases the order of the quantity operated upon: vectors become scalars, and 2nd order tensors, e.g. stress in this case, become vectors. The compatibility equation is used to impose that the integral of the deformation field, along any path, will equal to the displacement;

this, in infinitessimal deformation assumption is given as

$$\boldsymbol{\varepsilon} = \frac{1}{2}(\nabla \mathbf{u} + \nabla^T \mathbf{u}) \tag{1.2}$$

with the superscript ^{T} denoting the transpose and $\boldsymbol{\varepsilon}$ the Cauchy strain tensor. The nabla operator applied directly on a quantity signifies the gradient thereof, and the resultant term is one order higher than the original: displacement vectors are mapped to a 2nd order tensor. A constitutive equation is required to connect the displacement with the stress. Linear Elasticity is commonly used that reads

$$\boldsymbol{\sigma} = \mathbf{C} : \boldsymbol{\varepsilon} \tag{1.3}$$

with $\mathbf{C}$ Hooke's elasticity tensor (further detailed in next section). The double dot operation signifies contraction along two dimensions of the involved quantities. Equivalently, the above Eq. (1.3) is written as

$$\sigma_{ij} = C_{ijkl}\varepsilon_{kl}$$

.

The solution of the above also requires knowledge on the boundary $\partial\Omega$ of the problem. Dirichlet conditions are of the type

$$\mathbf{u} = \bar{\mathbf{u}} \quad \text{on} \quad \partial\Omega_u, \tag{1.4}$$

whereas Neumann conditions are prescribed as

$$\mathbf{t} = \boldsymbol{\sigma} \cdot \mathbf{n} \quad \text{on} \quad \partial\Omega_t. \tag{1.5}$$

The conditions are mutually exclusive, such that $\partial\Omega = \partial\Omega_u \cup \partial\Omega_t$ $\partial\Omega_u \cap \partial\Omega_t = \emptyset$.

Analytical solutions

The direct solution of Partial Differential Equations (PDE) is possible for a limited number of cases where some regularities in the domain exist. Mathematical techniques such as conformal mapping Muskhelishvili (1977) have been devised and used to extract an exact solution wherever possible. Solutions to relatively complex domains are commonly given as a series sum of infinite terms. The stress field around a crack is a problem of particular interest in fracture applications, as singularities appear on the crack tips. This problem is detailed in Chapter 2. Simplifying assumptions are made in engineering practice for several types of structures, such as beams (Euler, Timoshenko), plates (Kirchoff-Love and Reissner-Mindlin) and shells, allowing for reduced order modelling without loss of accuracy.

Numerical solution

Galerkin methods are commonly employed to find approximate solutions for PDEs. The Finite Element Method (FEM) is the most widely applied one in both industry and research. The variation of the total work of the sytem is taken as the sum of internal stresses and external forces. This is accomplished by imposing a virtual displacement $\delta\mathbf{u}$ and the subsequent strains.

$$\underbrace{\int_\Omega \left\{\delta\mathbf{u}^T\nabla\cdot\boldsymbol{\sigma} + \delta\mathbf{u}^T\mathbf{b}\right\}\mathrm{d}V}_{\delta\mathcal{U}^{int}} = \underbrace{\int_\Omega \delta\mathbf{u}^T\rho\ddot{\mathbf{u}}\mathrm{d}V}_{\delta\mathcal{U}^{ext}} \tag{1.6}$$

By invoking the divergence theorem and in the absence of body forces, the internal work can be written as

$$\delta\mathcal{U}^{int} = \int_\Omega \delta\boldsymbol{\varepsilon} : \boldsymbol{\sigma}\mathrm{d}V = \int_\Omega \boldsymbol{\varepsilon} : \mathbf{C}\boldsymbol{\sigma}\mathrm{d}V. \tag{1.7}$$

The Finite Element and other discrete methods discretize the displacement field in a finite number of unknowns. In the FEM case the unknowns are individual displacements on nodes, interpolated through polynomial functions. The unknonw fields take discrete values, and the differential equation is cast into a system of algebraic equations

$$\mathbf{K}\mathbf{u} + \mathbf{C}\dot{\mathbf{u}} - \mathbf{M}\ddot{\mathbf{u}} = \mathbf{F} \tag{1.8}$$

with **K** the stiffness, **C** damping and **M** mass matrices, **F** the external force and **u** the displacement and its time derivatives.

FEM, in particular, constructs a mesh, i.e. discretized the domain Ω in elements Ω^e, intersecting at the nodes, and the interpolation functions are supported at the neighbouring elements. Meshless Galerkin does not explicitly construct a mesh, but smears nodes and defines their support through e.g. Voronoi cell subdivision. The eXtended or Generalized FEM (XFEM/GFEM) introduce approximation functions specific to the projected behaviour of the analytical solution in the domain, along the classical polynomials, and are capable of mesh-independent simulation of discontinuities and have demonstrated improved convergence in singularities, without the need for extreme refinement. The Finite Difference method is another discrete method that approximates the infinitessimal derivative as a discrete difference.

Non-physical models

The category of non-physical models involves those models that emulate a system's response, without making assumptions about its inherent behaviour. They have multiple free parameters, which do not necessarily have physical meaning. Consequently, they require a large amount of data to calibrate or train. Artificial Neural Networks (ANN) (Lee et al., 2021), polynomial chaos expansion (Spiridonakos and Chatzi, 2015), nonlinear autoregressive models with exogenous input (NARX) (Mai et al., 2016), Gaussian process time-series (Avendaño-Valencia et al., 2020) are some of the available models. Lai et al. (2020) implement a physically-informed model, combining the generality of non-physical models with the anticipated behaviour of a beam structure.

Meta-modelling

The technique of meta-modelling comprises training a non-physical model on a numerical model. This is advantageous in cases where a physical model is particularly computationally taxing, its response however varies with a certain normality with respect to its parameters. Strategic sampling the response surface and training a surrogate model can lead to significant computational savings. Zhang et al. (2019) implement a surrogate-assisted GA for damage detection in composites. Oftentimes, ANNs are trained as surrogate models, with datasets produced through physical (e.g. FEM) models (Parra dos Anjos Lima et al., 2014; Yam et al., 2003).

1.2.2 Material behaviour and constitutive laws

The motivation of NDT and SHM is to detect and idenfity damage while it is at a subcritical stage, allowing for intervention before the structure succumbs to it. There exist several ways in which damage might manifest in a structure, depdendent mainly on the constituent materials. In fact, the damage of materials is intertwined with their mechanical behaviour. Furthermore, NDT and SHM methods are devised on the premise of measuring the effect damage has on material properties, be it mechanical, thermal or electrical.

Material constitutive models attempt to model the material behaviour including failure. They endeavor to achieve this via a set of parameters. Those may be explicit, or parameters with physical meaning that can be objectively determined, or implicit, that do not have a physical meaning and are fitted by experimental measurements Orifici et al. (2008). Generalized models, such as ANNs can be used to that end (e.g. Yang et al. (2020).

In this section available material models are overviewed, under the perspective of relevance with NDT and SHM applications, i.e. the capability of each constitutive model to interact with the NDT and SHM modelling approaches. Also, the contribution of constitutive models towards damage identification.

Linear elasticity

Linear elastic behaviour of materials is the most common modelling assumption. The theory of linear elasticity is based on the properties of the interatomic potential Naumann (2008), i.e. the energy-distance relationship. When atoms form a bond, they stabilize, or minimize their energy, at a specific distance; should they be perturbed from their position, they develop a force that tends to revert them back to position. If they are pulled very far apart, their bond eventually breaks. The interatomic potential, for small perturbation positions, is well-approximated through a parabola, and has a quadratic shape. Hence the theoretical basis for linear elasticity. Materials that exhibit inelastic behaviour, do so for large deformations. The nonlinear elastic behaviour is conventionally attributed to polymers. Polymers, are comprised of chains of large molecules. The bigger part of they display during loading is attributed to the displacement and realignment of those chains. When the external load is removed, the chains return to their initial configuration, thus restituting the elastic work. Hyperelasticity is the model conventionally used to describe this type of behaviour; its properties are outside the scope of this work.

Hooke's law is based on the quadratic interatomic potential

$$\mathcal{U} = \sigma_{ij}\varepsilon_{ij} = \varepsilon_{ij}C_{ijkl}\varepsilon_{kl} \tag{1.9}$$

with σ_{ij} the component of the stress tensor, ε_{ij} the strain and C_{ijkl} Hooke's tensor. Strain and stress are called conjugate quantities, and the stress can be derived from the elastic potential as

$$\sigma_{ij} = \frac{\partial \mathcal{U}}{\partial \varepsilon_{ij}}. \tag{1.10}$$

Hooke's tensor possesses major symmetry, such that

$$C_{ijkl} = \frac{\partial \mathcal{U}}{\partial \varepsilon_{ij}\partial \varepsilon_{kl}} = \frac{\partial \mathcal{U}}{\partial \varepsilon_{kl}\partial \varepsilon_{ij}} = C_{klij}. \tag{1.11}$$

This property entails the reciprocity principle for elastic bodies, such that deformation at a point $\mathbf{x}_I$ due to action at a point $\mathbf{x}_J$ equal to the deformation at the point $\mathbf{x}_I$ due to action at $\mathbf{x}_J$. Furthermore, Hooke's tensor possesses minor symmetries

$$C_{ijkl} = C_{jikl} = C_{ijlk}. \tag{1.12}$$

Thus the number of elastic parameters is drastically reduced.

In the case of isotropy, the constitutive relation is reduced to two parameters. Lamé's equation reads

$$\sigma_{ij} = \lambda \varepsilon_{kk} \delta_{ij} + 2\mu \varepsilon_{ij}, \tag{1.13}$$

δ_{ij} the Kronecker delta and μ the shear modulus, also referred to as G. Albeit Lamé's equation's elegance, elastic materials are characterized by E, ν, or, Young's modulus and Poisson's ratio respectively. Those are friendlier to experimental identification, as Young's modulus is the slope of a material's stress-strain curve in the elastic regime. Poisson's ratio represents the transverse contraction a material experiences in relation to some applied extension. Lamé's constants are related to Young's modulus and Poisson's ratio as

$$\lambda = \frac{E\nu}{(1+\nu)(1-2\nu)}, \quad \mu = \frac{E}{2(1+\nu)}. \tag{1.14}$$

Last, it is common in applications to use a convenient matrix notation. For a 2D stress state, Hooke's law can be written as

$$\begin{Bmatrix} \sigma_{11} \\ \sigma_{22} \\ \sigma_{12} \end{Bmatrix} = \begin{bmatrix} C_{11} & C_{12} & 0 \\ C_{21} & C_{22} & 0 \\ 0 & 0 & C_{33} \end{bmatrix} \begin{Bmatrix} \varepsilon_{11} \\ \varepsilon_{22} \\ \varepsilon_{12} \end{Bmatrix}. \tag{1.15}$$

For an isotropic material in plane stress, $C_{11} = C_{22} = E/(1-\nu^2)$, $C_{12} = C_{21} = \nu C_{11}$ and $C_{33} = \mu$.

Plasticity

When a material is loaded, it deforms; if the load is removed and the material has retained residual deformation, it has exhibited plastic behaviour. Plastic deformation is related to alterations in a material's microstructure. Plastic behaviour is default for soils and clay. For metals, plasticity is attributed to the movement of the dislocations of the crystal structure. Other materials, such as ceramics, composites and concrete, do not exhibit a plastic behaviour per se, as the residual or 'plastic' deformation they develop is directly connected with damage in the material, such as the appearance of microcracks or matrix-fibre debonding. Elastic-plastic constitutive laws split the deformation into an elastic and a plastic part. The material behaves elastically so long as its stress does not exceed a yielding threshold. When the thershold is exceeded, the material deforms without the load increasing, or, without developing further resistance. In practice, most materials do not exhibit perfect plastic behaviour, and some further resistance is developed in the plastic regime; this phenomenon is called hardening, and is attributed to the impeding of the dislocation motion, predominantly in grain boundaries and solute atoms of alloys (e.g. carbon atoms dissolved in the iron lattice in steels). Several other materials are capable of exhibiting some hardening behaviour. Reinforced concrete, for instance, yields after the concrete cracks, but is capable of developing further resistance with the rebars.

Continuum damage mechanics

Continuum Damage Mechanics (CDM) Lemaitre and Chaboche (1994) introduce the notion of stiffness loss of the material, when a stress threshold is exceeded. The damage relation postulates that, after a certain stress threshold is attained, damage due to microcracking results in loss of stiffness and energy release. This is expressed as

$$\sigma = (1 - \phi) E \varepsilon, \tag{1.16}$$

with ϕ a damage variable that takes values from 0 for pristine to 1 for fully damaged state. A more general tensor formulation of damage mechanics exists, implying that damage due to a stress component can reduce another component's respective stiffness. The increase of the damage parameter is connected with energy release of the system due to microckracking, which draws a parallel between continuum damage mechanics and fracture mechanics (Nairn, 2018). Nairn (2018) investigate the connection of CDM with

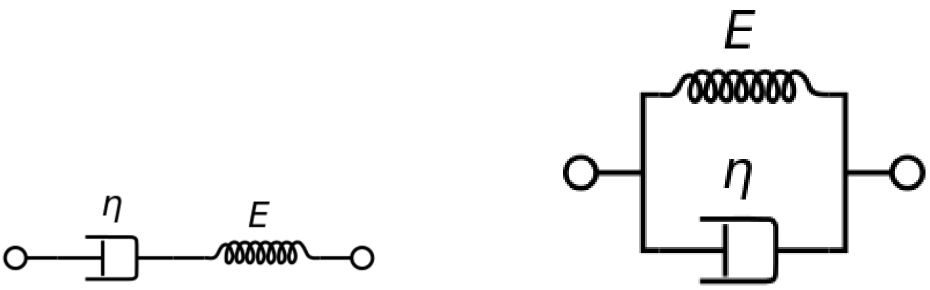

(a) Maxwell (b) Kelvin-Voigt

Figure 1.1: Viscoelasticity models

Fracture Mechanics (Chapter 2), by running parallel computational experiments with FE models that employ either model. Agreement of the two is achieved, provided some criteria be fulfilled regarding anisotropic damage.

Viscosity

Viscous behaviour of materials is exhibited when their mechanical response is not only dependent on the strain, but also on the strain rate. The two basic viscoelastic models are the Maxwell (Fig. 1.1a) and the Kelvin-Voigt model (Fig. 1.1b). The Maxwell model reads

$$\sigma = \frac{\eta}{E}\dot{\sigma} = \eta\dot{\varepsilon}, \tag{1.17}$$

and the Kelvin-Voigt model

$$\sigma = E\varepsilon + \eta\dot{\varepsilon} \tag{1.18}$$

with η the damping coefficient and $\dot{\circ}$ the time derivative of a quantity.

Maxwell's model describes a situation where a material, when loaded instantaneously, exhibits elastic behaviour. If the load persists, the material will deform further with time. The Kelvin-Voigt model describes a situation where a material that's subjected to constant stress, instantaneously takes zero deformation, but as time tends to infinity, the deformation stabilizes at σ/E. This behaviour a material exhibits, when deformations develop over time over constant load is called creep and it's observed typically in concrete, polymers, and in metals at temperatures close to the melting point.

In vibration, the presence of the viscous constant η implies that the system loses energy.

Looking at a the dynamic equilibrium equation of a 1 DoF oscillator

$$m\ddot{x} + c\dot{x} + kx = 0, \tag{1.19}$$

a solution of the form

$$x = Ae^{-\zeta t}\cos(\omega t) \tag{1.20}$$

is reached, with ζ a constant that depends on c, k, m and $\zeta = 0$ when $c = 0$, and ω the system's eigenfrequency. It can be seen that, when $c = 0$, the system oscillates with amplitude A. If $c > 0$, the amplitude decays exponentially.

Fatigue of metals

Beyond failure due to critical loading, materials generally fail when subjected to several cycles of sub-critical loads, a phenomenon called fatigue. Fatigue failure in metals occurs gradually. First, a small crack initiates, usually from points of stress concentration, such as notches and concave corners. The propagation of the crack has been connected to the stress range of the cycle. As facture is of concern, the Stress Intensity Factor is rather used to evaluate the stress field around the crack. Paris' law for fatigue crack propagation is applicable in metals, reading

$$\frac{da}{dN} = C(\Delta K)^m, \tag{1.21}$$

with da/dN the crack extension per load cycle. $\Delta K = K_{max} - K_{min}$ is the range of the SIF. C, m, are material parameters experimentally determined. Paris' law is applicable for an intermediate regime of the material's fatigue life, with the initial regime connected to crack initiation and the final regime to accelerated crack growth.

Fatigue cracks propagate forming striations (DeVries et al., 2010). Measuring and counting striations it is possible to obtain information about crack growth rates and load levels. The environmental conditions affect the material's fatigue life. Corrosion is found to compound fatigue —e.g. in pipelines Mansor et al. (2014). The detection and identification of fatigue cracks is an important aspect of NDT and SHM and most of the established methods have been implemented towards that end: microscopy, X-ray radiography, acoustic emission, ultrasound e.t.c. (Kong et al., 2020). Wave-based methods usually target the higher harmonics generated by nonlinear phenomena such as crack kissing, to detect and identify fatigue cracks (Yang et al., 2018; Dutta et al., 2009).

Mechanical behaviour of composite materials

The survey of damage modes in composite materials is of particular interest in engineering applications, as their usage dominates aircraft and automotive design, where demand for safety and reduced weight is high. A plethora of failure models exist for composites, and consensus on their usage has not yet been reached. To this date, three World Wide Failure Exercises (WWFE) have been convened (Singh, 2015), to test the robustness of the proposed models. While the first two WWFEs were concerned with the prediction of ultimate failure, WWFE III accounted for the damage initiation and the evolution of subcritical damage.

Failure criteria for composites appear in generalized and physics-based formulations (Icardi et al., 2007). Generalized criteria assume composites to be homogeneous, anisotropic continua, and implicitly describe failure with few intrinsic parameters, without attempting to delve into the physical processes. Among those criteria are Tsai-Wu and Tsai-Hill. Physics-based criteria attempt an approach that accounts for the separate modes of damage, their initiation, evolution and interaction; they use objectively measurable parameters and distinguish between tensile and compressive stress states. An example is the Hashin criterion, that accounts for different failure modes with different equations, and has successfully predicted progressive failure of laminates (Icardi et al., 2007).

Composites under axial tensile loading, develop ply cracks Singh (2015). Those are cracks that transverse the fibre grain. They appear in plies whose fibre alignment is transverse to the loading direction. As composites are usually comprised of several plies with different fibre orientations, the development of the cracks stops. The existence of those cracks has limited effect on the strength and stiffness of other directions of the material. It is possible, however, for the cracks to propagate on the inter-ply surface and branch out to cause delamination, which has adverse effects on the composite's strength.

Impact-induced damage is a commonly occurring damage mode in composites (Gaudenzi et al., 2015; Polimeno and Meo, 2009; Aymerich and Staszewski, 2010; Pérez et al., 2014). Impact damage is classified with respect to velocity, and even low-velocity impact is perceived to affect the structural integrity of the material Polimeno and Meo (2009). The campaign to model impact damage and assess its effect on the composite's redisual strength has been extensive (e.g. (Choi et al., 1991; Williams and Vaziri, 2001; Iannucci and Willows, 2006)). Iannucci and Willows (2006) present a FE model to describe impact damage, by incorporating in-plane CDM-based laws, along with a fracture mechanics approach for delamination using interface elements. Papa et al. (2021) investigate the extent of impact damage on C-G-BFRPs with phased array transducers.

Fatigue behaviour of composites has remained a field of intensive investigation for several decades. The multitude of mechanisms and their interaction, along with the very varied and oftentimes tailored layup of composite parts, have proven to make the formation of a unified theory of fatigue a possibly impossible task.

As factors that affect the fatigue behaviour of composites have been identified Wicaksono and Chai (2013) the type of fibre, the type of matrix, the reinforcement of the matrix with nanoparticles, the stacking sequence of plies, the loading and the environmental conditions. Carbon fibre has been found more resilient than glass, while kevlar reinforcement has exhibited uncertain behaviour. Thermoplastic resins are preferable over thermoset resins due to their ductility that leads to longer fatigue life. Tougher resins lead to higher interlaminar fracture toughness. The interface properties of the resin and fibre should be also taken into account though. The addition of nanoparticles (e.g. carbon nanotubes) has shown to improve tensile and impact strength and fatigue life, while easing the access to electrical conductivity-based SHM, which is prospectively useful in micro-damage detection, which is critical in composites.

Fatigue damage in composites is heavily dependent on the direction of reinforcement and the stacking sequence, as well as the load conditions. A certain composite may exhibit different damage progression depending on whether its load cycle comprises tension-tension, tension-compression, or pure compression. When composites are subjected to compressive load cycles, it is possible that failure will begin with fibre buckling, which is prone to occur in the fibres that have poor support, i.e. close to free surfaces or if their matrix is cracked. For composites subjected to tensile cycles, fatigue damage initiates in the form of matrix cracks (Fig 1.2 1), on the plies orientated transversely with respect to the load. The cracks progress and some fibre breakage occurs. As the crack density increases, fibre/matrix debonding occurs, allowing for the cracks to grow and interact. As cracks reach the inter-ply boundaries, they branch to delamination. Ultimate failure occurs when ply cracks and delaminations are connected.

The behaviour of woven composites differs from unidirectional ones, and several of the modes described above are not applicable. They exhibit better impact resistance, damage tolerance, dimensional stability over temperature and are relatively easy to manufacture. Common modes of damage are matrix microckracking, fibre breakage, crack coupling and fibre-matrix interfacial debonding.

Fatigue damage is compound when other forms of damage are present. Garnier et al. (2013) investigate the remaining life of impacted composites through experimentation with low speed impact. The extent of the damage is assessed through 3D photogrammetry and infrared thermography. Damage is found to evolve from the impacted area.

In conclusion, fatigue in composites is inconclusive. A general trend is microckracks that interact and evolve, branching out to delamination and ultimate fibre breaking. From a macroscopic perspective, the degradation over a composite's lifetime evlolves in this manner: an abrupt increase happpens in early fatigue life, which remains steady for the bigger time of the material's life; a second phase of decline begins after a critical point, which leads shortly to ultimate failure Gaurav and Singh (2018).

Most damage modes in composites have a direct effect on the material's stiffness, electrical and thermal conductivity. The detection thereof is possible with conventional means. For early damage, such as microcracking, very high resolution is required—i.e. very high frequency waves—which may make detection and identification difficult. The adverse behaviour of composites under different modes of loading and the interaction of different modes of damage from different causes, make SHM an attractive approach. It is normal

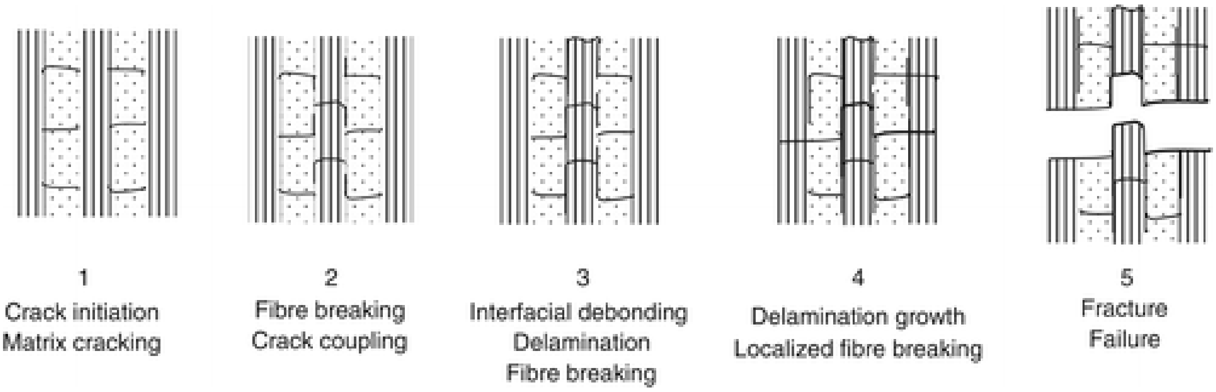

Figure 1.2: Damage progression in cross-ply laminates subjected to only tension load cycles Naik (2003)

for a structure's composite components to be experiencing different load cycles and have a different risk of random events such as impact damage. The assessment of damage evolution in composites is advantageous, both from an early intervention standpoint, as well as a repair-and-replace perspective of dynamic updating of the structure with more suitable components—e.g. different layup—for the loading they experience.

Conclusions

The laws for linear elasticity, plasticity, continuum damage and viscosity have been briefly presented, along with the fatigue behaviour of metals. The mechanical behaviour of composites in the nonlinear regime, failure and fatigue have also been examined.

It is of interest to be able to identify metal components that have been subjected to yielding. Even though plastic laws do not appear to have an effect on the dynamic properties of metals, i.e. density and elastic modulus, it is possible to detect yielded material through nonlinear interactions (Gaurav and Singh, 2018).

Damage mechanics are connected with the existence of micrcracks in the materials. As the stiffness of the material is affected, the dynamic properties are altered, creating possible scatterers. Small cracks require very high frequencies to interact with.

Fatigue cracks in metals are detectable, and exhibit nonlinear phenomena such as harmonic generation (Yang et al., 2018). Acoustic emission is also possible.

Failure in composites manifests in different ways, e.g. microcracking, debonding and delamination. It is possible to identify those modes of damage with various methods.

The development of smart materials aspires to establish high resolution SHM.

1.2.3 Vibrational methods for NDT and SHM

Vibration-based methods rely on changes in fundamental sturctural behaviour, which is proper frequencies and modes of vibration, to detect damage. A structure's vibrational behaviour is governed by its stiffness, mass and damping properties. Presence of damage results in local modification of any of those parameters, thus altering the structure's properties. By finding altered properties in a structure, it is logical to infer the presence of damage. Vibration-based methods have been extensively applied in NDT and SHM, for several decades Salawu (1997); Doebling et al. (1998); Zou et al. (2000); Della and Shu (2007); Gomes et al. (2019). They are commonly applied in large infrastructure, such as buildings, bridges and dams Avci et al. (2021) and wind turbines Li et al. (2015). Application in composite components is commonplace Zou et al. (2000), as the common damage modes they exhibit, delamination, matrix cracking, fibre breakage and perforation, have been demonstrated to affect the vibrational behaviour of composite components Kessler et al. (2002).

Vibration-based methods commonly comprise a number of discrete stages: actuation, measurement acquisition, model reconstruction, feature extraction and damage identification. The identification process might involve an inverse procedure, which is model-based. The different stages are examined below.

Actuation

In order to measure a structure's vibrational response, it needs to be somehow excited. Structures tend to resonate with external excitations: they will vibrate with their available eigenfrequencies closest to the frequency of the external load. Large infrastructure tends to exhibit default vibrational behaviour form ambient conditions Sevieri and De Falco (2020). Vibration due to the operational conditions of certain components is possible Avendaño-Valencia et al. (2020). In such SHM systems, ambient conditions are taken into account when measuring a structure's response. Forced excitation is possible, and is achieved commonly in NDT through PZTs or small strikes of a hammer for smaller components, as they require higher frequency input that is usually not possible within their environment. Excitation with user-defined signal e.g. sinusoidal sweep Yam et al. (2004), is possible with the usage of PZTs and shakers.

Sensors and measurement

For the acquisition of data, accelerometers, PZTs and laser vibrometers are commonly used. In larger structures, additional sensors for acquisition of wind, temperature, humidity and other data might be relevant. Those sensors are capable of collecting data at a specific point. PZTs and accelerometers are either glued or embedded on the structure, whereas laser vibrometer targets specified points to acquire measurements. Spurious mounted PZTs and accelerometers disturb the structure, as they act as added mass. This may affect the structure's vibrational properties and thus, to some extent, the measurement process will affect the outcome. Expecting the mode shapes of a structure, allows to optimize the placement of sensors, as in Ostachowicz et al. (2019); Gomes et al. (2018) where FE models are used together with optimization algorithms, so that maximal data is acquired with as few sensors as possible. Furthermore, PZTs are often embedded by design in smart materials, i.e. composites, as in Ji and Yun (2020); the PZTs there assume multiple roles, as actuators, sensors, but also converters of vibrational energy to electricity. Laser vibrometers are non-contact and thus less intrusive than PZTs and accelerometers, while very accurate and sensitive. Their downside is the need for an operator to target specified points on a structure, which might be an arduous task for high resolution data acquisition. Despite their accuracy, laser vibrometers are not suitable for continuous monitoring applications, unless this process is automated. Full-field data are possible to acquire from the use of cameras; Wang et al. (2012) use stereo placement of high speed cameras and extract mode shapes with Digital Image stereo-Correlation. Despite the undisputable advantage of full-field measurements, the data load from the cameras is too high to accommodate with contemporary technoeconomic means, for conventional usage. Lai et al. (2020) propose event cameras, that record only changes in pixel brightness, thus reducing the data load. This is developed further, with sampling at multiple time scales.

Model reconstruction

In NDT and SHM processes, data are acquired from disparate sensors in time-history form, meaning that values of the measured quantities are sampled at specified times. The sensors are capable of measuring the respective quantities soleley at the point they are located. In order to make sense of the structure's behaviour, a frequency domain interpretation is needed [4]. Frequency-domain transforms are available for that end. Fourier transform and its algorithmic implementation, FFT, are commonly used. When a system is artificially excited, it is possible to measure the input frequencies, and construct the Frequency Response Function Pérez et al. (2014).

Despite their undisputable useflulness, frequency domain representations banish the notion of 'event'. Time-frequency analyses are capable of representing both the frequency domain and time-dependent alterations thereof. Short-time Fourier Transform (STFT) is used by Khan et al. (2019) to extract features for damage identification in the time-frequency domain, to be used as images to train a CNN. Avendaño-Valencia et al. (2020) employ CWT in their time-domain signal, in conjunction with multiple temporal scale sampling, to extract a baseline low-frequency behaviour and a short-term high frequency response.

Feature extraction for damage identification

In order to detect and identify damage through a structure's vibration, some quantifiable index must be evaluated. Changes in fundamental frquencies are often used. Those allow damage detection and estimation of its severity; in informed cases, it is also possible to identify the damage mode and its location. This, however, requires, and its success depends on the boundary conditions of the structure, as structures whose modes are highly symmetric, would create very high ambiguity about the damage's location. Ooijevaar et al. (2010) use a citerion of the modal strain energy reduction at the presence of damage, that

---

[4] Our sense of hearing is based frequency identification in a similar manner

reduces local stiffness. Pérez et al. (2014) use a PrMAC criterion, that correlates the mode shape of the measured damage structure with the modelled pristine shape, and quantifies the damage extent. The curvature of the mode shape is often used to localise damage. Janeliukstis et al. (2015) use CWT on measured mode shapes of a beam to illuminate damage features. Fan and Qiao (2009) implement a 2D CWT, and extract damage features of a plate, in the form of iso-surfaces.

Inverse damage identification

Inverse identification of damage (Gomes et al., 2019) employs a model, in which the damage is represented through a set of finite parameters. The model's response is compared to the measured response of the structure, and its parameters are varied until a repsonse is obtained, that's identical—to some measure—to the actual measured one. Optimization algorithms (e.g. Zhang et al. (2019)) construct a positive scalar function from the norm of the differences of the model's response and the actual measurements, and seek the model parameters that will minimize said function. Artificial Intelligence based inversion refers to employing a generalized model, namely a neural network and calibrating—or training—it to feasible parameter configurations. When some measured data are input in the AI, it will classify their causal parameters according to its experience. Inverse models shift a method's complexity, from data acquisition to computation. Zhang et al. (2013, 2018, 2019) employ a surrogate-assisted Genetic Algorithm (GA) with a Finite Element (FE) model to locate damage. Gillich et al. (2014) develop an alnalytical model to assess transversal cracks in composite beams. Yin et al. (2010) employ an analytical model for plate containing a surface crack, and utilize Bayesian inference along with various sensor configurations to examine the identifiability of damage with few data. Rabinovich et al. (2007) use the eXtended Finite Element Method (XFEM) to solve the forward problem of a cracked plate, thus reducing computational complexity required for remeshing multiple possible configurations of the crack. Yam et al. (2003); Khan et al. (2019); Vega and Todd (2020); Zhang et al. (2019, 2018, 2013) employ Artificial Neural Networks (ANN) for the solution of the inverse problem. Yam et al. (2003) train an ANN with features extracted from CWT on the time-history response, with a single sensor. Khan et al. (2019) use Convolutional Neural Networks (CNN), which are, in principle, used in computer vision applications. The input data are Short-Time Fourier Transform (STFT) spectra in the time-frequency domain, from which the CNN extracts damage features. Zhang et al. (2019, 2018, 2013) compare the performance of ANN against optimization processes, namely surrogate-assisted GA. They report that GA are more robust, as ANN are sensitive to noise in data. Overfitting is an open issue with ANN, as they have a large number of free parameters, which can be fit on noisy data. Vega and Todd (2020) employ a Bayesian neural network, which is less sensitive to overfitting and displays better performance in the presence of noise. Pan et al. (2019) propose a noise response rate to identify frequencies most affected by noise, select the least sensitive ones, to obtain better accuracy. The aforementioned ANN are trained with FE models. An analogy can be drawn between optimization and ANN-based inversion: optimization-based methods solve the models on demand, with a variation in parameters specified by the optimization process, i.e. the gradient of the cost function. Better efficiency can be constructed by the usage of surrogate models, (e.g. Kriging) which adaptate to the sensitivity of the response and adjust their sampling. In ANN-based inversion, a set of data ought to be generated a priori, without informed knowledge. It is possible, however, to splice model-generated and measurement-generated data to train the model, thus taking into account existent experience. Such an approach would require extended parametrization and complicated model updating with FE models. In general, ANN approaches are attractive for cases where a structure's parameters are not easily accessible, but experimental response data can be collected.

Data-based surrogate models

Bearing in mind the distinction between physical and generalized models, one assumes the possibility of utilizing the latter to emulate a structure's behaviour. As already mentioned above, ANNs are useful when the reconstruction of a physical model from an existing structure is too costly, due to the number of parameters that need to be determined or estimated. For example, a structure whose geometry is very complex and material properties have degraded over time, introduces uncertainties that cannot be mapped in a FE model in a straightforward manner. With the management of big data and the high degree of interconnectivity that is being achieved with current technology, continuous collection of data is feasible, and data-driven models have become an attractive alternative. Those work generally by extracting a long-term ’normal’ behaviour of the structure; when some damage is introduced, outliers in the structure’s response are recorded and assessed. Avendaño-Valencia et al. (2020) employ a two time scale sampling approach in wind turbines. A sampling rate of a few seconds is used to account for the baseline operational vibration and rotation of the turbine; ambient data are also measured, and a causal approach is attempted through a gaussian-process auto-regressive time-series model. The SHM process utilizes a second short-term sampling in the order of milliseconds, that is actuated by mounted PZTs; this is activated only when it is indicated that further inspection is required. Lai et al. (2020) use event cameras to obtain full-field measurements at relatively small data cost. Two temporal-scale sampling is used, for baseline frequencies and for higher ones. A physics-based model is fitted, employing assumptions of the mechanical behaviour of the system modelled, without assuming any of the model’s parameters. Sevieri and De Falco (2020) utilize polynomial chaos expansion to model the vibrational behaviour of a dam; Bayesian inference is used in the identification process. Some auxiliary FE models are constructed to simulate possible damage modes.

Conclusions

Vibration-based methods for NDT and SHM have been current for several decades (Salawu, 1997; Doebling et al., 1998; Zou et al., 2000; Della and Shu, 2007; Gomes et al., 2019). The amount of literature is vast, spanning various possible configurations of the stages identified above. This review did not exhaust the extents thereof, but identified the stages and modulated the existing works, such that new works can be interpreted as a combination of the approaches outlined.

Damage identification in vibration-based methods depends on the resolution that can be achieved through measurements. The smaller the damage, the higher the frequency required, the smaller the characteristic length of the mode shape. Capturing higher frequencies is prone to higher levels of noise; capturing the mode shapes of higher frequencies requires more sensors mounted on the structure at different locations. Approaching a problem of monitoring structures, it is useful to expect the possible modes of damage. The extent of damage and the residual strength of the structure subject to it should always be accounted for: when implementing some approach, it should be able to identify damage whose severity is still sub-critical and avert catastrophic failure. For example, Ponte Morandi's fundamental eigenfrequency, in measurements conducted a few years before its collapse, was found to have a 10% deviation from what was expected from a healthy structure. Deviations of such magnitude are commonly detectable with the means discussed here. Wave-based monitoring is a viable alternative for identification of flaws whose size is small comparable to the size of the structure.

With the distinction between NDT and SHM introduced, vibration-based methods can be classified on whether they can be employed for continuous monitoring, or on scheduled inspection. For example, the process of disassembling a component from a vehicle and striking it at several points with a hammer, in order to obtain the FRF, cannot be straightforwardly adapted for continuous monitoring. To this end, forward methods and hammer-strike actuation, along with laser vibrometers, despite their undisputed merits, are not promising solutions for SHM applications. PZTs on the other hand, can be easily embedded in materials and act as both actuators and sensors, allowing for conceptually designed integrated monitoring.

Forward approaches generally demand a high volume of measurements, which cannot be made in situ and in real time. Inverse approaches shift the workload form data acquisition to computing possible scenarios. As computational capacity has increased dramatically in recent years, and available modelling techniques have progressed, inverse approaches are becoming more attractive. It is not far-fetched to be discussing about integrating computers in the structures, along with sensors (Yuan, 2016), that will continuously interpret data of the structure's condition.

There is no clear advantage between physical and statistical models for montioring and damage identification. Even though the former are based on hard, objectively measured parameters, their accuracy is well established and a lot of engineering experience has been amassed regarding their application. Generalized models, such as ANNs, on the other hand, are yet to be standardized in an engineer's formation; their advantages are constantly explored however, and they are envisaged to revolutionze our approaches to problem-solving. Notwithstanding the projected primacy of AI, physical models are needed. Training ANNs, for example, requires a large amount of data, which are generated by scenarios that physical models can create. Furthermore, it is interesting to explore the possibility of physical-informed models, as per Lai et al. (2020).

1.2.4 Wave-based methods for NDT and SHM

Waves are propagating disturbances of the position of material particles. They are observed in every state of matter that is of interest to common engineering applications, i.e. solids and fluids. The continuum mechanics assumption of materials being comprised of infinitesimal particles leads to a very simple equation

$$k\frac{\partial^2 \mathbf{u}}{\partial \mathbf{x}^2} = \rho\frac{\partial^2 \mathbf{u}}{\partial t^2} \tag{1.22}$$

based on the dynamic equilibrium where k is the constant describing the tendency of the particle to revert back to its undisturbed position, i.e. elasticity. The other term is the particle's inertial force dependent on acceleration and mass density.

Waves are ubiquitous in nature. Studies of the phenomenology of certain very commonly experienced waves have led to classifications of this general behaviour, into categories with waves exhibiting specific traits. These are a result of specific material properties or boundary conditions. Acoustic waves are the basis of hearing, as a pressure disturbance propagates through the air. As fluids are mostly incapable of bearing other stress than hydrostatic, acoustic waves are exclusively pressure disturbances.

Ultrasonic waves are defined as the waves humans can't hear, which is roughly above

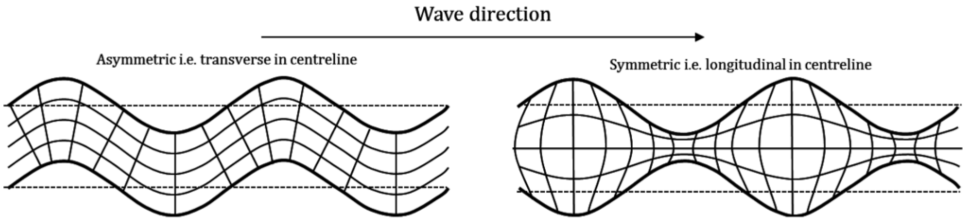

Figure 1.3: Fundamental symmetric and antisymmetric Lamb modes Marks et al. (2017).

20 kHz. As the wavelength is connected to frequency, their wavelengths are very short. This leads to them having a small feature length, and can map very well features in the environment. Animals such as bats, owls and cetaceans have adapted interesting contraptions that render them able to emit and receive such waves, useful to mapping their surroundings and catching prey. Humans have mimicked this for a variety of applications in imaging, commonly in medicine. Ultrasonic waves are widely applied in NDT.

Lamb wave propagation in solids

Lamb waves, named after Horace Lamb, are derived from the wave differential equation, when applied to the boundaries of plates. Plate components are common in engineering applications. Structure based on plate components need to fulfil requirements that combine reduced weight, high stiffness and strength. Composite materials and ligthweight alloys form the vast majority of plate components. Those suffer from modes of failure critical to detect, as discussed in the previous section. Lamb waves are, therefore, the backbone of wave-based monitoring.

Lamb's solution results in infinite discrete wave modes. Those are divided into symmetric and antisymmetric (Fig. 1.3), and further graded by their order. The fundamental Lamb modes are then denoted S0 and A0. The waves are defined by their modes, and each wave has its intrinsic properties, phase velocity, group velocity, wavelength, which are calculated from the dispersion relation. A more detailed insight on Lamb waves is given in Chapter 3

Actuation and sensing for Lamb waves

Lamb wave are generated artificially. An actuation in the desired frequency, causes predominant disturbances to take the form of Lamb waves. Proper mechanical excitation can advance actuation of the desired mode shape. Several instruments are available and commonly used, each with different advantages, availability and cost. Pure mode generation is advantageous, as monitoring the effects is easier. These obstacles can be partially surpassed with signal processing techniques. Common instruments for actuation and sensing of waves for NDT applications are ultrasonic probes, laser pulse, piezoelectrics.

Ultrasonic probes emit acoustic waves, that are transferred to the solid through some medium, air, liquid or solid. Air-Coupled Transducers (ACT) are quite common. Their advantage is the non-contact part, that does not affect the vibration properties of the plate. Liquid-coupled transducers are less common. An optimal angle exists that facilitates wave generation, relating the wave velocity in the coupling medium (air or otherwise) with that of the examined body, using Snell's law (Chennamsetti et al., 2013). Harb and Yuan (2016) examine the phase velocity of generated Lamb mode agains the coincidence angle of the Air Coupled Transducer (ACT). Bernhardt and Kreutzbruck (2020) propose a system that uses a stepped motor to adjust to the resonance angle that optimizes wave generation.

Transducers can be coupled by wedges. Sedaghati et al. (2019) use frustum wedges to focus the waves and create a circular front, along with a time-of-flight approach to locate corrosion holes. Feng et al. (2020) employ acrylic wedges to excite waves in high-temperature and evaluate the length of delaminations in rare-earth barium copper oxide lap joints.

Laser beams can be used for both actuation and sensing. Laser Doppler Vibrometers (LDV) utilize the phase shift of the reflected beam to calculate the out-of-plane displacement component. 3D LDVs use more than one beams to stereoscopically measure all the displacement components (Marks et al., 2017; Sherafat et al., 2016). This technique introduces trivial errors, as no material contact is made. Its disadvantage is the very localized measurement; if one needs a full filed, several points ought to be measured, either with multiple beams, or by repeating the whole measurement process (actuation and scattering of waves) several hundreds of times (Marks et al., 2017), with the laser targeting at a different point. To reduce the number of measurements with LDV, Dafydd and Sharif Khodaei (2020) input a chirp signal on a PZT, exciting multiple frequency waves and postprocessing the field in the frequency-wavenumber domain. Full-field wave propagation is visualized with multi-dimensional frequency or time-frequency domain transforms: with 2D space-windowed Fast Fourier Transform (FFT) (Yu and Tian, 2013), with Morlet wavelet transform based on time-of-flight along wave propagation directions Harb and Yuan (2016).

Wave emission by laser uses thermoelasticity, i.e. heats the surface it's cast on, causing dilation which propagates as a disturbance in the solid (Clough and Edwards, 2015; Webersen et al., 2018; Toyama et al., 2019; Sohn et al., 2011; Zhao et al., 2016). Hosoya et al. (2018) present a laser-generated plasma impulse technique for accurate actuation of waves on large structures. Davis et al. (2020) utilize a properly spaced additively manufactured grille that excites wave packets of very narrow band. Nanoparticle transducers that exhibit thermo-acoustic effect are used as lightweight actuators together with laser are presented in (Ding et al., 2020).

Patches of piezoelectric material [5] are very common means of both actuation and sensing. They produce an electric potential when deformed, and are capable of transforming some input electric signal into mechanical actuation. They can be used for both actuation and sensing; although a patch can be used for both, if the input channel is closed in a timely manner, this is not recommended, and in practice different PZTs are allocated for actuation and sensing. PZTs a good solution for permanent attachment, although the do affect the material properties: in contrast with LDV, it would be virtually impossible to obtain full-field measurements with PZTs due to this. PZTs are an integral part of smart material concepts, and can be incorporated in the design of smart composites and embedded between the layers.

The generation of guided waves is advantageous. In narrow structures waves are by quasi-default guided. In plate structures a wave emitted from a singular source propagates in a

---

[5] Colloquially referred to as PZTs, which is an acronym for "Lead (Pb) Zirconate Titanate", their constitutive ceramic material, and not an abbreviation for PieZoelecTric.

circular profile, with quick dispersion attenuation and complex reflections in the plate's boundaries. It is advantageous to generate waves of linear front focused on the damage and minimize miscellaneous reflections. Actuators ordered in phased arrays generate guided wave in plates by activating at proper phases, creating constructive or destructive interference (Serey et al., 2019; Shen and Giurgiutiu, 2016; Chen et al., 2015; Wang et al., 2018). This is advantageous in inspecting damage at long range. Spurious wave reflections are eliminated, allowing for a clearer signal, targeted at the defect. Leleux et al. (2013) use phased-array ultrasonic probes to generate guided Lamb waves and identify corrosion holes in aluminum plates and delamination in composite plates. Serey et al. (2019) generate guided pure-mode waves in long plates.

Signal processing and feature extraction

The raw signal received by a sensor is in a time series of data, usually of homogeneous sampling rate. The information carried are seldom useful as they are, and various levels of treatment exist to remove noise and various artefacts, such as reflections from a component's boundaries, and retain the information pertinent to damage identification.

The fundamental processing technique for signals is the time to frequency domain conversion, achieved by the Fourier transform. A signal is decomposed to an infinite sum of constitutive sinusoidal functions, of a certain amplitude, frequency and phase. In practice, the Fast Fourier Transform (FFT) algorithm is used, that drastically reduces the computational complexity by making use of available function symmetries. The resultant spectrum revelas the intensity of each frequency present in a signal. In monochromatic excitations, one expects a distinc peak around the respective frequency.

An extension to 2D and 3D FFT (Reed et al., 2018; Harb and Yuan, 2016) has been implemented. Applications are often made on the space-time domain, to obtain the wavenumber-frequency spectrum. An application to, e.g. a plate where waves of several frequency waves propagate, reveals the iso-surfaces of the present wavenumbers in different frequencies. In the frequency-wavenumber plane, the dispersion curves are depicted.

FFT does not preserve the time-aspect of the signal, losing the information of distinct events. The time-frequency transform approach has been adopted. A first approach is the Short Time Fourier Transform (STFT), which sweeps the FFT with a finite time window through the signal. Its main drawback is the fact that the resolution of the FFT depends on the number of time-samples, and thus a very finely discretized time signal is required. Space-windowed FFT (Yu and Tian, 2013) transforms waves into wavenumber domain, while retaining spatial infromation, i.e. where those waves occur. The Wavelet Transform (WT) decomposes a signal to a kernel of wavelets. Those have two defining variables, scale and shift. The shift variable refers to the centre time, whereas the scale to the frequency of the wavelet. They offer a solid time-frequency description of the signal, circumventing the downside of STFT, and are commonly used in signal processing for NDT and SHM.

Wigner-Ville decomposition (WVD) (Zoubi et al., 2019) is an alternative method proposed for time-frequency analysis of signals. Zoubi et al. (2019) implement WVD on multi-frequency multi-modal waves caused by chirp signal. The Matching pursuit algorithm Li et al. (2006) is based on iterative decomposition of a signal into a kernel of operator-defined functions; the algorithm finds a best fit of the defined function and subtracts it from the signal, and so proceeds iteratively applying it to the residual.

Features for damage identification

Damage identification is based on distinct features the signal bears. The signal reflection, i.e. a peak in displacement similar to the emitted signal, is a feature humans can easily identify. Now, if that signal has some reduced amplitude, one can infere that part of the signal has been reflected, allowing conclusions for the nature and size of the defect. The algorithmic NDT and SHM implementation requires that features be identifiable by computers. The richness of information is advantageous. Extracting rich information is costly, and some features are very sensitive to noise, reducing their reliability. The ability to extract features is directly related to the interrogation, i.e. actuation and sensing of the signal, and the available signal processing techniques. Furthermore, while most devised features are can be intuitively understood, others are designed with the computer implementation in mind. The advent of AI has contributed to that.

The Time of Flight (ToF) is the most common intuitive feature. It is the measure of the time a wave packet needs to traverse the actuator-damage-sensor system. With the location of the actuator and the sensor known, the distance of the damage is calculated. When multiple sensors exist, it is possible to triangulate the position and size of the damage. ToF is usually measured as the time between the peaks of a wave packet. It is extracted by Hilbert transform. Recently, the preference has shifted towards Continuous Wavelet Transform (CWT), as noises in other frequencies than the target can be filtered out.

Time reversal is used as a forward, baseline-free identification method. It is based on reciprocity of the wave behaviour. A wave packet is emitted from the actuator. It reaches the sensor altered. The sensor re-emitts the wave, reversed in time. The actuator should receive a wave packet same as the one emitted. Any alterations to the signal are attributed to damage.

The wave amplitude can also yield information about the damage. The wave packets scatter at the damage. The type and size of the damage cause different scattering patterns. It is possible to infer the size of the damage from the mangitude of the reflected or transmitted amplitude. Mode conversions are also reported. With proper signal processing tools, the different Lamb modes can be distinguished by their phase and group velocities, and the conversion magnitude can be identified.

Various damage indexes (DI) have also been introduced, based on correlation operations on the signal. Xiao et al. (2020) use cross-correlation imaging technique for fatigue cracks, using incident and crack-scattere waves.

The capability of AI to recognize patterns has introduced new possibilities. The DDF is a compressed time-frequency transformed index, that is used in ANN. The DCP has also been proposed (Atashipour et al., 2013).

Computational methods for wave propagation

Wave propagation is a computationally costly computation. Homogeneous isotropic materials and simple geometries allow for the analytical treatment of wave propagation. For complex geometries numerical solutions are sought, where the dynamic equilibrium equations are integrated through time, or linearized by frequency domain transform. The Courant condition connects the time and space discretization, to allow stability of the integration. Most problems are formulated in frequencies that are high with respect to the system's fundamental response, raising the computational cost to prohibitive levels for common applications, where e.g. HPC with multiple cores are unavailable. The LISA (local interaction) is a computationally optimized finite difference method Shen and Cesnik (2016). Severe computational savings have been reported compared to commercial FEM packages. The time domain spectral element method (SEM) utilizes elements of high degree polynomials (Żak and Krawczuk, 2011). The nodes are located in the roots of Legendre polynomials. Element integration leads to trivially diagonal mass matrices, providing stability of the time integration scheme and computational savings, eliminating the need of refining.

Frequency domain spectral elements use a frequency domain transform, Fourier or wavelet, of the displacements (Samaratunga et al., 2015).

A family of methods for guided waves has been developed based on Bloch-Floquet decomposition of wave propagation. The semi-analytical finite element (SAFE) assumes analytical propagation of the wave, discretizing only the transverse direction (Mazzotti et al., 2012). The Wave Finite Element discretizes (Zhong and Williams, 1995) a discrete characteristic cell of the material, assuming Bloch decomposition of displacements and forces. While SAFE is accurate and established, the WFE is advantageous for materials that possess inhomogeneity—but some regularity—and is based on FE and is available with little post-processing.

The modelling of the wave-damage interaction requires that the damage's behaviour be modelled. This is not always directly approachable be means of wave modelling. Therefore, hybrid approaches have been developed to model the wave-damage interaction, e.g.

Shen and Giurgiutiu (2016) use analytical wave propagation with local FEM modelling of defects.

Wave-based damage identification through inverse processes

ANN models have been used as means of solving the inverse problem of wave-based damage identification (Su and Ye, 2004; Atashipour et al., 2013; Dworakowski et al., 2015; SU et al., 2007; Ye Lu et al., 2009). As ANNs need to be trained, a finite number of input parameters and a smaller number of output parameters need to be identified. The output parameters are typically related to the damage, e.g. size and location of delamination (Pan et al., 2006; SU et al., 2007), or location, length and angle of a crack (Sbarufatti et al., 2014; Yan, 2013). A feature that is both sizeable and sensitive to the presence of damage is required for input. The Digital Damage Fingerprint (DDF) is presented in Su and Ye (2004, 2005); Pan et al. (2006); SU et al. (2007); Ye Lu et al. (2009); Lu et al. (2006). DDF consists of a compressed time-frequency transformation of the signal, taken for each of the actuator-sensor pairs on a given case. Atashipour et al. (2013) introduce the Damage Characteristic Point (DCP) feature, which consists of a time-discretized signal envelope from a scale-average CWT of the signal. DCP, contrary to DDF, is defined only in the time domain. Atashipour et al. (2013) report sufficient sensitivity of DCP, compared to the more complex DDF. Sbarufatti et al. (2014), Dworakowski et al. (2015) base the damage feature on various Damage Index definitions, based on cross-correlations between the baseline (pristine) and damaged state. For the training of the ANN, a number of input-output data are required. Those are usually generated by a physical model. SU et al. (2007), Ye Lu et al. (2009) develop parametrized FEM models. Sbarufatti et al. (2014), Dworakowski et al. (2015) use the LISA suite. ANNs need to be calibrated offline, but can be deployed for online SHM in structures with active sensors.

Bayesian wave-based damage identification approaches calculate a probability density function of the defining parameters of the damage. A prior belief can be placed on the PDFs, and the posterior is calculated with the introduction of new evidence, i.e. measurements. The calculation of the posterior requires a sampling process over the feasible data, which is performed efficiently with Markov-Chain Monte Carlo simulations, that create probability-based samples. He and Ng (2017) use a two-step approach, with a model class selection step to suit the number of cracks, and an identification step. The feature used is the displacement response, which is calculated efficiently with the time-domain SEM. Reed et al. (2018) identify delamination based on the wavenumber space of the damaged material. A FE model is used with the delaminations represented as circular regions, with the radius, centre and population of circles; the circles may overlap. A microCT scan is used to identify delaminations caused by impact and create accurate models. Yan (2013) identifies cracks in aluminum and delaminations in composite plates using the ToF calculated from CWT of the signal, from the actuator-sensor paths. The Bayesian approach is advantageous in actual cases where noise and uncertainties are present. Reed et al. (2018) perform a preliminary identification on the material properties of a pristine specimen to quantify the uncertainty. This approach is of interest in continuous monitoring approaches, where degradation of material parameters or environmental conditions might affect the model behaviour. The updating capability of the Bayesian approach renders it an attractive solution to that end.

Nonlinear waves

Recently, strongly nonlinear solitary waves, otherwise called solitons, have been tested for NDE applications. Those waves retain a permanent form due to the interaction of dispersion with nonlinearity. While primarily observed in fluids and regarding solids in granular materials and metamaterials, their propagation properties are being tested in solids, e.g. (Schiffer and Kim, 2019; Schiffer et al., 2020).

Solitons are generated using a granular chain—an array of slightly compressed steel beads, in contact with the test specimen, a composite beam. It is reported that the features of the primary and secondary reflected waves caused on the beam, are highly sensitive to the beam's properties, and have potential applications in NDE.

Conclusions

Defect characterization depends on relative size of defect to wavelength and feature size. The resolution of the waves is dependent on frequency. Higher frequency waves are more difficult to excite, have more noise, higher computational cost. Several inverse methods have been proposed, based both on ANN, Bayesian inference with Markov-Chain Monte Carlo simulations and optimization algorithms. Those require several solutions of a forward model, which is costly, especially in the context of wave propagation. The evolution of numerical methods for the solution of the physical equations for wave propagation offers an advantage to that end. The sophistication of novel features, unintuitive to humans but treatable with AI approaches, is another motivator for the novelty drive in the development of computational methods.

1.2.5 Miscellaneous NDT and SHM methods

Thermal

Thermal NDT techniques (Balageas et al., 2016) are based on the alteration of heat flux on damaged components. Common damage types such as cracks and delaminations introduce a layer of air, which acts as a barrier. Monitoring of the transient temperature field is possible with infrared cameras or temperature gauges. Thermal diffusion is easily modelled with FE, and inverse analysis schemes are based on similar reasoning.

Ultrasound excited thermography (Mendioroz et al., 2017) is based on the thermal response of damage from ultrasound emission in the material. The modes of damage examined are kissing cracks and delaminations, where friction occurs, thus producing heat. Infrared cameras are used for imaging the defects. The method has been rendered attractive at recent years with the introduction of novel cameras of 0.2 K resolution. The method is applied in plates, but an outlook to 3D materials with arbitrary damage is given.

Inverse identification methods and signal processing techniques can be implemented for defect detection and identification from thermal measurements. Poelman et al. (2020) implement a multi-scale gapped smoothing algorithm to detect multiple damages on plates, form noisy measurements, in a baseline-free manner. The proposed method improves on robustness, making feasible to extract useful information from flash non-uniform heating. Thermal techniques are sensitive to potentially small damage. The damage needs to be exposed on surface. Measurements need to be conducted under controlled conditions with steady temperatures and proper isolation from spurious heating sources. Very large structures require large heat input which would result in very high material temperatures locally, which can cause damage. This technique is therefore not applicable to large parts or structures, and cannot be used conventionally for continuous monitoring. It does not require, however, expensive specialized equipment, and it is an attractive alternative mean of local inspection.

Electric

Eddy current (AbdAlla et al., 2019) is the rotational motion of electrons in conductive materials caused by the relative motion of the inspected body through a magnetic field, called primary magnetic field, which is produced by an electric coil to which alternating voltage is applied. The body's eddy produces a secondary magnetic field. When a body is damaged, the eddy's path and intensity are altered, thus causing measurable alterations to the current intensity and the secondary magnetic field. Passive coils may be used to measure the magnetic field.

Eddy current is commonly used as an NDT in pipes and cylindrical objects, where the circular flow of the current is facilitated. It is commonly used in industry for quality control, and it is capable of detecting very small defects.

Damage detection and localisation in composite materials is achieved in through alterations of the electrical conductivity. By embedding CNTs in the polymer matrix (Augustin et al., 2018; Ku-Herrera et al., 2018), the conductivity is increased and the method becomes sensitive, such that very low voltage is sufficient. Ku-Herrera et al. (2018) propose a tailored CNT reinforcement of the polymer matrix, for accurate and hierarchical damage localisation.

Visual inspection

Visual inspection is a straightforward method to check components and structures for defects. The introduction of dyes in a material can facilitate the discerning of small damage. Visual inspection is heavily dependent on the operator and their experience; massive inspections and operator fatigue can lead to mistaken estimations (Shipway et al., 2019). Harnessing triboluminescence properties certain substances exhibit at fracture has also attracted research interest in its potential application for damage indication in engineering materials (Olawale et al., 2011).

Image processing and AI have reached a sufficiently mature stage to comprise applications of visual inspection. Fluorescent dyes and other aides can further facilitate the process with proper illumination and cameras, increasing the sensitivity of the method.Shipway et al. (2019) propose a random forest algorithm for automated detection of detects with the usage of fluorescent dye penetration.

Radiation and scanning

X-ray imaging is a method with a wide range of applications, NDT included. Rays are cast on the inspected body, which are attenuated as they travel through. Inhomogeneities and voids cause different degrees of attenuation, allowing detailed imaging.

X-rays and other short wavelength electromagnetic radiation give very detailed imaging, albeit with a costly process. The examined body required to be set into a device, prohibiting in situ inspection for NDT applications. The method is commonly used in experimental processes, to make detailed baseline assessments of damage.

1.2.6 Conclusions

A diverse gamut of NDT methods exists, such that an exhaustive review surpasses the scope of this work. A non-destructive method is able to interfere with the damage, without causing degradation to the material. The resolution of a non-destructive method, or its capacity to be sensitive to smaller features of e.g. damage, is proportional to its cost. The cost depends on many factors, prominently the equipment required to interrogate and measure the object, and the possibility to measure an object with minimal interruption of its function. Vibration-based methods operate in the natural frequencies of a structure, with detectable damage of large magnitude. Wave-based methods operate in several orders of magnitude higher frequencies, and are capable of identifying smaller damage, with a significantly higher cost of actuators, sensors and numerical analysis. Radiation-based methods work in very high frequencies and can give very detailed image of damage, with very expensive equipment and a very disruptive testing process.

Depending on the material and structure, there exists a threshold of useful magnitude for damage detection, below which, the damage is not projected to pose any threat to the structure's integrity. A reasoning for proper selection of an NDT and SHM method to apply thus emerges.

1.3 Conclusions on background and scope

The conclusions on the literature research for SHM and NDT techniques are further elaborated upon. The scope of this thesis is drawn as the target novelty it aims to introduce.

1.3.1 General remarks about the background survey

NDT and SHM techniques mainly target large infrastructure and mobile structures, mostly aerospace. The impact on the latter is found to be bigger, as demands for performance significantly increase. Furthermore, lightweight materials, mainly composites, are being developed towards the end of elevated performance of aerospace structures, which benefit the most from NDT and SHM techniques. The effort of ”smartening” aerospace materials by embedding sensory and computational capacity within aerospace materials is indicative of the perceived benefits of SHM.

With respect to the system's physical behaviour, techniques invoking mechanical, electromagnetic and optical phenomena have been identified. The merits of each class are judged by both the resolution, i.e. the ability to detect and identify damage on early, sub-critical stage, as well as the possibility of least-intrusive application and continuous monitoring are considered. Vibrational and wave-based methods are the best performers by those standards, as their resolution and continuous monitoring possibilities are many, and under constant surveying.

The available modelling techniques, along with computational power, have rendered certain solutions such as ANN attractive. Physical simulations, particularly Finite Elements, are common ground in both the conceptual stage of the structure, and during its life cycle. Physical and generalized models have their distinct roles, even with synergistic possibilities, i.e. when physical models are used to train generalized ones. To that end, the development of efficient and accurate computational methods for physical problems is an endeavour very relevant to the envisaged applications.

The availability of computational power renders two types of solutions attractive. First, the adoption of more complex methods, with higher resolution. Second, the embedding of more computers within structures, able to process collected data during a structure's operation and give indications about its condition. To that end, the development of efficient computational methods opens up prospective new applications. Embedded systems benefit from efficient modelling. For example, smart materials may not only be able to detect, but identify prospective damage, if they have embedded sensors along with a processor that can run some analysis.

1.3.2 Thesis scope

This thesis aims to introduce an efficient and accurate computational method to simulate the response of damaged structures. Focus is placed on shell structures, as they are cardinal load bearing and functional forms spanning aircraft, ships and several vessels. Furthermore, shells are sensitive to damage, and small local degradation of strength can possibly compromise the whole structure. The introduction of composite materials as main solution for such structures attracts further attention to that goal, as they are sensitive to adverse modes of damage.

Wave methods are found to be the most resilient method in combining good resolution with continuous monitoring capabilities. Wave actuators and sensors are possible to embed within the structure, and several choices exist to generate and target waves. The incorporation of wave methods in analysis schemes is challenging, as wave simulations require in principle heavy computations.

1.3.3 Thesis outline

This chapter has presented the background in SHM and NDT and outlined open challenges it aims to address.

In Chapter 2, the simulation of cracks is addressed. Methods for simulating cracks in materials and structures are reviewed. An XFEM code for plates and shells is developed and validation is provided.

Chapter 3 the simulation of waves is addressed. The Wave Finite Element, a method that models wave propagation efficiently and accurately is reviewed. The results of WFE are verified against analytical relations for wave propagation.

In Chapter 4 a hybrid XFEM/WFE scheme is developed that provides efficient and accurate calculations of guided wave scattering at cracks. The results are compared with those of explicit FE analysis. A signal processing scheme is also examined, to post-process time-transient wave scattering data and extract scattering coefficients. Remarks are made on the applicability of wave scattering in damage identification.

Concluding remarks and suggestions for future research are drawn in Chapter 6

Bibliography

AbdAlla, A. N., Faraj, M. A., Samsuri, F., Rifai, D., Ali, K., and Al-Douri, Y. Challenges in improving the performance of eddy current testing: Review. *Measurement and Control*, 52(1-2):46–64, 2019.

Atashipour, S. A., Mirdamadi, H. R., Hemasian-Etefagh, M. H., Amirfattahi, R., and Ziaei-Rad, S. An effective damage identification approach in thick steel beams based on guided ultrasonic waves for structural health monitoring applications. *Journal of Intelligent Material Systems and Structures*, 24(5):584–597, 2013.

Augustin, T., Karsten, J., and Fiedler, B. Detection and localization of impact damages in carbon nanotube–modified epoxy adhesive films with printed circuits. *Structural Health Monitoring*, 17(5):1166–1177, 2018.

Avci, O., Abdeljaber, O., Kiranyaz, S., Hussein, M., Gabbouj, M., and Inman, D. J. A review of vibration-based damage detection in civil structures: From traditional methods to Machine Learning and Deep Learning applications. *Mechanical Systems and Signal Processing*, 147:107077, 2021.

Avendaño-Valencia, L. D., Chatzi, E. N., and Tcherniak, D. Gaussian process models for mitigation of operational variability in the structural health monitoring of wind turbines. *Mechanical Systems and Signal Processing*, 142:106686, 2020.

Aymerich, F. and Staszewski, W. Impact damage detection in composite laminates using nonlinear acoustics. *Composites Part A: Applied Science and Manufacturing*, 41(9):1084–1092, 2010.

Balageas, D., Maldague, X., Burleigh, D., Vavilov, V. P., Oswald-Tranta, B., Roche, J.-M., Pradere, C., and Carlomagno, G. M. Thermal (IR) and Other NDT Techniques for Improved Material Inspection. *Journal of Nondestructive Evaluation*, 35(1):18, 2016.

Bao, Y., Chen, Z., Wei, S., Xu, Y., Tang, Z., and Li, H. The State of the Art of Data Science and Engineering in Structural Health Monitoring. *Engineering*, 5(2):234–242, 2019.

Bernhardt, Y. and Kreutzbruck, M. Integrated defect sensor for the inspection of fiber-reinforced plastics using air-coupled ultrasound. *Journal of Sensors and Sensor Systems*, 9(1):127–132, 2020.

Chen, X., Michaels, J., and Michaels, T. A methodology for estimating guided wave scattering patterns from sparse transducer array measurements. *IEEE Transactions on Ultrasonics, Ferroelectrics, and Frequency Control*, 62(1):208–219, 2015.

Chennamsetti, R., Khan, I., Hood, A., and Joshi, M. Changes observed in Ao mode due to rotational misalignment of air-coupled transducers in isotropic plates. *International Journal of Precision Engineering and Manufacturing*, 14(12):2209–2212, 2013.

Choi, H. Y., Wu, H. Y. T., and Chang, f. K. A New Approach toward Understanding Damage Mechanisms and Mechanics of Laminated Composites Due to Low-Velocity Impact: Part II—Analysis. *Journal of Composite Materials*, 25(8):1012–1038, 1991.

Clough, A. and Edwards, R. Characterisation of hidden defects using the near-field ultrasonic enhancement of Lamb waves. *Ultrasonics*, 59:64–71, 2015.

Dafydd, I. and Sharif Khodaei, Z. Analysis of barely visible impact damage severity with ultrasonic guided Lamb waves. *Structural Health Monitoring*, 19(4):1104–1122, 2020.

Davis, G., Balasubramaniam, K., Palanisamy, S., Nagarajah, R., and Rajagopal, P. Additively manufactured integrated slit mask for laser ultrasonic guided wave inspection. *The International Journal of Advanced Manufacturing Technology*, 110(5-6):1203–1217, 2020.

Della, C. N. and Shu, D. Vibration of Delaminated Composite Laminates: A Review. *Applied Mechanics Reviews*, 60(1):1, 2007.

Derriso, M., McCurry, C., and Schubert Kabban, C. A novel approach for implementing structural health monitoring systems for aerospace structures. In *Structural Health Monitoring (SHM) in Aerospace Structures*, pages 33–56. Elsevier, 2016.

DeVries, P. H., Ruth, K. T., and Dennies, D. P. Counting on fatigue: Striations and their measure. 2010.

Ding, X., Li, W., Xiong, J., Shen, Y., and Huang, W. A flexible laser ultrasound transducer for Lamb wave-based structural health monitoring. *Smart Materials and Structures*, 29(7):075006, 2020.

Doebling, S. W., Farrar, C. R., and Prime, M. B. A Summary Review of Vibration-Based Damage Identification Methods. *The Shock and Vibration Digest*, 30(2):91–105, 1998.

Dutta, D., Sohn, H., Harries, K. A., and Rizzo, P. A Nonlinear Acoustic Technique for Crack Detection in Metallic Structures. *Structural Health Monitoring: An International Journal*, 8(3):251–262, 2009.

Dworakowski, Z., Ambrozinski, L., Packo, P., Dragan, K., and Stepinski, T. Application of artificial neural networks for compounding multiple damage indices in Lamb-wave-based damage detection. *Structural Control and Health Monitoring*, 22(1):50–61, 2015.

Fan, W. and Qiao, P. A 2-D continuous wavelet transform of mode shape data for damage detection of plate structures. *International Journal of Solids and Structures*, 46(25-26):4379–4395, 2009.

Feng, B., Chen, W., Ito, S., Yusa, N., Hashizume, H., Ribeiro, A. L., and G. Ramos, H. Quantitative evaluation of the delamination length in mechanical lap joints of high-temperature superconducting tapes using Lamb waves. *Measurement*, 156:107606, 2020.

Garnier, C., Pastor, M.-L., Lorrain, B., and Pantalé, O. Fatigue behavior of impacted composite structures. *Composite Structures*, 100:443–450, 2013.

Gaudenzi, P., Nardi, D., Chiappetta, I., Atek, S., Lampani, L., Pasquali, M., Sarasini, F., Tirilló, J., and Valente, T. Sparse sensing detection of impact-induced delaminations in composite laminates. *Composite Structures*, 133:1209–1219, 2015.

Gaurav, A. and Singh, K. K. Fatigue behavior of FRP composites and CNT-Embedded FRP composites: A review. *Polymer Composites*, 39(6):1785–1808, 2018.

Gillich, G. R., Praisach, Z. I., Abdel Wahab, M., and Vasile, O. Localization of Transversal Cracks in Sandwich Beams and Evaluation of Their Severity. *Shock and Vibration*, 2014:1–10, 2014.

Gomes, G. F., da Cunha, S. S., da Silva Lopes Alexandrino, P., Silva de Sousa, B., and Ancelotti, A. C. Sensor placement optimization applied to laminated composite plates under vibration. *Structural and Multidisciplinary Optimization*, 58(5):2099–2118, 2018.

Gomes, G. F., Mendez, Y. A. D., da Silva Lopes Alexandrino, P., da Cunha, S. S., and Ancelotti, A. C. A Review of Vibration Based Inverse Methods for Damage Detection and Identification in Mechanical Structures Using Optimization Algorithms and ANN. *Archives of Computational Methods in Engineering*, 26(4):883–897, 2019.

Harb, M. and Yuan, F. Non-contact ultrasonic technique for Lamb wave characterization in composite plates. *Ultrasonics*, 64:162–169, 2016.

He, S. and Ng, C.-T. Guided wave-based identification of multiple cracks in beams using a Bayesian approach. *Mechanical Systems and Signal Processing*, 84:324–345, 2017.

Hosoya, N., Yoshinaga, A., Kanda, A., and Kajiwara, I. Non-contact and non-destructive Lamb wave generation using laser-induced plasma shock wave. *International Journal of Mechanical Sciences*, 140:486–492, 2018.

Iannucci, L. and Willows, M. L. An energy based damage mechanics approach to modelling impact onto woven composite materials-Part I: Numerical models. *Composites Part A: Applied Science and Manufacturing*, 37(11):2041–2056, 2006.

Icardi, U., Locatto, S., and Longo, A. Assessment of Recent Theories for Predicting Failure of Composite Laminates. *Applied Mechanics Reviews*, 60(2):76, 2007.

Janeliukstis, R., Rucevskis, S., Wesolowski, M., Kovalovs, A., and Chate, A. Damage identification in beam structure using spatial continuous wavelet transform. In *IOP Conference Series: Materials Science and Engineering*, volume 96, page 012058. Institute of Physics Publishing, 2015.

Ji, S. H. and Yun, J. S. Optimization of a flexible piezoelectric module structure based on a lead-free piezoceramic embedded in nanofiber composites. *Mechanical Systems and Signal Processing*, 136:106447, 2020.

Johns, C. H. The Code of Hammurabi. *The Expository Times*, 14(6):257–258, 1903.

Kessler, S. S., Spearing, S. M., and Soutis, C. Damage detection in composite materials using Lamb wave methods. *Smart Materials and Structures*, 11(2):269–278, 2002.

Khan, A., Ko, D. K., Lim, S. C., and Kim, H. S. Structural vibration-based classification and prediction of delamination in smart composite laminates using deep learning neural network. *Composites Part B: Engineering*, 161:586–594, 2019.

Kong, Y., Bennett, C. J., and Hyde, C. J. A review of non-destructive testing techniques for the in-situ investigation of fretting fatigue cracks. 2020.

Ku-Herrera, J. d. J., La Saponara, V., and Avilés, F. Selective damage sensing in multiscale hierarchical composites by tailoring the location of carbon nanotubes. *Journal of Intelligent Material Systems and Structures*, 29(4):553–562, 2018.

Lai, Z., Alzugaray, I., Chli, M., and Chatzi, E. Full-field structural monitoring using event cameras and physics-informed sparse identification. *Mechanical Systems and Signal Processing*, 145:106905, 2020.

Lee, S., Park, S., Kim, T., Lieu, Q. X., and Lee, J. Damage quantification in truss structures by limited sensor-based surrogate model. *Applied Acoustics*, 172:107547, 2021.

Leleux, A., Micheau, P., and Castaings, M. Long range detection of defects in composite plates using lamb waves generated and detected by ultrasonic phased array probes. *Journal of Nondestructive Evaluation*, 32(2):200–214, 2013.

Lemaitre, J. and Chaboche, J. L. *Mechanics of Solid Materials.* Cambridge University Press, 1994. ISBN 9780521477581.

Li, D., Ho, S. C. M., Song, G., Ren, L., and Li, H. A review of damage detection methods for wind turbine blades. *Smart Materials and Structures*, 24(3), 2015.

Li, F., Su, Z., Ye, L., and Meng, G. A correlation filtering-based matching pursuit (CF-MP) for damage identification using Lamb waves. *Smart Materials and Structures*, 15(6):1585–1594, 2006.

Lu, Y., Ye, L., and Su, Z. Crack identification in aluminium plates using Lamb wave signals of a PZT sensor network. *Smart Materials and Structures*, 15(3):839–849, 2006.

Mai, C. V., Spiridonakos, M. D., Chatzi, E. N., and Sudret, B. Surrogate modelling for stochastic dynamical systems by combining NARX models and polynomial chaos expansions. 2016.

Mansor, N., Abdullah, S., Ariffin, A. K., and Syarif, J. A review of the fatigue failure mechanism of metallic materials under a corroded environment. *Engineering Failure Analysis*, 42:353–365, 2014.

Marks, R., Clarke, A., Featherston, C. A., and Pullin, R. Optimization of acousto-ultrasonic sensor networks using genetic algorithms based on experimental and numerical data sets. *International Journal of Distributed Sensor Networks*, 13(11):155014771774370, 2017.

Mazzotti, M., Marzani, A., Bartoli, I., and Viola, E. Guided waves dispersion analysis for prestressed viscoelastic waveguides by means of the SAFE method. *International Journal of Solids and Structures*, 49(18):2359–2372, 2012.

Mendioroz, A., Celorrio, R., and Salazar, A. Ultrasound excited thermography: an efficient tool for the characterization of vertical cracks. *Measurement Science and Technology*, 28(11):112001, 2017.

Meyer, Y., Lachat, R., and Akhras, G. A review of manufacturing techniques of smart composite structures with embedded bulk piezoelectric transducers. *Smart Materials and Structures*, 28(5):053001, 2019.

Muskhelishvili, N. I. *Some Basic Problems of the Mathematical Theory of Elasticity.* Springer Netherlands, Dordrecht, 1977. ISBN 978-90-481-8245-9.

Naik, N. Woven-fibre thermoset composites. In *Fatigue in Composites*, pages 296–313. Elsevier, 2003.

Nairn, J. A. Direct comparison of anisotropic damage mechanics to fracture mechanics of explicit cracks. *Engineering Fracture Mechanics*, 203:197–207, 2018.

Naumann, R. J. *Introduction to the Physics and Chemistry of Materials.* CRC Press, 2008. ISBN 9780429148798.

Olawale, D. O., Dickens, T., Sullivan, W. G., Okoli, O. I., Sobanjo, J. O., and Wang, B. Progress in triboluminescence-based smart optical sensor system. *Journal of Luminescence*, 131(7):1407–1418, 2011.

Ooijevaar, T. H., Loendersloot, R., Warnet, L. L., de Boer, A., and Akkerman, R. Vibration based Structural Health Monitoring of a composite T-beam. *Composite Structures*, 92(9):2007–2015, 2010.

Orifici, A. C., Herszberg, I., and Thomson, R. S. Review of methodologies for composite material modelling incorporating failure. *Composite Structures*, 86(1-3):194–210, 2008.

Ostachowicz, W., Soman, R., and Malinowski, P. Optimization of sensor placement for structural health monitoring: a review. *Structural Health Monitoring*, 18(3):963–988, 2019.

Pan, N., Su, Z., Ye, L., Zhou, L. M., and Lu, Y. A quantitative identification approach for delamination in laminated composite beams using digital damage fingerprints (DDFs). *Composite Structures*, 75(1-4):559–570, 2006.

Pan, J., Zhang, Z., Wu, J., Ramakrishnan, K. R., and Singh, H. K. A novel method of vibration modes selection for improving accuracy of frequency-based damage detection. *Composites Part B: Engineering*, 159:437–446, 2019.

Papa, I., Lopresto, V., and Langella, A. Ultrasonic inspection of composites materials: Application to detect impact damage. *International Journal of Lightweight Materials and Manufacture*, 4(1):37–42, 2021.

Parra dos Anjos Lima, F., Silva Frutuoso de Souza, S., Chavarette, F. R., Martins Lopes, M. L., Turra, A. E., and Lopes Júnior, V. Monitoring and Fault Identification in Aeronautical Structures Using an ARTMAP-Fuzzy-Wavelet Artificial Neural Network. *Advanced Materials Research*, 1025-1026:1107–1112, 2014.

Pérez, M. A., Gil, L., and Oller, S. Impact damage identification in composite laminates using vibration testing. *Composite Structures*, 108:267–276, 2014.

Poelman, G., Hedayatrasa, S., Segers, J., Van Paepegem, W., and Kersemans, M. Multiscale gapped smoothing algorithm for robust baseline-free damage detection in optical infrared thermography. *NDT & E International*, 112:102247, 2020.

Polimeno, U. and Meo, M. Detecting barely visible impact damage detection on aircraft composites structures. *Composite Structures*, 91(4):398–402, 2009.

Pramanik, R. and Arockiarajan, A. Effective properties and nonlinearities in 1-3 piezocomposites: a comprehensive review. *Smart Materials and Structures*, 28(10):103001, 2019.

Qin, F. and Peng, H.-X. Ferromagnetic microwires enabled multifunctional composite materials. *Progress in Materials Science*, 58(2):183–259, 2013.

Rabinovich, D., Givoli, D., and Vigdergauz, S. XFEM-based crack detection scheme using a genetic algorithm. *International Journal for Numerical Methods in Engineering*, 71(9):1051–1080, 2007.

Reed, H., Leckey, C. A., Dick, A., Harvey, G., and Dobson, J. A model based bayesian solution for characterization of complex damage scenarios in aerospace composite structures. *Ultrasonics*, 82:272–288, 2018.

Salawu, O. Detection of structural damage through changes in frequency: a review. *Engineering Structures*, 19(9):718–723, 1997.

Samaratunga, D., Jha, R., and Gopalakrishnan, S. Wave propagation analysis in adhesively bonded composite joints using the wavelet spectral finite element method. *Composite Structures*, 122:271–283, 2015.

Sbarufatti, C., Manson, G., and Worden, K. A numerically-enhanced machine learning approach to damage diagnosis using a Lamb wave sensing network. *Journal of Sound and Vibration*, 333(19):4499–4525, 2014.

Schiffer, A., Alia, R., Cantwell, W. J., Lee, D., Kim, E., and Kim, T.-Y. Elastic interaction between nonlinear solitary waves in granular chains and composite beams: Experiments and modelling. *International Journal of Mechanical Sciences*, 170:105350, 2020.

Schiffer, A. and Kim, T.-Y. Modelling of the interaction between nonlinear solitary waves and composite beams. *International Journal of Mechanical Sciences*, 151:181–191, 2019.

Sedaghati, A., Honarvar, F., and Sinclair, A. N. Lamb wave-based experimental and numerical studies for detection and sizing of corrosion damage in metallic plates. *Proceedings of the Institution of Mechanical Engineers, Part C: Journal of Mechanical Engineering Science*, 233(6):2107–2120, 2019.

Serey, V., Quaegebeur, N., Micheau, P., Masson, P., Castaings, M., and Renier, M. Selective generation of ultrasonic guided waves in a bi-dimensional waveguide. *Structural Health Monitoring*, 18(4):1324–1336, 2019.

Sevieri, G. and De Falco, A. Dynamic structural health monitoring for concrete gravity dams based on the Bayesian inference. *Journal of Civil Structural Health Monitoring*, 10(2):235–250, 2020.

Shaver, A. You're more likely to be fatally crushed by furniture than killed by a terrorist. 2015.

Shen, Y. and Cesnik, C. E. Hybrid local FEM/global LISA modeling of damped guided wave propagation in complex composite structures. *Smart Materials and Structures*, 25(9):095021, 2016.

Shen, Y. and Giurgiutiu, V. Combined analytical FEM approach for efficient simulation of Lamb wave damage detection. *Ultrasonics*, 69:116–128, 2016.

Sherafat, M. H., Quaegebeur, N., Hubert, P., Lessard, L., and Masson, P. Finite element modeling of Lamb wave propagation in composite stepped joints. *Journal of Reinforced Plastics and Composites*, 35(10):796–806, 2016.

Shipway, N. J., Huthwaite, P., Lowe, M. J. S., and Barden, T. J. Performance Based Modifications of Random Forest to Perform Automated Defect Detection for Fluorescent Penetrant Inspection. *Journal of Nondestructive Evaluation*, 38(2):37, 2019.

Singh, C. V. A multiscale synergistic damage mechanics approach for modeling progressive failure in composite laminates. In *Structural Integrity and Durability of Advanced Composites*, pages 73–103. Elsevier, 2015.

Sohn, H., Dutta, D., Yang, J., Park, H., DeSimio, M., Olson, S., and Swenson, E. Delamination detection in composites through guided wave field image processing. *Composites Science and Technology*, 71(9):1250–1256, 2011.

Spiridonakos, M. D. and Chatzi, E. N. Metamodeling of dynamic nonlinear structural systems through polynomial chaos NARX models. *Computers and Structures*, 157:99–113, 2015.

SU, Z., YANG, C., PAN, N., YE, L., and ZHOU, L. Assessment of delamination in composite beams using shear horizontal (SH) wave mode. *Composites Science and Technology*, 67(2):244–251, 2007.

Su, Z. and Ye, L. An intelligent signal processing and pattern recognition technique for defect identification using an active sensor network. *Smart Materials and Structures*, 13(4):957–969, 2004.

Su, Z. and Ye, L. A fast damage locating approach using digital damage fingerprints extracted from Lamb wave signals. *Smart Materials and Structures*, 14(5):1047–1054, 2005.

Toyama, N., Yamamoto, T., Urabe, K., and Tsuda, H. Ultrasonic inspection of adhesively bonded CFRP/aluminum joints using pulsed laser scanning. *Advanced Composite Materials*, 28(1):27–35, 2019.

Tuloup, C., Harizi, W., Aboura, Z., Meyer, Y., Khellil, K., and Lachat, R. On the manufacturing, integration, and wiring techniques of in situ piezoelectric devices for the manufacturing and structural health monitoring of polymer–matrix composites: A literature review. *Journal of Intelligent Material Systems and Structures*, 30(16):2351–2381, 2019.

Vega, M. A. and Todd, M. D. A variational Bayesian neural network for structural health monitoring and cost-informed decision-making in miter gates. *Structural Health Monitoring*, 2020.

Wang, W., Mottershead, J. E., Siebert, T., and Pipino, A. Frequency response functions of shape features from full-field vibration measurements using digital image correlation. *Mechanical Systems and Signal Processing*, 28:333–347, 2012.

Wang, W., Zhang, H., Lynch, J. P., Cesnik, C. E., and Li, H. Experimental and numerical validation of guided wave phased arrays integrated within standard data acquisition systems for structural health monitoring. *Structural Control and Health Monitoring*, 25(6):e2171, 2018.

Webersen, M., Johannesmann, S., Düchting, J., Claes, L., and Henning, B. Guided ultrasonic waves for determining effective orthotropic material parameters of continuous-fiber reinforced thermoplastic plates. *Ultrasonics*, 84:53–62, 2018.

Wicaksono, S. and Chai, G. B. A review of advances in fatigue and life prediction of fiber-reinforced composites. *Proceedings of the Institution of Mechanical Engineers, Part L: Journal of Materials: Design and Applications*, 227(3):179–195, 2013.

Williams, K. V. and Vaziri, R. Application of a damage mechanics model for predicting the impact response of composite materials. *Computers & Structures*, 79(10):997–1011, 2001.

Worden, K., Farrar, C. R., Manson, G., and Park, G. The fundamental axioms of structural health monitoring. *Proceedings of the Royal Society A: Mathematical, Physical and Engineering Sciences*, 463(2082):1639–1664, 2007.

Wu, R.-T. and Jahanshahi, M. R. Data fusion approaches for structural health monitoring and system identification: Past, present, and future. *Structural Health Monitoring*, 19(2):552–586, 2020.

Xiao, W., Yu, L., Joseph, R., and Giurgiutiu, V. Fatigue-Crack Detection and Monitoring through the Scattered-Wave Two-Dimensional Cross-Correlation Imaging Method Using Piezoelectric Transducers. *Sensors*, 20(11):3035, 2020.

Yam, L. H., Wei, Z., and Cheng, L. Nondestructive Detection of Internal Delamination by Vibration-based Method for Composite Plates. *Journal of Composite Materials*, 38(24):2183–2198, 2004.

Yam, L. H., Yan, Y. J., and Jiang, J. S. Vibration-based damage detection for composite structures using wavelet transform and neural network identification. *Composite Structures*, 60(4):403–412, 2003.

Yan, G. A Bayesian approach for damage localization in plate-like structures using Lamb waves. *Smart Materials and Structures*, 22(3):035012, 2013.

Yang, Y., Ng, C. T., Kotousov, A., Sohn, H., and Lim, H. J. Second harmonic generation at fatigue cracks by low-frequency Lamb waves: Experimental and numerical studies. *Mechanical Systems and Signal Processing*, 99:760–773, 2018.

Yang, H., Qiu, H., Xiang, Q., Tang, S., and Guo, X. Exploring Elastoplastic Constitutive Law of Microstructured Materials Through Artificial Neural Network—A Mechanistic-Based Data-Driven Approach. *Journal of Applied Mechanics*, 87(9):1–16, 2020.

Ye Lu, Lin Ye, Zhongqing Su, Limin Zhou, and Li Cheng. Artificial Neural Network (ANN)-based Crack Identification in Aluminum Plates with Lamb Wave Signals. *Journal of Intelligent Material Systems and Structures*, 20(1):39–49, 2009.

Yin, T., Lam, H.-F., and Chow, H.-M. A Bayesian Probabilistic Approach for Crack Characterization in Plate Structures. *Computer-Aided Civil and Infrastructure Engineering*, 25(5):375–386, 2010.

Yu, L. and Tian, Z. Lamb wave Structural Health Monitoring Using a Hybrid PZT-Laser Vibrometer Approach. *Structural Health Monitoring: An International Journal*, 12(5-6):469–483, 2013.

Yuan, F. G. *Structural Health Monitoring (SHM) in aerospace structures.* Elsevier Inc., 2016. ISBN 9780081001585.

Żak, A. and Krawczuk, M. Certain numerical issues of wave propagation modelling in rods by the Spectral Finite Element Method. *Finite Elements in Analysis and Design*, 47(9):1036–1046, 2011.

Zhang, Z., He, M., Liu, A., Singh, H. K., Ramakrishnan, K. R., Hui, D., Shankar, K., and Morozov, E. V. Vibration-based assessment of delaminations in FRP composite plates. *Composites Part B: Engineering*, 144:254–266, 2018.

Zhang, Z., Pan, J., Luo, W., Ramakrishnan, K. R., and Singh, H. K. Vibration-based delamination detection in curved composite plates. *Composites Part A: Applied Science and Manufacturing*, 119:261–274, 2019.

Zhang, Z., Shankar, K., Ray, T., Morozov, E. V., and Tahtali, M. Vibration-based inverse algorithms for detection of delamination in composites. *Composite Structures*, 102:226–236, 2013.

Zhao, Y., Zhu, Y., Yuan, M., Wang, J., and Zhu, S. A Laser-Based Fiber Bragg Grating Ultrasonic Sensing System for Structural Health Monitoring. *IEEE Photonics Technology Letters*, 28(22):2573–2576, 2016.

Zhong, W. X. and Williams, F. W. On the direct solution of wave propagation for repetitive structures. *Journal of Sound and Vibration*, 181(3):485–501, 1995.

Zou, Y., Tong, L., and Steven, G. VIBRATION-BASED MODEL-DEPENDENT DAMAGE (DELAMINATION) IDENTIFICATION AND HEALTH MONITORING FOR COMPOSITE STRUCTURES — A REVIEW. *Journal of Sound and Vibration*, 230(2):357–378, 2000.

Zoubi, A. B., Kim, S., Adams, D. O., and Mathews, V. J. Lamb Wave Mode Decomposition Based on Cross-Wigner-Ville Distribution and Its Application to Anomaly Imaging for Structural Health Monitoring. *IEEE Transactions on Ultrasonics, Ferroelectrics, and Frequency Control*, 66(5):984–997, 2019.

Chapter 2

The eXtended Finite Element Method for dynamic modelling of plates and shells

2.1 Introduction

The simulation of fracture has been an open issue in solid mechanics. Fracture simulation is important in assessing the severity of a crack and remaining life of a damaged component, along with the severity of the impact of impending failure. For the requirements of detection and identification, the accurate simulation of a stationary crack's mechanical behaviour, quasi-static or dynamic, is also very useful. Information of the strain field extracted by a model, for example, can interpret the deformation of a component (e.g. a shaft or vessel) that contains a crack that would be undetectable by means of visual inspection.

This chapter examines the eXtended Finite Element Method (XFEM) as means of simulating cracks. The main scope is to construct means of simulation of stationary cracks; this is the case of existent defects in structures. Furthermore, a simulated crack can serve as an abstraction inside the modelling space, for a variety of defects, such as material degradation and local loss of stiffness.

2.1.1 Elements of Fracture Mechanics

Fracture mechanics emerged as its own field motivated by the catastrophic failure of Liberty ships in 1943. Irwin combined Griffith's theory of critical energy with Westergaard's solution of the stress fields around cracks (Sun and Jin, 2012; Anderson, 2017). While Westergaard solved the stress function, Irwin contributed an approximation in terms of r, θ. Williams performed a series expansion to provide a more accurate solution, with infinite terms. Notably, the stress fields are singular, with stresses tending towards infinity as the crack is approached radially. This is impossible in reality, as infinite stresses do not have any physical meaning[1]. First, because there exists no material whose strength tends to infinity, and any amount of far-field stress would cause the crack to propagate, which does not happen. Second, because stress is a concept of continuum mechanics, whose assumptions do not hold at the molecular scale. At the macroscale, where the continuum assumptions hold, fracture is found to be driven by the Stress Intensity Factor (SIF), which is directly connected to Griffith's critical energy, and can be considered as an intrinsic material parameter, that can be experimentally measured Sun and Blackman (2020).

Griffith posited that an amount of energy is required to create a new surface on the system Sun and Jin (2012). The intrinsic parameter per unit area is denoted as γ. The total potential energy of the system is Π. Then the loss of energy of the system, for a small extension of the crack da is expressed as

$$-\,d\Pi = 2\gamma da \quad \text{or} \quad -\frac{d\Pi}{da} = 2\gamma. \tag{2.1}$$

The criterion for crack propagation introduced by Irwin states that a crack propagates when a critical energy release rate is reached, the crack propagates, such that

$$G = G_c = 2\gamma. \tag{2.2}$$

---

[1] Higher order elasticity theories have tried to eliminate singularities from crack tips by including parameters dependent on microstructure conjugated with higher order deformations. Notably Aifantis (2003) presents a solution to eliminate the singularity of a screw dislocation, similar to a Mode III crack.

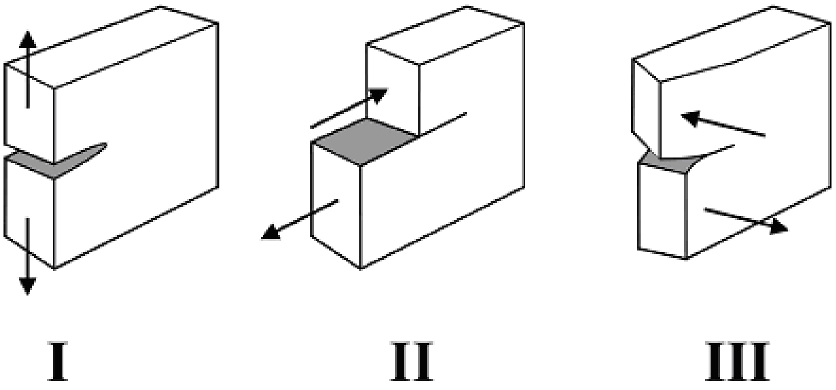

Figure 2.1: Modes of fracture.

Another observation provided by experimentation is that the applied failure stress to propagate a crack is proportional to the inverse square root of the crack length

$$\sigma_f = \sqrt{\frac{G_c E}{\pi a}}. \tag{2.3}$$

The solution for the stresses around the crack tip provided are applicable for an infinite plate, with stresses applied from infinity. Three modes of crack opening are distinguished, with the respective loads (Fig. 2.1): an extension mode, an in-plane shearing mode and an out-of-plane shearing mode. For the extension mode, the stress field around a crack tip, due to far-field stress is

$$\begin{aligned}\sigma_{xx} &= \tfrac{K_I}{\sqrt{2\pi r}} \cos(\tfrac{\theta}{2})(1 - \sin(\tfrac{\theta}{2})\sin(\tfrac{3\theta}{2}))\\ \sigma_{yy} &= \tfrac{K_I}{\sqrt{2\pi r}} \cos(\tfrac{\theta}{2})(1 + \sin(\tfrac{\theta}{2})\sin(\tfrac{3\theta}{2}))\\ \sigma_{xy} &= \tfrac{K_I}{\sqrt{2\pi r}} \cos(\tfrac{\theta}{2})\sin(\tfrac{\theta}{2})\cos(\tfrac{3\theta}{2})\end{aligned} \tag{2.4}$$

with the σ_{ij} the stress components on the respective axes, x, y, and r, θ the radius and angle from the crack tip. The term K_I is the SIF. This is directly connected to Griffith's critical energy in the manner of

$$G_c = \frac{\sigma_f^2 \pi a}{E} \tag{2.5}$$

$$K_c = \sigma_f \sqrt{\pi a} \tag{2.6}$$

$$G_c = \frac{K_c^2}{E}. \tag{2.7}$$

Depending on the direction of the external stress applied, three modes are distinguished: Mode I, the in-plane tension, Mode II, in-plane shear, and Mode III, out-of-plane shear. The energy release rate for a general multi-mode load takes a more general form as

$$G = \frac{1}{E^*}(K_I^2 + K_{II}^2) + \frac{1}{\mu}K_{III}^2 \tag{2.8}$$

with μ the shear modulus and $E^* = E$ in plane stress, $E^* = E/(1-\nu^2)$ in plane strain.

2.1.2 Understanding fracture via micromechanics

While the theory of Linear Elastic Fracture Mechanics (LEFM), elaborated upon above, is the kernel of understanding fracture in materials, its scope is bound by the assumption that the material is linear elastic, and does not fail at a threshold of critical stress. A handful of very brittle materials' fracture is accurately described by this model, such as glass and cast iron. Most materials, however, do exhibit some form of plasticity or post-fracture resistance—i.e. cohesive strength.

The knowledge of a material's microstructure and understanding of across-the-scales mechanical behaviour is useful in predicting its failure mechanisms and formulating a continuous fracture model. This is no trivial task however, and a multitude of interdependent phenomena have been found to contribute towards fracture.

The physics of fracture has largely begun with the study of metals. This is due to the metals being both the most common type of material used in engineering applications, as well as the complexity of their fracture behaviour. The mechanical behaviour of metals emanates from a variety of scales. In the molecular scale, metals are formed of atoms, connected in a crystal structure by the metallic bond. At the meso-scale, they are comprised of grains where the crystal structure is preserved. A bulk of metal contains several grains. Its behaviour depends on both the amount of grains relative to its size, as well as the absolute size of the grains. Materials generally exhibit plastic behaviour: they develop residual deformations if stressed enough. This is due to the motion of dislocations, or small discontinuities in the atomic lattice. In general, dislocations stop at grain boundaries, hence metals with larger grains tend to exhibit higher plastic deformation. Furthermore, the initiation of dislocation motion is dependent on the exerted shear stress. Known models for the plastic regime of metals are Von Mises and Tresca, that describe the effective stress contributing to the initiation of plastic deformation.

The fracture of metals is dependent on their structure. In general, plastic behaviour is observed around the crack tip, as very high stresses are reached in the vicinity. A plastic zone, however, affects the capacity of the material to develop higher stresses, and form of stress arrest is observed.

All materials fracture; not all materials are tough and brittle. Several modes of fracture exist, and extended phenomenology exists to account for it. Linear Elastic Fracture Mechanics (LEFM) is the standard paradigm for most applications of fracture mechanics, with inevitably the most developed computational methods. Inter-crystal cleavage is a common mechanism, attributed to the cutting of inter-atomic bonds. Plastic fracture leads to significantly higher deformations; the underlying mechanisms comprises coalescent voids. Several metals exhibit plastic fracture, at least to some degree. Plasticity is allowed because of metallic bond slippage. Fatigue fracture occurs in materials subjected to cyclic loading. In metals this takes the form of crazes on the fracture surface. The crack opens a little bit in every loading cycle, until it reaches a critical length, where the application of a load leads to unstable propagation Another treatment is identified for cohesive fracture and delamination. Fracture occurs in a strongly preferential direction, such as the lamina. Cohesive laws identify a certain strength/distance relation.

Plastic fracture

Metals and alloys, exhibit generally complex fracture behaviour, that is affected by multiple factors Pineau et al. (2016). Cracks emit dislocations (Lee and Beom, 2020; Gurrutxaga-Lerma et al., 2017), whose accumulation affects the stress field and thus the fracture toughness of the material (Wei and Xu, 2005). Dislocations form a stress field (Ventura et al., 2005) which is reported to both inhibit crack growth or cause transition to brittle fracture, i.e. cleavage. Liang et al. (2019) investigate the shielding mechanism of plastic crack propagation, i.e. the phenomenon at which fracture toughness increases due to the interaction of the dislocations emitted from the crack tip, and the grain boundary. Furthermore, they investigate the brittle transition of cracking at that stage. Under circumstances, alloys exhibit ductile fracture (Wells, 1969). This takes the form of void nucleation, growth and coalescence (Gao et al., 2018; Shakoor et al., 2018; Tran et al., 2019). Hsia and Argon (1994) investigate transition of the fracturing mode, from brittle to ductile, in Si. The presence of hydrogen diffused inside the metal, e.g. in pipes and vessels containing hydrocarbons, or in aquatic and acid environments, favour brittle fracture (Irani et al., 2017; Robertson et al., 2015).

Fatigue fracture

Cracks propagate due to fatigue, when they are subjected to sub-critical but repeated loads (Tavares et al., 2019; Behroozinia et al., 2019; Deshpande et al., 2002). The Paris law (Deshpande et al., 2002) identifies three stages: initiation, steady propagation and critical propagation. The second stage is experimentally found to follow $\mathrm{d}a/\mathrm{d}N = c\Delta K^n$, where c, n are experimentally determinable parameters, inherent to the material, $\mathrm{d}a$ is the crack propagation and $\mathrm{d}N$ the loading cycle. Elastomers (Behroozinia et al., 2019), as well as metals, exhibit fatigue crack propagation.

Atomic scale

The complexity of predicting the fracture behaviour of materials has motivated atomistic simulations (Stepanova and Bronnikov, 2020; Xu et al., 2016; Lee and Beom, 2020; Xu and Demkowicz, 2020; Hwu et al., 2020; Deng et al., 2020; Singh and Mahajan, 2020). Those employ a discrete representation of a representative atomic structure. The interatomic forces are prescribed by the atomic bond potential, and the crystalline structure is exactly represented. Such approaches offer a detailed understanding of underlying phenomena, such as dislocation emission (Lee and Beom, 2020), the plastic fracture mechanisms of void nucleation and coalescence (Deng et al., 2020), and the dependence of fracture toughness on plate thickness (Singh and Mahajan, 2020). A physics-based evaluation of the continuous approach, i.e. the near-tip stress fields, the intensity factor, and fracture criteria is possible (Stepanova and Bronnikov, 2020). The atomistic method is also used as a form of virtual experimentation to calculate the fracture toughness K_c of materials (Xu and Demkowicz, 2020). Despite their usefulness, atomic models are not close to engineering practice. Their very large computational costs usually prevail over their accuracy, and their setting and calibration are also complex tasks.

Multiscale approaches attempt to couple atomistic modelling with continuum methods (Xu et al., 2016; Hwu et al., 2020), applying the atomic resolution in the process zones together with the continuous approach on the boundary problem. Such approaches can allow for phenomena such as brittle-to-ductile transition to be modelled without complicated fracture laws (Xu et al., 2016).

Conclusions

In conclusion, engineering fracture mechanics is a field whose challenges extend into two major axes: the physical and the computational one. The former requires vigorous multiscale approaches and knowledge of the micromechanics and microstructure. The latter deals with accuracy and robustness of the models. Although XFEM addresses the computational scale, there is no panacea, one method to treat every problem. The engineer's judgement need be applied in every case and consideration of what is useful to model is always needed.

2.1.3 Computational fracture mechanics

The first stage of computational fracture mechanics is analytical solutions. Analytical solutions are difficult to produce for arbitrary boundaries and loads. Several analytical solutions have been provided however, for common yet solvable geometries. They connect the SIF to the external load, allowing to determine a critical load at which fracture occurs. These are often used to experimentally measure the K_c parameters. Some boundary value problems have been solved for simple geometries (Sih, 1974). Williams implemented the eigenomode expansion method in the Airy stress function to obtain an infinite series and improved upon the accuracy of Westergaard (Sun and Jin, 2012). The determination of the series' higher order coefficients is attempted (Hello et al., 2012; Ananthasayanam et al., 2007). Those may suffice in some cases for a first approximation, they are not applicable however in general engineering practice. Furthermore, when the crack evolution is of interest, the boundary problem changes rapidly and re-evaluation is required.

Crack-tip singularities with FEM

The Finite Element Method has been applied towards the end of approximating the stress field and calculating the fracture parameters. The high stress gradient at the vicinity of the crack tip requires very high refinement. This is problematic for both the increased computational complexity due to the sheer amount of degrees of freedom required, and the complications introduced by meshing requirements Potyondy et al. (1995). Isoparametric elements are able to represent the stress singularity at the crack tip by properly adjusting the positioning of the nodes. Barsoum (1976) formulates the quarter-node quadratic element, achieving an inverse square root singularity of the Jacobian. Benzley (1974) develop a quadrilateral finite element with a singular corner node. Henshell and Shaw (1975) obtain good results by moving the mid-side node of quadratic elements. ABAQUS implements this strategy by default; the positioning of the mid-side node is recommended to be positioned at 0.25 for LEFM analyses; for Elastic Plastic Fracture Mechanics (EPFM), a selection of 0.30 is suggested (Smith, 2009). Special elements to contain the crack tip have been presented (Karihaloo and Xiao, 2001; Hu et al., 2020). The scaled boundary element method (Chidgzey and Deeks, 2005) with proper placement of the scaling centre at the crack tip, can converge to the Williams series coefficients without additional post-processing. The fractal-like finite element method (Su and Feng, 2005; Su and Fok, 2007; Treifi et al., 2008) implements a self-similar refinement of the approximation, along with a spider-web discretization, emanating radially from the crack tip.

Meshless methods

Meshless methods (Memari and Khoshravan Azar, 2020; Yu and Bui, 2018; Rabczuk et al., 2007; Ren et al., 2017; Ma et al., 2020; Tanaka et al., 2019, 2017, 2015; Ma et al., 2019; Aduloju and Truster, 2019; Liu and Liu, 2018; Tanaka et al., 2013) are a counterpart to FEM. They employ the same approach of discretizing the quantity into discrete nodes and employ interpolation functions. They do not, however, construct a mesh, thus not predefining the support of interpolation functions. Their advantage of eschewing meshing operations is significant in refinement operations, e.g. around crack tips. The lack of predefined support of interpolation functions is their drawback though, as the Gauss quadrature employed in FEM is not directly applicable, and proper integration domains need to be defined. The re-discretization of the domain for a propagated crack is relatively simple, by addition of nodes Memari and Khoshravan Azar (2020). The usage of extended approximations, as in XFEM, through the PU, has become commonplace (Tanaka et al., 2015, 2017; Ma et al., 2020). The postprocessing for fracture parameters is conducted in a similar way, with J-Integral (Tanaka et al., 2017) and the interaction integral cast on domain form (Memari and Khoshravan Azar, 2020) are used. The meshless variant of peridynamics (Ren et al., 2017) employs an integral form of the equation of motion.

Recently, the phase field method for fracture has been introduced (Ahmadi, 2020; Dean et al., 2020; Pillai et al., 2020; Mandal et al., 2020; Raghu et al., 2020; Moshkelgosha and Mamivand, 2020; Alessi et al., 2020; Kakouris and Triantafyllou, 2019; Hai et al., 2020). The phase field represents the crack as a zero-value of a field; the undamaged body retains a constant value 1. The phase field decays from the uncracked to the cracked region smoothly, subject to a length-scale parameter l_0. A smoothing function dependent on the phase field and its gradient is introduced directly in the Griffith energy of the material Kakouris and Triantafyllou (2019) and the problem is cast on maximizing the energy release rate. The method is capable of representing crack branching and fragmentation.

Adaptive meshing

The convergence of stress fields, as well as the crack path resolution can be improved by adaptive meshing approaches. Cornejo et al. (2020) present a coupled Finite Element-Discrete Element method with a remeshing criterion based on the Hessian of a selected nodal value. Mapping of internal variables is performed and the crack faces are simulated with discrete elements.

Fracture criteria

Fracture under general or mixed-mode stress is complex (Wang et al., 2020). The crack propagation direction depends not only on the stresses, but also on the nature of the material. Erdogan and Sih (1963) theoretically predicated that a crack evolves perpendicularly to the maximum tangential stress at the crack tip in brittle materials under mixed mode loading. Sih (1974) proposed the minimum strain energy density criterion for predicting the direction of crack growth under mixed mode loading.

2.2 Formulation of the eXtended Finite Element

XFEM is colloquially called the GFEM centered around crack applications. Indeed, there is no clear distinction in Literature, with respect to the rigorous definition. It is, however, common to refer to a specific family of enrichments as XFEM. Discontinuous and crack-tip enrichments exist. Initially, the crack-tip solution was implemented in Moës et al. (1999); Belytschko and Black (1999). The discontinuous enrichment was also developed separately (Hansbo and Hansbo, 2004), for both weak and strong discontinuities, with the alias phantom node method.

The eXtended Finite Element method is introduced through Dolbow et al. (2000*a*), Moës et al. (1999), Daux et al. (2000). This is based on the partition of unity method (PUM) Melenk and Babuška (1996). The incorporation of specialized functions into the approximation space is something also found as generalized finite element method (GFEM) Strouboulis et al. (2000), Strouboulis et al. (2001). In XFEM the specialized functions

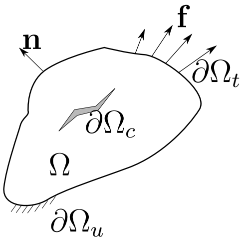

Figure 2.2: The domain Ω with boundary

are a kernel proportional to $\sqrt{r}$, along with some trigonometric function, discontinuous for $\pm\pi$.

The embedding cracks in the mesh has been discussed, and methodologies such as the phantom node method have been introduced Hansbo and Hansbo (2004). In XFEM the Heaviside enrichment is commonly implemented.

The discontinuous nature of the enrichment functions renders regular quadrature schemes ineffective or harmful. Several schemes for integration exist and are treated in the section.

The convergence properties of XFEM required an extension of the extant methods for FEM. Those are discussed in the section.

The estimation of fracture properties is the kernel of crack propagation simulation. A section is devoted to the implementation thereof.

The problem of solid mechanics

Consider a domain Ω (Fig. 2.2) with a boundary $\partial\Omega$ that's partitioned in $\partial\Omega = \partial\Omega_t \cup \partial\Omega_u \cup \partial\Omega_c$, and $\partial\Omega_t \cap \partial\Omega_u = \emptyset$. The following equations hold true, and describe the body's static equilibrium:

$$\nabla \cdot \boldsymbol{\sigma} + \mathbf{t} = \mathbf{0} \tag{2.9}$$

$$\boldsymbol{\varepsilon} = \nabla^{sym}\mathbf{u} \tag{2.10}$$

$$\boldsymbol{\sigma} = \mathbf{C} : \boldsymbol{\varepsilon} \tag{2.11}$$

$$\boldsymbol{\sigma} \cdot \mathbf{n} = \mathbf{f} \quad \text{on} \quad \partial\Omega_t \tag{2.12}$$

$$\mathbf{u} = \bar{\mathbf{u}} \quad \text{on} \quad \partial\Omega_u \tag{2.13}$$

where $\mathbf{u}$ is the displacement vector, $\boldsymbol{\sigma}$ the stress tensor, $\boldsymbol{\varepsilon}$ the strain tensor, $\mathbf{C}$ Hooke's tensor, $\mathbf{t}$ internally applied tractions, $\bar{\mathbf{u}}$ some prescribed displacement, $\mathbf{f}$ tractions applied on the external surface.

We consider a partition of the domain into non-overlapping elements $\Omega = \bigcup_{e=1}^{N} \Omega_e$. The elements are defined by their nodes. $\Omega_i \cap \Omega_j = \{N_I, N_J, ...\}$. The displacements in FEM are approximated through a discrete field $\mathbf{u}_i$, on a field of nodes. Certain interpolation functions are employed to express the field in any arbitrary point $\mathbf{x}$ inside the field. These functions are supported within the bounds of the elements, in a non-overlapping manner. The displacement field for XFEM employs some additional functions in such that

$$\begin{aligned} u^j(\mathbf{x}) \quad &= \textstyle\sum_{i\in\mathcal{I}} N_i(\mathbf{x}) u_i^j \\ &+ \textstyle\sum_{i\in\mathcal{J}} N_i(\mathbf{x}) H(\mathbf{x}) a_i^j \\ &+ \textstyle\sum_{i\in\mathcal{J}} N_i(\mathbf{x}) \left(\sum_{k=1}^{n_k} F_{ik}^j(\mathbf{x}) b_{ik}^j\right) \end{aligned} \tag{2.14}$$

with the nodal sets $\mathcal{J}$, $\mathcal{K}$ defined as enriched sets. Those are quasi-arbitrarily defined, or defined in a convenient manner. u^j denotes the jth degree of freedom (DoF), with possible values $u^j \in \{u, v, w, \beta_x, \beta_y, \beta_z\}$ three translational and three rotational DoF. For the Heaviside enrichment that allows elements to split, one extra DoF a_i^j is introduced. The function F_{ik}^j can take several values according to the instance used, which will be elaborated upon in Sec. 2.2.2, with a varying number n_k of extra DoF b_{ik}^j.

2.2.1 Kinematics of Reissner-Mindlin plates and shells

Plate structures are common in engineering applications. Theories have been developed to facilitate their analysis, based on their behaviour. The Kirchoff theory is based on the assumption that the deflection is a function of the section's rotation; this implicitly disregards the contribution of the transverse shear strains in the potential energy. The Reissner-Mindlin theory includes the work done by shear strains.

The in-plane displacements are split into a symmetric and an antisymmetric component.

The antisymmetric component reads

$$\mathbf{u}(x) = \begin{cases} u_1(x) = x_3\psi_1(x_1, x_2), \\ u_2(x) = x_3\psi_2(x_1, x_2), \\ u_2(x) = w(x_1, x_2), \end{cases} \tag{2.15}$$

with w the plate's deflection and ψ_1, ψ_2 the section rotations, such that

$$\begin{Bmatrix} \psi_1 \\ \psi_2 \end{Bmatrix} = \begin{bmatrix} 0 & 1 \\ -1 & 0 \end{bmatrix} \begin{Bmatrix} \beta_1 \\ \beta_2 \end{Bmatrix} \tag{2.16}$$

with β_1, β_2 the rotations about x_1, x_2. Those are defined for convenience's sake, so that the quantity ψ_i affects the respective u_i, notwithstanding vector operations.

The strain is defined in Eq. 2.10 and when applied to Eq. (2.15) reads

$$\boldsymbol{\varepsilon} = \begin{Bmatrix} \varepsilon_{11} \\ \varepsilon_{22} \\ \varepsilon_{12} \\ \varepsilon_{13} \\ \varepsilon_{23} \end{Bmatrix} = \begin{Bmatrix} x_3\psi_{1,1}(x_1, x_2) \\ x_3\psi_{2,2}(x_1, x_2) \\ \frac{1}{2}(x_3\psi_{1,2}(x_1, x_2) + x_3\psi_{2,1}(x_1, x_2)) \\ w_{,1} + \psi_1 \\ w_{,2} + \psi_2 \end{Bmatrix}. \tag{2.17}$$

The strain component ε_{33} is zero by assumption, which in practice holds true for plates. We define the moments and shear forces as

$$M_{ij} = \int_{-t/2}^{t/2} x_3\sigma_{ij}\mathrm{d}x_3 \tag{2.18}$$

$$Q_j = \int_{-t/2}^{t/2} \sigma_{j3}\mathrm{d}x_3 \tag{2.19}$$

The potential energy due to a virtual displacement field $\delta\mathbf{u}$ is

$$\delta\mathcal{U} = \int_{\Omega} \sigma_{ij}\epsilon_{ij}(\delta\mathbf{u})\mathrm{d}\Omega \tag{2.20}$$

which, when expanded and by the kinematic assumptions given in Eq. (2.17), become

$$\begin{aligned}\delta\mathcal{U} = \int_\Omega & \underbrace{x_3^2(\psi_{1,1}E\delta\psi_{1,1} + \psi_{2,2}E\delta\psi_{2,2} + \psi_{1,2}\mu\delta\psi_{1,2} + \psi_{2,1}\mu\psi_{2,1})}_{\delta\mathcal{U}^b} \\ & + \underbrace{\mu k\left[(w_{,1} + \psi_1)(\delta w_{,1} + \delta\psi_1) + (w_{,2} + \psi_2)(\delta w_{,2} + \delta\psi_2)\right]}_{\delta\mathcal{U}^s}\mathrm{d}\Omega, \end{aligned} \tag{2.21}$$

with E the Young's modulus, μ the shear modulus, as per Lamé's notation and $k = 5/6$ an equivalence factor for a parabolic distribution of shear stresses, so that the strain energy is preserved. The $\delta(\circ)$ denotes terms that result from the virtual displacement field $\delta\mathbf{u}$. Two different contributing terms are identified for the potential energy, $\delta\mathcal{U}^b$ the bending and $\delta\mathcal{U}^s$ the shear. Integrating through the thickness, one obtains

$$\delta\mathcal{U}^b = \int_A M_{11}\delta\psi_{1,1} + M_{22}\delta\psi_{2,2} + M_{12}(\delta\psi_{1,2} + \delta\psi_{2,1})\mathrm{d}A \tag{2.22}$$

$$\delta\mathcal{U}^s = \int_A Q_1(\delta w_{,1} + \delta\psi_1) + Q_2(\delta w_{,2} + \delta\psi_2)\mathrm{d}A \tag{2.23}$$

The external work is defined in terms of moments and shears

$$\delta\mathcal{W} = \int_{\partial\Omega_t} \bar{\mathbf{M}}\delta\boldsymbol{\psi} + \bar{Q}\delta w\mathrm{d}\Gamma. \tag{2.24}$$

with $\bar{\mathbf{M}} = M_{ij}n_j$ and $\bar{Q} = Q_jn_j$ the externally applied moments and forces and n_j the jth component of the outward normal unit vector of domain Ω. For equilibrium's sake, the variation of the internal potential energy and the external work must equal zero, and therefore

$$\delta\mathcal{U}^b + \delta\mathcal{U}^s - \delta\mathcal{W} = 0. \tag{2.25}$$

Eliminating the virtual field and applying the divergence theorem, the following equations are reached:

$$M_{ij,j} - Q_j = 0 \tag{2.26}$$

$$Q_j = 0 \tag{2.27}$$

$$\bar{M}_j = M_{ij} n_j \tag{2.28}$$

$$\bar{Q} = Q_j n_j \tag{2.29}$$

Weak form of the problem

The functions w, ψ_1, ψ_2 are assumed to take the form

$$\mathbf{u}(\mathbf{x}) = [\mathbf{N}(\mathbf{x})]\,\hat{\mathbf{u}} \tag{2.30}$$

with N_i interpolation functions and w_i a vector of discrete values. The virtual field is approximated in the same way. Then the potential energy becomes

$$\delta\mathcal{U} = \int_A \delta\hat{\mathbf{u}}^T \nabla\mathbf{N}^T \mathbf{C} \nabla\mathbf{N}\hat{\mathbf{u}} \tag{2.31}$$

with $\mathbf{C}$ the constitutive matrix, and the external work

$$\delta\mathcal{W} = \int_{\partial\Omega_t} \mathbf{N}\mathbf{f}\mathrm{d}\Gamma, \tag{2.32}$$

with $\mathbf{f}$ a vector containing all external forces acting on $\partial\Omega_t$.

The matrix $\nabla\mathbf{N}$ contains the derivatives of the element shape functions.

$$\nabla\mathbf{N}^b = \begin{bmatrix} 0 & N_{,1} & 0 \\ 0 & 0 & N_{,2} \\ 0 & N_{,2} & N_{,1} \end{bmatrix} \tag{2.33}$$

$$\nabla\mathbf{N}^s = \begin{bmatrix} N_{,1} & N & 0 \\ N_{,2} & 0 & N \end{bmatrix}. \tag{2.34}$$

Remark. *The shear strain energy needs to decay to zero, as the plate thickness tends to zero.*

$$\mathcal{U}^s = \|\nabla w - \boldsymbol{\psi}\| \to 0 \quad as \quad t \to 0$$

MITC for the alleviation of shear locking

Equation (2.34) does not provide enough functions to allow for the shear energy constraint to be fulfilled. Considering, for example, a state of constant rotation, eq. 2.23 is nonzero. This phenomenon is called locking. Bathe (1995) has demonstrated that the introduction of an independent interpolation for shear strains can alleviate this. This approach is also used in Dolbow et al. (2000*a*) with the XFEM for plates. Finally, the mixed interpolation formulation is used for the shear strains. This takes the form Gruttmann and Wagner (2004)

$$\mathbf{L}^s = \begin{bmatrix} \boldsymbol{\partial}_{,\xi} & (\mathbf{b}^{11}\boldsymbol{\partial}_{,\xi}) & (\mathbf{b}^{21}\boldsymbol{\partial}_{,\xi}) \\ \boldsymbol{\partial}_{,\eta} & (\mathbf{b}^{12}\boldsymbol{\partial}_{,\eta}) & (\mathbf{b}^{22}\boldsymbol{\partial}_{,\eta}) \end{bmatrix} \tag{2.35}$$

with the vector differential operator defined as

$$\boldsymbol{\partial}_{,\xi} = \begin{bmatrix} \partial_{,\xi} & \partial_{,\xi} & \partial_{,\xi} & \partial_{,\xi}, \end{bmatrix} \tag{2.36}$$

and similar for η. $\mathbf{b}^{ij}$ are diagonal matrices with components

$$\begin{aligned} b_I^{11} &= \xi_I x^M_{,\xi}, \quad b_I^{12} = \xi_I y^M_{,\xi} \\ b_I^{21} &= \eta_I x^L_{,\eta}, \quad b_I^{22} = \eta_I y^L_{,\eta}. \end{aligned} \tag{2.37}$$

I denotes the nodes and ξ_I, η_I are the isoparametric coordinates at the respective element node, such that $\xi_I \in \{-1, 1, 1, -1\}$ and $\eta \in \{-1, -1, 1, 1\}$. Finally, $(I, M, L) \in \{(1, B, A); (2, B, C); (3, D, C); (4, D, A)\}$, where A, B, C, D are the shear strain tying points defined in the isoparametric coordinates as displayed in Fig. 2.3b.

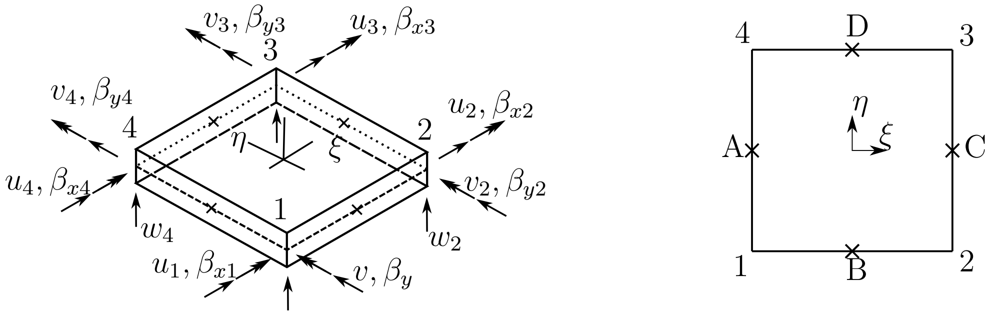

(a) Shell element with 5 DoF. (b) Shell element with 5 DoF.

Figure 2.3: MITC shell element.

2.2.2 Enrichment

The enrichment functions implemented in XFEM and GFEM have the properties of a priori known properties of the solution. For crack problems, one anticipates the form of the singularity of the stress field, proportional to $r^{-1/2}$, along with the discontinuity of both the normal displacement and stress, along the crack lips, expressed by trigonometric functions, e.g. $\sin(\theta/2)$, which is discontinuous at $\theta = \pm\pi$.

The common enrichment functions used in XFEM for fracture mechanics are

$$\mathbf{F} = \left[\sqrt{r}\sin\left(\frac{\theta}{2}\right) \quad \sqrt{r}\cos\left(\frac{\theta}{2}\right) \quad \sqrt{r}\sin\left(\theta\right)\sin\left(\frac{\theta}{2}\right) \quad \sqrt{r}\cos\left(\theta\right)\sin\left(\frac{\theta}{2}\right) \right]. \tag{2.38}$$

which are the sufficient functions to reconstruct the displacement field around a crack, as provided by the Westergaard solution. Another set of functions is used to approximate the out-of-plane deflections of plates

$$\mathbf{G} = \left[r^{\frac{3}{2}}\sin\left(\frac{\theta}{2}\right) \quad r^{\frac{3}{2}}\cos\left(\frac{\theta}{2}\right) \quad r^{\frac{3}{2}}\sin\left(\frac{3\theta}{2}\right) \quad r^{\frac{3}{2}}\cos\left(\frac{3\theta}{2}\right) \right]. \tag{2.39}$$

that follow the Sih, Sosa & Eischen solutions. The latter could be expanded to include a $\sqrt{r}\sin(\theta/2)$ term, that approximates the Mode III load, or the out-of-plane shearing.

It is demonstrated that the reconstruction of the displacement field from the solution Fries (2008) can be conveniently reconstructed if the additional DoF decay to zero at the nodes. This is achieved by the shifting enrichment approach, such that

$$\bar{\mathbf{F}}_I = \mathbf{F}(\mathbf{x}) - \mathbf{F}(\mathbf{x}_I) \tag{2.40}$$

where $\mathbf{x}_I$ is the position of the Ith node. Fries (2008) also addresses the problem of the lack of partition of unity on blending elements. As the elements which do not have all nodes enriched, fail to preserve the partition of unity. The introduction of a ramp function that decays to zero is introduced

$$\bar{\mathbf{F}}^* = R^*(\mathbf{x})\bar{\mathbf{F}} \tag{2.41}$$

where

$$R^*(\mathbf{x}_I) = 1 \quad \text{if} \quad I \in \mathcal{K}, \; 0 \, \text{otherwise}. \tag{2.42}$$

Different enrichment types have been proposed. Higher order enrichments are found in several papers, e.g. Xiao and Karihaloo (2003). Enrichments for anisotropic material and bi-material interfaces have been proposed by Motamedi and Mohammadi (2012). Enrichments for plates and shells are found in Dolbow et al. (2000*b*).

Fries and Belytschko (2006), Fries and Belytschko (2007) present a method of incorporating the enriched function and the classical shape functions, by a moving least squares approach, without additional degrees of freedom at the nodes.

Bayesteh and Mohammadi (2013) use an enrichment for orthotropic materials. They formulate the interaction integral to separate SIFs in mixed-mode fracture.

2.2.3 Crack representation with Level Sets

Level set is the representation of an entity of dimensionality n as an iso-surface of $n + 1$ dimension. For example a crack in 2D, of dimensionality $n = 1$ will be represented by a surface, where the crack is defined as the zero iso-line. The level set is used to trace the position and movement of interfaces Osher and Fedkiw (2001). The method is used in e.g. Osher and Santosa (2001) geometric constrained optimization problems.

Level sets have multiple applications in computational geometry. They can be used to track any surface.

In XFEM two level set functions are defined. First, the signed distance function

$$\phi(\mathbf{x}) = \operatorname{sign}(\mathbf{n} \cdot (\mathbf{x} - \mathbf{x}_c)) \min_{\mathbf{x}_c \in \mathcal{C}} \|\mathbf{x} - \mathbf{x}_c\| \tag{2.43}$$

with $\mathcal{C}$ a curve, $\mathbf{n}$ its outward normal vector. In open curves such as cracks, it is possible to define a second surface such that

$$\nabla\phi \cdot \nabla\psi = 0 \tag{2.44}$$

with $\psi = 0$ on the crack tip, $\psi < 0$ inside the crack and $\psi > 0$ outside.

The enrichment of weak discontinuities, such as inclusions, is effectuated through the absolute of the distance function $|\phi|$. Sukumar et al. (2001) models holes and inclusions, obtaining optimal rate of convergence in the energy norm.

For the polar enrichment functions of cracks, the coordinate transform can be done conveniently by

$$r = \sqrt{\phi^2 + \psi^2} \tag{2.45}$$

$$\theta = \arctan\left(\frac{\phi}{\psi}\right). \tag{2.46}$$

This function implicitly preserves the discontinuity of the enrichment Duflot (2007), as $\theta = \pm\pi$ on the crack, leading to a discontinuous $\sin(\theta/2)$ term. For the integration of the stiffness matrix, certain coordinate transformations are required. In order to perform those, one conveniently reaches the formulae

$$\begin{aligned} \tfrac{\partial r}{\partial \phi} &= \tfrac{\phi}{r}, & \tfrac{\partial r}{\partial \psi} &= \tfrac{\psi}{r}, \\ \tfrac{\partial \theta}{\partial \psi} &= \tfrac{\psi}{r^2}, & \tfrac{\partial \theta}{\partial \phi} &= -\tfrac{\phi}{r^2} \end{aligned} \tag{2.47}$$

The updating of level sets is treated in Duflot (2007), for existent kinks in cracks. Gravouil et al. (2002) use a Hamilton-Jacobi equation to update level sets in 3D.

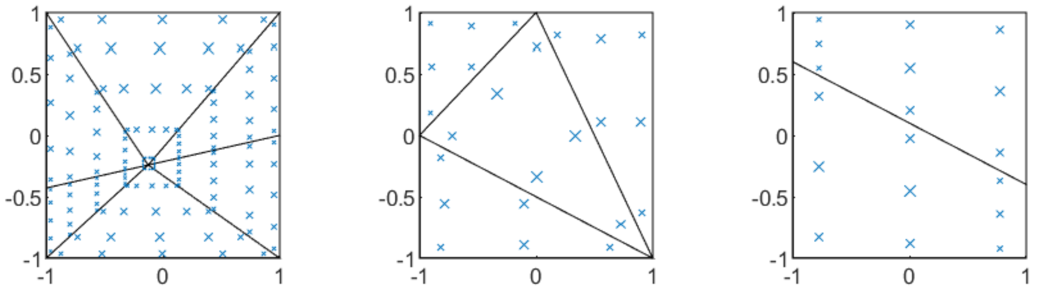

(a) Crack tip. (b) Corner. (c) Middle.

Figure 2.4: Integration scheme for cracked elements. (×) marks the Gauss points; scaling proportional to weight.

2.2.4 Integration

Integration in conventional elements is usually conducted through Gauss quadrature. The integration of enriched elements is a non-trivial process, as it involves discontinuous and singular functions. Several approaches have been tried. The quasi-polar integration has been reached as a consensus.

Natarajan et al. (2009),Natarajan et al. (2010) present an integration scheme that implements conformal mapping to transform the integration domain into a regular shape, avoiding element subdivision. Strouboulis et al. (2000) uses adaptive integration for the GFEM. Cheng and Fries (2009) demonstrate the usage of higher p order XFEM for curved discontinuities. The properties of higher order elements are exploited in subdivision of curved domains. Convergence properties are generally poorer than linear XFEM.

Figure 2.4 depicts the subdivision of the elements used in integration. In Fig. 2.4a a square 5×5 grid is employed. One of the corners of the sub-element is duplicated, creating the collapsing effect of the points. This scheme's merit is the mapping of the polar behaviour of the enrichment functions. Figures 2.4b and 2.4c denote two possible cases of the intersected element: when the crack intersects the element in the corner, cutting off a single node, or in the middle. In the former, a division in triangles is employed, along with the respective Gauss quadrature. In the latter, subdivision is possible into quadrilaterals. The markers in Fig 2.4 are scaled by their relative weight. When a scheme of subdivision is used, the weight is normalized to preserve consistency.

2.2.5 Convergence

Convergence of XFEM has been investigated in various works. Almost exclusively a posteriori error estimation is used. Several factors that affect convergence have been identified. Convergence may be tested on global energy or SIF calculation, for crack problems. Ainsworth and Oden (1997) reviews and traces error estimation for FEM. A distinction is made between *a priori* and *a posteriori* error estimation.

Higher order elements do not in general improve convergence.

Partially enriched elements cause problems because of the lack of partition of unity, introducing spurious strains. Fries (2008) introduced a ramp function whose value is 1 in representing elements, while decaying to 0 in blending elements, preserving the partition of unity.

Bordas and Duflot (2007) utilizes the L_2 norm of the difference between the XFEM strain field and an enhanced strain field computed by extended moving least squares, i.e. opting for a base of approximation functions extending beyond polynomials and in particular those selected to represent the displacement fields around a crack. The derivative of the smooth displacement field is taken and compared to the default strains calculated at the Gauss points. For the smoothed displacement field, extra points are often employed, such as those at the lips of the crack, along with a diffraction criterion to limit the support of points at the discontinuity. The diffraction criterion is also used in Tanaka et al. (2017, 2015) to construct a meshless approach. Bordas et al. (2008) use the extended global derivative recovery (XGR) which has lower continuity of the recovered fields compared to XMLS. It is shown that increased enrichment radius may be beneficial for the strain difference norm. Duflot and Bordas (2008) presents the XGR. It is a fit of the strain field directly on the default derivative. The enhanced strain field reads

$$\boldsymbol{\varepsilon}^s(\mathbf{x}) = \sum_{i=1}^{N} \phi_i(\mathbf{x})\mathbf{d}_i + \sum_{j\in\mathcal{J}} \phi_j(\mathbf{x})h(\mathbf{x})\mathbf{e}_j + \sum_{k\in\mathcal{K}} \phi_k(\mathbf{x}) \left(\sum_{l}^{4} G_l(\mathbf{x})\mathbf{f}_{kl} \right) \tag{2.48}$$

where $h(\mathbf{x})$ is the discontinuous function and $G_l(\mathbf{x})$ a kernel of functions to represent the Westergaard solution for strains and stresses. The problem is then to determine the coefficients $\mathbf{d}_i$, $\mathbf{e}_j$, $\mathbf{f}_{kl}$, through the minimization of a quadratic functional. González-Estrada et al. (2012) use the extended superconvergent patch recovery technique and show improved convergence for K_2 loading. Panetier et al. (2010) calculate a bound for the convergence rate of fracture problems against mesh refinement. Extraction of SIFs via the displacement jump is mentioned, but very fine elements near the tip are needed. Error of XFEM is smaller than FEM for K_1 mode loading, but for K_2 this is not the case. Gallimard and Panetier (2006) develop an estimator for the error of mixed-mode ($K_1 - K_2$) stress intensity factors. Prange et al. (2012) use the Fries (2008) correction. They produce an enhanced stress field that can be extended to accommodate for plasticity, by adjusting the exponents of the $r^{\beta-1}$ term, with r the radius emanating from the crack tip.

José Ródenas et al. (2008) adapt the superconvergent patch recovery (Zienkiewicz and Zhu, 1992; Kvamsdal and Okstad, 1998) to XFEM by splitting the stress field into a smooth and a singular part

$$\boldsymbol{\sigma} = \boldsymbol{\sigma}_{smooth} + \boldsymbol{\sigma}_{singular}. \tag{2.49}$$

Ródenas et al. (2010) using this methodology, extend it to create a nearly statically admissible recovered stress field. Xiao and Karihaloo (2006) use a Gauss quadrature scheme that subdivides intersected elements, along with statically admissible stress recovery. Strouboulis et al. (2001) demonstrates good convergence properties of re-entrant corner enrichment functions for GFEM. Strouboulis et al. (2006) presents an *a posteriori* error estimator for GFEM.

Fries (2008) demonstrated that a restitution of partition of unity in the blending elements, improves convergence.

2.3 Calculation of fracture parameters with XFEM

The usage of XFEM in fracture problems has been well established. Issues lie on various axes. The estimation of fracture parameters is one. Here, some applications of methods to estimate fracture parameters. In the 2.2.5 the convergence of XFEM was studied. Several works aim towards the accurate calculation of Stress Intensity Factors, as the end goal of a crack simulation. Several schemes have been developed towards that goal; Xiao and Karihaloo (2003), Liu et al. (2004) reordered the enrichment functions to directly derive SIFs.

Zi and Belytschko (2003) develop an XFEM for cohesive fracture. The crack-tip can be represented within an element, without the crack-tip enrichment functions.

The J-Integral Rice (1964) is the most common method by which fracture parameters are extracted. It calculates the energy release rate, and it's valid for both elastic and plastic problems. Fracture problems are generally mixed-mode, and all SIFs need to be evaluated. This is difficult to achieve with a single evaluation of the J-Integral, as it yields the total energy release rate. The connection between the energy release rate and the SIF is given.

The interaction integral is an extension of the J-Integral, with an auxiliary field. This is being used extensively for fracture mechanics applications. It is possible to transform the contour to a plane domain, making integration more suitable for FEM.

2.3.1 The J-Integral

The J-Integral (Rice, 1964) is defined as

$$J_n = \int_\Gamma \left(W \mathrm{d}x_2 - \mathbf{t} \cdot \frac{\partial \mathbf{u}}{\partial x_2} \mathrm{d}s \right) \tag{2.50}$$

where $\mathbf{t} = \sigma \cdot \mathbf{n}$ is the traction vector on the contour infinitessimal ds with the outward normal vector $\mathbf{n}$.

$$W = \int_0^\epsilon \sigma : \mathrm{d}\epsilon \tag{2.51}$$

is the strain energy density. Eq. 2.51 is general to account for plastic and generally nonlinear strains. The J-Integral is zero over a closed path; it is also path-independent, meaning that, regardless the contour, it should yield the same value.

The evaluation of J-Integral requires knowledge about the fields around the crack. The strains and consequently the stresses are derivatives of the displacement field, and deriva-

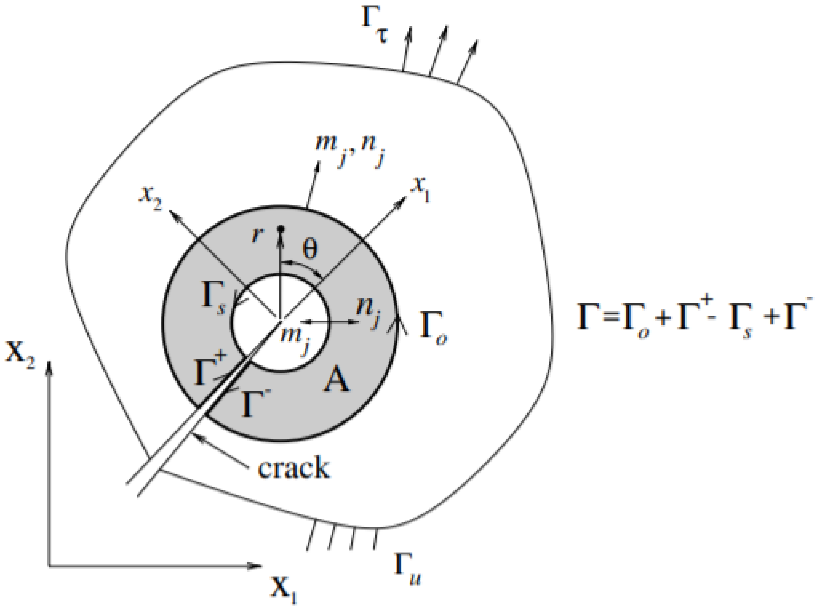

Figure 2.5: Transform of the J-Integral to the domain form Kim and Paulino (2003).

tives are evaluated in the Gauss points. When postprocessing involves smoothing, stresses may be calculated at nodes. Some works have reported superconvergence when implementing patch recovery, leading to very accurate results. This process involves on its own a least-squares fitting operation, that defeats the purpose of evaluating a J-Integral, as the fracture parameters are already fitted constants. The usage of higher terms of the Williams expansion can lead to slight improvement of the results, and as a compromise between near and far-field solutions.

2.3.2 Domain form of the integral

The properties of the J-Integral permit the transformation to an equivalent domain integral (Dolbow et al., 2000*b*; Kim and Paulino, 2003). This is especially convenient in the FEM and XFEM context, as integration can be made directly through known and retained quantities of the shape functions, along with the predefined weights and positions of the Gauss points.

A weight function q is defined, which takes the value 1 inside Γ_s and decays to zero at an outer Γ_0. In the presence of a crack, one defines $\Gamma = \Gamma_0 + \Gamma^+ - \Gamma_s + \Gamma^-$. The integral then becomes(Kim and Paulino, 2003):

$$\mathcal{H} = \oint_{\Gamma} (W\delta_{1j} - \sigma_{ij}u_{i,1})m_j q \mathrm{d}\Gamma, \tag{2.52}$$

where m_j and n_j are unit vectors; m_j is outward with respect to the contour Γ that encircles the shaded domain A of Fig. 2.5.

$$\begin{aligned}
\lim_{\Gamma_s \to 0} \mathcal{H} &= \lim_{\Gamma_s \to 0} \oint_{\Gamma} (\mathcal{W}\delta_{1j} - \sigma_{ij}u_{i,1})m_j q \mathrm{d}\Gamma \\
&= \lim_{\Gamma_s \to 0} \oint_{\Gamma_0 + \Gamma^+ + \Gamma^- - \Gamma_s} (\mathcal{W}\delta_{1j} - \sigma_{ij}u_{i,1})m_j q \mathrm{d}\Gamma \\
&= \lim_{\Gamma_s \to 0} \left[\oint_{\Gamma_0 + \Gamma^+ + \Gamma^-} (\mathcal{W}\delta_{1j} - \sigma_{ij}u_{i,1})m_j q \mathrm{d}\Gamma + \oint_{-\Gamma_s} (\mathcal{W}\delta_{1j} - \sigma_{ij}u_{i,1})m_j q \mathrm{d}\Gamma \right] \\
&= \lim_{\Gamma_s \to 0} \left[\oint_{\Gamma_0 + \Gamma^+ + \Gamma^-} (\mathcal{W}\delta_{1j} - \sigma_{ij}u_{i,1})m_j q \mathrm{d}\Gamma - \oint_{\Gamma_s} (\mathcal{W}\delta_{1j} - \sigma_{ij}u_{i,1})n_j q \mathrm{d}\Gamma \right].
\end{aligned} \tag{2.53}$$

As $q = 0$ on Γ_0 and the crack surfaces are traction-free, the above can be simplified to

$$J = -\lim_{\Gamma_s \to 0} \oint_{\Gamma} (\mathcal{W}\delta_{1j} - \sigma_{ij}u_{i,1})m_j q \mathrm{d}\Gamma \tag{2.54}$$

and applying the divergence theorem

$$J = \int_A (\sigma_{ij}u_{i,1} - \mathcal{W}\delta_{1j})q_{,j} \mathrm{d}A + \int_A (\sigma_{ij}u_{i,1} - \mathcal{W}\delta_{1j})_{,j} q \mathrm{d}A. \tag{2.55}$$

2.3.3 General derivation of the Interaction Integral

The Interaction Integral between two states, the actual $(\mathbf{u}, \boldsymbol{\varepsilon}, \boldsymbol{\sigma})$ and an auxiliary $(\mathbf{u}^{aux}, \boldsymbol{\varepsilon}^{aux}, \boldsymbol{\sigma}^{aux})$ one is written as

$$J^s = J + J^{aux} + M = \oint_{\Gamma} \left\{ \mathcal{W}^s \delta_{1j} - (\sigma_{ij} + \sigma_{ij}^{aux})(\varepsilon_{ij} + \varepsilon_{ij}^{aux}) \right\} n_j \mathrm{d}\Gamma \tag{2.56}$$

with J defined in Eq. (2.55) and J^{aux} same. M is the Interaction Integral, which, in the surface form of Eq. (2.55), reads

$$M = \int_A \left\{ (\sigma_{ij} u_{i,1}^{aux} + \sigma_{ij}^{aux} u_{i,1}) - \mathcal{W}^{int} \delta_{1j} \right\} q_{,j} \mathrm{d}A \\ + \left\{ (\sigma_{ij} u_{i,1}^{aux} + \sigma_{ij}^{aux} u_{i,1}) - \mathcal{W}^{int} \delta_{1j} \right\}_{,j} q \mathrm{d}A \quad (2.57)$$

with $\mathcal{W}^{int}$ the interaction energy defined as

$$\mathcal{W}^{int} = \sigma_{ij} \varepsilon_{ij}^{aux} = \varepsilon_{ij} C_{ijkl} \varepsilon_{kl}^{aux}. \quad (2.58)$$

2.3.4 The Interaction Integral for plates

It is possible to reformulate the above relations for plates, considering the kinematic assumptions that have been made above. An actual and an auxiliary state are considered as ($\mathbf{M}$, $\mathbf{Q}$, $\boldsymbol{\psi}$, w) and ($\mathbf{M}^{aux}$, $\mathbf{Q}^{aux}$, $\boldsymbol{\psi}^{aux}$, w^{aux}). First, we define the strain energy as

$$\mathcal{W} = \frac{1}{2} \left[\frac{1}{2} M_{ij} \left(\psi_{i,j} + \psi_{j,i} \right) + Q_i \left(w_{,i} + \psi_i \right) \right]. \quad (2.59)$$

The J-Integral takes the form

$$J = \oint_\Gamma \left\{ \mathcal{W} \delta_{1j} - \left[M_{ij} \psi_{i,j} + Q_i w_{,i} \right] \right\} n_j \mathrm{d}\Gamma. \quad (2.60)$$

Similar to Eq. (2.57), the interaction integral for plates is formulated as

$$I = \oint_\Gamma \left\{ \mathcal{W}^{int} \delta_{1j} - \left[M_{ij} \psi_{i,1}^{aux} + M_{ij}^{aux} \psi_{i,1} + Q_j w_{,1}^{aux} + Q_j^{aux} w_{,1} \right] \right\} \mathrm{d}\Gamma, \quad (2.61)$$

and, in domain form,

$$I = \int_A \left\{ \left[M_{ij} \psi_{i,1}^{aux} + M_{ij}^{aux} \psi_{i,1} + Q_j w_{,1}^{aux} + Q_j^{aux} w_{,1} \right] \right\} q_{,j} \mathrm{d}A \\ + \int_A \left\{ \left[M_{ij} \psi_{i,1}^{aux} + M_{ij}^{aux} \psi_{i,1} + Q_j w_{,1}^{aux} + Q_j^{aux} w_{,1} \right] \right\}_{,j} q \mathrm{d}A \quad (2.62)$$

The energy release rate is connected to the SIF. When a superposition of two states exists, one may write

$$G^s = \frac{12\pi}{Et^3}\left[(K_1 + K_1^{aux})^2 + (K_2 + K_2^{aux})^2\right] + \frac{6\pi}{10\mu t}\left(K_3 + K_3^{aux}\right)^2 \tag{2.63}$$

and, by expanding the squares and noting the definition of J_1, J_1^{aux}, reform Eq. (2.63) into

$$G^s = J_1 + J_1^{aux} + \frac{24\pi}{Et^3}\left(K_1K_1^{aux} + K_2K_2^{aux}\right) + \frac{12\pi}{10\mu t}K_3K_3^{aux} \tag{2.64}$$

and, noting that the J-Integral represents the energy release rate, by Eq. (2.57)

$$I = \frac{24\pi}{Et^3}\left(K_1K_1^{aux} + K_2K_2^{aux}\right) + \frac{12\pi}{10\mu t}K_3K_3^{aux}. \tag{2.65}$$

Equation (2.65) depends on the SIF of the actual and the auxiliary state. By proper selection of the auxiliary terms, it is possible to calculate the separate SIF. For example, by setting $K_1^{aux} = 1$, K_2^{aux}, $K_3^{aux} = 0$, a straightforward inversion of the equation as

$$K_1 = \frac{Et^3}{24\pi}I \tag{2.66}$$

immediately yields the requested SIF. The auxiliary fields utilize the analytical relations for stresses and displacements, as provided by Sosa and Eischen (1986), Dolbow et al. (2000*b*). As Dolbow et al. (2000*b*) suggest, the leading singular terms need be used for calculations made sufficiently close to the crack tip.

Dolbow et al. (2000*b*) remark that further simplifications can be made in the domain form of the Interaction Integral (Eq. (2.62)). Those emanate from the properties of the auxiliary fields. Namely, for non-zero K_1, K_2 but zero K_3, all the shear terms are zero. As the shear strains are defined as $\varepsilon_{i3} = w_{,i} + \psi_i$ and $w_{,i} \neq 0$, the strain-displacement relationship is not satisfied. Conversely for non-zero K_3 and zero K_1, K_2, the moments are zero, but rotations and the derivatives thereof are not. Those simplifications aid the usage of only-first-terms approximation in auxiliary fields. It is possible to incorporate higher-order fields, as per Sosa and Eischen (1986) that will converge towards equilibrium.

After proper simplifications the following formulae are derived. For K_1, K_2

$$I = \int_A \left\{ \left[M_{ij}\psi_{i,1}^{aux} + M_{ij}^{aux}\psi_{i,1} \right] - \mathcal{W}^{int}\delta_{1j} \right\} q_{,j} \mathrm{d}A + \int_A \left(Q_j \psi_{j,1}^{aux} \right) \mathrm{d}A \tag{2.67}$$

and for K_3

$$I = \int_A \left\{ \left[Q_j w_{,1}^{aux} + Q_j^{aux} w_{,1} \right] - \mathcal{W}^{int}\delta_{1j} \right\} q_{,j} \mathrm{d}A - \int_A \left(Q_j^{aux} \psi_{j,1} \right) \mathrm{d}A. \tag{2.68}$$

2.3.5 Remarks on the computational aspect of domain integrals with FEM and XFEM

The motivation to cast the J-Integral on a domain form is to reduce and streamline postprocessing, integrating with the intrinsic integration procedures of FEM and XFEM. Those are related to the evaluation of the required functions and derivatives on the predefined Gauss points. Otherwise, a line integral would require interpolation of the computed values on desirable nodes along a defined trajectory of calculation. This is a task that requires computational geometry libraries, and can be performed in MATLAB with the command `contour(x,y)`.

The definition of the ramp function is examined here more closely. The ramp function requires that two contours be defined, the inner, inside of which $q = 1$ and the outer, at which $q = 0$. Two possible ways exist to define the function. First, a distance-based, where every node's q value inside the enclosed domain A_1 is a function of its distances from the contours. The second is mesh-based and defines a number of element zones for the inner contour, and a number of element zones at which the ramp decays. The zone increment is calculated from a logical operation, as the elements that do not have all their nodes inside the previous contour. The distance-based method is more applicable to rounder domains. The mesh-based method is much more accurate in meshes that possess at least some degree of regularity, as uniform values of the derivatives guarantee preservation of the field's divergence, and therefore the integral's accuracy.

Figure 2.6 shows the ramp function for a uniform mesh. The function has been evaluated

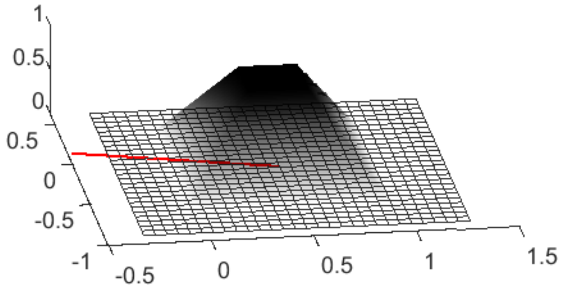

(a) q

(b) $\partial q/\partial\phi$ (c) $\partial q/\partial\psi$

Figure 2.6: Ramp function and the derivatives thereof, with respect to the crack coordinate system calculated by the level set.

at the nodes, whereas the derivatives in the Gauss points. The derivatives are taken with respect to the crack coordinate system. This is conveniently coincident to the values of the level set. It is noted that the calculation of fracture parameters is done on the local coordinate system.

2.4 Implementation of XFEM in MATLAB

The development of an XFEM code is presented herein. The necessary steps are remarked, and a comparison is made with what a conventional FE code requires.

A FE code involves a number of basic functions. The meshing function partitions a given geometry into finite elements connected at nodes, and outputs a connectivity matrix. An element essentially corresponds to the support of the shape functions of its constituent nodes. Once the elements, material properties and external loads have been defined, integration of the stiffness and mass matrices ensues. For the integration of the stiffness matrix, the derivatives of the test and trial functions are required. Those are calculated inside the elements. The element integration is commonly conducted numerically. Thus the shape functions and derivatives are evaluated at quadrature points. Several numeric integration schemes exist, e.g. the Simpson rule for trapezoids and Gaussian quadrature. The latter is preferred in FE.

The differences for the XFEM begin with the meshing process: while FEM requires an explicit geometric representation of cracks or voids/inclusions, the XFEM can incorporate those through some additional functions. The information of the existence of those discontinuities needs to be entered though somehow. The level set of the discontinuity is the common paradigm. The level set translates the domain into discontinuity-specific coordinates, that allow the evaluation of the approximating functions. Concluding the first difference, instead of a single mesh, a mesh and some level set functions are constructed. The additional functions used in the XFEM, are not supported within the element, but within a larger and not easily definable domain. Level sets define a local coordinate system, emanating from the crack tip. The level sets are interpolated within the element in the same manner as coordinates, i.e.

$$\phi(\mathbf{x}) = \sum_{I \in \mathcal{I}} N_I(\mathbf{x}) \phi_I, \tag{2.69}$$

with ϕ_I the calculated value on each node I of the set $\mathcal{I}$ that contains all nodes.

The evaluation of the shape functions and their derivatives is another major issue with XFEM. Many functions—most of the commonly used enrichments—contain singularities. Those would cause errors with common numerical integration schemes, as they yield invalid numbers. A strategic selection of evaluation and integration points is required. This is achieved by sub-meshing the elements that are crossed by the discontinuity. It is relatively easy to determine which are those elements, by looking at the level set values of their nodes.

The integration procedure for the XFE is similar to the FE one. The resultant matrices are, however, partitioned into a classical and an enriched part.

Meshing

The meshing function partitions the given geometry. It does not need to Account for the cracks or inclusions, as those are treated through the introduction of extended interpolation functions.

Level set

Level set calculates the fields ϕ, ψ. The former is defined as the minimum vertical distance between the crack and each node. For cracks defined as lines or Bézier curves, it is possible to define this analytically. If a crack consists of multiple segments, a sorting operation is required to compute the minimal distance for each node and each segment. The level set ψ is required for cracks. It is defined such that $\nabla\phi \cdot \nabla\psi = 0$, i.e. it is vertical to ϕ.

Enriched set

The scope of this function is the construction of the enriched sets. $\mathcal{J}$ is the set of nodes enriched with jump functions and $\mathcal{K}$ the crack-tip enriched functions. First $\mathcal{K}$ is defined as $\mathcal{K} \equiv \{I|\mathbf{x}_I \leq R_{enr}\}$, or the nodes that lie within the selected enrichment radius from the crack tip. $\mathcal{J}$ is then defined by all the nodes whose support is intersected by the crack, and do not belong in $\mathcal{K}$. The connectivity matrix is employed to find the node supports intersected by the crack, such that when the signs on an element's level set nodal values is different, it is intersected. Different intersection cases are discerned (Fig. 2.4).

The global mapping of degrees of freedom (Dof) is also created based on the number of extra Dof of the enrichment functions.

Shape function evaluation

The shape functions and their derivatives are evaluated at the defined integration points, and assembled in matrix form. It is advantageous to export the functions for postprocessing.

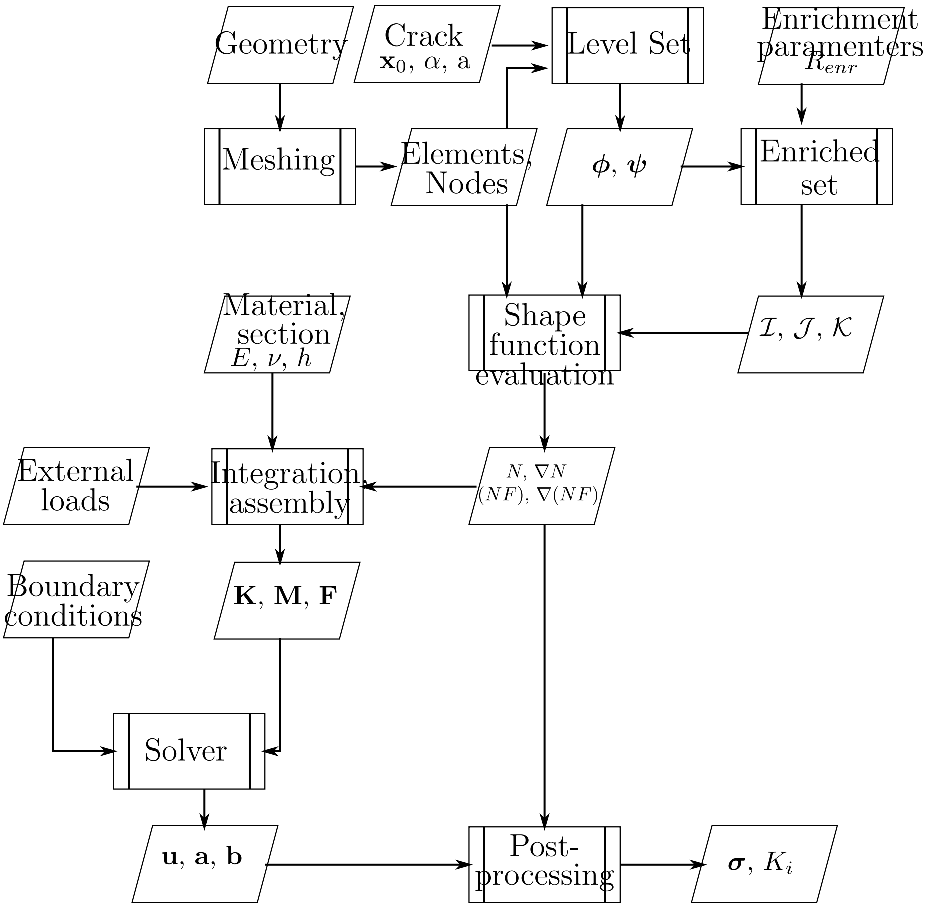

Figure 2.7: Schematic of the XFEM code procedures.

2.5 Fracture applications

For fracture problems, the computation of the Stress Intensity Factor is of interest. There exists an experimentally determined quantity K_c, or a critical SIF which, when overcame, causes the crack to propagate. For multi-mode stress states, several criteria exist to determine whether the crack propagates, and the direction it propagates towards. It is therefore useful to calculate the factors for different modes.

The surface cast interaction integral appears to be a very convenient way to compute the fracture parameters. The virtual fields allow the extraction of each of the modes separately. The surface nature requires that only a few shape function and gradient matrices be retained, while they have been calculated already at the matrix integration step.

A crack propagation scheme would apply a criterion for crack propagation and test it at every increment, such that, if it is fulfilled, the crack propagates. While remeshing is not required, significant savings can be made from the integration and assembly of the stiffness matrix. Given the partition in classical and enriched parts, integration of solely the latter is desired.

2.5.1 Stress Intensity Factors of a simply supported plate subjected to pure bending

A simply supported plate is subjected to uniform moment. The dimensions of the plate are $b = 10mm$, $c = 40mm$. The far field moment is cumulatively $M_0 = 1000Nmm$, uniformly distributed on the edges, as per Fig. 2.8. The crack half-length is denoted as a; for the purposes of testing against crack angle, a constant $a = 1mm$ is taken. The plate thickness is also taken as $t = 1mm$, such that $t/a = 1$. The results are directly compared to the analytical solution available by Sih et al., Dolbow et al. (2000b), Tanaka et al. (2017).

The size of the crack is much smaller than the plate. A number of meshes was tried, and a configuration with an orthogonal refined patch was opted for. A number of 40 elements

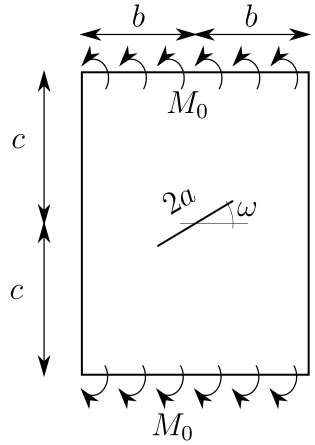

Figure 2.8: Simply supported plate of dimensions $2b \times 2c$ containing a center crack of length $2a$ and rotation ω, loaded with a uniform moment M_0.

along the crack has been opted for, as it was deemed the optimal compromise between computational burden and accuracy; for the amount of refinement required for fracture applications with conventional FE, this is a relatively coarse mesh.

In the following sections the dependencies on crack angle, plate thickness and crack size are studied. Those parameters are also studied in literature. The effect of thickness has been discussed in Tanaka et al. (2017), where inconsistencies were found between their numerical solution and the analytical one from Sih (1974). Furthermore, the results of the latter are contested by Tanaka et al. (2017); Erdogan and Sih (1963), for thinner plates, i.e. $t/a < 1$.

The SIFs are extracted through the method of the interaction integral, as presented in the previous section. The integral's contour-independence is verified, and holds for any size of the ramp. The contour integration is best achieved for regular meshes. Regularity is achieved best when the mesh is orthogonal and the ramp follows the mesh's geometry rather than the crack's. Implementation-wise this means that an input of an auxiliary level set, for a crack of zero angle needs to be constructed. In this work a ramp with a 5x5 element crest is opted for, along with a 3-element inclined zone. As most of the values are computed on the inclined zone, where the derivatives of the ramp function are non-zero, it is perceived advantageous to maintain an at least 2-element wide inclined zone in the ramp.

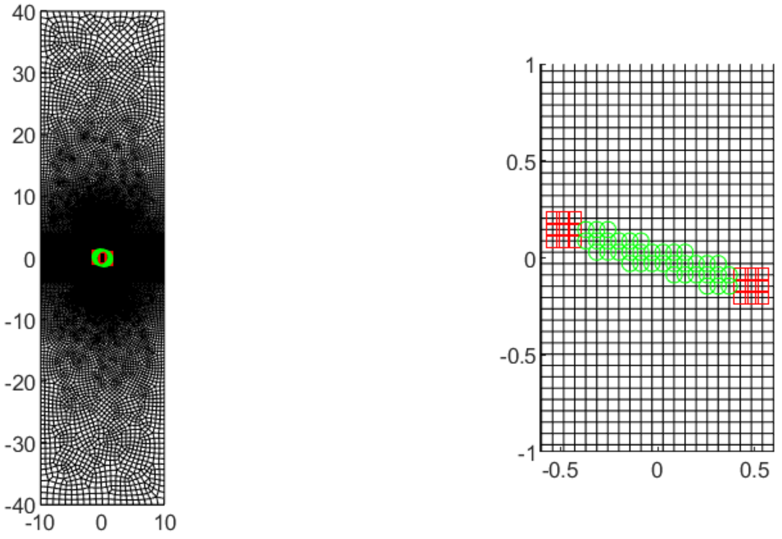

(a) Whole mesh (b) Close-up on crack.

Figure 2.9: Mesh. (□) crack tip enrichment ($\mathcal{K}$ set), (○) jump enrichment ($\mathcal{J}$) set.

Moments and shear forces

The moments and shear forces of the center-cracked plate are shown in Figure 2.10. The figure is centered and zoomed in the region of the crack. To aid visualization, the maximum stresses are cut-off at a threshold of the 99.5th percentile. This is because very high stresses are concentrated at very few points, misplacing the colour gradient. The stresses are calculated at the Gauss points. A Delaunay triangulation and linear interpolation of values is then implemented. It is noted here, that post-processing in XFEM is not as straightforward as conventional FEM, as the Gauss points are not evenly distributed. In conventional FEM it is possible to calculate nodal stresses by averaging neighbouring Gauss points; in XFEM, for enriched elements, this treatment would have to be extended to the sub-elements. For example, crack-tip elements contain several points to evaluate the derivatives. This approach would still be problematic though, as the enriched elements contain steep gradients: the crack tip element is able to accommodate for the contained singularity and averaging the nodal stresses would lead to loss of information. Fig. 2.10a displays the right and shear moments. Right moments are M_{11} and M_{22} and are produced through integration of the antisymmetric right stresses σ_{11} and σ_{22}, while the so-called shear moment is the result of the same process applied to shear stress σ_{12}.

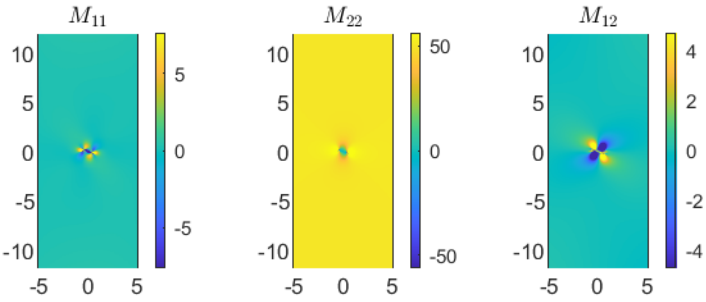

(a) Right moments.

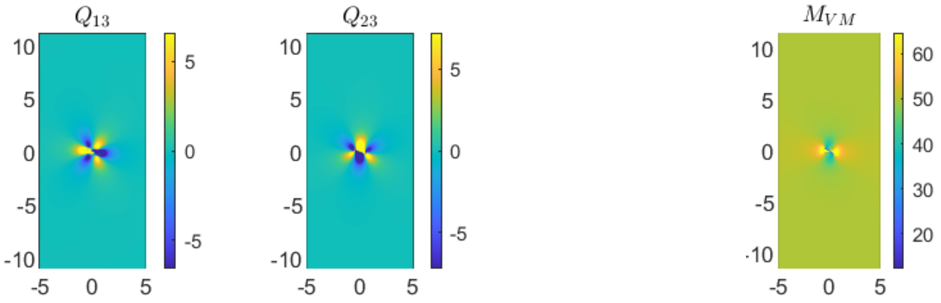

(b) Shear forces.

(c) Von Mises moment.

Figure 2.10: Right moments, shear force and Von Mises monents.

In Finite Element convention, the term τ_{12} is often used instead, which is $\tau_{12} = 2\sigma_{12}$; this is the case for this work. M_{22} is the moment of the loaded direction and can be seen to hold an average value of 50, which is commensurate with the external loading. In the vicinity of the crack, the moment is zero, as the discontinuity cannot transfer it. The crack-tip singularities appear and are similar to the stresses of a plane stress problem. Fig. 2.10b shows the shear forces. For a plate subjected in pure bending, shear force would theoretically be zero; in the presence of a crack, however, those shear forces appear and are equilibrated at the boundaries. Fig. 2.10c displays the Von Mises moment, defined as $M_{VM} = \sqrt{M_{11}^2 - M_{11}M_{22} + M_{22}^2 + 3M_{12}^2}$, or, equivalently, the integration of the Von Mises stress along the thickness of the plate.

Dependency on crack angle

Figure 2.11 depicts the direct comparison of the aforementioned plate with the analytical solution available by Sih et al. The analytical relations to yield the SIF are

$$\begin{aligned} K_1 &= \Phi(1) M_0 \sqrt{a} \cos^2 \omega \\ K_2 &= \Psi(1) M_0 \sqrt{a} \cos \omega \sin \omega \\ K_3 &= -\tfrac{\sqrt{10}}{(1+\nu)t} \Omega(1) M_0 \sqrt{a} \cos \omega \sin \omega \end{aligned} \tag{2.70}$$

where the factors $\Phi(1)$, $\Psi(1)$ $\Omega(1)$ are derived numerically from integral equations. The values used for the given $t/a = 1$ are 0.82, 0.68, 0.06. It is noted that the units for the bending SIFs, namely K_1 and K_2 are $Nmm^{3/2}$, whereas for K_3 the units are $N\sqrt{mm}$.
The results exhibit very good agreement with the ones proposed in literature. The variation of 1° is selected to display existent mesh instabilities with the XFEM. Indeed, selected points appear to exhibit very large aberrations from the analytical curve. This is due to poor numerical conditioning, caused due to disproportional placement of Gauss points in subdivided elements, when cracks intersect or nearly intersect mesh nodes, resulting in poor evaluation of the derivatives. For K_3 this becomes especially apparent, as cracks with angles between 30° and 60° yield consistently more inaccurate results. Dolbow et al. (2000*b*) have treated this by constructing a mesh patch orthogonal to the crack locally. Tanaka et al. (2017) implement a mesh-free method that allows discretization to follow the geometry of the crack, and also show preference in a locally orthogonal patch.

Dependency on plate thickness

The dependency of the stress intensity factors on thickness is shown in Figure 2.12. The factors are normalized with respect to moment and the square root of crack length. The factors are then equivalent of $\Phi(1)$, $\Psi(1)$ $\Omega(1)$ in Eq. (2.70), and are henceforth presented as the reference basis for the results.

The results in Fig. 2.12 have been plotted—for clarity's sake—in two separate graphs: for $t/a < 1$ (2.12a) and $t/a > 1$ (2.12b). The results are compared with those from Tanaka et al. (2017), which also demonstrates agreement with the analytical derivations of Sih et

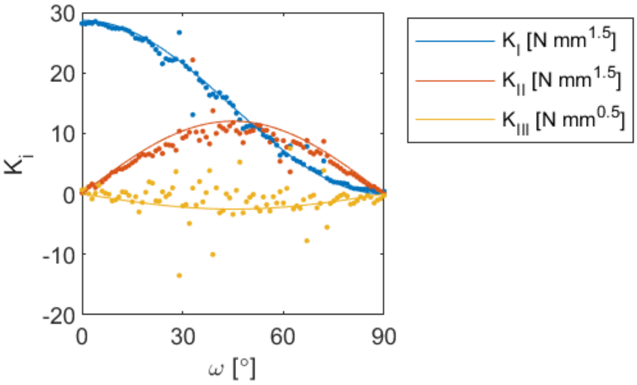

Figure 2.11: SIF of center-cracked simply supported plate against crack angle. Continuous lines depict theoretical values, dots XFEM results.

al. Excellent agreement holds for the latter. For very thin plates, the present formulation does not appear to be optimal. Dolbow et al. (2000*b*) report the same issue for very thin plates, where it is attributed to shear locking in very thin plates. Indeed, for $t/a < 0.1$, non-enriched models appear to provide better results. For thicker plates though, the convergence of the normalized SIF F_1 significantly improves with the introduction of crack tip enrichment. Tanaka et al. (2017) managed to perform an improved calculation of that aspect.

In general, SIFs appear to display a cross dependency of thickness and angle. Preliminary analyses for various crack angles against plate width demonstrate that normalization with respect to the crack angle, as per Eq. (2.70) do not yield a consistent result. Therefore, the analysis is outside the analytical solution's scope.

Dependency on crack size

The dependency of the SIFs on the relative crack size is shown in Fig. 2.13. The factors are normalized proportionally to the square root of the crack length. Although, some dependency is shown for smaller cracks, the factors tend to converge for relatively larger ones. Care must be taken to account for increased stiffness of very small cracks due to insufficient meshing, i.e. 5 elements per crack length, which yield erroneous results. The relative stability of the factors for $a/b > 0.1$ allow for empirical and analytical relations to be used, where $K_i \propto \sqrt{a}$.

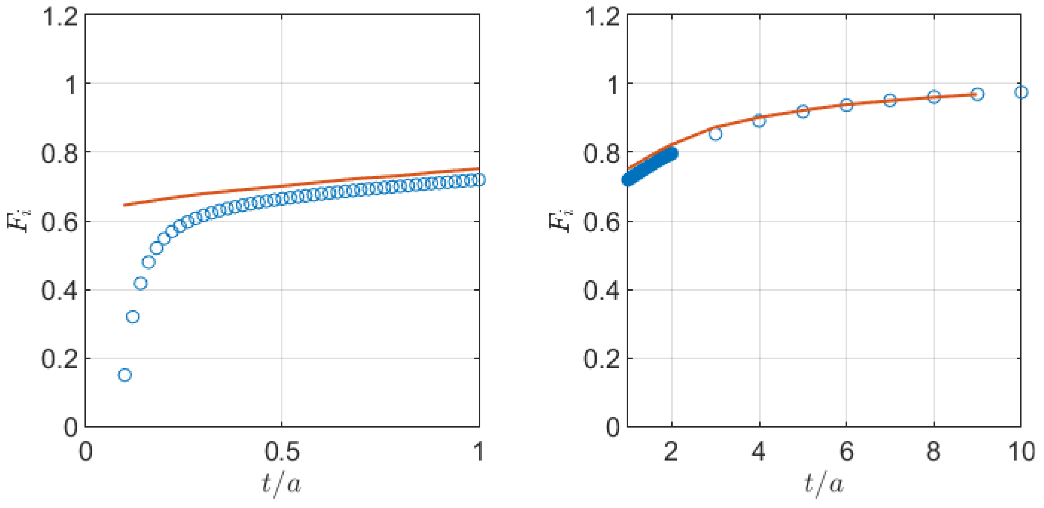

(a) $t/a < 1$ (b) $t/a \geq 1$

Figure 2.12: F_1 against plate thickness. (○) XFEM, (—) Tanaka et al. (2017).

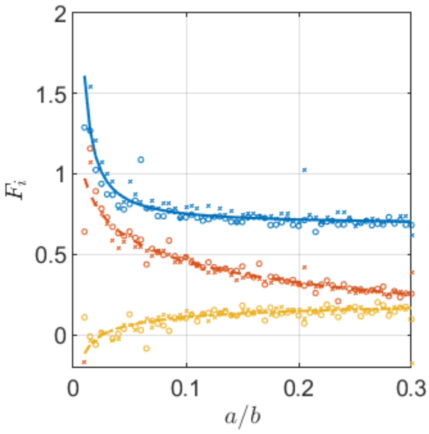

Figure 2.13: SIF against crack size. K_1 (—), K_2 (– –), K_3 (– ·). Markers denote analysis on different crack angles, (×) 30°, (○) 60°.

The analysis of the results of Fig. 2.13 has been run for two distinct angles, 30° and 60°. The factors F_i were then normalized for these angles, as per Eq. (2.70). Unlike the dependency on thickness discussed in the previous section (i.e. Fig. 2.12), there is no codependency between crack size and angle, and by normalizing, the data sufficiently match, save for mesh-induced noise, as shown in Fig. 2.11.

2.6 Dynamics for XFEM

Crack propagation is often a dynamic phenomenon and the development of accurate models is, therefore, important. Usage of FEM for dynamic fracture is not very popular, as stability issues with the time-steps interfere with the mesh refinement. Furthermore, crack bifurcations and multi-fragmentation that often occur in dynamic fracture, cannot be captured sufficiently by the presented fracture criteria. Alternative methods, e.g. phase field, are applicable to dynamic fracture problems (Kakouris and Triantafyllou, 2019). Discrete methods for dynamic fracture rely on discretization of the material in elementary particles or discrete elements. Continuous constitutive laws are not applicable in such cases, and interaction laws are instead used that adhere to the micro-scale, such as contact and traction-separation, between blocks. This accounts for more generalist models, but at the cost of difficult calibration of parameters (er Wang et al., 2017).

The XFEM offers several advantages over conventional FEM in dynamics, while maintaining a relatively manageable complexity. Stability issues occur with the intersected elements. Mass lumping, that's prescribed for explicit dynamics to allow for an easily invertible mass matrix—which is the one that undergoes the solution—has been explored Elguedj et al. (2009). Intersected elements are generally unstable, with the time step diminishing when discontinuities pass too close to the nodes.

The transitioning of the propagating crack through the elements has been identified as source of instability for the SIFs (Menouillard and Belytschko, 2010). The solution proposed in Menouillard and Belytschko (2010) is the construction of a meshfree approximation patch, in place of the conventionally enriched elements. This approach aims at smoothing the stresses around the crack tip. Asareh et al. (2018) develop a method of enrichment with node-independent enrichments.

Liu et al. (2011) develop an enriched spectral element, combining the high p order spectral element, with nodes collocated at the roots of Legendre polynomials, achieving implicitly lumped mass matrices. The critical time steps for consistent and lumped mass matrices for cracked elements are computed. The critical time step for cracked elements tends to zero for cracks that intersect the nodes very closely. Oscillations of the dynamic SIF are suppressed to a high degree. The $p-$refinement is advantageous for the accuracy of crack-tip stress, against $h-$refinement. Only $\sqrt{r}\sin(\theta/2)$ enrichment is employed.

2.6.1 Natural frequencies and vibration modes with XFEM

The linear dynamic Finite Element problems can be posed in an equation of the form

$$\mathbf{M}\ddot{\mathbf{u}} + \mathbf{C}\dot{\mathbf{u}} + \mathbf{K}\mathbf{u} = \mathbf{F}(t) \tag{2.71}$$

with $\dot{\bullet}$ denoting the time derivative of a quantity, $\mathbf{C}$ a damping matrix and $\mathbf{F}(t)$ an external, time-dependent force. The inertial terms are connected to the second derivative of displacement with respect to time, i.e. the acceleration, as the displacements are connected with the stiffness, same as with static problems.

The numerical time integration of Eq. (2.71) is commonly accomplished in two ways. The most straightforward way is to assume a finite time step Δt and create a discretization of the form

$$\mathbf{u}_k = (\alpha\dot{\mathbf{u}}_{k-1} + \beta\dot{\mathbf{u}}_k + \gamma\dot{\mathbf{u}}_{k+1})\,\Delta t \tag{2.72}$$

where the kth term is taken from a discrete series of n terms. The parameters α, β, γ can take values from 0 to 1. When, for example, $\alpha = 1$ and β, $\gamma = 0$, one arrives at the formula of forward Euler. These belong to the time domain family of methods.

Another possible approach exists. First, a fundamental assumption for dynamic problems needs to be stated. The displacements are a function of both time and space, in a manner such that

$$\mathbf{u}(\mathbf{x}, t) = \mathbf{U}(\mathbf{x})V(t) \tag{2.73}$$

meaning that the time and space variables can be separated. It is the possible to express the displacements in a form of an infinite sum, such that

$$\mathbf{u}(\mathbf{x}, t) = \sum_{i=0}^{\infty} A_i\boldsymbol{\phi}_i \exp(-i\omega_i t) \tag{2.74}$$

with i the imaginary number, A_i some amplitude. The mode shape $\boldsymbol{\phi}$ is proprietary to the system and is derived from the solution of the equation

$$\mathbf{K}\boldsymbol{\phi}_i = \omega_i^2 \mathbf{M}\boldsymbol{\phi}_i. \tag{2.75}$$

The eigenmodes $\boldsymbol{\phi}$ have size $n \times n$ with n the number of degrees of freedom (DoF). A given structure can vibrate in only that manner and all possible displacements can be taken as the sum of a number of terms. In the continuous sense, these modes are infinite. In discrete systems though, the resolution is bounded by the magnitude of n. A finer discretized system should, therefore, exhibit convergent properties. The eigenvalues ω^2 are an indication of convergence. In computational practice, eigenmode solvers converge upon a solution by varying the components of ϕ. The eigenvalue is then derived as

$$\omega^2 = \frac{\boldsymbol{\phi}^T \mathbf{K}\boldsymbol{\phi}}{\boldsymbol{\phi}^T \mathbf{M}\boldsymbol{\phi}}, \tag{2.76}$$

which coincides with the Ritz method.

In conclusion, the study of the eigenvalue convergence for the XFEM can sufficiently reveal their capabilities in simulating dynamic problems. Notably, buckling is also formulated in a sense of geometric eigenvalue problem (Nasirmanesh and Mohammadi, 2017).

Numerical results

Figure 2.14 depicts the first 20 eigenfrequencies compared to mesh size. Three different cases have been tried, with an aligned and two inclined cracks at 30°and 45°. The enriched zone has been kept to a minimum, with only 1 enriched element at the stop of the crack tip. Generally, spurious enrichment of the crack-tip does not contribute to the accuracy and convergence of higher vibrational modes, as the far-field stress assumption used and the displacement field derived thereof, does not generally coincide with the displacements of the vibrational modes. A relatively fine discretization has been opted for, with around 40 elements per side.

The XFEM results presented in Fig. 2.14a exhibit excellent agreement with those produced by ABAQUS. This holds for both the parallel (Fig. 2.14a) and the oblique (Fig. 2.14b) crack. A further observation is that, in the presence of a crack, not all modes are affected equally. Modes that are affected by the crack opening are affected more. A mode whose nodes lie on the crack tend to be less affected than those for which points on the crack are a crest.

XFEM in general does not exhibit monotonous convergence with the refinement of the mesh. It appears that convergence for XFEM depends on the relative distance of the crack from the nodes. As the present XFEM code cannot accommodate for a crack intersecting the nodes, a small offset is imposed on the crack where needed. This means that, inevitably, the crack passes close to some nodes. As the enrichment functions become almost identical to the shape functions, poor conditioning of the elements occurs, undermining the model's accuracy. Furthermore, the de facto non-symmetry, however small, affects the modes.

The crack-tip enrichment appears to have an adverse effect on the accuracy of the eigenmodes. In general, the models without a crack-tip enrichment appear to be more consistent for dynamic problems.

Figure 2.15 depicts the 14th mode of the simply supported plate with a centre crack at 45°angle. The mode is moderately high-order, and relatively feature-rich, i.e. rippled with standing waves. In Fig. 2.15a, the FEM solution by ABAQUS is depicted. The conforming mesh can be observed. It is noted that this mode has two symmetries, with respect to the ±45° diagonals. Fig. 2.15b depicts the same problem solved with XFEM, with a 1-element enrichment radius. The mode shape can be seen to be inaccurate, as it is asymmetric, with respect to the -45°diagonal. The crack lies on the +45°diagonal and the source of asymmetry can be seen on the crack tips. Fig. 2.15c is the same without the crack-tip enrichment; the mode shape is much more accurate.

The inaccuracy of the crack-tip enriched model emanates from the absence of a proper enrichment function to accommodate for the asymmetric, or Mode III opening of that particular shape. This is indeed observed in other modes for which the crack opens in that certain way. The enrichment contemplated in Dolbow et al. (2000*b*) involves a fifth term, $\sqrt{r}\sin(\theta/2)$, along with the $r^{3/2}$ terms, for the out-of-plane deflections. This is

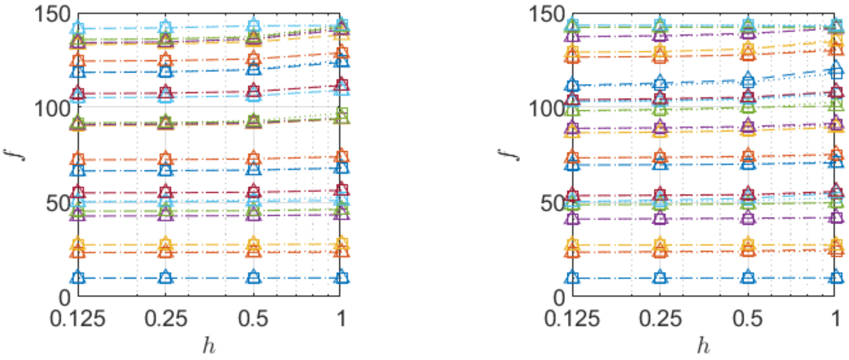

(a) $\theta = 0°$ (b) $\theta = 30°$

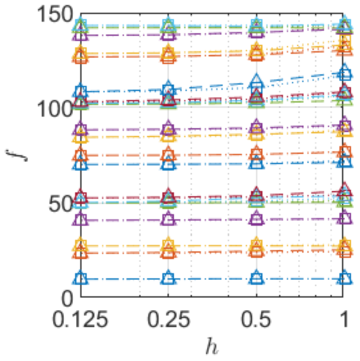

(c) $\theta = 45°$

Figure 2.14: Convergence of the 20 first eigenfrequencies for a straight and an inclined crack. (□) ABAQUS, (○) XFEM.

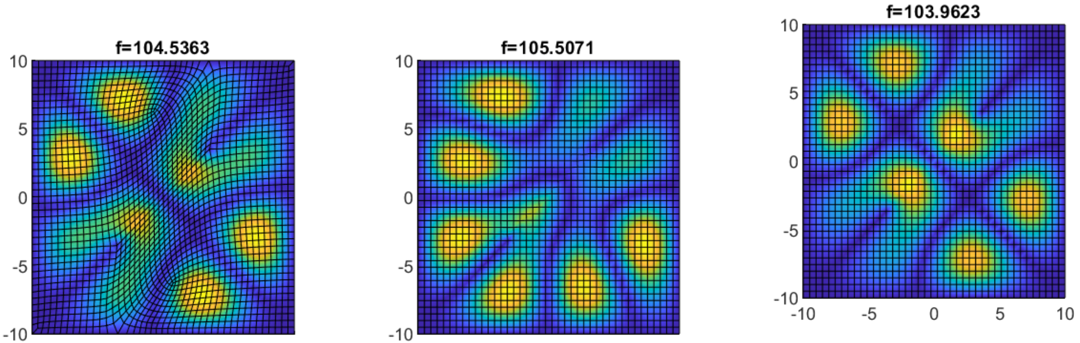

(a) FEM (b) XFEM, enriched crack tip tip (c) XFEM, not-enriched crack

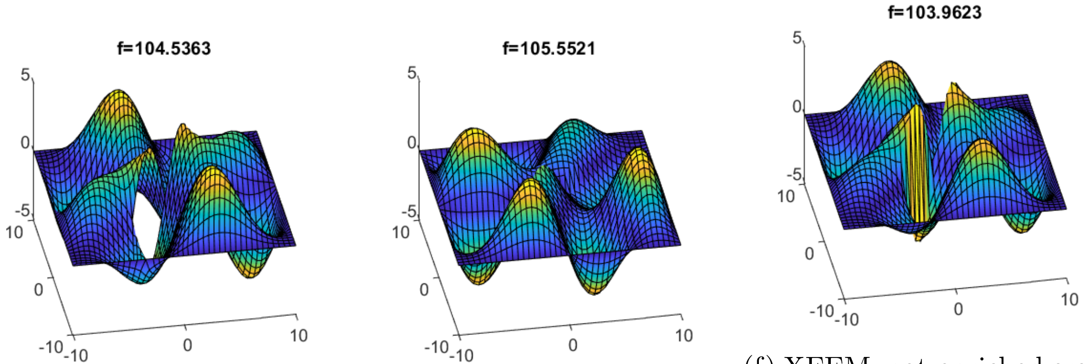

(d) FEM (e) XFEM, enriched crack-tip tip (f) XFEM, not-enriched crack

Figure 2.15: Mode 14, $h = 1.0$.

postulated as a kernel for the solution of the shearing mode. Although Dolbow et al. (2000*b*) do not use it, several others involving Tanaka et al. (2017) have involved solely this enrichment term in their approximations.

2.7 Conclusions

The eXtended Finite Element method for plane stress and plates has been investigated. The possibility to accurately simulate flat shells, i.e. with out-of-plane deflection and rotations, along with in-plane displacements, has been established, in the dynamic context. The calculation of mixed-mode SIFs has been achieved by the XFEM along with the Interaction Integral, in plates and plane problems. Good agreement has been shown to hold with analytical Sih (1974) and numerical Tanaka et al. (2017) methods. The usage of the Fries (2008) correction for bending elements is shown to improve convergence in plate problems.

The dynamic behaviour of shells is demonstrated to be accurately simulated with XFEM. The eigenmodes predicted are very accurate, while the discretization remains within reasonable limits. The mesh-independent incorporation of cracks allows for manageable uniform meshes to be constructed, a quintessential requirement of dynamic simulations, where the minimum time-step is dependent on the smallest element. The ill-conditioning of elements that are intersected too closely to the nodes by the crack remains an open problem. This is circumvented though, as small perturbations of the crack location can treat this problem while yielding insignificant errors.

Overall, the XFEM has become a standard paradigm in fracture simulation. The amount of work required on the user's end is minimal, while the yield is equal or better than conventional FEM. While not as accurate and general as phase field or peridynamics, it is less costly. Furthermore, the versatility of the FEM allows it to be implemented in a multitude of tasks, with little to no adaptation. This renders it an attractive solution to inverse problems, where the description of one or more cracks with as few parameters as possible, while maintaining robust modelling is required.

Bibliography

Aduloju, S. C. and Truster, T. J. A variational multiscale discontinuous Galerkin formulation for both implicit and explicit dynamic modeling of interfacial fracture. *Computer Methods in Applied Mechanics and Engineering*, 343:602–630, 2019.

Ahmadi, M. A hybrid phase field model for fracture induced by lithium diffusion in electrode particles of Li-ion batteries. *Computational Materials Science*, 184:109879, 2020.

Aifantis, E. C. Update on a class of gradient theories. *Mechanics of Materials*, 35(3-6):259–280, 2003.

Ainsworth, M. and Oden, J. A posteriori error estimation in finite element analysis. *Computer Methods in Applied Mechanics and Engineering*, 142(1):1–88, 1997.

Alessi, R., Freddi, F., and Mingazzi, L. Phase-field numerical strategies for deviatoric driven fractures. *Computer Methods in Applied Mechanics and Engineering*, 359, 2020.

Ananthasayanam, B., Capitaneanu, M., and Joseph, P. F. Determination of higher order coefficients and zones of dominance using a singular integral equation approach. *Engineering Fracture Mechanics*, 74(13):2099–2131, 2007.

Anderson, T. L. *Fracture mechanics: fundamentals and applications.* CRC press, 2017.

Asareh, I., Yoon, Y. C., and Song, J.-H. A numerical method for dynamic fracture using the extended finite element method with non-nodal enrichment parameters. *International Journal of Impact Engineering*, 121:63–76, 2018.

Barsoum, R. S. On the use of isoparametric finite elements in linear fracture mechanics. *International Journal for Numerical Methods in Engineering*, 10(1):25–37, 1976.

Bathe, K.-J. *Finite Element Procedures*. Prentice Hall, 1st edition, 1995. ISBN 0-13-301458-4.

Bayesteh, H. and Mohammadi, S. XFEM fracture analysis of orthotropic functionally graded materials. *Composites Part B: Engineering*, 44(1):8–25, 2013.

Behroozinia, P., Mirzaeifar, R., and Taheri, S. A review of fatigue and fracture mechanics with a focus on rubber-based materials. *Proceedings of the Institution of Mechanical Engineers, Part L: Journal of Materials: Design and Applications*, 233(5):1005–1019, 2019.

Belytschko, T. and Black, T. Elastic crack growth in finite elements with minimal remeshing. *International Journal for Numerical Methods in Engineering*, 45(5):601–620, 1999.

Benzley, S. E. Representation of singularities with isoparametric finite elements. *International Journal for Numerical Methods in Engineering*, 8(3):537–545, 1974.

Bordas, S. and Duflot, M. Derivative recovery and a posteriori error estimate for extended finite elements. *Computer Methods in Applied Mechanics and Engineering*, 196(35-36):3381–3399, 2007.

Bordas, S., Duflot, M., and Le, P. A simple error estimator for extended finite elements. *Communications in Numerical Methods in Engineering*, 24(11):961–971, 2008.

Cheng, K. W. and Fries, T.-P. Higher-order XFEM for curved strong and weak discontinuities. *International Journal for Numerical Methods in Engineering*, 82(November 2009):564–590, 2009.

Chidgzey, S. R. and Deeks, A. J. Determination of coefficients of crack tip asymptotic fields using the scaled boundary finite element method. *Engineering Fracture Mechanics*, 72(13):2019–2036, 2005.

Cornejo, A., Mataix, V., Zárate, F., and Oñate, E. Combination of an adaptive remeshing technique with a coupled FEM–DEM approach for analysis of crack propagation problems. 2020.

Daux, C., Moës, N., Dolbow, J. E., Sukumar, N., and Belytschko, T. Arbitrary branched and intersecting cracks with the extended finite element method. *International Journal for Numerical Methods in Engineering*, 48(12):1741–1760, 2000.

Dean, A., Asur Vijaya Kumar, P. K., Reinoso, J., Gerendt, C., Paggi, M., Mahdi, E., and Rolfes, R. A multi phase-field fracture model for long fiber reinforced composites based on the Puck theory of failure. *Composite Structures*, 251:112446, 2020.

Deng, Q. Q., Gao, Y. J., Liu, Z. Y., Huang, Z. J., Li, Y. X., and Luo, Z. R. Atomistic simulation of void growth by emitting dislocation pair during deformation. *Physica B: Condensed Matter*, 578:411767, 2020.

Deshpande, V. S., Needleman, A., and Van Der Giessen, E. Discrete dislocation modeling of fatigue crack propagation. *Acta Materialia*, 50(4):831–846, 2002.

Dolbow, J. E., Moës, N., and Belytschko, T. Discontinuous enrichment in finite elements with a partition of unity method. *Finite elements in analysis and design*, 36(3):235–260, 2000*a*.

Dolbow, J. E., Moës, N., and Belytschko, T. Modeling fracture in Mindlin–Reissner plates with the extended finite element method. *International Journal of Solids and Structures*, 37:7161–7183, 2000*b*.

Duflot, M. A study of the representation of cracks with level sets. *International Journal for Numerical Methods in Engineering*, 70(11):1261–1302, 2007.

Duflot, M. and Bordas, S. <i>A posteriori</i> error estimation for extended finite elements by an extended global recovery. *International Journal for Numerical Methods in Engineering*, 76(8):1123–1138, 2008.

Elguedj, T., Gravouil, A., and Maigre, H. An explicit dynamics extended finite element method. Part 1: Mass lumping for arbitrary enrichment functions. *Computer Methods in Applied Mechanics and Engineering*, 198(30-32):2297–2317, 2009.

er Wang, X., Yang, J., feng Liu, Q., mei Zhang, Y., and Zhao, C. A comparative study of numerical modelling techniques for the fracture of brittle materials with specific reference to glass. *Engineering Structures*, 152:493–505, 2017.

Erdogan, F. and Sih, G. C. On the crack extension in plates under plane loading and transverse shear. *Journal of Fluids Engineering, Transactions of the ASME*, 85(4):519–525, 1963.

Fries, T.-P. A corrected XFEM approximation without problems in blending elements. *International Journal for Numerical Methods in Engineering*, 75(5):503–532, 2008.

Fries, T.-P. and Belytschko, T. The intrinsic XFEM: a method for arbitrary discontinuities without additional unknowns. *International Journal for Numerical Methods in Engineering*, 68(13):1358–1385, 2006.

Fries, T. P. and Belytschko, T. The intrinsic partition of unity method. *Computational Mechanics*, 40(4):803–814, 2007.

Gallimard, L. and Panetier, J. Error estimation of stress intensity factors for mixed-mode cracks. *International Journal for Numerical Methods in Engineering*, 68(3):299–316, 2006.

Gao, B., Li, Y., Guo, T. F., Guo, X., and Tang, S. Void nucleation in alloys with lamella particles under biaxial loadings. *Extreme Mechanics Letters*, 22:42–50, 2018.

González-Estrada, O. A., José Ródenas, J., Pierre Alain Bordas, S., Duflot, M., Kerfriden, P., and Giner, E. On the role of enrichment and statical admissibility of recovered fields in a posteriori error estimation for enriched finite element methods. *Engineering Computations*, 29(8):814–841, 2012.

Gravouil, A., Moës, N., and Belytschko, T. Non-planar 3D crack growth by the extended finite element and level sets-Part II: Level set update. *International Journal for Numerical Methods in Engineering*, 53(11):2569–2586, 2002.

Gruttmann, F. and Wagner, W. A stabilized one-point integrated quadrilateral Reissner-Mindlin plate element. *International Journal for Numerical Methods in Engineering*, 61(13):2273–2295, 2004.

Gurrutxaga-Lerma, B., Balint, D. S., Dini, D., and Sutton, A. P. A Dynamic Discrete Dislocation Plasticity study of elastodynamic shielding of stationary cracks. *Journal of the Mechanics and Physics of Solids*, 98:1–11, 2017.

Hai, L., Wu, J.-Y., and Li, J. A phase-field damage model with micro inertia effect for the dynamic fracture of quasi-brittle solids. *Engineering Fracture Mechanics*, 225, 2020.

Hansbo, A. and Hansbo, P. A finite element method for the simulation of strong and weak discontinuities in solid mechanics. *Computer Methods in Applied Mechanics and Engineering*, 193(33-35):3523–3540, 2004.

Hello, G., Ben Tahar, M., and Roelandt, J. M. Analytical determination of coefficients in crack-tip stress expansions for a finite crack in an infinite plane medium. *International Journal of Solids and Structures*, 49(3-4):556–566, 2012.

Henshell, R. D. and Shaw, K. G. Crack tip finite elements are unnecessary. *International Journal for Numerical Methods in Engineering*, 9(3):495–507, 1975.

Hsia, K. and Argon, A. Experimental study of the mechanisms of brittle-to-ductile transition of cleavage fracture in Si single crystals. *Materials Science and Engineering: A*, 176(1-2):111–119, 1994.

Hu, X., Chen, W., Zhang, P., Bui, T. Q., and Yao, W. A new crack-tip singular element for cracks in three-dimensional elastic bodies. *Engineering Fracture Mechanics*, 235:107148, 2020.

Hwu, C., Aggarwal, M., and Lee, J. Prediction of fracture toughness and crack propagation of graphene via coupling of boundary element and nonlinear beam element. *International Journal of Fracture*, 224(2):167–185, 2020.

Irani, N., Remmers, J., and Deshpande, V. A discrete dislocation analysis of hydrogen-assisted mode-I fracture. *Mechanics of Materials*, 105:67–79, 2017.

José Ródenas, J., González-Estrada, O. A., Tarancón, J. E., and Fuenmayor, F. J. A recovery-type error estimator for the extended finite element method based on singular+smooth stress field splitting. *International Journal for Numerical Methods in Engineering*, 76(4):545–571, 2008.

Kakouris, E. G. and Triantafyllou, S. P. Phase-Field Material Point Method for dynamic brittle fracture with isotropic and anisotropic surface energy. *Computer Methods in Applied Mechanics and Engineering*, 357:112503, 2019.

Karihaloo, B. L. and Xiao, Q. Z. Accurate determination of the coefficients of elastic crack tip asymptotic field by a hybrid crack element with p-adaptivity. *Engineering Fracture Mechanics*, 68(15):1609–1630, 2001.

Kim, J. H. and Paulino, G. H. T-stress, mixed-mode stress intensity factors, and crack initiation angles in functionally graded materials: A unified approach using the interaction integral method. *Computer Methods in Applied Mechanics and Engineering*, 192(11-12):1463–1494, 2003.

Kvamsdal, T. and Okstad, K. M. Error Estimation based on Superconvergent Patch Recovery using Statically Admissible Stress Fields. *International Journal for Numerical Methods in Engineering*, 42(3):535–559, 1998.

Lee, G. H. and Beom, H. G. Mixed-mode fracture toughness testing of a Cu/Ag bimetallic interface via atomistic simulations. *Computational Materials Science*, 183:109806, 2020.

Liang, S., Zhu, Y., Huang, M., and Li, Z. Simulation on crack propagation vs. crack-tip dislocation emission by XFEM-based DDD scheme. *International Journal of Plasticity*, 114:87–105, 2019.

Liu, R. and Liu, Z. An implicit discontinuous Galerkin finite element framework for modeling fracture failure of ductile materials undergoing finite plastic deformation. *International Journal for Numerical Methods in Engineering*, 115(11):1383–1409, 2018.

Liu, Z. L., Menouillard, T., and Belytschko, T. An XFEM/Spectral element method for dynamic crack propagation. *International Journal of Fracture*, 169(2):183–198, 2011.

Liu, X. Y., Xiao, Q. Z., and Karihaloo, B. L. XFEM for direct evaluation of mixed mode SIFs in homogeneous and bi-materials. *INTERNATIONAL JOURNAL FOR NUMERICAL METHODS IN ENGINEERING Int. J. Numer. Meth. Engng*, 59(October 2002):1103–1118, 2004.

Ma, W., Liu, G., and Ma, H. A smoothed enriched meshfree Galerkin method with two-level nesting triangular sub-domains for stress intensity factors at crack tips. *Theoretical and Applied Fracture Mechanics*, 101:279–293, 2019.

Ma, W., Liu, G., and Wang, W. A coupled extended meshfree–smoothed meshfree method for crack growth simulation. *Theoretical and Applied Fracture Mechanics*, 107:102572, 2020.

Mandal, T. K., Nguyen, V. P., and Wu, J.-Y. A length scale insensitive anisotropic phase field fracture model for hyperelastic composites. *International Journal of Mechanical Sciences*, 188:105941, 2020.

Melenk, J. M. and Babuška, I. The partition of unity finite element method: Basic theory and applications. *Computer Methods in Applied Mechanics and Engineering*, 139(1-4):289–314, 1996.

Memari, A. and Khoshravan Azar, M. R. A hybrid FE-MLPG method to simulate stationary dynamic and propagating quasi-static cracks. *International Journal of Solids and Structures*, 190:93–118, 2020.

Menouillard, T. and Belytschko, T. Dynamic fracture with meshfree enriched XFEM. In *Acta Mechanica*, volume 213, pages 53–69. Springer Vienna, 2010.

Moës, N., Dolbow, J. E., and Belytschko, T. A finite element method for crack growth without remeshing. *Int. J. Numer. Methods Eng.*, 46(February):131–150, 1999.

Moshkelgosha, E. and Mamivand, M. Phase field modeling of crack propagation in shape memory ceramics – Application to zirconia. *Computational Materials Science*, 174, 2020.

Motamedi, D. and Mohammadi, S. Fracture analysis of composites by time independent moving-crack orthotropic XFEM. *International Journal of Mechanical Sciences*, 54(1):20–37, 2012.

Nasirmanesh, A. and Mohammadi, S. Eigenvalue buckling analysis of cracked functionally graded cylindrical shells in the framework of the extended finite element method. *Composite Structures*, 159:548–566, 2017.

Natarajan, S., Bordas, S., and Roy Mahapatra, D. Numerical integration over arbitrary polygonal domains based on Schwarz-Christoffel conformal mapping. *International Journal for Numerical Methods in Engineering*, 80(1):103–134, 2009.

Natarajan, S., Roy Mahapatra, D., and Bordas, S. Integrating strong and weak discontinuities without integration subcells and example applications in an XFEM/GFEM framework. *International Journal for Numerical Methods in Engineering*, 83(3):269–294, 2010.

Osher, S. J. and Fedkiw, R. P. Level Set Methods: An Overview and Some Recent Results. *Journal of Computational Physics*, 169(2):463–502, 2001.

Osher, S. J. and Santosa, F. Level Set Methods for Optimization Problems Involving Geometry and Constraints I. Frequencies of a Two-Density Inhomogeneous Drum. *Journal of Computational Physics*, 171(1):272–288, 2001.

Panetier, J., Ladevèze, P., and Chamoin, L. Strict and effective bounds in goal-oriented error estimation applied to fracture mechanics problems solved with XFEM. *International Journal for Numerical Methods in Engineering*, 81(6):671–700, 2010.

Pillai, U., Triantafyllou, S. P., Essa, Y., and de la Escalera, F. M. An anisotropic cohesive phase field model for quasi-brittle fractures in thin fibre-reinforced composites. *Composite Structures*, 252:112635, 2020.

Pineau, A., Benzerga, A., and Pardoen, T. Failure of metals I: Brittle and ductile fracture. *Acta Materialia*, 107:424–483, 2016.

Potyondy, D. O., Wawrzynek, P. A., and Ingraffea, A. R. Discrete crack growth analysis methodology for through cracks in pressurized fuselage structures. *International Journal for Numerical Methods in Engineering*, 38(10):1611–1633, 1995.

Prange, C., Loehnert, S., and Wriggers, P. Error estimation for crack simulations using the XFEM. *International Journal for Numerical Methods in Engineering*, 91(13):1459–1474, 2012.

Rabczuk, T., Bordas, S., and Zi, G. A three-dimensional meshfree method for continuous multiple-crack initiation, propagation and junction in statics and dynamics. *Computational Mechanics*, 40(3):473–495, 2007.

Raghu, P., Rajagopal, A., Jalan, S. K., and Reddy, J. N. Modeling of brittle fracture in thick plates subjected to transient dynamic loads using a hybrid phase field model. *Meccanica*, 2020.

Ren, H., Zhuang, X., and Rabczuk, T. Dual-horizon peridynamics: A stable solution to varying horizons. *Computer Methods in Applied Mechanics and Engineering*, 318:762–782, 2017.

Rice, J. R. A path independent integral and the approximate analysis of strain concentration by notches and cracks. *Journal of Applied Mechanics, Transactions ASME*, 35(2):379–388, 1964.

Robertson, I. M., Sofronis, P., Nagao, A., Martin, M. L., Wang, S., Gross, D. W., and Nygren, K. E. Hydrogen Embrittlement Understood. *Metallurgical and Materials Transactions B: Process Metallurgy and Materials Processing Science*, 46(3):1085–1103, 2015.

Ródenas, J. J., González-Estrada, O. A., Díez, P., and Fuenmayor, F. J. Accurate recovery-based upper error bounds for the extended finite element framework. *Computer Methods in Applied Mechanics and Engineering*, 199(37-40):2607–2621, 2010.

Shakoor, M., Bernacki, M., and Bouchard, P. O. Ductile fracture of a metal matrix composite studied using 3D numerical modeling of void nucleation and coalescence. *Engineering Fracture Mechanics*, 189:110–132, 2018.

Sih, G. C. Strain-energy-density factor applied to mixed mode crack problems. *International Journal of Fracture*, 10(3):305–321, 1974.

Singh, R. and Mahajan, D. K. On the transition of fracture toughness in metallic materials with thickness: An atomistic viewpoint. *Computational Materials Science*, 171:109268, 2020.

Smith, M. *ABAQUS/Standard User's Manual, Version 6.9.* Dassault Systèmes Simulia Corp, United States, 2009.

Sosa, H. A. and Eischen, J. W. Computation of stress intensity factors for plate bending via a path-independent integral. *Engineering Fracture Mechanics*, 25(4):451–462, 1986.

Stepanova, L. and Bronnikov, S. A computational study of the mixed–mode crack behavior by molecular dynamics method and the multi – Parameter crack field description of classical fracture mechanics. *Theoretical and Applied Fracture Mechanics*, 109:102691, 2020.

Strouboulis, T., Copps, K., and Babuška, I. The generalized finite element method: an example of its implementation and illustration of its performance. *International Journal for Numerical Methods in Engineering*, 47(8):1401–1417, 2000.

Strouboulis, T., Copps, K., and Babuška, I. Computational mechanics advances. The generalized finite element method. *Computer Methods in Applied Mechanics and Engineering*, 190(32-33):4081–4193, 2001.

Strouboulis, T., Zhang, L., Wang, D., and Babuška, I. A posteriori error estimation for generalized finite element methods. *Computer Methods in Applied Mechanics and Engineering*, 195(9-12):852–879, 2006.

Su, R. K. and Feng, W. J. Accurate determination of mode I and II leading coefficients of the Williams expansion by finite element analysis. *Finite Elements in Analysis and Design*, 41(11-12):1175–1186, 2005.

Su, R. K. and Fok, S. L. Determination of coefficients of the crack tip asymptotic field by fractal hybrid finite elements. *Engineering Fracture Mechanics*, 74(10):1649–1664, 2007.

Sukumar, N., Chopp, D. L., Moës, N., and Belytschko, T. Modeling holes and inclusions by level sets in the extended finite-element method. *Computer Methods in Applied Mechanics and Engineering*, 190(46-47):6183–6200, 2001.

Sun, F. and Blackman, B. A DIC method to determine the Mode I energy release rate G, the J-integral and the traction-separation law simultaneously for adhesive joints. *Engineering Fracture Mechanics*, 234:107097, 2020.

Sun, C. T. and Jin, Z.-H. *Fracture Mechanics.* Elsevier, 2012. ISBN 9780123850010.

Tanaka, S., Dai, M. J., Sadamoto, S., Yu, T. T., and Bui, T. Q. Stress resultant intensity factors evaluation of cracked folded structures by 6DOFs flat shell meshfree modeling. *Thin-Walled Structures*, 144:106285, 2019.

Tanaka, S., Okada, H., Okazawa, S., and Fujikubo, M. Fracture mechanics analysis using the wavelet Galerkin method and extended finite element method. *International Journal for Numerical Methods in Engineering*, 93(10):1082–1108, 2013.

Tanaka, S., Suzuki, H., Sadamoto, S., Imachi, M., and Bui, T. Q. Analysis of cracked shear deformable plates by an effective meshfree plate formulation. *Engineering Fracture Mechanics*, 144:142–157, 2015.

Tanaka, S., Suzuki, H., Sadamoto, S., Okazawa, S., Yu, T. T., and Bui, T. Q. Accurate evaluation of mixed-mode intensity factors of cracked shear-deformable plates by an enriched meshfree Galerkin formulation. *Archive of Applied Mechanics*, 87(2):279–298, 2017.

Tavares, S. M., Reis, L., Freitas, M., and Castro, P. M. Mixed mode fatigue and fracture in planar geometries: Observations on <i>K</i> _{eq} and crack path modelling. *Fatigue & Fracture of Engineering Materials & Structures*, 42(11):2441–2456, 2019.

Tran, A. S., Fang, T. H., and Hsiao, J. W. Incipient plasticity and voids nucleation of nanocrystalline gold nanofilms using molecular dynamics simulation. *Current Applied Physics*, 19(3):332–340, 2019.

Treifi, M., Olutunde Oyadiji, S., and Tsang, D. K. Computations of modes I and II stress intensity factors of sharp notched plates under in-plane shear and bending loading by the fractal-like finite element method. *International Journal of Solids and Structures*, 45(25-26):6468–6484, 2008.

Ventura, G., Moran, B., and Belytschko, T. Dislocations by partition of unity. *International Journal for Numerical Methods in Engineering*, 62(11):1463–1487, 2005.

Wang, Y., Wang, W., Zhang, B., and Li, C. Q. A review on mixed mode fracture of metals. 2020.

Wei, Y. and Xu, G. A multiscale model for the ductile fracture of crystalline materials. *International Journal of Plasticity*, 21(11):2123–2149, 2005.

Wells, A. A. Crack opening displacements from elastic-plastic analyses of externally notched tension bars. *Engineering Fracture Mechanics*, 1(3):399–410, 1969.

Xiao, Q. Z. and Karihaloo, B. L. Direct evaluation of accurate coefficients of the linear elastic crack tip asymptotic field. *Fatigue and Fracture of Engineering Materials and Structures*, 26(8):719–729, 2003.

Xiao, Q. Z. and Karihaloo, B. L. Improving the accuracy of XFEM crack tip fields using higher order quadrature and statically admissible stress recovery. *International Journal for Numerical Methods in Engineering*, 66(9):1378–1410, 2006.

Xu, G. Q. and Demkowicz, M. J. Computing critical energy release rates for fracture in atomistic simulations. *Computational Materials Science*, 181:109738, 2020.

Xu, S., Xiong, L., Deng, Q., and McDowell, D. L. Mesh refinement schemes for the concurrent atomistic-continuum method. *International Journal of Solids and Structures*, 90:144–152, 2016.

Yu, T. and Bui, T. Q. Numerical simulation of 2-D weak and strong discontinuities by a novel approach based on XFEM with local mesh refinement. *Computers and Structures*, 196:112–133, 2018.

Zi, G. and Belytschko, T. New crack-tip elements for XFEM and applications to cohesive cracks. *International Journal for Numerical Methods in Engineering*, 57(15):2221–2240, 2003.

Zienkiewicz, O. and Zhu, J. The superconvergent patch recovery (SPR) and adaptive finite element refinement. *Computer Methods in Applied Mechanics and Engineering*, 101(1-3):207–224, 1992.

Chapter 3

The Wave Finite Element

3.1 Introduction

The prediction of wave propagation and the dynamic response of structures is of interest in several applications. Elongated structures such as pipes, rails, beams and aircraft shells, among others, exhibit default vibrational behaviour whose prediction is required in engineering analysis. The conventional Finite Element Method delivers solutions at a very high computational cost. The Courant condition for the stability of the integration of the partial differential equations connects the stable time-step to the discretization fineness. Evidently, simulations in the frequency domain are bounded by this condition; a demand for at least 7 linear elements per characteristic length of the vibration mode is indicated in the literature to obtain acceptable results. Oftentimes simulations of high frequency vibrational phenomena are required, demanding very fine discretisation of the problem, thus compounding the computational cost.

The necessity for efficient numerical modelling tools has motivated the development of several and diverse computational methods to address the aforementioned issues. The local interaction simulation approach (LISA) Shen and Cesnik (2016); Willberg et al. (2015); Sbarufatti et al. (2014); Dworakowski et al. (2015) is a computational framework that employs a 3D finite difference scheme which exploits GPU capabilities which casts the complexity of the problem onto parallel operations and reduces computation times. The time-domain spectral element method Livani et al. (2018); Żak and Krawczuk (2018) exploits the trivial inversion of a diagonal mass matrix in explicit time integration. High-order elements with nodes located at the roots of high-order Legendre-Chebyshev polynomials ensure both the shape richness and the diagonality of the mass matrix. Coarser discretisation is thus achieved, compared to FEM. Frequency-domain finite elements have also been proposed, that utilize Fourier Sreekanth Kumar et al. (2004) or wavelet transform Samaratunga et al. (2015) on the default time-dependent displacement, allowing for solution in the wave domain. A family of numerical methods based on the Bloch decomposition of waves and subsequent periodicity of the problem has been developed for waveguide simulations. The semi-analytical FE (SAFE) assumes the properties of the displacement field on the propagation direction and discretizes the perpendicular 1D or 2D section. A similar approach has been adopted in the scaled boundary FEM (SBFEM) Gravenkamp et al. (2015); Gravenkamp (2018). The WFE (e.g. Zhong and Williams (1995); Ichchou et al. (2007); Mace et al. (2005); Mace and Manconi (2008)) imposes periodicity conditions on a representative structural cell. Through the displacement assumptions and the periodicity conditions, an eigenvalue problem is reached whose solutions are the wavemodes with respective wavenumbers. Wave methods achieve model reduction by limiting the simulation scope onto wavemodes. The unknown degrees of freedom become the wave amplitudes Renno and Mace (2010); Waki et al. (2009); Mencik (2012).

The domain of application for computational wave methods is specific to slender structures, such as beams, pipes or rail. The wave properties of fluid-filled pipes are investigated in Bocquillet et al. (2003); Mencik and Ichchou (2007); Maess et al. (2006). Vibration transmission through beams of thin-walled sections is investigated in Houillon et al. (2005). The determination of stress on waveguides such as rails through their dispersion properties via wave anaysis is proposed in Chen and Wilcox (2007) with the WFE and Mazzotti et al. (2012) with SAFE. Extension to 2D structures has been proposed Mace and Manconi (2008) to materials with structural anisotropy. Recently, the usage of metamaterials as means of noise reduction in aircraft has become feasible, part due to advances in 3D-printing Miranda Jr. et al. (2020). Research interest thereupon has been attracted, and structure designs have been investigated Ampatzidis et al. (2018); Ampatzidis and Chronopoulos (2019). Smart structures that utilize shunted piezoelectrics have been proposed for the active control of waves. Furthermore, the wave properties of composites, e.g. sandwich panels Chronopoulos et al. (2014), woven composites Thierry et al. (2018, 2020); Thierry and Chronopoulos (2020) and honeycomb Yang et al. (2019) have been studied. The power flow due to vibration due to engine operation in automotives is studied in Fan et al. (2016). Chronopoulos et al. (2014) investigate the vibrational properties of conical structures (e.g. rockets) with statistical energy analysis (SEA). Wave-based NDT greatly benefits from hybrid wave methods. Hybrid WFE/FEM models Mencik (2012) can calculate wave scattering around damage. SBFEM Gravenkamp (2018), SAFE and SFEM have also been used in hybrid approaches. Stochastic WFE approaches propagate the perturbation of uncertainty of material properties Bouchoucha et al. (2017); Ichchou et al. (2011) onto resulting wave properties and are proposed in identification problems through waves.

3.2 Lamb wave propagation on a narrow plate

Lamb waves are the most common waves that propagate on plates. Their solution was derived by Horace Lamb, by assuming free boundaries on an isotropic continuum of infinite x_1, x_2 and finite x_3. The characteristic equation derived

$$\frac{\tan \beta h}{\tan \alpha h} = \left[\frac{-4\alpha\beta k^2}{(k^2 - \beta^2)} \right]^{\pm 1} \tag{3.1}$$

with α, β denoting

$$\alpha^2 = \frac{\omega^2}{c_L^2} - k^2, \quad \beta^2 = \frac{\omega^2}{c_S^2} - k^2 \tag{3.2}$$

and c_L the longitudinal, c_S the shear wave velocities defined as

$$c_L^2 = \frac{E}{\rho}, \quad c_S^2 = \frac{\mu}{\rho} \tag{3.3}$$

with E Young's modulus, μ the shear modulus and ρ the material density.

Equation (3.1) holds for certain pairs of ω, k. In order to solve it numerically, the following strategy is implemented. First, the terms are brought together and set to zero; complex as they are, in order to find the zero, the real and the imaginary part must be zero simultaneously.

$$f^a = \frac{\tan \beta h}{\tan \alpha h} - \left[\frac{-4\alpha\beta k^2}{(k^2 - \beta^2)} \right]^{\pm 1} \tag{3.4}$$

$$F^a = \Re\{f^a\} + \Im\{f^a\} \tag{3.5}$$

with a denoting the symmetric or antisymmetric function.

```
Data: $c_L$, $c_T$, $\omega_{min}$, $\omega_{max}$, $\Delta\omega$, $k_{max}$
Result: $\{\hat{k}_i, \{\hat{\boldsymbol{\omega}}_i\}\}$
initialization;
for $k = 1 : k_{max}$ do
    $\{\boldsymbol{\omega}\} = \omega_{min} : \Delta\omega : \omega_{max}$;
    calculate $\boldsymbol{\alpha}(\omega)$, $\boldsymbol{\beta}(\omega)$;
    calculate $\{\mathbf{F}^a\}$;
    find $R = \{n | F^a_n \times F^a_{n+1} < 1 \, \mathrm{for} \, n = 1..N_\omega\}$;
    for $i$=1:$N_R$ do
        find root $\hat{\omega}_i$ in $[\hat{\omega}_i, \hat{\omega}_j]$;
    end
    return $\{\hat{k}_i, \{\hat{\boldsymbol{\omega}}_i\}\}$;
end
```

Algorithm 1: Solution of the Lamb characteristic equations

with N_R the length of the list R. A good approximation of the exact roots can be easily effectuated through the Newton-Raphson scheme.

Algorithm 1 finds a list of possible angular frequencies $\{\hat{\boldsymbol{\omega}}_i\}$ for each of the selected wavenumbers $\hat{k}_i$.

The resultant curves require further processing, as each $\hat{\omega}_{ik}$ needs to be assigned to the wavemode of the proper order. This is achieved by a criterion of the curve continuity. A windowed sweep spline extrapolation has been used. The characterization of the wave is then done, assigning S_0, A_0 to the fundamental modes and incrementing. In most

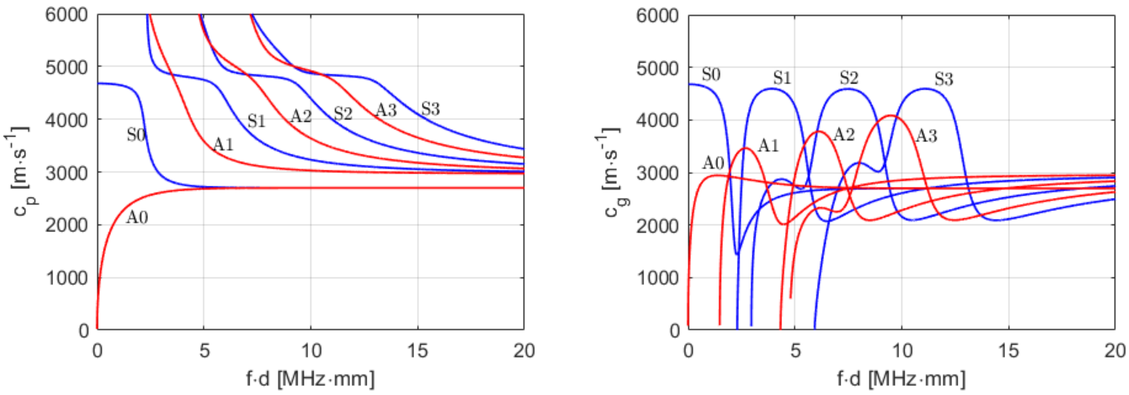

(a) Phase velocity (b) Group velocity

Figure 3.1: Wave phase and group velocities. Symmetric wavemodes (blue), antisymmetric (red).

practical applications, only the fundamental modes are retained.

It is convenient to depict the dispersion relation in terms of group and phase velocities Fig. 3.1. The frequency axis can be normalized by multiplying with the plate's thickness; an implication evoked is that higher order waves are more difficult to excite in thinner plates. Phase velocity (Fig. 3.1a) expresses the movement of a particular phase of the wave, e.g. a crest. Group velocity (Fig. 3.1b) at which a wave packet travels. When the two velocities are different, a wave packet tends to disperse and loses amplitude as it travels. This is the case for $S0$ for around 2 MHz·mm.

3.3 WFE for 1D repetitive structures

The formulation of the WFE through the transfer matrix is presented here. The state matrices of a structural subcell are partitioned through the continuity and internal equilibrium conditions of the structure. The Bloch decomposition of propagating waves introduces a periodicity condition. The combination of those introduces the transfer matrix problem Zhong and Williams (1995), whose solutions are the wavemodes.

3.3.1 Periodicity of structures

A periodic structure of infinite length (Figure 3.2) is comprised of similar subcells $\Omega^{(i)}$, with surfaces $\partial\Omega_0^{(i)}$, $\partial\Omega_L^{(i)}$, $\partial\Omega_R^{(i)}$ at the free, left and right sides of the domain respectively.

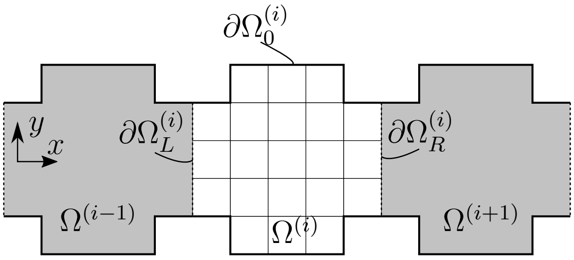

Figure 3.2: Periodic waveguide comprised of subcells $\Omega^{(i)}$.

Equilibrium and continuity conditions require that the displacements and forces on either side of the subcell be

$$\mathbf{u}_R^{(i-1)} = \mathbf{u}_L^{(i)} \tag{3.6}$$

and

$$\mathbf{f}_R^{(i-1)} = -\mathbf{f}_L^{(i)} \tag{3.7}$$

Assuming a Galerkin discretization, FE or otherwise, the mass and stiffness matrices produced from the weak formulation of the dynamic equilibrium are $\mathbf{K}$, $\mathbf{M}$. The dynamic stiffness matrix is expressed

$$\mathbf{D} = (1 + \mathrm{i}\eta)\mathbf{K} - \omega^2\mathbf{M} \tag{3.8}$$

with ω the angular frequency and η a damping constant.

The matrices of the system can be partitioned according to the Dof they refer to, as

$$\mathbf{D}^* = \begin{bmatrix} \mathbf{D}^*_{LL} & \mathbf{D}^*_{LI} & \mathbf{D}^*_{LR} \\ \mathbf{D}^*_{IL} & \mathbf{D}^*_{II} & \mathbf{D}^*_{IR} \\ \mathbf{D}^*_{RL} & \mathbf{D}^*_{RI} & \mathbf{D}^*_{RR} \end{bmatrix}, \quad \mathbf{f} = \begin{Bmatrix} \mathbf{f}_L \\ \mathbf{0} \\ \mathbf{f}_R \end{Bmatrix}, \tag{3.9}$$

with zero internal forces. The internal DoFs can be eliminated through the Guyan reduction process (Waki et al., 2009) as

$$\mathbf{D}_{MM} = \mathbf{D}^*_{MM} - \mathbf{D}^*_{MS}(\mathbf{D}^*_{SS})^{-1}\mathbf{D}^*_{SM} \tag{3.10}$$

with S, M the slave and master DoFs, corresponding to $S \equiv I$ and $M \in \{L, R\}$. The condensed matrix reads

$$\mathbf{D} = \begin{bmatrix} \mathbf{D}_{LL} & \mathbf{D}_{LR} \\ \mathbf{D}_{RL} & \mathbf{D}_{RR} \end{bmatrix} \tag{3.11}$$

3.3.2 Transfer Matrix

The state vector of a section of the structure is defined as

$$\mathbf{q}_L = \begin{bmatrix} \mathbf{u}_L^T & \mathbf{f}_L^T \end{bmatrix}^T \tag{3.12}$$

and the transfer matrix $\mathbf{T}$ is the matrix that connects the right and the left state vectors of the domain as

$$\mathbf{T}\mathbf{q}_L = \mathbf{q}_R, \tag{3.13}$$

with terms

$$\mathbf{T} = \begin{bmatrix} \mathbf{T}_{11} & \mathbf{T}_{12} \\ \mathbf{T}_{21} & \mathbf{T}_{22} \end{bmatrix} \tag{3.14}$$

with

$$\mathbf{T}_{11} = -\mathbf{D}_{LR}^{-1}\mathbf{D}_{LL} \tag{3.15}$$

$$\mathbf{T}_{12} = \mathbf{D}_{LR}^{-1} \tag{3.16}$$

$$\mathbf{T}_{21} = -\mathbf{D}_{RL} + \mathbf{D}_{RR}\mathbf{D}_{LR}^{-1}\mathbf{D}_{LL} \tag{3.17}$$

$$\mathbf{T}_{22} = -\mathbf{D}_{RR}\mathbf{D}_{LR}^{-1} \tag{3.18}$$

It is further proven that $\mathbf{T}$ is symplectic (Zhong and Williams, 1995), i.e.

$$\mathbf{T}^T\mathbf{J}_n\mathbf{T} = \mathbf{J}_n \tag{3.19}$$

with

$$\mathbf{J}_n = \begin{bmatrix} \mathbf{0} & \mathbf{I}_n \\ -\mathbf{I}_n & \mathbf{0} \end{bmatrix}. \tag{3.20}$$

Eq. (3.19) is useful when formulating the method, in verifying that the calculations are correct. Attention must be paid that ^{T} is the classical transpose, and not the Hermitian. As the latter is used often, it is possible to confuse the two[1].

A corollary of the matrix's property is that its eigenvalues appear in pairs of reciprocals, such that

$$\lambda_i = 1/\lambda_{i+n}, \quad i = 1, .., n. \tag{3.21}$$

3.3.3 Bloch decomposition of waves

For a wave travelling in one dimension, the displacements and forces of a section are connected to those of the other as

$$\mathbf{q}_L = \lambda \mathbf{q}_R, \quad \text{with} \quad \lambda = \exp(-\mathrm{i}k\Delta x) \tag{3.22}$$

with Δx the cell's length.

3.3.4 Wavemode solution

Combining equations (3.12) and (3.22)

$$\mathbf{T}\mathbf{q}_L = \lambda \mathbf{q}_L, \tag{3.23}$$

which is solved for eigenvalues λ_i and eigenvectors $\mathbf{\Phi}$. Following the postulate of Eq. (3.21), a number $2n$ of reciprocal pairs of λ_i are produced. Those correspond to pairs of negative and positive-travelling wavemodes. Inverting Eq. (3.22) for the wavenumber k, the values appear in opposite pairs. Generally, k is complex, with the real part denoting the wavelength and the imaginary part the attenuation ratio.

---

[1] In MATLAB the Hermitian transpose syntax is `A'`. To enforce classical transpose on complex matrices, `A.'` should be used instead.

Following the definition of $\mathbf{q}$, the eigenmodes $\boldsymbol{\Phi}$ are split into

$$\boldsymbol{\Phi} = \begin{bmatrix} \boldsymbol{\Phi}_u \\ \boldsymbol{\Phi}_f \end{bmatrix}, \tag{3.24}$$

a force and a displacement part.

3.3.5 Numerical issues and convergence of the WFE

The state vectors $\mathbf{q}$ contain both displacements and forces, resulting in several orders of magnitude discrepancy within the vector. The transfer matrix and the subsequent eigenvalue problem are subject to ill-conditioning, meaning that small perturbations in matrix values can cause large discrepancies in the results. Several techniques have been proposed, with Zhong and Williams (1995) proposing a recast of the problem via appropriate pre-multiplications (see also Waki et al. (2009)).

The basic convergence requirement for dynamics in FE is that the fineness of discretization must be pertinent to the wavelength, with a number of at least 7 elements per wavelength suggested. The effects of aliasing in higher frequencies is investigated in Ichchou et al. (2007). Furthermore, Waki et al. (2009) find that when elements are too small compared to the wavelengths analysed, they are prone to round-off errors.

3.4 Power flow and group velocities with WFE

The phase and group velocities of the waves are of interest for many applications. The group velocity is connected to the rate of energy transmission of the waves. Normalization of waves with respect to energy is advantageous in prospective applications of WFE and is discussed.

3.4.1 Power transmission

To take the energy of a given cross section, the force is multiplied by the respective displacement. The power is the time derivative thereof, which, when working in spectral form, is conveniently connected through multiplication by the angular frequency. Accounting for the vector formalism used in WFE, a ready expression for the power carried by a wave is given as [cite Ichchou 2007 and Langley 1999] (Ichchou et al., 2007; Langley, 1999)

$$P(\omega) = \frac{-\mathrm{i}\omega}{4} \begin{Bmatrix} \mathbf{u}_L \\ -\mathbf{F}_L \end{Bmatrix}^H \mathbf{J} \begin{Bmatrix} \mathbf{u}_L \\ -\mathbf{F}_L \end{Bmatrix} = \mathbf{Q}_L^H \mathbf{P}^{\boldsymbol{\Phi}} \mathbf{Q}_L \tag{3.25}$$

with $\mathbf{P}^{\boldsymbol{\Phi}}$ henceforth defining the power flow matrix

$$\mathbf{P}^{\boldsymbol{\Phi}} = \frac{-\mathrm{i}\omega}{4} \begin{bmatrix} \boldsymbol{\Phi}_u \\ \boldsymbol{\Phi}_F \end{bmatrix}^H \mathbf{J} \begin{bmatrix} \boldsymbol{\Phi}_u \\ \boldsymbol{\Phi}_F \end{bmatrix} \tag{3.26}$$

with H denoting the Hermitian conjugate transpose.

$\mathbf{Q}_L$ in eq. (3.25) denotes the modal amplitude. In the wave context it is convenient to express forces and displacements in terms of wavemodes and amplitudes. Thus the problems are cast onto what can be called wave space. A reduction of wave problems is therefore achieved.

3.4.2 Mode normalization

The expression of unknown fields in terms of amplitudes begs the question on the normalization of modes. Considering the definition of an eigenvalue problem, as per eq. (3.23), substituting to a more familiar notation

$$\mathbf{T}\boldsymbol{\Phi} = \boldsymbol{\lambda}\boldsymbol{\Phi} \tag{3.27}$$

$$\boldsymbol{\Psi}\mathbf{T} = \boldsymbol{\lambda}\boldsymbol{\Psi} \tag{3.28}$$

yields the left and right eigenvalue problem respectively.

In most practical applications, eq. 3.28 are solved numerically. Several methods are available. In general, the output magnitude of the eigenvectors is irrelevant, and depends on the solver. Often a normalization of the form

$$\boldsymbol{\phi}_i^H \boldsymbol{\phi}_j = \delta_{ij} \tag{3.29}$$

is offered by default. This allows for a simple reform of eq. (3.28) such that

$$\mathbf{\Phi}^H \mathbf{T} \mathbf{\Phi} = \boldsymbol{\lambda}, \tag{3.30}$$

with $\boldsymbol{\lambda}$ a diagonal matrix. A left-right normalization is also proposed in several works (e.g. Renno and Mace (2010)), such that

$$\mathbf{\Psi}^H \mathbf{\Phi} = \mathbf{I}. \tag{3.31}$$

This property allows for the improvement of conditioning, when systems of equations are formed that include the displacement fields, boundary conditions for example Mencik (2014); Malik et al. (2020). Its main disadvantage is the twofold computation of the eigenvalues, which may add computational cost for larger problems.
Similar to eq. (3.31), self-consistent power-based normalization can be made with respect to modal energies. This is done such that

$$\mathbf{\Phi}^H \mathbf{J} \mathbf{\Phi} = \mathbf{I}. \tag{3.32}$$

The merit of this formula is that it normalizes modes with respect to power. This means that a mode of amplitude Q_i will carry power $P \propto Q_i^2$, for any i. This allows for direct comparison of intra-mode converted waves in wave scattering problems (see Chapter 4).

3.4.3 Group velocity

The group velocity is defined as the velocity at which the energy flows. Having calculated the power, the group velocity can be straightforwardly computed through Ichchou et al.

(2007)

$$(c_g)_j = \frac{4\Delta x P^{\Phi}_{jj}}{\omega^2 M^{\Phi}_{jj} + K^{\Phi}_{jj}}, \tag{3.33}$$

with $\mathbf{P}^{\Phi}$ calculated from Eq. (3.26) and $\mathbf{M}^{\Phi}$, $\mathbf{K}^{\Phi}$ the wave mass and stiffness, calculated as

$$\mathbf{K}^{\Phi} = \begin{bmatrix} \mathbf{I} & \mathbf{0} \\ \mathbf{0} & \mathbf{I} \\ \boldsymbol{\mu} & \mathbf{0} \\ \mathbf{0} & \boldsymbol{\mu}^{-1} \end{bmatrix}^H \begin{bmatrix} \boldsymbol{\Phi}_u & \mathbf{0} \\ \mathbf{0} & \boldsymbol{\Phi}_u \end{bmatrix}^H \mathbf{K} \begin{bmatrix} \mathbf{I} & \mathbf{0} \\ \mathbf{0} & \mathbf{I} \\ \boldsymbol{\mu} & \mathbf{0} \\ \mathbf{0} & \boldsymbol{\mu}^{-1} \end{bmatrix} \begin{bmatrix} \boldsymbol{\Phi}_u & \mathbf{0} \\ \mathbf{0} & \boldsymbol{\Phi}_u \end{bmatrix} \tag{3.34}$$

and similar for mass. It is also noted that the denominator of Eq. (3.33) can be rewritten as

$$\omega^2 \mathbf{M}^{\Phi} + \mathbf{K}^{\Phi} = 2\omega^2 \mathbf{M}^{\Phi} = 2\mathbf{K}^{\Phi}. \tag{3.35}$$

It is remarked that the group velocity formula is independent of the wave amplitude, therefore independent of any eigenvector normalization.

3.4.4 Mode sorting

The solution of the eigenvalue problem produces a set of eigenvalues of equal size as the transfer matrix. As discussed earlier, a limited number of mode pairs are propagating. The number of propagating modes is also dependent on the frequency. Dependent on the eigenvalue solver, modes are sorted by magnitude. Modes that become propagating enter with smaller magnitudes, displacing the position of already calculated modes in the vector. It is useful to be able to identify and classify each mode. Two methods are studied here.

Modal Assurance Criterion (MAC)

MAC exploits the mode orthogonality

$$\phi_i^H \phi_j = \alpha \delta_{ij}, \tag{3.36}$$

with ϕ_i the i^{th} wave mode and δ_{ij} the Krönecker delta and α some constant. With proper normalization, α may be set to 1.

While the above assertion holds true for structural eigenmodes. Wavemodes on the other hand are generally biorthogonal, and it only holds true for those of the modes that are propagating and not the evanescent ones. Furthermore, it is possible to misidentify evanescent modes that appear in conjugate pairs. The best practice for wave sorting, should evanescent modes be retained, is with Eq. (3.32).

For modes that are dependent on the angular frequency ω, an approximate relation can be constructed as

$$\phi_i(\omega)^H \phi_j(\omega + \Delta\omega) \to \delta_{ij}, \quad \text{as} \quad \Delta\omega \to 0, \tag{3.37}$$

invoking that the modes vary smoothly and a sufficiently small frequency step is chosen. MAC works with preselected baseline modes. Best results are produced for a number of modes requested and tracked across the selected frequency band. Newer modes will be missed with this approach, and a frequency-dependent extension of the mode basis is required, adding complexity to the implementation of this approach.

Sorting by curve extrapolation

It is possible to sort wavemodes through curve extrapolation. A reference configuration is first assumed, where modes are computed in the same position for more than two ω_i, such as 20-80 kHz in Fig. 3.3. The modes are identified in the next frequency step by extrapolating the dispersion curve, and finding its best continuation.

An extrapolation can be constructed from two or more points of a curve. In the finite difference approximation, the derivatives of a function are

$$\Delta f(x_i) \approx f(x_i - 1) - f(x_i), \tag{3.38}$$

for evenly sampled x_i. Higher order polynomial extrapolation is available, although not necessarily more accurate.

3.5 Results and discussion

Numerical results are considered here. A long plate of width 200 mm and thickness 2 mm is examined. The plate is elastic isotropic with E=70 GPa, ν=0.3. Shell elements are used for the mesh, as detailed in Chapter2.2. A frequency band of up to 500 kHz is examined.

A mesh of one band of elements is preferred for a homogeneous cell, as the solution of k is π-periodic. More elements result in arduous post-processing, which is necessary when more complicated cells are studied.

Figure 3.3 shows the raw dispersion curves produced by WFE. The relation of wavenumber versus frequency is depicted. The wavenumber is generally complex, with the real part denoting the spatial characteristic of the wave, i.e. $\Re\{k\} = 2\pi/\lambda$, where λ is the wavelength, and the imaginary part quantifying the wave's attenuation. Waves appear in positive and negative-travelling pairs, with respective positive and negative wavenumbers. Waves are classified as propagating when the condition $|\Re\{k\}|/|\Im\{k\}| > c$, is fulfilled, with c a positive constant, usually selected around 10. Also $\text{sign}(\Re\{k\}) = -\text{sign}(\Im\{k\})$, denoting that the wave loses energy towards its travelling direction; this is due to the imaginary part governing the attenuation term of the imaginary exponential term e^{-ikx}. Waves with a larger imaginary than real part, i.e. with supercritical attenuation rates, are called evanescent. Figure 3.3b shows the unclassified imaginary part of the waves; as the frequency increases, more waves become propagating, with their imaginary part decaying to zero.

Mode sorting is implemented to trace the evolution of wavemodes across frequencies. The MAC criterion is used, along with elimination of the traced modes. In principle, eigenvectors are bi-orthogonal. Propagating wavemodes are also orthogonal, while non-propagating wavemodes do not necessarily preserve this condition, and sorting of evanescent modes is unstable. The direct calculation of group velocity aids towards classification of positive and negative-propagating waves. Propagating modes, when normalized, have imaginary parts of equal magnitude and sign depending on whether they travel towards the positive or negative direction.

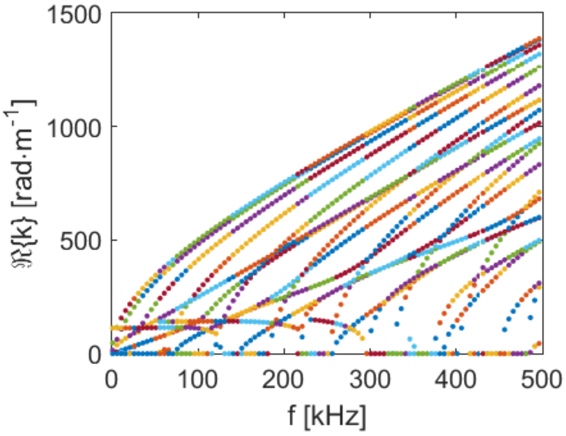

(a) $\Re\{k\}$

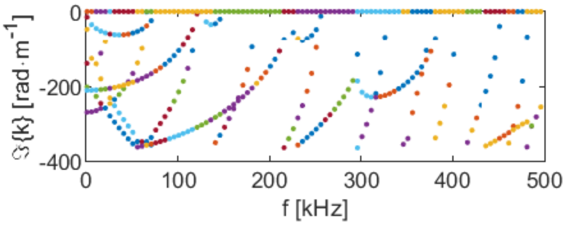

(b) $\Im\{k\}$

Figure 3.3: Raw WFE dispersion curves.

Figure 3.4 shows the resulting dispersion curves after the classification. Wavemodes transitioning from evanescent to propagating give false correlations with the MAC criterion. Hence, parts of the curves are omitted.

3.5.1 Lamb waves with the WFE

The finite boundary nature of the waveguide leads to the appearance of both Lamb and non-Lamb waves. This is due to the fact that Lamb equations refer to infinite plates. Lamb waves exhibit the typical symmetric-antisymmetric profile.

The narrow plate examined has width H and thickness h. When H is substituted to the thickness, the axial symmetric Sn and shear-like antisymmetric SHn modes are produced. It is noted here that commonly, SHn are not classified as Lamb modes. In the finite problem, SHn behaves as an in-plane bending wave, which is approximated by the antisymmetric part of the Lamb equation with sufficient accuracy.

Colloquial antisymmetric, in the sense of out-of-plane mode wave, is produced when h is substituted for the thickness prescribed in the Lamb equations. In this case the

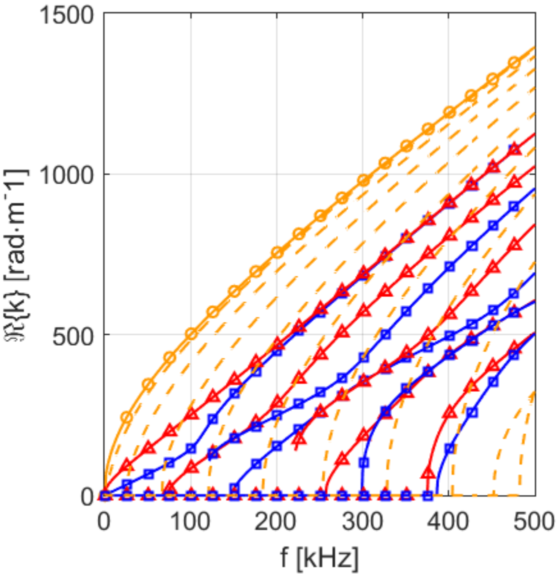

Figure 3.4: Classified dispersion curves. Lamb modes: $A0$ (○), Sn (□), SHn (△) ; cross sectional modes (− −).

element operates as a plate. The Reissner-Mindlin assumption for linear distribution of displacements along the plate thickness leads to one sole $A0$ Lamb mode. This assumption can be seen to hold for up to very high frequencies (Fig. 3.5a) where the cut-off frequency is dependent on the thickness of the plate.

The usage of shell elements introduces a plane stress assumption on the in-plane Dofs. Section deformations and subsequent inertial forces occur alongside both section axes. Plane stress neglects the small axis however. This does not introduce large errors, save for very large frequencies. For plates with larger thickness to width ratio, those terms ought to be taken into account through the introduction of inertial terms first, and through-the-thickness meshing eventually.

Figure 3.5 shows the phase (Fig. 3.5a) and group (Fig. 3.5b) velocities of the Lamb modes produced with the WFE, alongside the analytical curves. Excellent agreement holds, especially for lower frequencies. The $A0$ mode diverges, as planarity of the cross-section is not preserved in the boundary problem.

Figures 3.6, 3.7 display the fundamental Lamb modes $S0$ and $SH0$. The notation of $SH0$ is adopted to emphasize the horizontal feature of the wave, although it is technically governed by the antisymmetric Lamb equation. The field visualization is achieved by

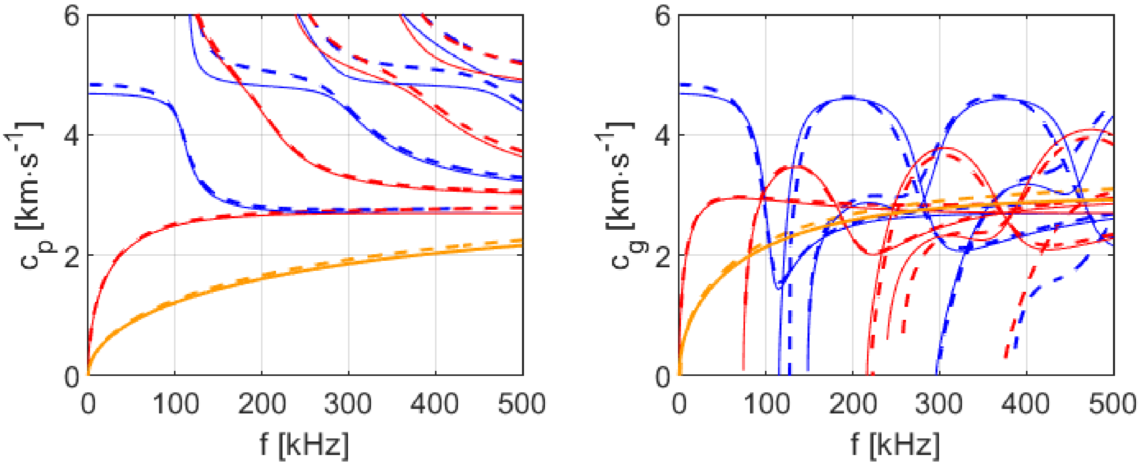

(a) Phase velocity (b) Group velocity

Figure 3.5: Wave phase and group velocities. Sn (blue), SHn (red), An (orange). Characteristic equation (—), WFE (– –).

extending the mesh of WFE and projecting the wavemode as

$$\mathbf{u}(x) = \boldsymbol{\phi}_u \exp(-1ikx) \tag{3.39}$$

with k the corresponding wavenumber of wavemode ϕ. The wavelength becomes shorter as the frequency increases, and does so at a similar rate for either mode, as evident from the dispersion curves.

Figures 3.8, 3.9 show some higher order symmetric and horizontal antisymmetric modes respectively. Those propagate at significantly higher frequencies. Their wavelengths are relatively shorter when compared at the frequency base with their zero order counterparts. Their feature size is, however, smaller, and usage in NDT applications should be considered.

Figure 3.10 shows the evolution of the fundamental out-of-plane antisymmetric wavemode $A0$. $A0$ has significantly shorter wavelength compared to $S0$ and $SH0$ for the same frequency, that also decreases at a high rate. As this mode functions through the plate domain, convergence issues may occur first. It has been noted (Waki et al., 2009) that the convergence of WFE requires that the element be short enough compared to the wavelength. Shell elements exhibit asymmetric convergence in that sense, as plane-dominated waves have larger wavelengths compared to plate-dominated ones. The critical

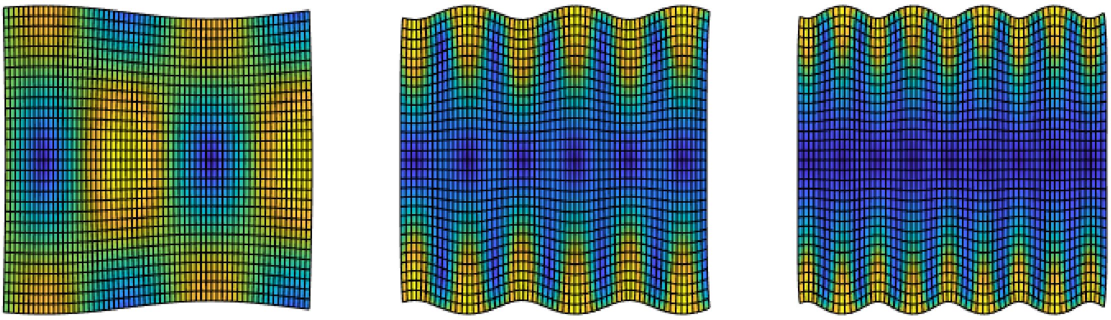

(a) 100 kHz (b) 200 kHz (c) 300 kHz

Figure 3.6: Evolution of the $S0$ mode.

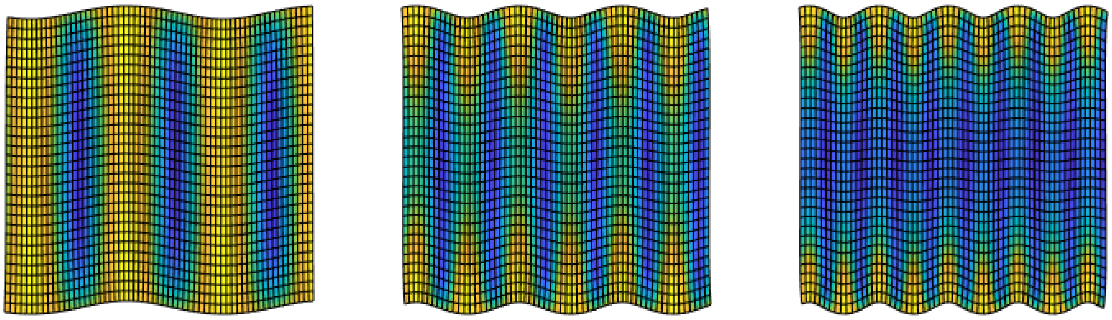

(a) 100 kHz (b) 200 kHz (c) 300 kHz

Figure 3.7: Evolution of the $SH0$ mode.

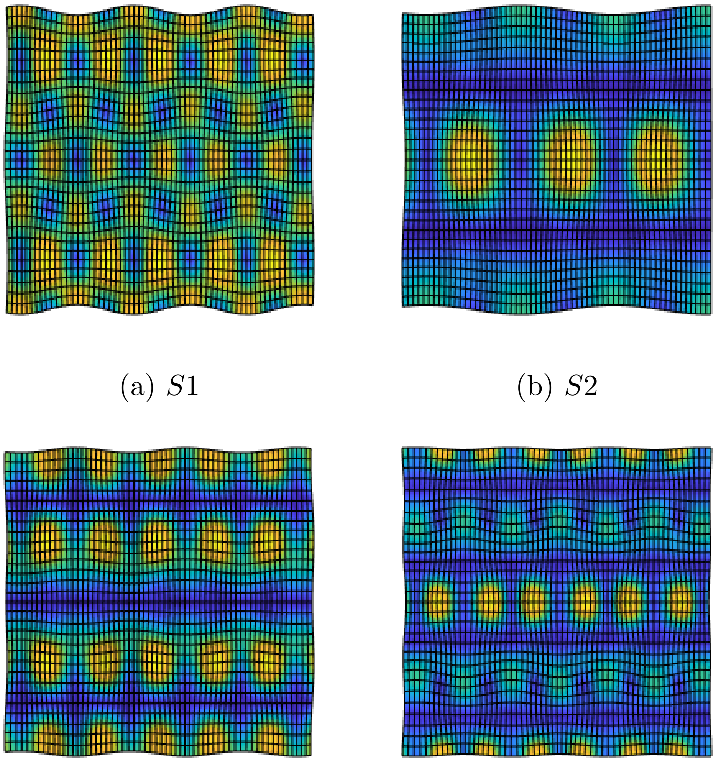

(a) $S1$

(b) $S2$

(c) $S3$

(d) $S4$

Figure 3.8: Higher order Sn modes.

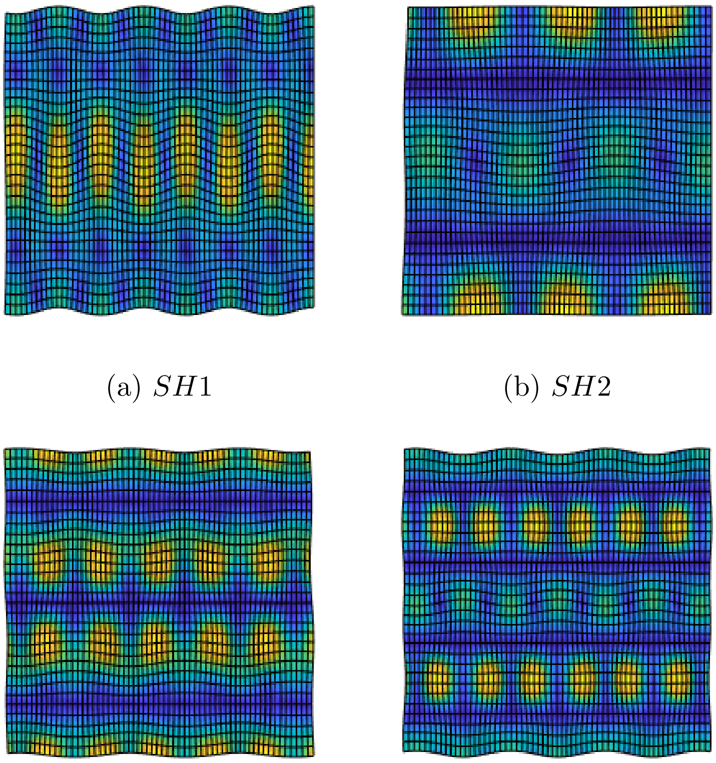

(a) $SH1$ (b) $SH2$

(c) $SH3$ (d) $SH4$

Figure 3.9: Higher order SHn modes.

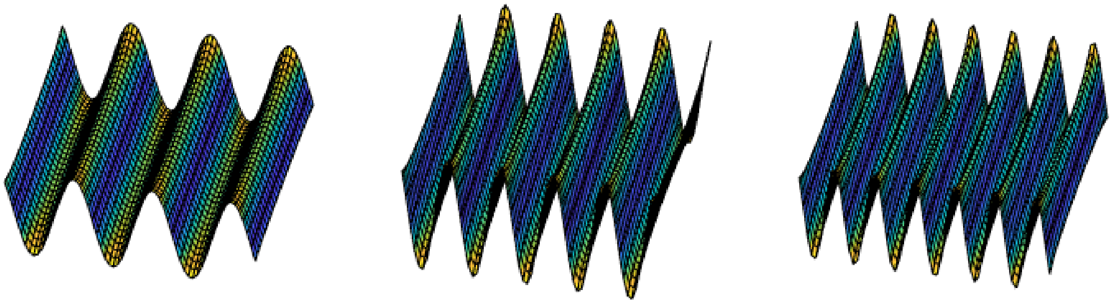

(a) 100 kHz (b) 200 kHz (c) 300 kHz

Figure 3.10: Evolution of the $A0$ mode.

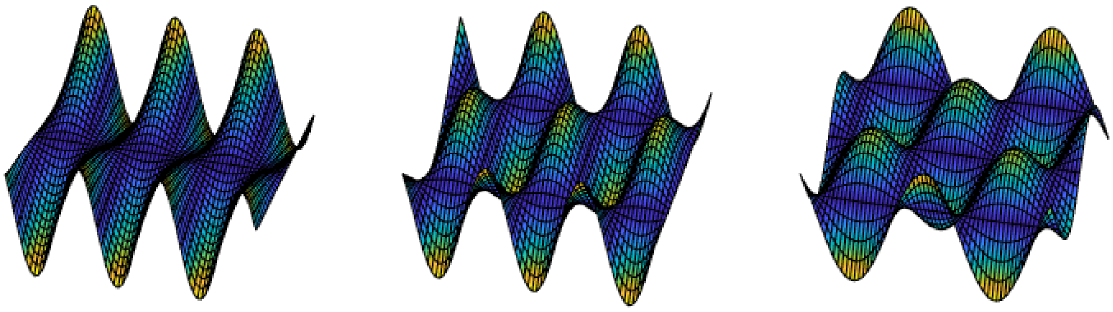

(a) $A0, 1$ (b) $A0, 2$ (c) $A0, 3$

Figure 3.11: Cross-sectional $A0, n$ modes.

discretization is then governed by the shortest wavelength that appears.

3.5.2 Cross-sectional wavemodes

Cross-sectional are called the wavemodes that are not explained by the Lamb theory, and depend on the examined cross-section geometry. In the plate-like cross section studied, those appear in terms of folds in the out-of-plane displacements.

Figure 3.11 displays the first three of the cross-sectional modes. They are named incrementally after the fundamental $A0$. They are either symmetric or antisymmetric about the longitudinal axis. The mode of Fig. 3.11a is often called torsional.

3.5.3 Wave actuation and measurement

As reviewed in Chapter 1.2.4, the discussion on the available actuation and measurement techniques for waves is of interest in wave-based NDT applications.

The available techniques for wave actuation and measurement are briefly recalled. Laser pulses generate waves by causing local thermal dilation. PZTs are mounted on a surface and deform when voltage is applied. Ultrasound probes generate acoustic waves that transfer energy in the solid through a coupling medium, oftentimes air.

The excitation of symmetric and antisymmetric waves depends on both the imposed deformation and frequency by means of actuation. Coupled PZTs mounted on the top and bottom surface of a plate will preferentially produce symmetric or antisymmetric waves dependent on whether they operate in simultaneous or opposite phase. PZTs on a single surface will generate simultaneous modes, biased towards symmetric for thinner plates and antisymmetric for thicker ones.

Laser pulse wave generation operates on a similar principle as PZTs, with the caveat of cost of the equipment, which allows for a single head in most cases. Laser sensing in done by interferometry; the beam is affected by out-of-plane motion of the measured body. It is thus much more sensitive to antisymmetric waves (see e.g. the measurements of Thierry and Chronopoulos (2020)).

Ultrasound probes cannot by default generate bias on the preferred mode. The parameter tunable is the incidence angle, which allows for an optimal energy transmission, and can be tuned accordingly by Snell's law applied onto the wave velocities of the coupling medium and the waveguide.

Cross section modes appear to present another challenge on actuation and measurement. Their antisymmetric nature requires that multiple measurements be acquired per section. This is possible with either multiple PZT patches or repeated laser measurements.

For general wave excitations, multiple modes propagate simultaneously. Isolating the displacements of a measured point due to some specific wavemode, requires certain post-processing. High resolution measurements, such as full-field or repeated laser, can accommodate for a multi-dimensional (2D or 3D) frequency-domain transform, which instantaneously reveals the dispersion curves and amplitudes of the waves. PZTs do not allow high spatial resolution, as the mere mounting affects the waveguide's properties. The WFE or other wave methods provide the advantage of calculable wavemodes; this opens the possibility of modal decomposition.

3.6 Conclusions

The behaviour of guided waves on width-wise bounded plates has been investigated through the WFE framework. A homogeneous plate has been solved with the MITC shell element. Results demonstrate that the WFE is capable of accurate solution of Lamb wavemodes, S0 and A0. Furthermore, the SH0 is shown to behave as a Lamb wave in the examined setting. Higher order S and SH modes can be attained with the proposed solution. This is not the case for higher order A modes, as plate kinematics inherently assume linear distribution of displacements along the plate's thickness, which is not the case for A1 or higher. These modes, however, do not appear but for frequencies higher than the conventional cut-off used for most NDT applications.

The conventional cut-off is defined as the frequency for which waves become highly dispersive. S0 is highly dispersive even in lower frequencies, whereas A0 and SH0 are more consistent for a bigger band.

WFE is capable of reproducing the Lamb waves on a plate, along with several other wavemodes. Examining the nature of the waves, i.e. their dispersion curves and mode shapes, allows educated decisions to be made regarding their actuation and measurement, along with dispersive properties.

In employing the WFE, the user effort is minimal, as the stiffness and mass matrices that are required can be easily obtained through any FE code, commercial or not; this is in contrast with e.g. SAFE, where a full analytical treatment on the direction of the wave propagation requires new elements to be designed. The numerical treatment of the representative cell allows for arbitrary cells to be represented (Ampatzidis et al., 2018, e.g.). The processing is then straightforward and easily achieved with MATLAB or other computational libraries.

Bibliography

Ampatzidis, T. and Chronopoulos, D. Mid-frequency band gap performance of sandwich composites with unconventional core geometries. *Composite Structures*, 222:110914, 2019.

Ampatzidis, T., Leach, R., Tuck, C., and Chronopoulos, D. Band gap behaviour of optimal one-dimensional composite structures with an additive manufactured stiffener. *Composites Part B: Engineering*, 153:26–35, 2018.

Bocquillet, A., Ichchou, M., and Jezequel, L. Energetics of axisymmetric fluid-filled pipes up to high frequencies. *Journal of Fluids and Structures*, 17(4):491–510, 2003.

Bouchoucha, F., Ichchou, M. N., and Haddar, M. Stochastic wave finite element method in uncertain elastic media through the second order perturbation. *Journal of Applied Mechanics and Technical Physics*, 58(2):362–370, 2017.

Chen, F. and Wilcox, P. D. The effect of load on guided wave propagation. *Ultrasonics*, 47(1-4):111–122, 2007.

Chronopoulos, D., Ichchou, M. N., Troclet, B., and Bareille, O. A. Predicting the broadband response of a layered cone-cylinder-cone shell. *Composite Structures*, 107(1):149–159, 2014.

Dworakowski, Z., Ambrozinski, L., Packo, P., Dragan, K., and Stepinski, T. Application of artificial neural networks for compounding multiple damage indices in Lamb-wave-based damage detection. *Structural Control and Health Monitoring*, 22(1):50–61, 2015.

Fan, Y., Collet, M., Ichchou, M., Li, L., Bareille, O. A., and Dimitrijevic, Z. Energy flow prediction in built-up structures through a hybrid finite element/wave and finite element approach. *Mechanical Systems and Signal Processing*, 66-67:137–158, 2016.

Gravenkamp, H. Efficient simulation of elastic guided waves interacting with notches, adhesive joints, delaminations and inclined edges in plate structures. *Ultrasonics*, 82:101–113, 2018.

Gravenkamp, H., Birk, C., and Song, C. Simulation of elastic guided waves interacting with defects in arbitrarily long structures using the Scaled Boundary Finite Element Method. *Journal of Computational Physics*, 295:438–455, 2015.

Houillon, L., Ichchou, M., and Jezequel, L. Wave motion in thin-walled structures. *Journal of Sound and Vibration*, 281(3-5):483–507, 2005.

Ichchou, M. N., Akrout, S., and Mencik, J.-M. Guided waves group and energy velocities via finite elements. *Journal of Sound and Vibration*, 305(4-5):931–944, 2007.

Ichchou, M. N., Bouchoucha, F., Ben Souf, M. A., Dessombz, O., and Haddar, M. Stochastic wave finite element for random periodic media through first-order perturbation. *Computer Methods in Applied Mechanics and Engineering*, 200(41-44):2805–2813, 2011.

Langley, R. S. Wave evolution, reflection, and transmission along inhomogeneous waveguides. *Journal of Sound and Vibration*, 227(1):131–158, 1999.

Livani, M., Khaji, N., and Zakian, P. Identification of multiple flaws in 2D structures using dynamic extended spectral finite element method with a universally enhanced meta-heuristic optimizer. *Structural and Multidisciplinary Optimization*, 57(2):605–623, 2018.

Mace, B. R., Duhamel, D., Brennan, M. J., and Hinke, L. Finite element prediction of wave motion in structural waveguides. *The Journal of the Acoustical Society of America*, 117(5):2835–2843, 2005.

Mace, B. R. and Manconi, E. Modelling wave propagation in two-dimensional structures using finite element analysis. *Journal of Sound and Vibration*, 318(4-5):884–902, 2008.

Maess, M., Wagner, N., and Gaul, L. Dispersion curves of fluid filled elastic pipes by standard FE models and eigenpath analysis. *Journal of Sound and Vibration*, 296(1-2):264–276, 2006.

Malik, M. K., Chronopoulos, D., and Tanner, G. Transient ultrasonic guided wave simulation in layered composite structures using a hybrid wave and finite element scheme. *Composite Structures*, 246:112376, 2020.

Mazzotti, M., Marzani, A., Bartoli, I., and Viola, E. Guided waves dispersion analysis for prestressed viscoelastic waveguides by means of the SAFE method. *International Journal of Solids and Structures*, 49(18):2359–2372, 2012.

Mencik, J.-M. A model reduction strategy for computing the forced response of elastic waveguides using the wave finite element method. *Computer Methods in Applied Mechanics and Engineering*, 229-232:68–86, 2012.

Mencik, J.-M. New advances in the forced response computation of periodic structures using the wave finite element (WFE) method. *Computational Mechanics*, 54(3):789–801, 2014.

Mencik, J.-M. and Ichchou, M. N. Wave finite elements in guided elastodynamics with internal fluid. *International Journal of Solids and Structures*, 44(7-8):2148–2167, 2007.

Miranda Jr., E. J. P., Nobrega, E. D., Rodrigues, S. F., Aranas Jr., C., and Dos Santos, J. Wave attenuation in elastic metamaterial thick plates: Analytical, numerical and experimental investigations. *International Journal of Solids and Structures*, 204-205:138–152, 2020.

Renno, J. M. and Mace, B. R. On the forced response of waveguides using the wave and finite element method. *Journal of Sound and Vibration*, 329(26):5474–5488, 2010.

Samaratunga, D., Jha, R., and Gopalakrishnan, S. Wave propagation analysis in adhesively bonded composite joints using the wavelet spectral finite element method. *Composite Structures*, 122:271–283, 2015.

Sbarufatti, C., Manson, G., and Worden, K. A numerically-enhanced machine learning approach to damage diagnosis using a Lamb wave sensing network. *Journal of Sound and Vibration*, 333(19):4499–4525, 2014.

Shen, Y. and Cesnik, C. E. Hybrid local FEM/global LISA modeling of damped guided wave propagation in complex composite structures. *Smart Materials and Structures*, 25(9):095021, 2016.

Sreekanth Kumar, D., Roy Mahapatra, D., and Gopalakrishnan, S. A spectral finite element for wave propagation and structural diagnostic analysis of composite beam with transverse crack. *Finite Elements in Analysis and Design*, 40(13-14):1729–1751, 2004.

Thierry, V., Brown, L., and Chronopoulos, D. Multi-scale wave propagation modelling for two-dimensional periodic textile composites. *Composites Part B: Engineering*, 150:144–156, 2018.

Thierry, V. and Chronopoulos, D. The impact of mesoscale textile architecture on the structural damping in composite structures. *Composite Structures*, 249:112475, 2020.

Thierry, V., Mesnil, O., and Chronopoulos, D. Experimental and numerical determination of the wave dispersion characteristics of complex 3D woven composites. *Ultrasonics*, 103:106068, 2020.

Waki, Y., Mace, B. R., and Brennan, M. J. Numerical issues concerning the wave and finite element method for free and forced vibrations of waveguides. *Journal of Sound and Vibration*, 327(1-2):92–108, 2009.

Willberg, C., Duczek, S., Vivar-Perez, J. M., and Ahmad, Z. A. B. Simulation Methods for Guided Wave-Based Structural Health Monitoring: A Review. *Applied Mechanics Reviews*, 2015.

Yang, Y., Mace, B. R., and Kingan, M. J. A wave and finite element based homogenised model for predicting sound transmission through honeycomb panels. *Journal of Sound and Vibration*, 463:114963, 2019.

Żak, A. and Krawczuk, M. A higher order transversely deformable shell-type spectral finite element for dynamic analysis of isotropic structures. *Finite Elements in Analysis and Design*, 142:17–29, 2018.

Zhong, W. X. and Williams, F. W. On the direct solution of wave propagation for repetitive structures. *Journal of Sound and Vibration*, 181(3):485–501, 1995.

Chapter 4

A hybrid Wave/XFEM scheme for wave scattering at cracks

4.1 Introduction

The detection and identification of damage modes such as cracks and delaminations is of cardinal interest in NDT applications. Both delaminations and cracks are connected to critical failure of components, leading to devastating results. Early detection is desirable, as it allows for timely intervention. While delamination modes are applicable to composite materials, cracks are a mode of damage that appears on any type of material, on itself, or as part of more complex damage.

Wave methods are often employed for the characterization of cracks Mitra and Gopalakrishnan (2016). Guided waves travel large enough distances within solids and allow for inspection of otherwise inaccessible or hardly accessible locations. Cracks are sensitive to waves, acting as scatterers. A variety of actuators and sensors are available, allowing for optimal configuration per case, as well as continuous monitoring. It is noted that waves operate in very small strain regime, and are virtually non-invasive.

Waves are tunable to some extent, meaning that their feature shapes and wavelengths can be adjusted to better interact with the damage. The wavelength is connected to the frequency in an inverse-proportional relation via the dispersion. The employment of numerical methods—predominantly FEM—in the simulation and, ultimately, the inversion of crack identification problems, comes at increased computational cost. In wave problems, the fineness of discretization must increase with the wavelength, with at least 7 elements per wavelength required for acceptable accuracy. The computational complexity is compounded by the Courant condition for stability of the time-integration, which connects the time step to the element size, through the speed of sound in the material. Very expensive models ought then to be created for the simulation of wave scattering.

Several methods have been developed to overcome the obstacle of the prohibitive computational cost of wave simulations. Analytical approaches for wave propagation and local hybrid interactions with defects (Bhuiyan et al., 2016; Shen and Giurgiutiu, 2016). The local interaction simulation approach (LISA) (Shen and Cesnik, 2016) is a computational framework that harnesses the parallelization capabilities of GPUs for explicit dynamic simulations. Hybridization with FE is proposed to simulate wave scattering duet to damage or actuation from PZTs. The time-domain spectral element method (Livani et al., 2018; Żak and Krawczuk, 2018; Liu et al., 2017, 2011; Munian et al., 2018) utilizes high-order finite elements whose nodes are located at the roots of Legendre-Chebyshev polynomials. Those have the property of a trivially diagonal mass matrix, allowing fast explicit time integration. Their high order circumvents the necessity of very fine discretization. A generalized FEM (GFEM) enrichment with sinusoidal functions has been proposed to eliminate spurious oscillations related to wave propagation (Komijani and Gracie, 2017). Frequency-domain spectral elements transform the default time-dependent displacements onto the frequency domain. Fourier (Sreekanth Kumar et al., 2004) and wavelet (Samaratunga et al., 2015) elements have been proposed. Wave decomposition approaches have been proposed, such as the semi-analytical (SAFE) (Spada et al., 2020; Serey et al., 2019) and the wave FE (WFE) (Waki et al., 2009; Zhong and Williams, 1995).

Hybrid wave and FE methods (Mencik and Ichchou, 2005; Renno and Mace, 2013; Mitrou et al., 2017; Malik et al., 2020) have been used to predict the scattering of guided waves due to elements of singular behaviour. Those may be damaged elements, with delaminations or cracks, joints of different types, or non-linear elements.

Simulation of crack behaviour in FE models is on its own an open question and another factor that adds towards the complexity of scattering problems. Cracks in general exhibit singular behaviour, with infinite stresses at the crack tips. An acceptable convergence is achieved with very fine discretization around the crack tips. The meshing of a cracked domain is non-trivial, as the geometry of the crack need be accounted for explicitly. In both crack propagation problems and inverse analyses, the crack geometry is varied, imposing the requirement for one mesh generation step per analysis. The mesh-independent crack representation of XFEM has been used to that end. Several inverse schemes have been proposed. The identification of cracks or voids is achieved through means of genetic algorithms (GA) (Chatzi et al., 2011; Jung et al., 2013; Jung and Taciroglu, 2014), mutli-step strategies (Zhao et al., 2018; Ma et al., 2017; Agathos et al., 2018), or Bayesian inference (Wang, 2018). Proof of concept was initially developed in plane problems (Rabinovich et al., 2007, 2009). XFEM for solids presents additional complexities in the implementation due to issues raised from the tracking of the crack and the front thereof (Agathos et al., 2018). Both static (Chatzi et al., 2011; Rabinovich et al., 2007) and dynamic approaches exist (Elguedj et al., 2009; Jung et al., 2013; Jung and Taciroglu, 2014). A notable formulation of extended spectral elements has been implemented for crack identification with dynamic analysis (Livani et al., 2018). XFEM formulations for plates and shells exist (Dolbow et al., 2000; Bayesteh and Mohammadi, 2011) but insofar no inverse works have been presented.

This work introduces XFEM in the procedure of wave scattering calculation. The problem of a cracked waveguide, i.e. a long beam is investigated.

4.2 An eXtended shell element for wave applications

In this work, we employ an extended plate element formulation to assess the performance of the X-WFE when damaged segments undergoing bending wave modes are considered. Membrane actions are also accounted for. The enrichment functions for the out-of-plane deflections near the crack tip have been examined by Dolbow et al. (2000) and have indicated good convergence. The Mixed Interpolation of Tensorial Components (MITC)

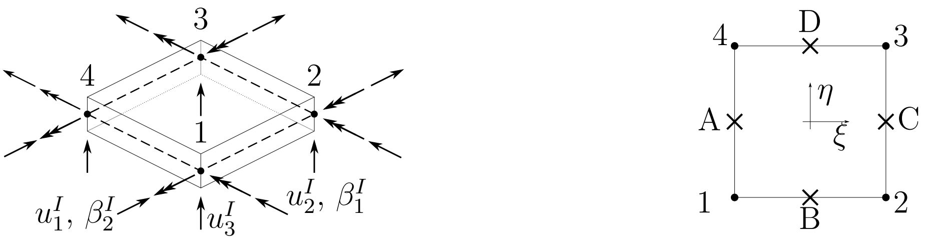

(a) Degrees of freedom.

(b) MITC tying points.

Figure 4.1: Degrees of freedom (a), nodes, tying points and isoparametric coordinates (b).

element of Bathe (1995) is implemented to alleviate locking due to spurious transverse shear terms.

A convenient matrix formulation for the MITC is formulated in Gruttmann and Wagner (2004). The performance of the extended MITC element for plates has been investigated in Bordas et al. (2010); Nguyen-Xuan et al. (2008), where element integration without the usage of derivatives was proposed, through strain smoothing and the divergence theorem. It is demonstrated that the convergence of the element is not monotonous with the decrease of mesh size. The enrichment functions for out-of-plane displacements and rotations are introduced in Dolbow et al. (2000); further discussion ensues in Bayesteh and Mohammadi (2011). Poor conditioning is resulted from the crack intersecting or passing close to the nodes, creating linear dependencies of the stiffness matrix Dof, as for example discontinuous functions tend to become similar to the shape functions.

The approach of Fries (2008) is utilised to alleviate spurious terms arising from the lack of partition of unity property in the blending elements, i.e. elements who have at least one but not all of their nodes enrichment. In the same work, the shifted enrichment is introduced, as means of zeroing the enrichment terms at the nodes, making the classical Dof sufficient to describe the displacement field.

4.2.1 Shell kinematics

The displacement field is represented by 5 independent components (Fig. 4.1a), three displacements u_i, $i = 1, 2, 3$ and two rotations β_i, $i = 1, 2$. The indices correspond to the component along the unit vector $\hat{\mathbf{e}}_i$. The rotations are defined such that they occur in the

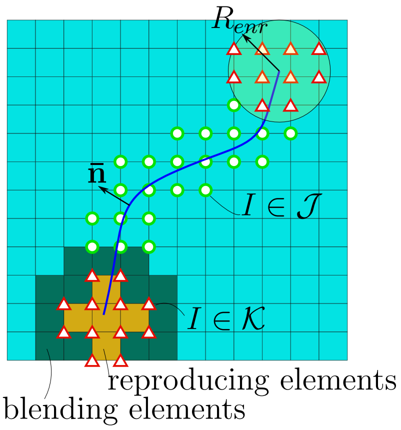

Figure 4.2: Types of enrichment and enriched sets for XFEM.

same plane as the displacement. The rotation of the shell's section is assumed to cause an antisymmetric displacement linearly distributed about the shell's thickness

$$u_i^A = -x_3 \beta_i. \tag{4.1}$$

The strains are defined

$$\varepsilon_{ij} = \frac{1}{2}\left(u_{i,j} + u_{j,i}\right), \quad i = 1,\, 2 \tag{4.2}$$

$$\gamma_j = u_{3,j} + \beta_j, \quad i = 1,\, 2. \tag{4.3}$$

By introducing Eq. (4.1) into Eq. (4.2), the formula for the antisymmetric strain $\varepsilon_{ij}^A(x_3) = -x_3\kappa_{i,j}$ with κ_{ij} the curvature defined as

$$\kappa_{ij} = \frac{1}{2}\left(\beta_{i,j} + \beta_{j,i}\right) \quad i = 1,\, 2. \tag{4.4}$$

4.2.2 Displacement interpolation

The displacements are interpolated from the nodes through the shape functions. A choice of enrichment function stems from the assumptions of specific behaviour of the displacement field in the vicinity of any introduced cracks

$$u_i = \sum_{I \in \mathcal{I}} N_I u_I + \sum_{I \in \mathcal{J}} N_I H_I a_I + \sum_{I \in \mathcal{K}} N_I \sum_{k=1}^{n} F_{Ik} b_{Ik} \tag{4.5a}$$

$$w = \sum_{I \in \mathcal{I}} N_I u_I + \sum_{I \in \mathcal{J}} N_I H_I a_I + \sum_{I \in \mathcal{K}} N_I \sum_{k=1}^{n} G_{Ik} b_{Ik} \tag{4.5b}$$

$$\beta_i = \sum_{I \in \mathcal{I}} N_I u_I + \sum_{I \in \mathcal{J}} N_I H_I a_I + \sum_{I \in \mathcal{K}} N_I \sum_{k=1}^{n} F_{Ik} b_{Ik} \tag{4.5c}$$

It is convenient to express the displacement interpolation in matrix notation as

$$\mathbf{u} = \begin{Bmatrix} u \\ v \end{Bmatrix} = \mathbf{N}_u \hat{\mathbf{u}}, \quad \mathbf{w} = \begin{Bmatrix} w \\ \beta_1 \\ \beta_2 \end{Bmatrix} = \mathbf{N}_w \hat{\mathbf{w}} \tag{4.6}$$

with $\mathbf{N}_u$, $\mathbf{N}_w$ the matrices containing the shape functions of Eq. (4.5) and $\hat{\mathbf{u}}, \hat{\mathbf{w}}$, respective vectors containing the discrete displacements and extended degrees of freedom. The latter express an amplitude of the prescribed displacement mode. The enriched sets $\mathcal{J}$, $\mathcal{K}$ are displayed in Fig. 4.2. A node belongs in $\mathcal{J}$ when its support—the region where $N_I \neq 0$—is intersected by the crack. Set $\mathcal{K}$ is comprised of nodes inside R_{enr}, which stems from the crack tip. The sets are non-intersecting, and nodes that are defined to belong in $\mathcal{K}$ are excluded from $\mathcal{J}$.

4.2.3 Strains and curvatures

We define the interpolation matrices for strains and curvatures, based on the definitions of strains in Equations (4.2), (4.4), (4.3) as

$$\boldsymbol{\epsilon} = \begin{Bmatrix} \epsilon_{11} \\ \epsilon_{22} \\ \gamma_{12} \end{Bmatrix} = \mathbf{B}\hat{\mathbf{u}}, \tag{4.7a}$$

$$\boldsymbol{\kappa} = \begin{Bmatrix} \kappa_{11} \\ \kappa_{22} \\ \kappa_{12} \end{Bmatrix} = \mathbf{G}\hat{\mathbf{w}}, \tag{4.7b}$$

$$\boldsymbol{\gamma} = \begin{Bmatrix} \gamma_{13} \\ \gamma_{23} \end{Bmatrix} = \mathbf{E}\hat{\mathbf{w}}, \tag{4.7c}$$

where the matrices $\mathbf{B}$, $\mathbf{G}$, $\mathbf{E}$ contain appropriate derivatives of the interpolation functions.

$$\mathscr{B}_I = \begin{bmatrix} N_{I,x} & 0 \\ 0 & N_{I,y} \\ N_{I,y} & N_{I,x} \end{bmatrix} \tag{4.8a}$$

$$\mathscr{H}_I = \begin{bmatrix} (N_I H_I)_{,x} & 0 \\ 0 & (N_I H_I)_{,y} \\ (N_I H_I)_{,y} & (N_I H_I)_{,x} \end{bmatrix} \tag{4.8b}$$

$$\mathscr{F}_I^k = \begin{bmatrix} (N_I F_I^k)_{,x} & 0 \\ 0 & (N_I F_I^k)_{,y} \\ (N_I F_I^k)_{,y} & (N_I F_I^k)_{,x} \end{bmatrix} \tag{4.8c}$$

$$\mathbf{B} = \begin{bmatrix} \{\mathscr{B}_I\}_{I=1,..,4} & \{\mathscr{H}_I\}_{I\in\mathscr{J}} & \{\mathscr{F}_I\}_{I\in\mathcal{K}}^{k=1,..,n_k} \end{bmatrix} \tag{4.9}$$

$$\mathscr{B}_I^b = \begin{bmatrix} 0 & N_{I,x} & 0 \\ 0 & 0 & N_{I,x} \\ 0 & N_{I,y} & N_{I,x} \end{bmatrix} \tag{4.10a}$$

$$\mathscr{H}_I^b = \begin{bmatrix} 0 & (N_I H_I)_{,x} & 0 \\ 0 & 0 & (N_I H_I)_{,y} \\ 0 & (N_I H_I)_{,y} & (N_I H_I)_{,x} \end{bmatrix} \tag{4.10b}$$

$$\mathscr{F}_I^b = \begin{bmatrix} 0 & (N_I F_I)_{,x} & 0 \\ 0 & 0 & (N_I F_I)_{,y} \\ 0 & (N_I F_I)_{,y} & (N_I F_I)_{,x} \end{bmatrix} \tag{4.10c}$$

$$\mathbf{E} = \left[\left\{\mathscr{B}_I^b\right\}_{I=1,..,4} \quad \left\{\mathscr{H}_I^b\right\}_{I\in\mathcal{J}} \quad \left\{\mathscr{F}_I^b\right\}_{I\in\mathcal{K}}^{k=1,..,n_k} \right] \tag{4.11}$$

the number of element nodes that belong in either set $\mathcal{J}$, $\mathcal{K}$ and n_k the number of enrichment functions used.

4.2.4 Variational formulation

The element matrices are produced invoking the equilibrium of the work variation. The rotations correspond to a linear antisymmetric strain distributed over the shell thickness h; as the displacements u_1, u_2 cause uniformly distributed strains, the energy is expressed by two uncoupled terms, referring to the in and out-of-plane deformation.

$$\begin{aligned} \delta\mathcal{U} = \int_\Omega \delta\boldsymbol{\varepsilon} : \boldsymbol{\sigma}\mathrm{d}V &= \int_\Omega \left\{(\delta\boldsymbol{\varepsilon}^S + \delta\boldsymbol{\varepsilon}^A)^T(\boldsymbol{\sigma}^S + \boldsymbol{\sigma}^A) + \delta\boldsymbol{\gamma}^T\boldsymbol{\tau}\right\}\mathrm{d}V \\ &= \underbrace{\int_\Omega (\delta\boldsymbol{\varepsilon}^S)^T\boldsymbol{\sigma}^S\mathrm{d}V}_{\delta\mathcal{U}^{(IP)}} + \underbrace{\int_\Omega (\delta\boldsymbol{\varepsilon}^A)^T\boldsymbol{\sigma}^A\mathrm{d}V}_{\delta\mathcal{U}_b^{(OP)}} + \underbrace{\int_\Omega \delta\boldsymbol{\gamma}^T\boldsymbol{\tau}\mathrm{d}V}_{\delta\mathcal{U}_s^{(OP)}} \end{aligned} \tag{4.12}$$

The transverse stresses σ_{33} are considered negligible. The strain energy is split into the uncoupled in-plane (IP) and out-of-plane (OP) terms. We examine the two separately. The in-plane term gives

$$\delta\mathcal{U}^{(IP)} = \int_\Omega \delta\boldsymbol{\varepsilon}^T\boldsymbol{\sigma}\mathrm{d}V = \delta\hat{\mathbf{u}}^T \int_\Omega \mathbf{B}^T\mathbf{C}\mathbf{B}\mathrm{d}V\hat{\mathbf{u}} \tag{4.13}$$

The out-of-plane energy receives contributions from bending and transverse shear.

$$\delta\mathcal{U}_b^{(OP)} = \delta\hat{\mathbf{w}}^T \int_\Omega x_3^2\mathbf{E}^T\mathbf{C}\mathbf{E}\mathrm{d}V\hat{\mathbf{w}} = \int_A \delta\hat{\mathbf{w}}^T\mathbf{E}^T\mathbf{C}^b\mathbf{E}\mathrm{d}A\hat{\mathbf{w}}^T \tag{4.14}$$

with $\mathbf{C}^b$ the bending stiffness defined as $h^3/12\mathbf{C}$, after the integration of x_3^2 on h.

MITC formulation

The shear part of the potential energy is written

$$\delta \mathcal{U}_s^{(OP)} = \delta \hat{\mathbf{w}}^T \int_\Omega \mathbf{G}^T \mu \mathbf{G} \mathrm{d}V \hat{\mathbf{w}} = \delta \hat{\mathbf{w}}^T \kappa \mu h \int_A \mathbf{G}^T \mu \mathbf{G} \mathrm{d}A \hat{\mathbf{w}}, \tag{4.15}$$

with μ the shear modulus. $\kappa = 5/6$ is a constant that equates the area of the parabolic distribution of shear stresses to an equivalent uniform distribution. The choice of interpolation functions cause spurious shear strains in cases of constant curvature, resulting in increased element stiffness. The mixed interpolation of tensorial components (MITC) approach is capable of eliminating spurious shear strains, by introducing an assumed strain calculated at the tying points of the element (Fig. 4.1b) and special interpolation functions. Gruttmann and Wagner (2004) demonstrated that an equivalent matrix form can be written as

$$\mathbf{G} = \begin{bmatrix} \{\mathscr{B}_I^s\}_{I=1,..,4} & \{\mathscr{H}_I^s\}_{I\in\mathcal{J}} & \{\mathscr{F}_I^s\}_{I\in\mathcal{K}} \end{bmatrix} \tag{4.16}$$

with

$$\mathscr{B}_s^b = \begin{bmatrix} N_{I,x} & b_{11}^I N_I & b_{12}^I N_I \\ N_{I,y} & b_{21}^I N_I & b_{22}^I N_I \end{bmatrix} \tag{4.17a}$$

$$\mathscr{H}_s^b = \begin{bmatrix} (N_I H_I)_{,x} & b_{11}^I N_I H_I & b_{12}^I N_I H_I \\ (N_I H_I)_{,x} & b_{21}^I N_I H_I & b_{22}^I N_I H_I \end{bmatrix} \tag{4.17b}$$

$$\mathscr{F}_s^b = \begin{bmatrix} \left\{(N_I G_I^k)_{,x}\right\}^{k=1\ldots n_G} & \left\{b_{11}^I N_I F_I^k\right\}^{k=1\ldots n_F} & \left\{b_{12}^I N_I F_I\right\}^{k=1\ldots n_F} \\ \left\{(N_I G_I^k)_{,x}\right\}^{k=1\ldots n_G} & \left\{b_{21}^I N_I F_I^k\right\}^{k=1\ldots n_F} & \left\{b_{22}^I N_I F_I\right\}^{k=1\ldots n_F} \end{bmatrix} \tag{4.17c}$$

where n_G, n_F the number of approximation functions of the respective class; it is noted that a different number of functions may be used to approximate each quantity, with respect to the desired order of approximation (Dolbow et al., 2000; Bayesteh and Mohammadi, 2011).

The terms b_{ij} are defined as Gruttmann and Wagner (2004)

$$b_{11}^I = \xi_I x_{,\xi}^M, \quad b_{12}^I = \xi_I y_{,\xi}^M \quad b_{21}^I = \eta_I x_{,\eta}^L, \quad b_{22}^I = \eta_I y_{,\eta}^L. \tag{4.18}$$

I denotes the nodes and ξ_I, η_I are the isoparametric coordinates at the respective element node, such that $\xi_I \in \{-1,1,1,-1\}$ and $\eta \in \{-1,-1,1,1\}$. Finally, $(I,M,L) \in \{(1,B,A);(2,B,C);(3,D,C);(4,D,A)\}$, where A,B,C,D are the shear strain tying points defined in the isoparametric coordinates as displayed in Fig. 4.1b.

The terms for kinetic energy and external work involve only the displacement terms. The displacement interpolation matrices are thus used.

$$\begin{aligned}\delta\mathcal{P} = \int_\Omega (\delta\hat{\mathbf{u}})^T \rho \mathbf{u} \mathrm{d}V \hat{\mathbf{u}} = (\delta\mathbf{u})^T \rho h \int_A \mathbf{N}_u^T \mathbf{N}_u \mathrm{d}A \hat{\mathbf{u}} \\ + (\delta\hat{\mathbf{w}})^T \rho \int_A \mathbf{N}_w^T \left\lceil\, h, \;\; \tfrac{h^3}{12}, \;\; \tfrac{h^3}{12} \,\right\rfloor \mathbf{N}_w \mathrm{d}A \hat{\mathbf{w}} \qquad (4.19)\end{aligned}$$

with $\lceil\cdot\rfloor$ denoting a diagonal matrix.

External forces

The external work is expressed as

$$\delta\mathcal{W} = \int_\Omega \delta\mathbf{u}\mathbf{f}\mathrm{d}V \qquad (4.20)$$

The integration of stresses through the thickness of the plate defines

$$\int_{-h/2}^{h/2} x_3 \varepsilon_{ij}^A \mathrm{d}x_3 = M_{ij}, \quad i = 1,2 \qquad (4.21a)$$

$$\int_{-h/2}^{h/2} \gamma_{3j} \mathrm{d}x_3 = Q_j \qquad (4.21b)$$

where M_{ij} is the distributed moment and Q_j the shear force.

Element matrices

The final discrete form of the internal and external work variation reads

$$\delta\hat{\mathbf{u}}^T\mathbf{K}\hat{\mathbf{u}} + \delta\hat{\mathbf{w}}^T\mathbf{K}^b\hat{\mathbf{w}} + \delta\hat{\mathbf{w}}^T\mathbf{K}^s\hat{\mathbf{w}} + \delta\hat{\mathbf{u}}^T\mathbf{M}\ddot{\hat{\mathbf{u}}} + \delta\hat{\mathbf{w}}^T\mathbf{M}^b\ddot{\hat{\mathbf{w}}} = \delta\hat{\mathbf{u}}^T\mathbf{F}\hat{\mathbf{u}} + \delta\hat{\mathbf{w}}^T\mathbf{F}^b\hat{\mathbf{w}} \qquad (4.22)$$

with $\mathbf{K}$, $\mathbf{M}$ the in-plane mass and stiffness. $\mathbf{K}^b$, $\mathbf{K}^s$ are the bending and shear stiffness matrices that both contribute to out-of-plane stiffness, and $\mathbf{M}^b$ is the out-of-plane mass. The matrices are generally comprised of the classical and enriched parts,

$$\mathbf{K} = \begin{bmatrix} \mathbf{K}_{uu} & \mathbf{K}_{uu} & \mathbf{K}_{uu} \\ \mathbf{K}_{ua} & \mathbf{K}_{ua} & \mathbf{K}_{ua} \\ \mathbf{K}_{ub} & \mathbf{K}_{ub} & \mathbf{K}_{ub} \end{bmatrix}, \quad \mathbf{F} = \begin{Bmatrix} \mathbf{F}_u \\ \mathbf{F}_a \\ \mathbf{F}_b \end{Bmatrix}, \tag{4.23}$$

4.2.5 Enrichment functions

Specialized functions are used to approximate the properties of the displacement fields near the crack tip and the discontinuity of the crack body. Those are defined as (Dolbow et al., 2000; Bayesteh and Mohammadi, 2011).

$$F = \sqrt{r}\left\{\sin\left(\tfrac{\theta}{2}\right), \quad \cos\left(\tfrac{\theta}{2}\right), \quad \sin(\theta)\sin\left(\tfrac{\theta}{2}\right), \quad \cos(\theta)\sin\left(\tfrac{\theta}{2}\right)\right\}, \tag{4.24}$$

$$G = r^{\frac{3}{2}}\left\{\sin\left(\tfrac{\theta}{2}\right), \quad \cos\left(\tfrac{\theta}{2}\right), \quad \sin\left(\tfrac{3\theta}{2}\right), \quad \cos\left(\tfrac{3\theta}{2}\right)\right\}. \tag{4.25}$$

where the necessary discontinuous term along the crack arises from the $\sin(\theta/2)$ term. Functions F are used to enrich the in-plane displacements and rotations, whereas G are used for the out-of-plane deflections (Dolbow et al., 2000; Bayesteh and Mohammadi, 2011; Bordas et al., 2010). An optional term proportional to $\sqrt{r}$ has been proposed by Dolbow et al. (2000) for G, but is omitted in most applications.

The discontinuous function reads

$$H = \text{sign}(\phi). \tag{4.26}$$

with ϕ the signed distance function also called level set.

Level sets

The information of the crack in XFEM is conveyed through the values of the level sets, entities of dimensionality $D+1$, where D is the number of dimensions of the crack, e.g. $D = 1$ for plane problems. The crack is represented by the zero iso-line of a surface ϕ, which is defined as the signed distance function

$$\phi = \operatorname{sign}\left((\mathbf{x}-\mathbf{x}_c)\cdot\bar{\mathbf{n}}\right)\min_{\mathbf{x}_c\in\mathcal{C}}\|\mathbf{x}-\mathbf{x}_c\|. \tag{4.27}$$

where $\bar{\mathbf{n}}$ is a unit normal vector on the crack (Fig. 4.2), $\mathbf{x}$ is the position vector of a generic point in Ω, and $\mathbf{x}_c$ is a point that belongs on the crack Γ_c.

An additional level set is defined for crack problems to allow tracking the crack tips.

$$\nabla\psi\cdot\nabla\phi = 0 \quad \text{and} \quad \psi = 0 \quad \text{at the crack tip,} \tag{4.28}$$

respectively. The level set ψ is perpendicular to ϕ and takes negative values inside the crack, positive outside and zero at the crack-tip.

The polar coordinate the enrichment functions are defined in (4.25) is conveniently derived from $Or\theta$ where

$$r = \sqrt{\phi^2+\psi^2}, \tag{4.29}$$

and

$$\theta = \arctan\left(\frac{\phi}{\psi}\right). \tag{4.30}$$

The discontinuity of the crack is fulfilled, as $\theta = \pm\pi$ on either one of the crack lips.

Blending elements

When all of an element's nodes belong in $\mathcal{K}$, it is called a reproducing element (Fries, 2008), as it is capable of forming a partition of unity of the enriched function. The blending elements are those for which at least one but not all their nodes belong in $\mathcal{K}$. The enrichment functions are not reproduced completely, introducing errors when the element undergoes solid translation. Fries (2008) proposed a correcting approach. A ramp function is constructed, whose value is 1 every node in $\mathcal{K}$ and 0 on any other.

$$R^*(\mathbf{x}_I) = \begin{cases} 1, & I\in\mathcal{K} \\ 0, & I\in\mathcal{I}\setminus\mathcal{K} \end{cases} \tag{4.31}$$

The multiplication of the crack-tip enrichment functions with R^*, e.g.

$$\bar{F}_I^* = R^*(\mathbf{x}_I)\left(F(\mathbf{x}) - F(\mathbf{x}_I)\right), \tag{4.32}$$

and same for G, H, causes them to decay to zero on unenriched nodes, restoring the partition of unity.

The shifted enrichment approach (Fries, 2008) is also implemented (Eq. (4.32)) to impose zero value of the enrichment functions on the nodes. This allows for the representation of the displacement field with only the classic displacement Dof, simplifying postprocessing.

4.3 The hybrid Wave/XFEM as a multi-body dynamics problem

In this work, the Diffusion Matrix Method (DMM) is revisited and originally established within an XFEM framework. A variational formulation of the frequency-domain dynamics of a multi-body system is first established. The discretization of the domain is done by adopting the XFEM framework, with enriched approximation functions to represent the displacements of the cracked domain. The elongated shape of the sub-domains allows for the wave decomposition of the displacement fields. The propagating wave modes are calculated with the WFE framework. The scattering matrix establishes a relation between the amplitudes of the reflected and transmitted waves of the system.

4.3.1 Variational formulation

The case of the cracked coupling domain Ω_c with an internal interface Γ_c shown in Fig. 4.3 is considered. Substructures Ω_i, $i = 1 \dots n$ join Ω_c along the boundaries Γ_{ic}, $i = 1 \dots n$ of Ω_c such that $\Omega = \bigcup_{i=1}^{n} \Omega_i \cup \Omega_c$ and $\Gamma_{ic} = \Omega_i \cap \Omega_c$. The substructures Ω_i have an outer boundary $\Gamma_{i\infty}$ and are subjected to external loads $F_{i\infty}$ at $\Gamma_{i\infty}$.

The dynamic behaviour of the system is examined by implementing a variational approach in the frequency domain (Mencik and Ichchou, 2005; Ichchou et al., 2009).

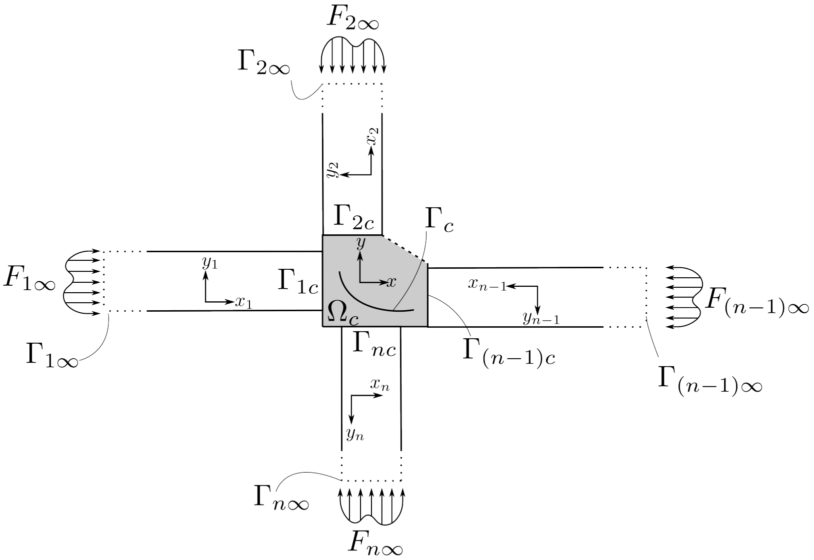

Figure 4.3: Multiple waveguides connected with a coupling element.

The total potential energy Π in the system is established as

$$\Pi = \sum_{i=1}^{n} \mathcal{W}_i + \mathcal{W}_c - \sum_{i=1}^{n} \mathcal{F}_i - \sum_{i=1}^{n} \mathcal{L}_i. \tag{4.33}$$

The internal work $\mathcal{W}_i$, $i = 1 \ldots n, c$ is defined in the frequency domain as

$$\mathcal{W}_i = \omega^2 \int_{\Omega_i} \frac{1}{2} \mathbf{u}^T \rho \mathbf{u} \mathrm{d}V - \int_{\Omega_i} \boldsymbol{\epsilon}(\mathbf{u})^T \boldsymbol{\sigma} \mathrm{d}V, \tag{4.34}$$

The work $\mathcal{F}_i$ of the external loads f is

$$\mathcal{F}_i = \int_{\Gamma_{i\infty}} \mathbf{u}^T \mathbf{f} \mathrm{d}V. \tag{4.35}$$

External loads are only considered on the far boundaries $\Gamma_{i\infty}$ of the substructures Ω_i as shown in Fig. 4.3. The terms $\mathcal{L}_i$ emerge from the imposition of the continuity constraints on the surfaces $\boldsymbol{\Gamma}_{ic}$ through the set of Lagrange multipliers $\boldsymbol{\lambda_i}$, $i = 1 \ldots n$, i.e.,

$$\mathcal{L}_i = \int_{\Gamma_{ic}} \boldsymbol{\lambda}_i^T (\mathbf{u}_i - \mathbf{u}_c) \mathrm{d}s. \tag{4.36}$$

4.3.2 Discretization

The domains Ω_i, $i = 1 \ldots n$ and c are discretized in a set of non overlapping elements, such that $\Omega_i = \bigcup_{e=1}^{N_e} \Omega_i^e$, where Ω_i^e are joined at their corresponding nodes. The nodes comprise the set $\mathcal{I}$. The displacement field is interpolated at the nodes according to Eq. (4.5). We assume a discretization of the Lagrange multipliers on each surface Γ_i

$$\boldsymbol{\lambda}_i = \boldsymbol{\xi}\mathbf{p}_i \tag{4.37}$$

where $\boldsymbol{\xi}$ is a matrix of shape functions and $\mathbf{p}_i$ a vector of equal size as the number of Dof on the interface n_c, Eq. (4.36) assumes the discretized form

$$\mathcal{L}_i = \mathbf{p}_i^T \left(\mathbf{L}_c^{(i)} \mathbf{u}_c - \mathbf{L}_i^{(i)} \mathbf{u}_i \right). \tag{4.38}$$

with

$$\mathbf{L}_c^{(i)} = \int_{\Gamma_{ci}} (\boldsymbol{\xi})^T \mathbf{N} \mathrm{d}s \tag{4.39a}$$

$$\mathbf{L}_i^{(i)} = \int_{\Gamma_{ic}} (\boldsymbol{\xi})^T \mathbf{N} \mathrm{d}s \tag{4.39b}$$

where Γ_{ci} is the surface of Ω_c interfacing with Ω_i, and Γ_{ic} the respective surface of Ω_i. In the general case, the number of Dof n_{ic} on Γ_{ic} is different than n_{ci}. The discretization of the interface, i.e. the size of $\mathbf{p}$, is independent and arbitrary. The matrices $\mathbf{L}_c^{(i)}$ impose displacement continuity in a weak sense. Unlike Mencik and Ichchou (2005); Ichchou et al. (2009) however, the usage of XFEM allows for a conforming mesh along the propagating substructures and the coupling element.

Finally, through Eq. (4.22) the discrete form of the potential is reached:

$$\begin{aligned} \delta\Pi = \sum_{i=1}^{n} \delta\mathbf{u}_i^T \mathbf{D}_i \mathbf{u}_i + \delta\mathbf{u}_c^T \mathbf{D}_c \mathbf{u}_c + \sum_{i=1}^{n} \delta\mathbf{p}_i^T (\mathbf{L}_c^{(i)} \mathbf{u}_c - \mathbf{L}_i^{(i)} \mathbf{u}_i) \\ + \sum_{i=1}^{n} \left\{ (\delta\mathbf{u}_c)^T (\mathbf{L}_c^{(i)})^T \mathbf{p}_i - (\delta\mathbf{u}_i)^T (\mathbf{L}_i^{(i)})^T \mathbf{p}_i \right\} - \sum_{i=1}^{n} (\delta\mathbf{u}_i)^T \mathbf{F}_i = 0 \end{aligned} \tag{4.40}$$

with $\mathbf{D}_i = (1 + i\omega\eta)\mathbf{K}_i + \omega^2 \mathbf{M}_i$ the dynamic stiffness matrix and η a damping constant.

This leads to independent equations

$$\mathbf{D}_i\mathbf{u}_i = \mathbf{F}_i + (\mathbf{L}_c^{(i)})^T\mathbf{p}_i, \quad i = 1\ldots N, \tag{4.41}$$

$$\mathbf{D}_c\mathbf{u}_c = -\sum_{i=1}^{N}(\mathbf{L}_i^{(i)})^T\mathbf{p}_i, \tag{4.42}$$

$$\mathbf{L}_c^{(i)}\mathbf{u}_c = \mathbf{L}_i^{(i)}\mathbf{u}_i. \tag{4.43}$$

Equations (4.41) and (4.42) express the dynamic equilibrium of the propagating substructures and the coupling element respectively. Equation (4.43) expresses the tying of the displacements between the substructure and the coupling element.

Mesh tying and interpretation of Lagrange constraints

Matrices $\mathbf{L}_c^{(i)}$, $\mathbf{L}_i^{(i)}$ act as Boolean operators on the whole of Dof of Ω_c, Ω_i respectively, operating on terms

$$\mathbf{L}_c^{(i)} = \begin{bmatrix}\mathbf{0} & \mathbf{L}_c^{(i)*}\end{bmatrix}, \tag{4.44a}$$

$$\mathbf{L}_i^{(i)} = \begin{bmatrix}\mathbf{L}_i^{(i)*} & \mathbf{0}\end{bmatrix}, \tag{4.44b}$$

where $\mathbf{L}_i^{(j)*}$ is of size $n_i \times n_I$, with n_I denoting the number of Dofs at the interface. If the coordinate system of the coupling element is taken as a reference, then $\mathbf{L}_c^{(i)*} = \tilde{\mathbf{R}}^{(ic)}$ and $\mathbf{L}_c^{(j)*} = -\mathbf{I}$, where $\mathbf{I}$ is the identity matrix.

The terms $\mathbf{p}_i$, as they appear on Eqs. (4.41), (4.42) are, in the natural sense, the inter-body forces $\mathbf{F}_{\Gamma_i}$ and are substituted:

$$\mathbf{D}_i\mathbf{u}_i = \mathbf{F}_i + (\mathbf{L}_i^{(c)})^T\mathbf{F}_{\Gamma_i}^i \tag{4.45}$$

$$\mathbf{D}_c\mathbf{u}_c = \sum_{i=1}^{N}(\mathbf{L}_i^{(i)})^T\mathbf{F}_{\Gamma_i}^c \tag{4.46}$$

Considering the equilibrium requirement of equilibrium on Γ_i, the relation

$$\mathbf{F}_{\Gamma_i} = (\mathbf{L}_c^{(i)})^T\mathbf{F}_c = -(\mathbf{L}_i^{(i)})^T\mathbf{F}_i \tag{4.47}$$

is reached, with $\mathbf{F}_c$, $\mathbf{F}_i$ the force vectors of Ω_c, Ω_i. The Boolean nature of operators $\mathbf{L}$ leads to writing

$$\mathbf{L}_c^{(i)}\mathbf{F}_c = \left(\mathbf{L}_c^{(i)*}\right)^T \mathbf{F}_c|_{\Gamma_i} \tag{4.48a}$$

$$\mathbf{L}_i^{(i)}\mathbf{F}_i = \left(\mathbf{L}_i^{(i)*}\right)^T \mathbf{F}_i|_{\Gamma_i} \tag{4.48b}$$

with $\mathbf{F}_c|_{\Gamma_i}$ the isolated forces of Ω_c at the interface. Eq. (4.47) is further reduced to

$$\left(\mathbf{L}_c^{(i)*}\right)^T \mathbf{F}_c|_{\Gamma_i} = -\left(\mathbf{L}_i^{(i)*}\right)^T \mathbf{F}_i|_{\Gamma_i} \tag{4.49}$$

or

$$\mathbf{F}_c|_{\Gamma_i} = -\tilde{\mathbf{R}}\mathbf{F}_i|_{\Gamma_i}. \tag{4.50}$$

A similar process stems for displacements, resulting in

$$\mathbf{u}_c|_{\Gamma_i} = \tilde{\mathbf{R}}\mathbf{u}_i|_{\Gamma_i}. \tag{4.51}$$

It is noted that, in case of nonconforming meshes, matrices $\mathbf{L}_c^{(i)*}$, $\mathbf{L}_i^{(i)*}$ have a common dimension, allowing for a pseudo-inversion operation to fulfil the projection.

4.3.3 Wave expression of the state vectors

In the dynamic context of the proposed method, the forces and displacements can be expressed in terms of propagating waves. Those waves propagate in discrete wavemodes $\boldsymbol{\phi}$. The decomposition of the state vector $\mathbf{q}$ is expressed as

$$\mathbf{q} = \begin{Bmatrix} \mathbf{u} \\ \mathbf{F} \end{Bmatrix} = \sum_{i=1}^{N} Q_i \boldsymbol{\phi}_i \exp[\mathrm{j}(k_i x - \omega t)], \tag{4.52}$$

with $j = -\sqrt{-1}$ and Q_i the modal amplitude.

4.3.4 Wavemode calculation through the WFE

The wavemodes are calculated using the WFE (Waki et al., 2009; Mencik and Ichchou, 2005). A representative cell of the propagating substructure is selected, of length Δx. The convergence of the method depends on the selection of the cell length with respect to the wavelength (Waki et al., 2009). The mesh size in this work is derived from the convergence of the coupling element, hence the cell size provides acceptable convergence. The state vectors on the left and the right are connected through

$$\mathbf{q}_R = \lambda \mathbf{q}_L \tag{4.53}$$

$$\mathbf{q}_R = \mathbf{T}\mathbf{q}_L \tag{4.54}$$

where $\lambda = e^{(jk\Delta x)}$ a phase constant and $\mathbf{T}$ the transfer matrix (Mencik and Ichchou, 2005; Waki et al., 2009) defined as

$$\mathbf{T} = \begin{bmatrix} (\mathbf{D}^*_{LR})^{-1}\mathbf{D}^*_{LL} & (\mathbf{D}^*_{LR})^{-1} \\ \begin{array}{c} -\mathbf{D}^*_{RL} \\ +\mathbf{D}^*_{RR}(\mathbf{D}^*_{LR})^{-1}(\mathbf{D}^*_{LL})^{-1} \end{array} & -\mathbf{D}^*_{RR}(\mathbf{D}^*_{LR})^{-1} \end{bmatrix}, \tag{4.55}$$

where $\mathbf{D}^*_{IJ}$, $\{I, J\} \in \{L, R\}$ denotes the condensed form of $\mathbf{D}_{IJ}$, i.e. with the internal nodes eliminated through Guyan reduction, per Eq. (79). Combining Equations (4.54), (4.53) the eigenvalue problem

$$\mathbf{\Phi}\mathbf{T} = \boldsymbol{\lambda}\mathbf{\Phi} \tag{4.56}$$

where $\mathbf{q} = \{\mathbf{u}^T\ \mathbf{F}^T\}^T$ the state vector, $\boldsymbol{\lambda}$ the diagonal eigenvalue matrix and $\mathbf{\Phi}$ the corresponding eigenvectors. The size of matrix $\mathbf{T}$ and the number of solutions is $2n$, where n is the number of Dof on either $\mathbf{q}_R$, $\mathbf{q}_L$. Those come as pairs of reciprocals (Mencik and Ichchou, 2005) so that $\lambda_j = 1/\lambda_{n+j}$, $j = 1 \ldots n$. This represents pairs of positive and negative-travelling waves. The resulting eigenvectors, named wavemodes, are partitioned as

$$\boldsymbol{\Phi} = \left[\begin{array}{ccc|ccc} \boldsymbol{\phi}^+_{u(1)} & \cdots & \boldsymbol{\phi}^+_{u(n)} & \boldsymbol{\phi}^-_{u(1)} & \cdots & \boldsymbol{\phi}^-_{u(n)} \\ \hline & & & & & \\ \boldsymbol{\phi}^+_{F(1)} & \cdots & \boldsymbol{\phi}^+_{F(n)} & \boldsymbol{\phi}^-_{F(1)} & \cdots & \boldsymbol{\phi}^-_{F(n)} \end{array}\right] \tag{4.57}$$

with $\boldsymbol{\phi}_i = \{\boldsymbol{\phi}^T_{u(i)}\, \boldsymbol{\phi}^T_{F(i)}\}^T$ the wavemode i, divided into the force and displacement part, respective to the state vector $\mathbf{q}$.

The value of λ is shown to be close to 1 for propagating waves. When the phase constant is solved for the wavenumber k, generally complex values are obtained, with the real part representing the wavelength and the imaginary part the attenuation. When the imaginary part is large comparable to the real part, a wave attenuates rapidly; such waves are called evanescent. For low damping constant η, propagating waves have imaginary parts close to zero.

$\boldsymbol{\Phi}$ is by default a square matrix, as a discrete system of size n_{Dof} has n_{Dof} eigenvalues. The selection of the wave basis retained for the DMM analysis is suggested to retain propagating modes, as both the computational cost and numerical stability of the method are ensured (Mencik and Ichchou, 2005). The resultant $\boldsymbol{\Phi}$ is non-square, of size $2n_{Dof} \times 2n_{wave}$, where n_{Dof} is the number of Dof of the section, and n_{wave} the number of positive retained waves.

4.3.5 Wavemode normalization

The default normalization of $\boldsymbol{\Phi}$ is dependent on the solver used. DMM requires that the wavemodes be normalized on basis of power, such that two modes of the same amplitude Q carry the same power. The power flow of the wave is defined as (Ichchou et al., 2007)

$$\mathbf{P}(\omega) = \frac{-\mathrm{i}\omega}{4} \left\{ \begin{array}{c} \mathbf{u}_L \\ -\mathbf{F}_L \end{array} \right\}^H \mathbf{J} \left\{ \begin{array}{c} \mathbf{u}_L \\ -\mathbf{F}_L \end{array} \right\} = \mathbf{Q}^H \mathbf{P}^{\boldsymbol{\Phi}} \mathbf{Q} \tag{4.58}$$

with $\mathbf{P}^{\boldsymbol{\Phi}}$ the power flow matrix

$$\mathbf{P}^{\boldsymbol{\Phi}} = \frac{-\mathrm{i}\omega}{4} \begin{bmatrix} \boldsymbol{\Phi}_u \\ \boldsymbol{\Phi}_F \end{bmatrix}^H \mathbf{J} \begin{bmatrix} \boldsymbol{\Phi}_u \\ \boldsymbol{\Phi}_F \end{bmatrix} \tag{4.59}$$

with H denoting the Hermitian conjugate transpose and $\mathbf{J}$ a matrix defined as

$$\mathbf{J} = \begin{bmatrix} \mathbf{0} & \mathbf{I} \\ -\mathbf{I} & \mathbf{0} \end{bmatrix}. \tag{4.60}$$

$\mathbf{Q}$ in eq. (4.58) denotes the modal amplitude. In the wave context it is convenient to express forces and displacements in terms of wavemodes and amplitudes. This reduces the problem to a relatively small number of unknowns, while expressing them in terms of scalars.

The wavemodes are normalized as

$$\boldsymbol{\phi}_j = \frac{\boldsymbol{\phi}_j^*}{\sqrt{P_{jj}^{\Phi}}} \tag{4.61}$$

with $\sqrt{P_{jj}^{\Phi}}$ the diagonal term of the power flow matrix and $\boldsymbol{\phi}_j^*$ the unnormalized wavemode. It is noted that $\mathbf{P}^{\boldsymbol{\Phi}}$ is diagonal when only propagating wavemodes are retained.

4.3.6 Calculation of the diffusion matrix

For the sake of brevity, a system of two propagating substructures Ω_1, Ω_2 coupled with the element Ω_c are considered (Fig. 4.6). The equilibrium of the coupling element of Eq. (4.46) is rewritten

$$\begin{bmatrix} \mathbf{D}_{11} & \mathbf{D}_{12} & \mathbf{D}_{1I} \\ \mathbf{D}_{21} & \mathbf{D}_{22} & \mathbf{D}_{2I} \\ \mathbf{D}_{I1} & \mathbf{D}_{I2} & \mathbf{D}_{II} \end{bmatrix} \begin{Bmatrix} \mathbf{u}_1^{(c)} \\ \mathbf{u}_2^{(c)} \\ \mathbf{0} \end{Bmatrix} = \begin{Bmatrix} \mathbf{F}_1^{(c)} \\ \mathbf{F}_2^{(c)} \\ \mathbf{0} \end{Bmatrix} \tag{4.62}$$

with subscripts 1, 2 denoting the quantities referring to interfacing nodes and I the internal ones. As no external force is acted on the internal nodes, those can be eliminated through Guyan reduction (Eq. (79))

$$\begin{bmatrix} \mathbf{D}^*_{11} & \mathbf{D}^*_{12} \\ \mathbf{D}^*_{21} & \mathbf{D}^*_{22} \end{bmatrix} \begin{Bmatrix} \mathbf{u}^{(c)}_1 \\ \mathbf{u}^{(c)}_2 \end{Bmatrix} = \begin{Bmatrix} \mathbf{F}^{(c)}_1 \\ \mathbf{F}^{(c)}_2 \end{Bmatrix}. \tag{4.63}$$

The displacements $\mathbf{u}^{(c)}_i$ and forces $\mathbf{F}^{(c)}_i$ of Ω_c are related to those of Ω_1, Ω_2 through equations (4.43), (4.50), thus writing

$$\mathbf{u}^{(c)}_i = \tilde{\mathbf{R}}_i \mathbf{u}^{(i)}_i \tag{4.64a}$$

$$\mathbf{F}^{(c)}_i = -\tilde{\mathbf{R}}_i \mathbf{F}^{(i)}_i \tag{4.64b}$$

where $\tilde{\mathbf{R}}_i$ is the coordinate transform matrix projecting the Dof of Ω_i on Ω_c. In the present case those are unit diagonal except for the terms $\hat{u}^{(c)}_1 = -\hat{u}^{(2)}_1$, $\hat{\beta}^{(c)}_1 = -\hat{\beta}^{(2)}_1$.

Following the wave decomposition for forces and displacements (Eq. (4.52)) and the subsequent calculation of wavemodes through Eq. (4.56),

$$\mathbf{u}^{(c)}_i = \begin{bmatrix} \tilde{\boldsymbol{\Phi}}^+_{u(i)} & \tilde{\boldsymbol{\Phi}}^-_{u(i)} \end{bmatrix} \begin{Bmatrix} \mathbf{Q}^+_{(i)} \\ \mathbf{Q}^-_{(i)} \end{Bmatrix} \tag{4.65}$$

$$\mathbf{F}^{(c)}_i = \begin{bmatrix} \tilde{\boldsymbol{\Phi}}^+_{F(i)} & \tilde{\boldsymbol{\Phi}}^-_{F(i)} \end{bmatrix} \begin{Bmatrix} \mathbf{Q}^+_{(i)} \\ \mathbf{Q}^-_{(i)} \end{Bmatrix} \tag{4.66}$$

for each of the propagating substructures Ω_1, Ω_2. This allows rewriting the equilibrium of Ω_c (Eq. (4.63)) as

$$\mathbf{D}^* \left(\begin{bmatrix} \tilde{\boldsymbol{\Phi}}^+_{u_{(1)}} & \mathbf{0} & \tilde{\boldsymbol{\Phi}}^-_{u_{(1)}} & \mathbf{0} \\ \mathbf{0} & \tilde{\boldsymbol{\Phi}}^+_{u_{(2)}} & \mathbf{0} & \tilde{\boldsymbol{\Phi}}^-_{u_{(2)}} \end{bmatrix} - \right.$$

$$\left. - \begin{bmatrix} \tilde{\boldsymbol{\Phi}}^+_{F_{(1)}} & \mathbf{0} & \tilde{\boldsymbol{\Phi}}^-_{F_{(1)}} & \mathbf{0} \\ \mathbf{0} & \tilde{\boldsymbol{\Phi}}^+_{F_{(2)}} & \mathbf{0} & \tilde{\boldsymbol{\Phi}}^-_{F_{(2)}} \end{bmatrix} \right) \begin{Bmatrix} Q^+_{(1)} \\ Q^+_{(2)} \\ Q^-_{(1)} \\ Q^-_{(2)} \end{Bmatrix} = \mathbf{0} \tag{4.67}$$

where $\tilde{\mathbf{\Phi}}_{(i)} = \tilde{\mathbf{R}}_{ci}\mathbf{\Phi}_{(i)}$ is the wavemode produced by the substructures Ω_1, Ω_2, projected upon the coordinate system of Ω_c. Noting the definition of the scatter matrix

$$\begin{Bmatrix} \mathbf{Q}^-_{(1)} \\ \mathbf{Q}^-_{(2)} \end{Bmatrix} = \mathbb{C} \begin{Bmatrix} \mathbf{Q}^+_{(1)} \\ \mathbf{Q}^+_{(2)} \end{Bmatrix}, \tag{4.68}$$

one can calculate $\mathbb{C}$ as

$$\mathbb{C} = \left(\mathbf{D}^* \begin{bmatrix} \tilde{\mathbf{\Phi}}^+_{u(1)} & \mathbf{0} \\ \mathbf{0} & \tilde{\mathbf{\Phi}}^+_{u(2)} \end{bmatrix} - \begin{bmatrix} \tilde{\mathbf{\Phi}}^+_{F(1)} & \mathbf{0} \\ \mathbf{0} & \tilde{\mathbf{\Phi}}^+_{F(2)} \end{bmatrix} \right)^{-1} \left(\mathbf{D}^* \begin{bmatrix} \tilde{\mathbf{\Phi}}^-_{u(1)} & \mathbf{0} \\ \mathbf{0} & \tilde{\mathbf{\Phi}}^-_{u(2)} \end{bmatrix} - \begin{bmatrix} \tilde{\mathbf{\Phi}}^-_{F(1)} & \mathbf{0} \\ \mathbf{0} & \tilde{\mathbf{\Phi}}^-_{F(2)} \end{bmatrix} \right). \tag{4.69}$$

The amplitudes are correlated in the least square sense, i.e. an incident wavemode's response is decomposed into a superposition of wavemodes and amplitudes.

The matrix inversion in the equation above (Eq. (4.69)) cannot necessarily be achieved algebraically , as the matrices $\mathbf{\Phi}$ might not be square in practice, as further discussed in Section 4.6. In this work, Gauss elimination has been used, as incorporated in MATLAB. The scatter or diffusion matrix contains elements that are generally complex. The Reflection-Transmission Coefficients are taken as the absolute thereof.

4.4 Wave propagation

The properties of propagating waves are first discussed. A plate of width $B = 15mm$ and thickness $h = 2mm$ of homogeneous solid with $E = 70GPa$ and $\nu = 0.33$ is examined for a frequency band of $0 - 400kHz$.

The wave eigenvalue problem (Eq. (4.56)) is solved for discrete values of the frequency band, with a step of 1 kHz. The resulting waves are characterized by their wavenumber and wavemode vector. The wavenumber is calculated by solving for k and is generally complex, with the real part referring to the wavelength and the imaginary to the attenuation. Propagating waves are characterized by a prevalent real and a diminishing imaginary part and can be filtered such that $|\Re\{k\}|/|\Im\{k\}| > c$, with c a positive constant selected to be around 10. It is advantageous for the ease of distinguishing propagating modes, to allow a small positive damping constant η in Eq. (4.55), such that $\mathbf{D} = (1+\mathrm{i}\eta)\mathbf{K}+\omega^2\mathbf{M}$. For propagating modes, the real and the imaginary part signs are always opposite, as the wave needs to lose energy towards the direction it travels. The wavemodes are further classified regarding the sign of $\Re\{k\}$, with positive denoting positive travelling waves and conversely for negative ones.

The inter-frequency classification of wavemodes is further required, as waves appear in different positions in the eigenvector matrix $\mathbf{\Phi}$. The orthogonality criterion of modes is employed, such that

$$\boldsymbol{\phi}_i^H(\omega)\mathbf{J}\boldsymbol{\phi}_j(\omega+\Delta\omega) \to \delta_{ij}, \quad \text{when} \quad \Delta\omega \to 0, \tag{4.70}$$

with $\delta_{ij} = 1$ for $i = j$, else 0. As the frequency increases, more modes become propagating. Figure 4.4a-4.4b depicts the resulting phase and group velocities calculated through the WFE. The Lamb characteristic equation results are noted with $(*)$.

$$\frac{\tan\beta h}{\tan\alpha h} = \left[\frac{-4\alpha\beta k^2}{(k^2-\beta^2)}\right]^{\pm 1} \tag{4.71}$$

with α, β denoting

$$\alpha^2 = \frac{\omega^2}{c_L^2} - k^2, \quad \beta^2 = \frac{\omega^2}{c_S^2} - k^2 \tag{4.72}$$

and c_L the longitudinal, c_S the shear wave velocities defined as

$$c_L^2 = \frac{E}{\rho}, \quad c_S^2 = \frac{\mu}{\rho} \tag{4.73}$$

with E Young's modulus, μ the shear modulus and ρ the material density. Solution of Eq. (4.71) provided the results noted with $(*)$ in Figure 4.4b-4.4a. The thickness h of Eq. 4.71 has been set equal to the plate's width to provide the SH0 and S0 modes, and equal to the plate's thickness for the A0. This implies a higher influence of the in-plane stiffness and inertial terms for S0. Furthermore, the analytical dispersion relation for

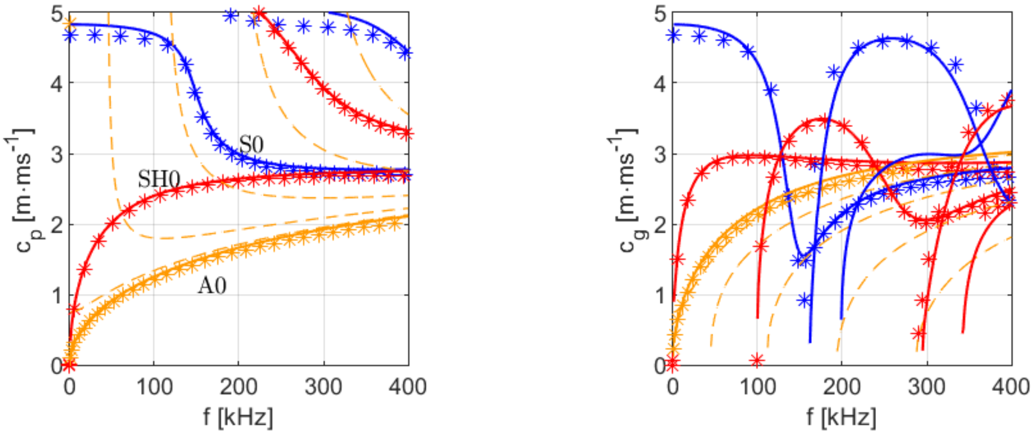

(a) Phase velocity.

(b) Group velocity.

Figure 4.4: Wave velocities: phase and group. Continuous lines denote Lamb modes, with (∗) marking Lamb characteristic equation solutions. Dashed line (- -) denotes cross-sectional modes.

Lamb waves is formulated under the assumption of an infinite plate, and usage in the finite case presented here is approximate, though indicative of the wave behaviour.

Several Lamb modes are found, alongside non-Lamb or cross-sectional modes. In the case of finite width, the shear horizontal (SHn) waves coincide with antisymmetric in-plane waves. The shell elements used produce only the fundamental A0 Lamb waves, as higher order modes require displacement distribution of higher order polynomials along the thickness, which is limited by the planar section assumption introduced with plate theories. The excitation of higher order modes is dependent upon the product of frequency by thickness, which sets the threshold to higher frequencies for thinner plates; hence in the band used in this work, no A1 or higher appear.

Cross-sectional modes appear for the out-of-plane waves. They are denoted A0,n, with n the number of nodes along the section; A0,1 is the torsional mode for example. A0,2 is shown in Fig. 4.5f. A0,1 or the torsional mode, appears from 0 kHz.

Wave dispersion occurs when c_p (Fig. 4.4a) is different from c_g (Fig. 4.4b). The wave envelope and the individual wave —e.g. a wave crest—travel at different velocities. An initial wave packet cannot retain its form and extends, spilling the carried energy. Waves are

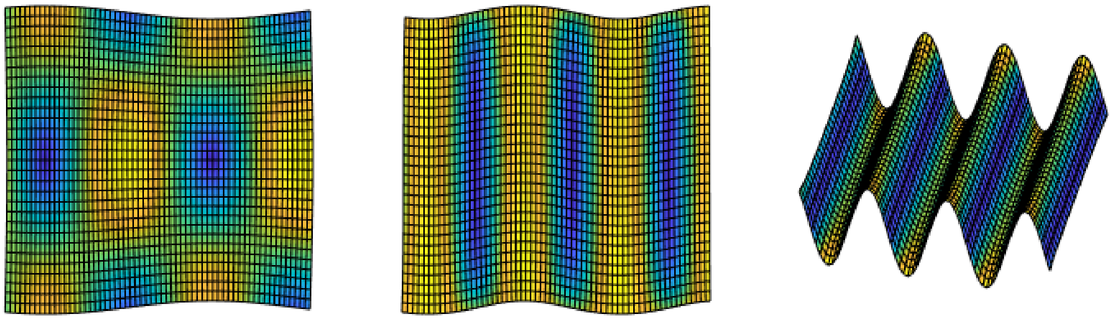

(a) S0 (b) SH0 (c) A0

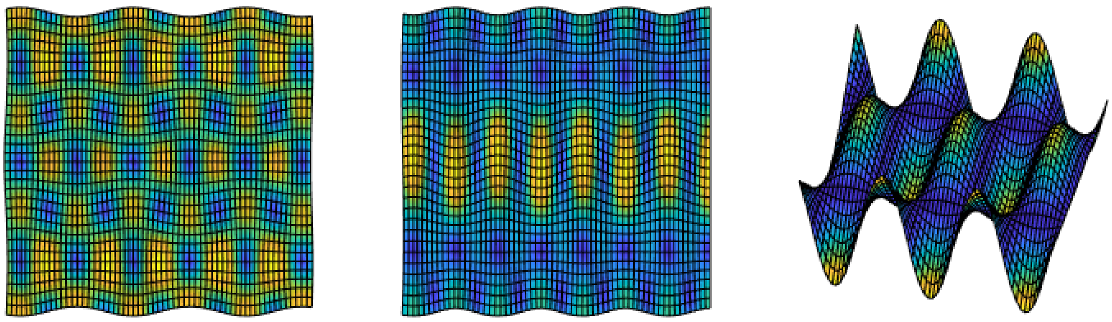

(d) S1 (e) SH1 (f) A0,2

Figure 4.5: Wave shapes.

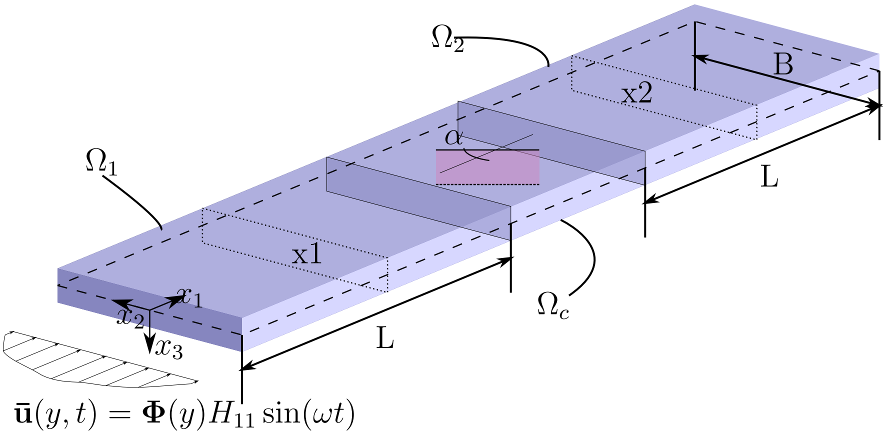

Figure 4.6: Geometry of the explicit model. x1, x2 denote the probing sections for the scattered waves, α the crack angle.

4.5 Explicit FE for wave scattering

An explicit FE model is constructed for cross-referencing the results of wave scattering. A sketch of the model is shown in Fig. 4.6. The width is $B = 15mm$ and thickness $h = 2mm$. The material is homogeneous with $E = 70GPa$ and $\nu = 0.33$; damping is not considered. Single-mode excitation is used to allow calculation of mode conversion without interference. The fundamental Lamb modes S0, SH0 and A0 are excited. A parametric model is constructed in ABAQUS using Python. Shell elements of selective reduced integration (S4R) have been used. The mesh is adapted on frequency, with an element size dependent on the wavelength, to minimize computational costs, while preserving accuracy. The coupling element uses finer elements to accommodate for the crack behaviour, and Lagrange constraints are used to tie the nonconforming mesh to the propagating substructures. Time-history data are collected at the middle of each of the propagating substructures and are denoted x1, x2 (Fig. 4.6). The post-processing is done with mode separation and signal processing techniques.

4.5.1 Mode excitation

Each wavemode is generated by applying the respective displacements at the fore boundary of the beam, as they result from the WFE analysis. The input amplitude is a sine function, multiplied by an 11-cycle Hann window. This generates a monochromatic signal and remains as a distinguishable pattern throughout the analysis time, provided the waves are not highly dispersive, i.e. their phase and group velocities remain loosely equal.

$$\bar{\mathbf{u}} = H(\omega)\sin(\omega t)\boldsymbol{\phi}_u a \tag{4.74}$$

with $\bar{\mathbf{u}}$ the prescribed displacement, $H(\omega)$ the Hann window, $\boldsymbol{\phi}_u$ the displacement part of $\boldsymbol{\Phi}$ as per Eq. (4.57), a the amplitude.

4.5.2 Adaptive meshing

A number of different FE models need be formulated and run, one for each of the frequencies and the wavemodes analysed. As the wavelength is generally different across frequency and mode, different mesh size is required for each model, in order to maintain a sufficient fineness of 15 elements per wavelength. Also, the required beam length to avoid spurious reflections from the boundaries, is dependent on the signal duration and wave velocities—or, equivalently, the frequency and wavelength. A length of about $1.75L_{Signal}$ is opted for, to avoid interference from scattered waves. $L_{Signal} = 11\lambda$, with λ the wavelength. For the highly dispersive regime of membrane or longitudinal waves, this is increased to $3L_{Signal}$. Wave conversions should be taken into account: testing for example S0 mode, will generate SH0 waves when the angle is oblique, thus requiring more length.

4.5.3 Mode separation

The displacements are analysed as a sum of wavemodes with an amplitude factor each. This invokes the assumption that the displacements can sufficiently be described by a number of discrete wavemodes

$$\mathbf{u} = \boldsymbol{\Phi}_u \mathbf{a}(t) \tag{4.75}$$

with $\mathbf{a}(t)$ the time-series of modal amplitudes. The amplitudes are found through least-squares fitting of the wavemodes onto the displacement vector.

4.5.4 Post-processing

The scattering coefficients are calculated from the time-transient data. The incident and the scattered amplitudes are extracted and measured. The usage of a distinctive incident wave packet allows tracking, provided no dispersion occurs, as in Fig. 4.7a. For frequencies of 100 kHz or less, the group and phase velocities of S0 waves are roughly equal (Fig. 4.4a-4.4b), preserving the wave packets. At higher frequencies (Fig. 4.7b) the two velocities are drastically different, causing leakage of energy outside the wave packet.

$$c_{ij} = \frac{a_i}{a_j} \tag{4.76}$$

with a_i the scattered and a_j the incident amplitude. Those are the instantaneous amplitudes. In practice it is not feasible to excite single-frequency single-mode waves of instantaneous amplitudes, without causing leaks into other waves. Approaches such as sinusoidal waves over a Hann window are the common paradigm.

The wave envelopes in Fig. 4.7 are calculated using the Hilbert transform. Hilbert transform shifts a signal f by $\pi/2$, creating $\hat{f}$, so that the signal envelope can be calculated as $|f + \mathrm{i}\hat{f}|$ (Ng, 2014). The peak of the $j-$th wave at the location x_i is found at time $t_{ij} = \sum \|\mathrm{x}_i\| / c_g^j$ with $\|\mathrm{x}_i\|$ the total distance travelled by a wave to reach location x_i and c_g^j the respective group velocity. When wave conversion occurs, the group velocity changes after scattering. Dispersion causes amplitude loss, undermining the accuracy of the approach.

The Continuous wavelet transform (CWT) is used for time-frequency analysis of the signal (Ng, 2014). The results of CWT on the highly dispersive signal of Fig. 4.7b are shown in Fig. 4.8. The vertical axis of the plots refers to the present frequencies, while the horizontal axis represents the time. An immediate connection of the peaks between the time domain and the wavelet can be made. The distribution among frequencies is centred at 150 kHz, but spanning from 100-200 kHz. This shows extensive leakage of the wave packet; it is noted that, for non-dispersive waves, the distribution is much narrower and centred at the excited frequency.

Other signal processing techniques are available. Short-time Fourier transform (STFT) performs Fourier transform on a finite window, allowing for time-frequency analysis. The FFT frequencies are connected to the sampled time and time discretization of the transient signal. This is a problem CWT does not have, and is generally a preferable alternative (Ng, 2014). Matching pursuit algorithms are capable of identifying specific features in a signal, such as peaks and other patterns (Li et al., 2006). An alternative of a shifted Hann window that adapts to wave dispersion would be a possible alternative to the proposed methods.

The effective amplitude takes into account dispersed waves by summing the coefficients across the frequencies as

$$a_i = \sqrt{\sum_j |\hat{a}(t_i, \omega_j)|^2}. \tag{4.77}$$

The peaks of the incident and scattered waves are selected by the criterion of distance over velocity.

4.5.5 Discussion

The two cases depicted in Figure 4.7 refer to one non-dispersive (Fig. 4.7a) and one dispersive case (Fig. 4.7b).

For the former, the envelope shape appears to be preserved, and the amplitude is affected by scattering. The incident S0 peak appears to pass from x1 at less than 0.2 ms, and reflects back immediately after 0.4 ms. A secondary peak from the converted SH0 wave appears later, as its group velocity is smaller. Further peaks at 0.7 ms appear due to reflections from the boundaries of the model.

For the latter, dispersive case, envelopes spill as the waves travel. Peaks are less prevalent, and interference from the boundary becomes significant.

Figure 4.8 depicts the CWT of the dispersive analysis of Fig. 4.7b. Peaks appear for the incident and scattered waves, at the same times as the respective time-transient imaging. From the frequency analysis, the wave appears to have components in neighbouring frequencies. This is more pronounced than the non-dispersive case, where the frequency components are more concentrated around the excitation frequency.

4.6 Results and discussion

The model with the properties prescribed in Sec. 4.5 is resolved with the XWFE. A mesh of 31 elements width-wise is constructed. This has shown to exhibit adequate convergence of the dynamic properties of the coupling element, while preserving sufficient resolution for the representation of the behaviour of the crack. Preliminary analysis with enrichment radius R_{enr} of about $1.5h_{elem}$ and without any crack-tip enrichment has shown that, in dynamic applications, crack tip enrichment has minimal influence. The length of the coupling element was initially selected equal to the width. The crack size is a $= B/2$ and is located at the centre of the coupling element.

Results are displayed in Fig. 4.10 for incident S0 waves and Fig. 4.11 for incident A0. The reflection and transmission coefficients are marked in blue and red respectively. The energy sum is also displayed with the dashed line. The dotted markers depict the time-transient results of Section 4.5. The scattering coefficients are in normalized units ranging from 0 to 1. For each case of S0, A0, conversions of interest are also shown.

4.6.1 Wave basis

The stability of the XWFE depends on the wave basis selected for the analysis. The usage of only propagating modes is generally suggested (Mencik and Ichchou, 2005). The consistency of the analysis depends on mode sorting across the frequencies ω_i.

The inclusion of non-propagating modes introduces errors in the numerical results. Evanescent modes are generally non-orthogonal. This introduces poor conditioning in the operation of the matrix inversion of Eq. (4.67). This is the case with SH1 close to 100 kHz, when it has a small wavenumber, where it interferes with SH0.

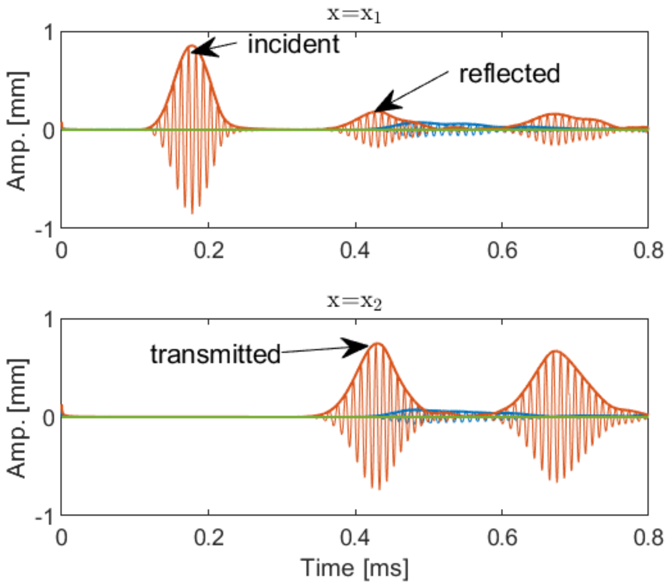

(a) 100 kHz

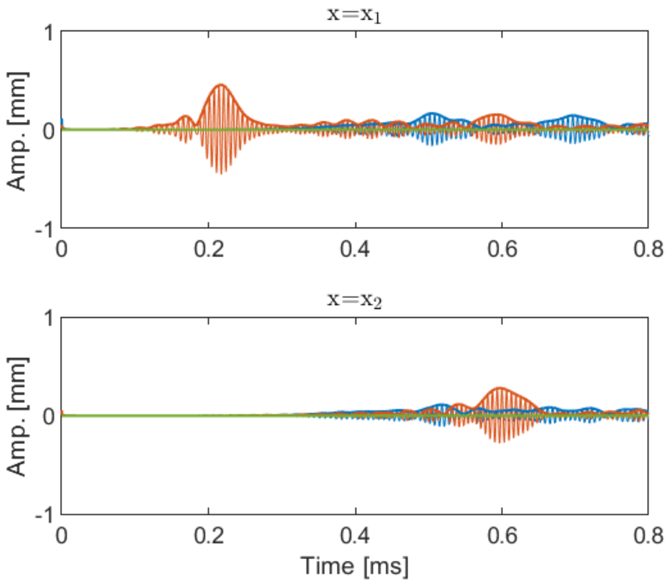

(b) 150 kHz

Figure 4.7: Modal amplitude time history for single-mode S0 excitation. Converted SH0 in blue. Envelope constructed with Hilbert transform.

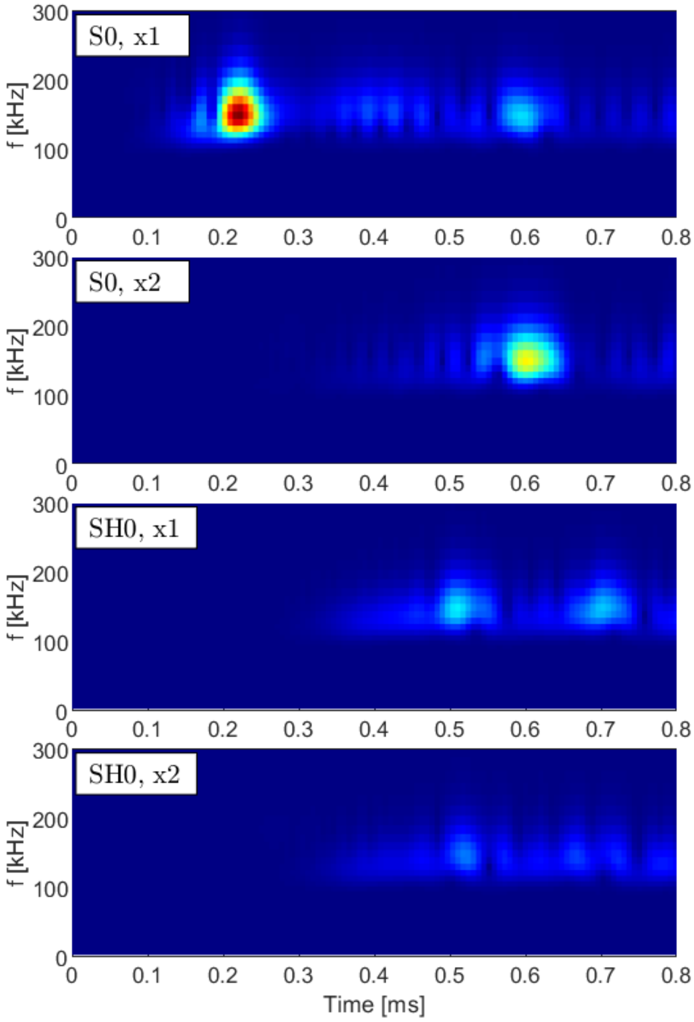

Figure 4.8: CWT for an incident S0 mode at 150 kHz.

4.6.2 Energy conservation

A corollary of the definition of the scatter matrix is its subsequent energy conservation. The matrix represents the amplitudes of the scattered wave amplitudes a_i due to an incident wave j of unitary amplitude. The power bearing has been demonstrated to be proportional to the square of the amplitude (Eq. (4.58)). The waves have been normalized with respect to power, meaning that different waves of the same amplitude bear the same energy. The sum of the energies for each wave is $e_j = \sum_i c_{ij}^2 = 1$. Figures 4.11, 4.10 display the energy balance result in the dashed line. For the standing wave case of S0, the energy is not preserved, which is a result of ill conditioning of the dynamic stiffness matrix. A0 wave in oblique angles (Fig. 4.11b) exhibits significant conversion to A0,3 which needs to be accounted for even in evanescent state, hence the energy deficit.

4.6.3 Validation with explicit FE

The validity of the results are checked. Figure 4.10 displays the comparison of the explicit and XWFE data for different crack angles. Agreement is exhibited for frequencies under 100 kHz where S0 is non-dispersive. In the band 100-150 kHz, several waves become propagating, interfering with the accuracy of XWFE.

Figure 4.11 displays the respective comparison of A0 scattering. Due to their non-dispersive nature, A0 waves compare better across the frequency range.

4.6.4 Standing wave for parallel crack

The standing wave behaviour predicted by XWFE for S0 at 100 kHz (Fig. 4.10a) at a 0°angle is affirmed with the explicit FE. XWFE is, however, prone to overestimating reflections. This is attributed to the fact that for the given configuration, the wave has a standing effect inside the coupling element, or, the frequency at which this occurs is an eigenfrequency of the coupling element.

To assert the physical meaning of the above, additional analyses were run for different dimensions of the coupling element. Besides the default $L = B = 15mm$ initially used, a $L = 2B$ is also tried; the results displayed have been calculated with this configuration.

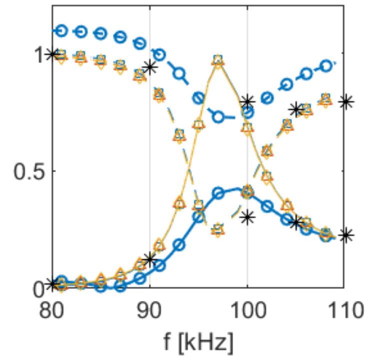

Figure 4.9: XWFE: Reflection and transmission of S0 for a 0°crack, against damping coefficient of the stiffness matrix. $\eta = 10^{-1}$ (◯), 10^{-2}, (□), 10^{-3} (△), 10^{-4} (◇); transient ($*$).

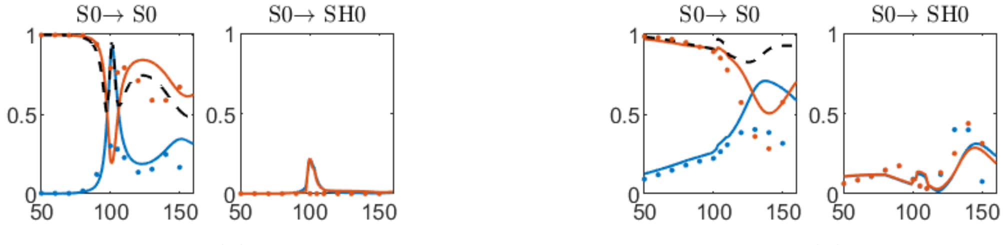

(a) $\alpha = 0°$

(b) $\alpha = 45°$

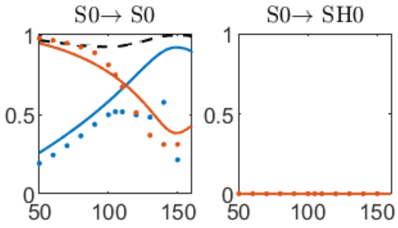

(c) $\alpha = 90°$

Figure 4.10: XWFE: Scattering coefficient vs. frequency [kHz] for a centre crack of different angles for an incident S0 wave. Dots (·) denote results of explicit FE. Dashed line (- -) denotes the energy sum.

Even with the change of geometry, the resonating eigenfrequency is preserved, save for small shifts of the order of 1 kHz.

The introduction of damping in the dynamic stiffness matrix of the coupling element alleviates the reflection, but produces erroneous scattering coefficients for other frequencies, e.g. transmission larger than 1 for less than 100 kHz. Figure 4.9 displays the effect of different attenuation ratios η. Small η has barely any effect; the regime between $10^{-1} - 10^{-2}$ has the maximum impact.

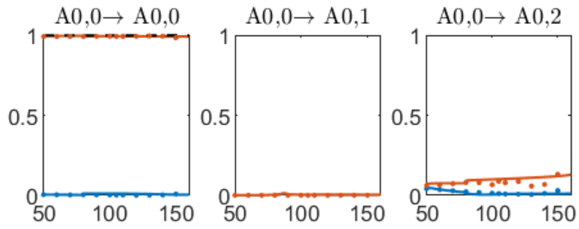

(a) $\alpha = 0°$

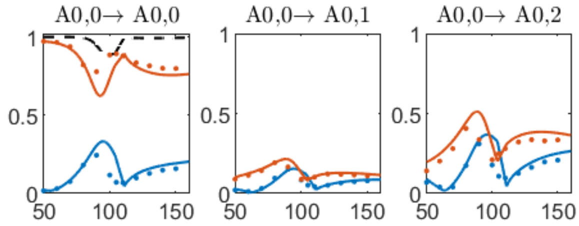

(b) $\alpha = 45°$

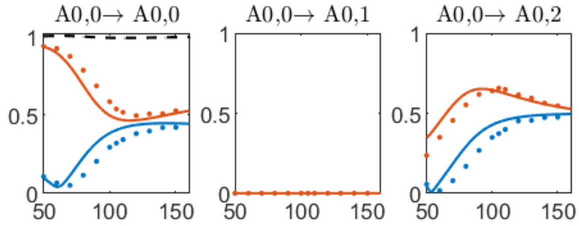

(c) $\alpha = 90°$

Figure 4.11: XWFE: Scattering coefficient vs. frequency [kHz] for a centre crack of different angles for an incident A0 wave. Dots $(\cdot)$ denote results of explicit FE. Dashed line (- -) denotes the energy sum.

4.6.5 Sensitivity of scattering coefficients to crack parameters

The suitability of scattering coefficients as crack identification feature is connected to their sensitivity with respect to the crack's parameters, e.g. angle, size and location. The scattering behaviour of the crack is dependent on the incident wave length and shape, i.e. wavenumber and wavemode, and is examined with respect to the incident wavemode and its frequency. The fundamental Lamb modes S0, A0 are selected for the examination of their scattering behaviour, as the most common ones excited in common practice and studied in literature. Inter-modal conversions are investigated with respect to the incident mode; as the in and out-of-plane behaviour is decoupled, the scattering behaviour follows this pattern, with S0 only converting to SH0 and A0 to A0,n.

Frequency

Wave interaction with cracks is found to increase the higher the frequency. Wavelength becomes shorter as frequency increases, via the dispersion relation. Specific features of waves aid the interaction with cracks. For example A0,0 exhibits significant conversion to A0,2, due to the compatibility of the mode shapes with the projection of the crack. Notably, a smaller crack would predominantly excite a higher A0,n, for which higher frequency testing would be required.

Angle

The crack angle is seen to have major effect on the scattering coefficients. S0 wave reflection is found to increase with vertical cracks. Oblique cracks also cause conversion of S0 waves into SH modes.

Parallel cracks are shown to be detectable with S0 waves, through the entrapment of standing waves, when the wavelength is related to the crack size. This mechanism has been investigated in Munian et al. (2018) with the horizontal antisymmetric mode (referred here as SH0) and time-domain spectral elements.

Scattering amplitudes are symmetric with respect to the crack angle, i.e. yield the same value for $\pm\alpha$. In order to resolve the angle, the phase of the scattered wave can be taken

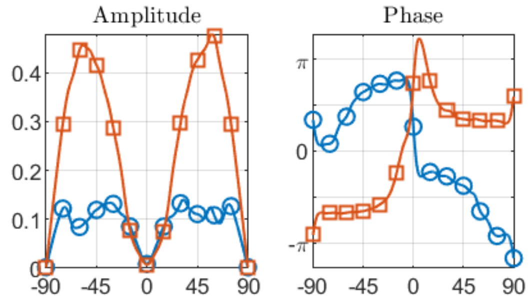

Figure 4.12: XWFE: Reflection coefficient and phase change against crack angle for S0→SH0 conversion. f=100 kHz (◯), 200 kHz (□).

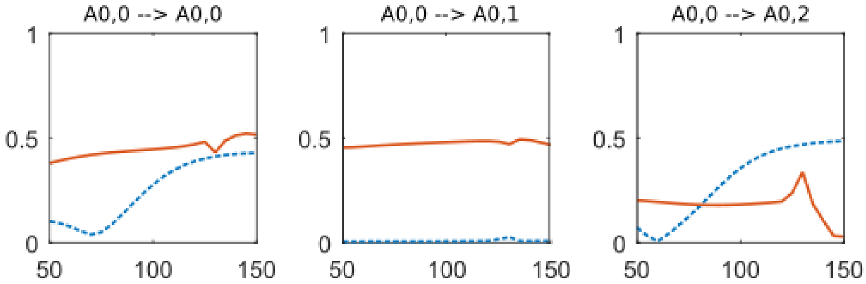

Figure 4.13: XWFE: Reflection coefficient of an incident A0 wave against frequency [kHz]. Edge crack: continuous line (—); centre crack: dashed line (- -).

into account. This is found as $\phi = \arctan(\Re(\mathbb{C})/\Im(\mathbb{C}))$. Figure 4.12.

Position

The crack position affects significantly the conversion of A0,0. An edge crack favours the generation of A0,1 instead of A0,2 for a centre crack 4.13. Symmetry is evident in this case and the phase can also resolve the information. The length-wise position of the crack is not resolved with the XWFE in its current form. A time-of-flight approach is, however, straightforward to implement.

Size

The sensitivity of crack size is connected more to the wave frequency and the higher order waves generated thereupon. The identification of damage of smaller size requires analysis in higher frequencies. Higher order modes that have richer features interact with smaller size damage.

4.6.6 Considerations on experimental setup for crack identification

The generation and measurement of pure waves of single frequency and mode very difficult in practice, especially in structures of finite cross section such as beams (Serey et al., 2019). Specific vibration generation devices exist, and most common are PZTs (Serey et al., 2019), laser pulses Shen and Cesnik (2016) and ultrasonic transducers. Wave generation depends on both the actuated frequency and the favourable excitation of wave shapes. For example, PZTs are mounted on the surface of the plate; mounting them on a single surface creates mixed Sn and An modes. Mounting PZTs on both sides and pulsating in or out of phase favours Sn and An respectively. The excitation of single Lamb modes, along with the modal separation of the scattered signal are addressed in Serey et al. (2019), with multiple piezoelectric transducers along the section of the beam.

Laser vibrometry is advantageous as it is non invasive and measurements at multiple locations can be acquired, at the cost of multiple repeat measurements. Multi-dimensional CWT and FFT can extract the wave-time-frequency domain, with the incident and scattered amplitudes of waves yielded straightforwardly.

The usage of scattering coefficients as a feature for crack identification is shown to be sensitive to the dispersive nature of waves and adverse complexities of wavemode separation and identification. The measurement of displacements at individual points is more straightforward. An alternative approach is the calculation of the time-domain problem and the displacement response (e.g. Mallouli et al. (2018); Malik et al. (2020)) and extension to the present method is straightforward.

The present model, along with the majority of the literature, operates on the assumption of linear behaviour, with non-kissing cracks. This is a valid assumption when cracks have a relatively large width, and excitations are of small amplitude. Narrow cracks are governed by nonlinear mechanisms, such as friction and heat dissipation Mendioroz et al. (2017), along with crack kissing. Higher harmonic generation has been demonstrated, and is even implemented as means of crack identification (Yang et al., 2018). A WFE formulation to account for higher harmonics has been proposed (Chronopoulos, 2018).

4.7 Conclusions

A computational method for calculating wave scattering, combining wave methods with XFEM is proposed. A numerical experiment with explicit FE has been conducted and a method for the calculating scattering coefficients through time-transient data has been presented, with discussion pertinent to the design of relevant experiments and acquisition of measurements.

Scattering coefficients have been calculated through a hybrid XFEM/WFE approach, extending the capabilities of known hybrid FE/WFE schemes (Mencik and Ichchou, 2005; Malik et al., 2020; Mitrou et al., 2017). The measurement of scattering coefficients from time-transient data is sensitive to errors and prone to additional complexities, due to the dispersive behaviour that propagating waves exhibit. An alternative of transient analysis with wave-based methods exists (e.g. Malik et al. (2020)) and allows crack identification through the feature of displacement time-history; implementation of XFEM/WFE in transient analysis is straightforward.

The introduction of XFEM allows for the generation of uniform meshes along the coupling element and the propagating substructures, eliminating the necessity of mortar method mesh tying (Mencik and Ichchou, 2005) when arbitrary damage geometries need to be meshed. XFEM/WFE is readily parametrizable and can resolve arbitrary cracks in plates, compared to hybrid FE/WFE and FE/SAFE methods. The usage of WFE allows ready integration with available finite elements, commercial or custom.

The accuracy of XFEM/WFE depends on the wave basis used. This is shown to be variable along the frequencies, with more waves becoming propagating as the frequency increases. Higher frequencies can raise multiple wavemodes for which identification and sorting becomes complicated. Proper wave sorting is deemed critical for XFEM/WFE and FE/WFE in order to profit from computational savings of the method and better resolution in higher frequencies.

Appendix

Guyan reduction refers to the elimination of dependent or *Slave* nodes of a system

$$\begin{bmatrix} \mathbf{D}_{MM} & \mathbf{D}_{MS} \\ \mathbf{D}_{SM} & \mathbf{D}_{SS} \end{bmatrix} \begin{Bmatrix} \mathbf{u}_M \\ \mathbf{u}_S \end{Bmatrix} = \begin{Bmatrix} \mathbf{F}_M \\ \mathbf{0} \end{Bmatrix}. \tag{78}$$

As the slave nodes do not receive any external forces, it is possible to express them as a function of the $Master$ nodes

$$\mathbf{D}^*_{MM} = \mathbf{D}_{MM} - \mathbf{D}_{MS}\mathbf{D}^{-1}_{SS}\mathbf{D}_{SM}. \tag{79}$$

Bibliography

Agathos, K., Chatzi, E., and Bordas, S. P. Multiple crack detection in 3D using a stable XFEM and global optimization. *Computational Mechanics*, 62(4):835–852, 2018.

Bathe, K.-J. *Finite Element Procedures*. Prentice Hall, 1st edition, 1995. ISBN 0-13-301458-4.

Bayesteh, H. and Mohammadi, S. XFEM fracture analysis of shells: The effect of crack tip enrichments. *Computational Materials Science*, 50(10):2793–2813, 2011.

Bhuiyan, M. Y., Shen, Y., and Giurgiutiu, V. Guided wave based crack detection in the rivet hole using global analytical with local FEM approach. *Materials*, 9(7):602, 2016.

Bordas, S. P., Rabczuk, T., Hung, N.-X., Nguyen, V. P., Natarajan, S., Bog, T., Quan, D. M., and Hiep, N. V. Strain smoothing in FEM and XFEM. *Computers & Structures*, 88(23-24):1419–1443, 2010.

Chatzi, E. N., Hiriyur, B., Waisman, H., and Smyth, A. W. Experimental application and enhancement of the XFEM-GA algorithm for the detection of flaws in structures. *Computers and Structures*, 89(7-8):556–570, 2011.

Chronopoulos, D. Calculation of guided wave interaction with nonlinearities and generation of harmonics in composite structures through a wave finite element method. *Composite Structures*, 186:375–384, 2018.

Dolbow, J. E., Moës, N., and Belytschko, T. Modeling fracture in Mindlin–Reissner plates with the extended finite element method. *International Journal of Solids and Structures*, 37:7161–7183, 2000.

Elguedj, T., Gravouil, A., and Maigre, H. An explicit dynamics extended finite element method. Part 1: Mass lumping for arbitrary enrichment functions. *Computer Methods in Applied Mechanics and Engineering*, 198(30-32):2297–2317, 2009.

Fries, T.-P. A corrected XFEM approximation without problems in blending elements. *International Journal for Numerical Methods in Engineering*, 75(5):503–532, 2008.

Gruttmann, F. and Wagner, W. A stabilized one-point integrated quadrilateral Reissner-Mindlin plate element. *International Journal for Numerical Methods in Engineering*, 61(13):2273–2295, 2004.

Ichchou, M. N., Akrout, S., and Mencik, J.-M. Guided waves group and energy velocities via finite elements. *Journal of Sound and Vibration*, 305(4-5):931–944, 2007.

Ichchou, M. N., Mencik, J.-M., and Zhou, W. Wave finite elements for low and mid-frequency description of coupled structures with damage. *Computer Methods in Applied Mechanics and Engineering*, 198(15-16):1311–1326, 2009.

Jung, J., Jeong, C., and Taciroglu, E. Identification of a scatterer embedded in elastic heterogeneous media using dynamic XFEM. *Computer Methods in Applied Mechanics and Engineering*, 259:50–63, 2013.

Jung, J. and Taciroglu, E. Modeling and identification of an arbitrarily shaped scatterer using dynamic XFEM with cubic splines. *Computer Methods in Applied Mechanics and Engineering*, 278:101–118, 2014.

Komijani, M. and Gracie, R. An enriched finite element model for wave propagation in fractured media. *Finite Elements in Analysis and Design*, 125:14–23, 2017.

Li, F., Su, Z., Ye, L., and Meng, G. A correlation filtering-based matching pursuit (CF-MP) for damage identification using Lamb waves. *Smart Materials and Structures*, 15(6):1585–1594, 2006.

Liu, Z. L., Menouillard, T., and Belytschko, T. An XFEM/Spectral element method for dynamic crack propagation. *International Journal of Fracture*, 169(2):183–198, 2011.

Liu, M., Schmicker, D., Su, Z., and Cui, F. A Benchmark Study of Modeling Lamb Wave Scattering by A Through Hole Using A Time-domain Spectral Element Method. *Journal of Nondestructive Evaluation, Diagnostics and Prognostics of Engineering Systems*, 2017.

Livani, M., Khaji, N., and Zakian, P. Identification of multiple flaws in 2D structures using dynamic extended spectral finite element method with a universally enhanced meta-heuristic optimizer. *Structural and Multidisciplinary Optimization*, 57(2):605–623, 2018.

Ma, C., Yu, T., Van Lich, L., and Quoc Bui, T. An effective computational approach based on XFEM and a novel three-step detection algorithm for multiple complex flaw clusters. *Computers and Structures*, 193:207–225, 2017.

Malik, M. K., Chronopoulos, D., and Tanner, G. Transient ultrasonic guided wave simulation in layered composite structures using a hybrid wave and finite element scheme. *Composite Structures*, 246:112376, 2020.

Mallouli, M., Ben Souf, M., Bareille, O. A., Ichchou, M., Fakhfakh, T., and Haddar, M. Transient wave scattering and forced response analysis of damaged composite beams through a hybrid finite element-wave based method. *Finite Elements in Analysis and Design*, 147:1–9, 2018.

Mencik, J.-M. and Ichchou, M. N. Multi-mode propagation and diffusion in structures through finite elements. *European Journal of Mechanics, A/Solids*, 24(5):877–898, 2005.

Mendioroz, A., Celorrio, R., and Salazar, A. Ultrasound excited thermography: an efficient tool for the characterization of vertical cracks. *Measurement Science and Technology*, 28(11):112001, 2017.

Mitra, M. and Gopalakrishnan, S. Guided wave based structural health monitoring: A review. *Smart Materials and Structures*, 25(5), 2016.

Mitrou, G., Ferguson, N., and Renno, J. Wave transmission through two-dimensional structures by the hybrid FE/WFE approach. *Journal of Sound and Vibration*, 389:484–501, 2017.

Munian, R. K., Mahapatra, D. R., and Gopalakrishnan, S. Lamb wave interaction with composite delamination. *Composite Structures*, 206:484–498, 2018.

Ng, C. T. On the selection of advanced signal processing techniques for guided wave damage identification using a statistical approach. *Engineering Structures*, 67:50–60, 2014.

Nguyen-Xuan, H., Rabczuk, T., Bordas, S., and Debongnie, J. F. A smoothed finite element method for plate analysis. *Computer Methods in Applied Mechanics and Engineering*, 197(13-16):1184–1203, 2008.

Rabinovich, D., Givoli, D., and Vigdergauz, S. XFEM-based crack detection scheme using a genetic algorithm. *International Journal for Numerical Methods in Engineering*, 71(9):1051–1080, 2007.

Rabinovich, D., Givoli, D., and Vigdergauz, S. Crack identification by 'arrival time' using XFEM and a genetic algorithm. *International Journal for Numerical Methods in Engineering*, 77(3):337–359, 2009.

Renno, J. M. and Mace, B. R. Calculation of reflection and transmission coefficients of joints using a hybrid finite element/wave and finite element approach. *Journal of Sound and Vibration*, 332(9):2149–2164, 2013.

Samaratunga, D., Jha, R., and Gopalakrishnan, S. Wave propagation analysis in adhesively bonded composite joints using the wavelet spectral finite element method. *Composite Structures*, 122:271–283, 2015.

Serey, V., Quaegebeur, N., Micheau, P., Masson, P., Castaings, M., and Renier, M. Selective generation of ultrasonic guided waves in a bi-dimensional waveguide. *Structural Health Monitoring*, 18(4):1324–1336, 2019.

Shen, Y. and Cesnik, C. E. Hybrid local FEM/global LISA modeling of damped guided wave propagation in complex composite structures. *Smart Materials and Structures*, 25(9):095021, 2016.

Shen, Y. and Giurgiutiu, V. Combined analytical FEM approach for efficient simulation of Lamb wave damage detection. *Ultrasonics*, 69:116–128, 2016.

Spada, A., Capriotti, M., and Lanza di Scalea, F. Global-Local model for guided wave scattering problems with application to defect characterization in built-up composite structures. *International Journal of Solids and Structures*, 182-183:267–280, 2020.

Sreekanth Kumar, D., Roy Mahapatra, D., and Gopalakrishnan, S. A spectral finite element for wave propagation and structural diagnostic analysis of composite beam with transverse crack. *Finite Elements in Analysis and Design*, 40(13-14):1729–1751, 2004.

Waki, Y., Mace, B. R., and Brennan, M. J. Numerical issues concerning the wave and finite element method for free and forced vibrations of waveguides. *Journal of Sound and Vibration*, 327(1-2):92–108, 2009.

Wang, G. Beam damage uncertainty quantification using guided Lamb wave responses. *Journal of Intelligent Material Systems and Structures*, 29(3):323–334, 2018.

Yang, Y., Ng, C. T., Kotousov, A., Sohn, H., and Lim, H. J. Second harmonic generation at fatigue cracks by low-frequency Lamb waves: Experimental and numerical studies. *Mechanical Systems and Signal Processing*, 99:760–773, 2018.

Żak, A. and Krawczuk, M. A higher order transversely deformable shell-type spectral finite element for dynamic analysis of isotropic structures. *Finite Elements in Analysis and Design*, 142:17–29, 2018.

Zhao, W., Du, C., and Jiang, S. An adaptive multiscale approach for identifying multiple flaws based on XFEM and a discrete artificial fish swarm algorithm. *Computer Methods in Applied Mechanics and Engineering*, 339:341–357, 2018.

Zhong, W. X. and Williams, F. W. On the direct solution of wave propagation for repetitive structures. *Journal of Sound and Vibration*, 181(3):485–501, 1995.

Chapter 5

Improvement of computational aspects of hybrid FE/WFE and XFEM/WFE methods with Neumann series

5.1 Introduction

A class of wave methods has been proposed to construct efficient simulations of high frequency-short wavelength wave propagation problems with the Finite Element (FE) and other Galerkin methods. Those methods are harmonic, i.e. solve problems in the frequency and wave domain, contrary to the direct time-transient models.

A response spectrum is calculated for a requested band of frequencies. Evaluation of the system's response is done on discrete frequencies. The calculation of the response requires repeating operations over those discrete frequencies, that lead to increased computational burden. Those involve solution of linear systems of equations, where the system's dynamic stiffness matrix is inverted multiple times.

To overcome the inflation of computational cost, different approaches have been proposed. Adaptive or Kriging models attempt to identify the variability of the response, investing computational time on more irregular regions, letting smoother ones to be computed through interpolation. The Craig-Bampton method (Fan et al., 2016) transforms a system by eigenvalue decomposition. The system is then represented by a number of significant eigenvalues, which is less than the total Degrees of Freedom (Dof). Consequently, operations are performed on a reduced system that emulates the original one with some fidelity.

The Neumann series expansion is available for the approximation of a perturbed matrix's inverse, based on an initial calculated value. Applications have been investigated as early as (Yamazaki et al., 1988) for stochastic variability of material properties in structures. Lallemand et al. (1999) expand on the applications on this approach, implementing structural parameter identification. Liem et al. (2019); Liem and McDaniel (2019) expand upon the previous works and investigate the series convergence properties.

This work draws from the computational complexities introduced by a class of Wave FE and hybrid approaches, an overview of which is given on Section 5.2. An overview of the derivation, convergence and approximation properties of Neumann series is given in Section 5.3. Focus is placed on the performance of the series approximation, with respect to a direct solution approach, and its particularities are discussed in Section 5.4. Discussion is made on representative results from the case prescribed in Section 5.5.

5.2 Wave and hybrid Wave Finite Elements

Guided wave problems with FEM that involve propagation and scattering can be solved with transfer matrix methods, such as the semi analytical and wave FEM (SAFE,WFE) (Waki et al., 2009). Those methods take a representative cell of the waveguide and form the transfer matrix that connects the boundary (e.g. left and right) state vectors $\mathbf{q} = \{\mathbf{u}^T \mathbf{f}^T\}$ via the transfer matrix. Existence of internal Degrees of freedom (Dof) in the representative cell are eliminated via Guyan reduction(Waki et al., 2009), which requires the calculation of the inverse dynamic stiffness matrix for the internal nodes. An inversion is required for every frequency ω_i the problem in solved in. Waki et al. (2009) propose the possibility of a series expansion to ease computational burden on this process, but do not discuss further.

We present a basic case of Guyan reduction pertinent to WFE applications for wave propagation and scattering. The dynamic stiffness matrix is defined as

$$\mathbf{D} = \mathbf{K} - \omega^2 \mathbf{M}, \tag{5.1}$$

with $\mathbf{K}$ the stiffness matrix, $\mathbf{M}$ the mass matrix and ω the angular frequency.

We consider a waveguide, e.g. a very long plate, where positive waves propagate from left to right, and conversely for negative waves. If $\mathbf{D}$ is the stiffness matrix of a representative cell, it is connected at the left and right boundaries with the rest of the structure. The Dofs are then categorized as

$$\mathbf{D} = \begin{bmatrix} \mathbf{D}_{II} & \mathbf{D}_{IL} & \mathbf{D}_{IR} \\ \mathbf{D}_{LI} & \mathbf{D}_{LL} & \mathbf{D}_{LR} \\ \mathbf{D}_{RI} & \mathbf{D}_{RL} & \mathbf{D}_{RR} \end{bmatrix}. \tag{5.2}$$

where L, R, I corresponds to left, right and internal Dofs.

The boundary Dofs are collocated such that $B \equiv \{L, R\}$. Guyan reduction eliminates the internal Dofs by

$$\mathbf{D}^*_{BB} = \mathbf{D}_{BB} - \mathbf{D}_{BI}{\mathbf{D}_{II}}^{-1}\mathbf{D}_{IB}, \tag{5.3}$$

expressing them as a function of the boundary Dofs.

5.3 Neumann series

We consider an evaluation of the dynamic stiffness matrix at a centre frequency ω_0. Neighbouring frequencies can be written as $\omega = \omega_0 + \Delta\omega$. The expression for the dynamic stiffness matrix becomes

$$\begin{aligned}\mathbf{D} &= \mathbf{K} - (\omega_0 + \Delta\omega)^2\mathbf{M} \\ &= \mathbf{K} - \omega_0^2\mathbf{M} - 2\omega_0\Delta\omega\mathbf{M} - \Delta\omega^2\mathbf{M} \\ &= \mathbf{D}_0 - 2\omega_0\Delta\omega\mathbf{M} - \Delta\omega^2\mathbf{M} \\ &= (\mathbf{I} - 2\omega_0\Delta\omega\mathbf{C} - \Delta\omega^2\mathbf{C})\mathbf{D}_0\end{aligned} \tag{5.4}$$

The inverse of the above is

$$\mathbf{D}^{-1} = \left(\mathbf{I} + \sum_{n=1}^{N} \Delta\omega^n \mathbf{A}_n + \mathbf{O}\{\Delta\omega^{(n+1)}\}\right)\mathbf{D}_0{}^{-1} \tag{5.5}$$

for up to fourth order terms, with $\mathbf{O}$ the order of the remainder. The formulae for the terms $\mathbf{A}_n$ read

$$\mathbf{A}_1 = 2\mathbf{C}\omega_0 \tag{5.6a}$$

$$\mathbf{A}_2 = 4\mathbf{C}^2\omega_0^2 + \mathbf{C} \tag{5.6b}$$

$$\mathbf{A}_3 = 8\mathbf{C}^3\omega_0^3 + 4\mathbf{C}^2\omega_0 \tag{5.6c}$$

$$\mathbf{A}_4 = 16\mathbf{C}^4\omega_0^4 + 15\mathbf{C}^3\omega_0^2 + \mathbf{C}^2 \tag{5.6d}$$

for up to the fourth order term. Production of higher order terms is straightforward albeit arduous, by Taylor expansion of Equation (5.4). Furthermore, this study concluded that computational efficiency is retained for up to 4 terms. $\mathbf{C}$ is defined as

$$\mathbf{C} = \mathbf{M}\mathbf{D}_0{}^{-1}, \tag{5.7}$$

with $\mathbf{D}_0{}^{-1}$ the dynamic stiffness matrix evaluated at ω_0.

Low order perturbation

In Eq. (5.4), we observe that for $\Delta\omega \ll \omega_0$, the squared terms can be ignored, leading to a more compact approximation

$$\mathbf{D}^{-1}\mathbf{D}_0 \approx \mathbf{I} + 2\mathbf{C}\omega_0\omega + 4\mathbf{C}^2\omega_0^2\Delta\omega^2 + 8\mathbf{C}^3\omega_0^3\Delta\omega^3 + 16\mathbf{C}^4\omega_0^4\Delta\omega^4 + \mathbf{O}\{\Delta\omega^5\}. \qquad (5.8)$$

We note that, if $\omega_0 = 0$ is substituted in Eq. (5.8), the approximation will yield $\mathbf{D}_0$.

5.3.1 Convergence

The series converges under the condition that $\rho(\omega^n\mathbf{C}) < 1$, where ρ here denotes the spectral radius, or, the largest eigenvalue, and $\mathbf{C}$ is defined in Eq. (5.7). The direct implication is that the series converges within an interval $\Omega \equiv (\omega_i, \omega_j)$, diverges otherwise. The spectral radius is equivalent to the largest eigenvalue of the matrix, or, its 2-norm. Consequently, multiple evaluations are costly, and defeat the purpose of calculation speed-up.

Liem and McDaniel (2019) utilize the d'Alembert condition for series convergence, which reads

$$r_{(n+1)} = \frac{\left\|\Delta\omega^{(n+1)}\mathbf{A}_{n+1}\right\|}{\left\|\Delta\omega^{n}\mathbf{A}_{n}\right\|} < 1. \qquad (5.9)$$

The ratio is shown to converge as $n \to \infty$. Liem and McDaniel (2019) propose pre-emptive evaluation of high order terms, so that an estimate of the series' convergence for each approximation point can be made. The evaluation of high-order terms $\mathbf{A}_n$, however, depends on evaluating powers $\mathbf{C}^n$, which is computationally costly.

5.3.2 Approximation error

In practice the series is truncated to a finite number of terms. Furthermore, evaluation of higher order terms is computationally non-trivial, as high powers of $\mathbf{C}^n$ are required. The evaluation of the approximation error is an open issue. Taylor series has an explicit expression for error, and approximate bounds thereof. The implementation of those on a given matrix require, however, several evaluations of norms. A fast formula for the estimation of the error bound based on norm properties is examined. In practice, an adaptive evaluation of the relative error of terms can be performed (Liem and McDaniel, 2019). By this approach, the error is given as

$$\varepsilon_{(n+1)} = \frac{\left\|\mathbf{D}_{approx}^{(n+1)} - \mathbf{D}_{approx}^{(n)}\right\|}{\left\|\mathbf{D}_{approx}^{(n)}\right\|} = \frac{\left\|\Delta\omega^{(n+1)}\mathbf{A}_{n+1}\right\|}{\left\|\mathbf{D}_{approx}^{(n)}\right\|}, \tag{5.10}$$

with $\mathbf{D}_{approx}^{(n)}$ the approximate matrix with n terms. When the series convergence is assured, ε_n is demonstrated to be a reliable estimate. The goal for the error can be anywhere from 1-0.01%, depending on desired convergence and accuracy. For the estimation of the error it is possible to use any of the available norms on the matrices. Liem and McDaniel (2019) calculate the error on the response of the structure, which is of vector nature. In hybrid WFE applications, response calculation requires several operations and the comparison of matrix norms is opted for instead.

Taylor remainder

The estimation of the remainder of Eqs. (5.5) is useful in knowing a priori the accuracy of the approximation. The remainder of a Taylor approximation of order n is

$$\mathbf{R} = \frac{1}{(n+1)!}\mathbf{B}, \tag{5.11}$$

with

$$\mathbf{B} = \max_{\Omega} \frac{\mathrm{d}^{(n+1)}}{\mathrm{d}\omega^{(n+1)}}\mathbf{D}(\omega)^{-1} \tag{5.12}$$

where $\Omega \equiv [\omega_0, \omega]$ the space in which the function is approximated. If $\mathbf{D}^{-1}$ and its derivatives monotonously increase in Ω, then

$$\mathbf{C}(\omega) \geq \mathbf{C}(\omega_j), \quad \forall\omega > \omega_j, \tag{5.13}$$

so that the greatest value of **C** in the approximation interval is its current one. It is then valid to write

$$\mathbf{R}(\omega) \leq \frac{1}{(n+1)!}\frac{\mathrm{d}^{(n+1)}}{\mathrm{d}\omega^{(n+1)}}\mathbf{D}(\omega)^{-1}. \tag{5.14}$$

The evaluation of Eq. 5.14 requires the explicit calculation of terms up to $\mathbf{D}^{-(n+1)}$. As this approach is constructed to circumvent multiple matrix inversions, explicitly evaluating the remainder would defeat the purpose of the approximation.

The inequality of matrices show in above Equations (5.14), (5.13) can be understood in the same sense as the definition of a positive definite matrix, i.e. $\mathbf{u}^T\mathbf{M}\mathbf{u} \geq 0$, with $\mathbf{u}$ a non-zero real vector. It is trivial to write for Eq. (5.14)

$$\|\mathbf{R}(\omega)\| \leq \frac{1}{(n+1)!}\left\|\frac{\mathrm{d}^{(n+1)}}{\mathrm{d}\omega^{(n+1)}}\mathbf{D}(\omega)^{-1}\right\|. \tag{5.15}$$

The right-hand term of Eq. (5.15) can be expanded upon, being mindful of the known norm inequalities for matrices

$$\|\mathbf{A}\mathbf{B}\| \leq \|\mathbf{A}\|\,\|\mathbf{B}\| \tag{5.16a}$$

$$\|\mathbf{A}+\mathbf{B}\| \leq \|\mathbf{A}\| + \|\mathbf{B}\|. \tag{5.16b}$$

Depending on the choice of norm, those inequalities can be more or less conservative. The estimation of $\|D^{-1}\|$ is required. Given that **D** is symmetric, the 2-norm of its inverse is

$$\left\|\mathbf{D}^{-1}\right\| = \min(\sigma(\mathbf{D}))^{-1}, \tag{5.17}$$

with $\sigma(\mathbf{D})$ the matrix's singular values. Although the 2-norm inverse estimate is readily available, the estimation of other, more computationally efficient norms is not possible for non-diagonally dominant matrices (Cvetković and Doroslovački, 2014; Cvetković et al., 2016; Volkov and Miroshnichenko, 2009).

5.3.3 Polynomial symmetry and antisymmetry

The truncated power series of Equation. (5.5) is a polynomial with powers of $\Delta\omega^n$. As $\Delta\omega$ takes both negative and positive values, the even and odd terms are respectively symmetric and antisymmetric with respect to ω_0. This property can be exploited by the solver to minimize the number of evaluations for $\mathbf{A}_k$ such that

$$(\mathbf{D}^{-1})^{+} \approx \sum_{k=0}^{n} \mathbf{A}_k |\Delta\omega|^k, \tag{5.18a}$$

$$(\mathbf{D}^{-1})^{-} \approx \sum_{k=0}^{n} \mathbf{A}_k (-1)^k |\Delta\omega|^k, \tag{5.18b}$$

with $(\mathbf{D}^{-1})^{\pm}$ the inverse matrices for $\omega \to \pm\infty$. The efficiency of the approximation increases with the proper choice of ω_0 such that the effective approximated region is maximized, with minimal evaluations of $\mathbf{A}_k$ and memory usage.

5.4 Computational considerations

The series expansion approach aims at reducing the computational burden of multiple explicit matrix inversions, when solving for dynamic systems in the frequency domain. The viability of the approach has to be considered on the basis of the computational complexity of the arithmetic operations it comprises.

5.4.1 Sparse matrices

Sparse matrices are often employed in FE and other computational applications where differential operators are involved. Sparse matrices store only the non-zero values, along with their position indices. Usually, with proper adaptation of algorithms for matrix operations, significant speed-ups of the computation is achieved.

The common matrix inversion refers to the solution of a linear system $\mathbf{K}\mathbf{u} = \mathbf{f}$, where a solution $\mathbf{u} = \mathbf{K}^{-1}\mathbf{f}$ is sought. Explicit inversion is not recommended in such applications, and LU factorization is opted for, where the matrix is factored into upper and lower triangular components. The values of the vector are finally found through Gauss elimination.

This process does not require the computation of an explicit inverse matrix.

In the case of Guyan reduction (Equation (5.3)), Gauss elimination has no certain computational advantage, and the calculation of an explicit inverse is viable.

While Gauss elimination is optimally performed on sparse matrices, explicit inversions are disadvantageous. The inverse of a sparse matrix is generally not sparse though, rendering the operation cumbersome, considering that a fully populated sparse matrix requires three times as much memory as a conventional one. We establish that, in calculating the explicit inverse matrix with MATLAB, a priori conversion of sparse to full matrices is faster.

5.4.2 Matrix operations

The complexity of the individual matrix operations is more closely examined here. Commonly performed operations are multiplication, inversion and eigenvalue decomposition. Those are generally given as $O(n^3)$, when attempting to compute those by the mathematical definition. More efficient algorithms exist, depending on the properties of matrices (e.g. symmetric or Hermitian matrices). The inversion and eigenvalue decomposition are generally slower than the multiplication operation. Matrix inversion depends to some extent on the condition number, i.e. the ratio of the smallest to the largest singular value. This is a measure of the sensitivity of the system to small perturbations, and well-conditioned systems converge faster to their solutions.

The eigenvalue decomposition of a matrix is a computationally intensive procedure. Algorithms exist to calculate a limited number of eigenvalues, that are relatively fast, dependent on the conditioning of the matrix and the number of eigenvalues requested.

Several norms are defined for matrices, namely the 1 , 2 , ∞, Frobenius and others. The 1 and ∞ norms are defined as the maximum of the sums of the absolutes of the rows and columns respectively. The 2-norm is otherwise called the spectral radius $r(\mathbf{A})$ and is the matrix's largest eigenvalue. Generally, the calculation of the 2-norm is slow, while 1 and ∞ norms are fast to compute.

For this work, the 1 and 2-norms have both been employed and compared. It is found that, in terms of comparing norm ratios, as e.g. the d'Alembert ratio for the series convergence estimates, the 1-norm is as reliable as the 2-norm, and preserves the computational advantage of the series approximation. The 2-norm is a good indicator of the matrix similarity, and are used to compare the approximate to the directly evaluated inverse matrix.

5.4.3 Computational complexity of Neumann approximation

Considering the equations for the Neumann series, the number of operations is estimated. The initial calculation of ${\mathbf{D}_0}^{-1}$ is common for either the direct and approximate method. The approximate method involves the calculation of $\mathbf{C}^n$. The calculation of matrix powers is conventionally done as

$$\mathbf{C}^n = \mathbf{C}^{(n-1)}\mathbf{C}. \tag{5.19}$$

As the algorithm demands all powers of $\mathbf{C}$ up to n, it is advantageous to store the matrices. The alternative to compute high powers of matrix is via eigenvalue decomposition, i.e. the matrix is decomposed into its singular values and respective eigenvectors. Then the diagonal matrix of eigenvalues is raised to the required power. As all the powers up to n are required, this approach does not contribute in the implementation of the proposed algorithm. Furthermore, a full eigenvalue decomposition of the system allows for the adoption of the Craig-Bampton system reduction method (Fan et al., 2016), that's subject to the same complexity.

Concluding, a total of $n + 1$ matrix multiplications is required. The proposed algorithm calculates the terms as indicated by the relative error ε_n, such that $\varepsilon_n \leq \varepsilon^{tol}$. The efficiency of the algorithm depends upon the number of points that can be evaluated reliably with a specific order.

5.5 Applications

A flat shell of homogeneous solid material, with $E = 70 \times 10^9$ Pa, $\nu = 0.33$ and thickness $h = 2$ mm is discretized in $n \times n$ elements. Rigid supports are considered at two opposite edge boundaries, and the free nodes are denoted as I for internal. We consider the internal elimination Dof procedure for the dynamic stiffness matrix of the system, outlined in Section 5.2.

The structure's first few eigenfrequencies are 41, 47, 75, 91 and 101 kHz (Fig. 5.3).

5.5.1 Series convergence

The convergence properties of the Neumann series are investigated first. A starting frequency $\omega_0 = 10$ kHz is assumed. A number of trial frequencies are defined, summarized in Fig. 5.1. The frequencies are selected at various distances from ω_0 and its neighbouring eigenfrequency of 41 kHz.

An analysis of increasing approximation order is ran. The approximation properties of the series are evaluated with respect to the direct inverse matrix, as well as the relative error. The convergence of the series is first indicated by $\|\Delta\omega^2\mathbf{C}\|_2$, which is summarized in Fig. 5.1. For reference, the 1-norm is also given.

A discussion of available norms is of interest, as several defined norms for matrices exist. The 2-norm coincides with the maximum eigenvalue of the matrix, and appears to be the slowest one to compute. 1-norm and ∞-norms are defined as the maximum of the sum of the absolute values of the columns or rows. In this analysis, the 1-norm has been used to calculate both the relative error (Fig. 5.2b) and d'Alembert ratio (Fig. 5.2a). The ratio of norms appears to be reliable, notwithstanding the type used. Furthermore, for d'Alembert ratio where the ratio of terms is considered, 1-norm is more consistent with the respective definition for scalar values. For comparisons of the absolute norms and norm difference of the direct and approximate inverse matrix, the 2-norm has been opted for, as the calculation thereof is outside the timed process and is done for reference reasons.

To estimate the convergent properties for each locus, the d'Alembert ratio is evaluated and depicted in Figure 5.2a. The ratio tends to some constant for each point, as the order approaches infinity. A fluctuation is observed though, which is significant up to the 5th term. The degree of this fluctuation though varies, and it is seen that points closer to ω_0 and further from $\hat{\omega}_1$ have smaller ratio. The evaluation of high-order terms is proposed

	ω_1	ω_2	ω_3	ω_4
f [kHz]	15	20	45	50
$\|\mathbf{C}\|_2$	0.0156	0.0626	0.7665	1.0011
$\|\mathbf{C}\|_1$	11.1224	44.4895	544.9967	711.8324

Figure 5.1: 1 and 2-norm of **C** matrix, for $f_0 = 10$ kHz.

(e.g. (Liem and McDaniel, 2019)). In this work it is demonstrated that order 5 or higher is inefficient in most cases, and the convergent properties are instead evaluated by the relative error.

The relative error is shown in Figure 5.2b. For well-convergent cases, it is seen to decrease quasi-exponentially. For the non-convergent cases shown, it appears to be stationary. The decrease rate of error as a function of the convergeability (e.g. $||\Delta\omega^2\mathbf{C}||$) would yield useful information in pre-estimating convergence properties of a new evaluated locus.

The absolute error is shown normalized over the actual norm of the inverse matrix in Figure 5.2c. For well converged cases the absolute error decreases quasi-exponentially. A stabilization for ω_1 in 10^{-13} is attributed to rounding errors, as the calculations cannot accommodate for smaller numbers with the prescribed precision. Non-convergent cases are seen to diverge. As the d'Alembert ratio is close or larger than 1 in those cases, a power series is conditioned to grow to infinity.

5.5.2 Algorithm effectiveness and timing

We consider the system and a centre frequency $f_0 = 20$ kHz. We construct an algorithm such that the relative error is evaluated at each step. The algorithm exploits the polynomial symmetries and antisymmetries to save on memory and evaluations of terms $\mathbf{A}_n$. The algorithm increments the frequency Δf by 1 kHz at each step. The relative error is calculated, and a threshold tolerance (RelErrTol) is set. If the relative error surpasses the tolerance, additional terms of the series are added until the error sufficiently decreases. A maximum of 10 terms is considered. The absolute error ε is evaluated at each frequency, by evaluating the direct inverse matrix.

The powers of $\mathbf{C}^n$ are computed on demand, i.e. when a term $\mathbf{A}_n$ is required, the $\mathbf{C}^n$

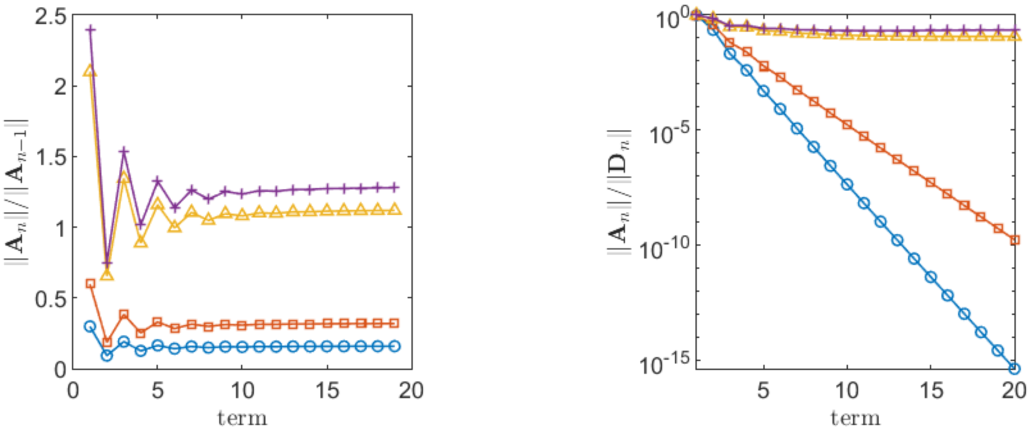

(a) d'Alembert ratio.

(b) Relative error.

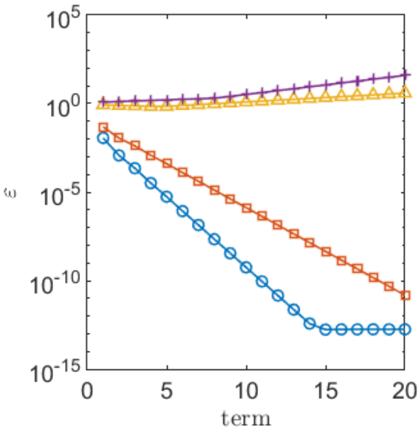

(c) Absolute error.

Figure 5.2: d'Alembert ratio, relative and absolute error. $\omega = \omega_1$ ($\bigcirc$), ω_2 ($\square$), ω_3 ($\triangle$), ω_4 ($+$).

is requested. It is implied that all values of $\mathbf{C}^k$ for $k = 1 \dots n$ are stored. It would be possible to slightly improve memory efficiency by removing the low-order $\mathbf{C}^k$ after the order of $\mathbf{A}_n$ is high enough to not require them any more; this is a feature to be added in future work.

Indicative results for the time comparison of direct and approximate methods are shown in Figure 5.7a. The evaluation of each frequency step is timed separately. For reference, the matrix inversion is also timed. The first step evaluates only one inverse matrix, whereas the rest evaluate two. The first step for the approximate method requires the evaluation of $\mathbf{C}$. It is possible to request a pre-emptive high-order evaluation of $\mathbf{C}^n$ from the first step, however it is found to reduce efficiency. When increased order is requested, the approximate method is slower than the direct inversion. Otherwise, for at most 4th order, the series approximation is faster.

The series approximation maintains computational advantage, the more terms it evaluates with its current order. Increasing order makes it disadvantageous. A speed-up index is defined as

$$\sum_{i=1}^{k} t_i^{dir} / \sum_{i=1}^{k} t_i^{approx}, \tag{5.20}$$

i.e. the total time for the direct method over the respective for the approximate method to converge up to k steps from the initial evaluation point. A value greater that 1 means that the approximate method is more efficient. Figure 5.7 shows the relative speed-up, in direct comparison with the absolute error. If we colloquially define an acceptable absolute error threshold of 0.01, the maximum efficiency is commensurate with it. Consequently, the selection of RelErrTol=0.2 is a good choice.

The direct comparison of relative and absolute error is shown in Figure 5.6b. A steep increase of the absolute error is commensurate with the increase of the relative error. As the evaluated frequencies expand symmetrically, the one whose error is higher dictates the increase of series order. Although from Fig. 5.6b the relative error is shown to be consistently smaller for $+\Delta\omega$, the absolute error also consistently increases. This is attributed to the fact that the 1-norm of the evaluated matrices in the $-\Delta\omega$ decreases, something that is shown in Fig. 5.7, effectively decreasing the denominator of the relative

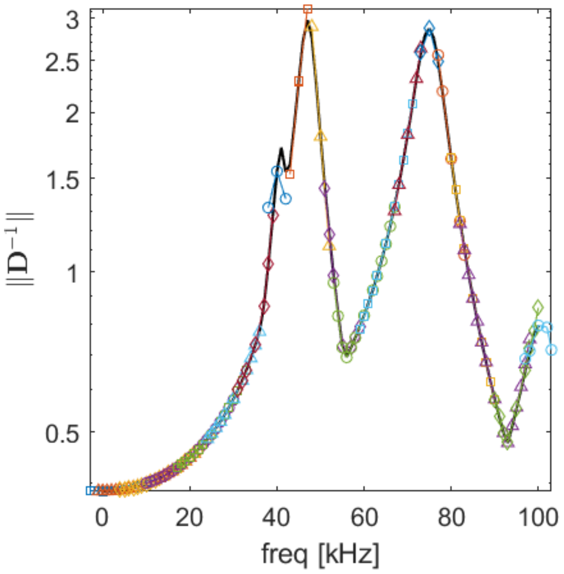

Figure 5.3: 2-norm computed directly (-) and by series approximation (*markers*).

error index.

Figure 5.5 displays the speed-up index for various cases of different numbers of nDof and different RelErrTol.

5.5.3 Efficiency-based design of a solver

The efficiency of the series approximation solver is found to be dependent on the convergence radius, or, the population of evaluation points where the series will converge in a satisfactory manner without exceeding the maximum order.

A series of calculations is ran for $\omega_0 = \{0, 5\ \ldots, 100\}$ kHz, results shown in Figure 5.3. The continuous line represents the 2-norm of the direct solution, whereas the marked lines denote the extents within which the solver converged. We note here that, although the 2-norm is kinked. This is explained by its definition as the maximum eigenvalue. The matrix values are, however, continuous and can be approximated for the valleys shown (e.g. 58, 92 kHz). It is not possible though to construct approximations between singular values, e.g. approximate the matrix value at 80 kHz with an initial evaluation at 60 kHz. The maximum efficiency for each case is summarized and plotted against $\left\|\mathbf{D}_0{}^{-1}\right\|$ in Figure 5.4. Effectiveness is retained for cases of sufficiently small norm, whereas, above a certain threshold, the computational advantage is lost.

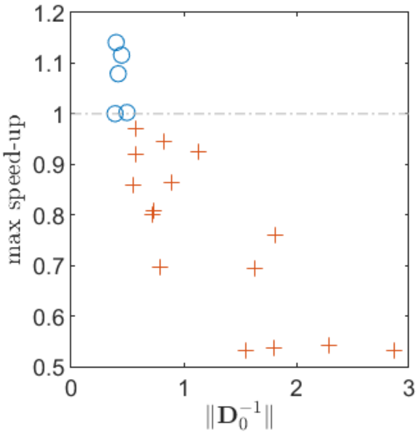

Figure 5.4: Effectiveness of the method, against starting $\|\mathbf{D}_0{}^{-1}\|$. (○) efficient cases, (+) inefficient cases.

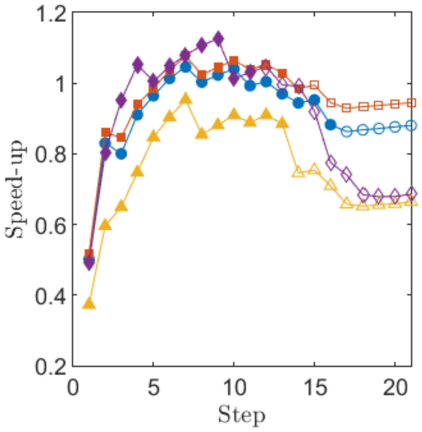

Figure 5.5: Speed-up. RelErr 0.1, nDof 2000 (◯); RelErr 0.1, nDof 3400 (□); RelErr 0.1, nDof 4500 (△); RelErr 0.2, nDof 4500 (◇). Filled markers indicate well-converged cases.

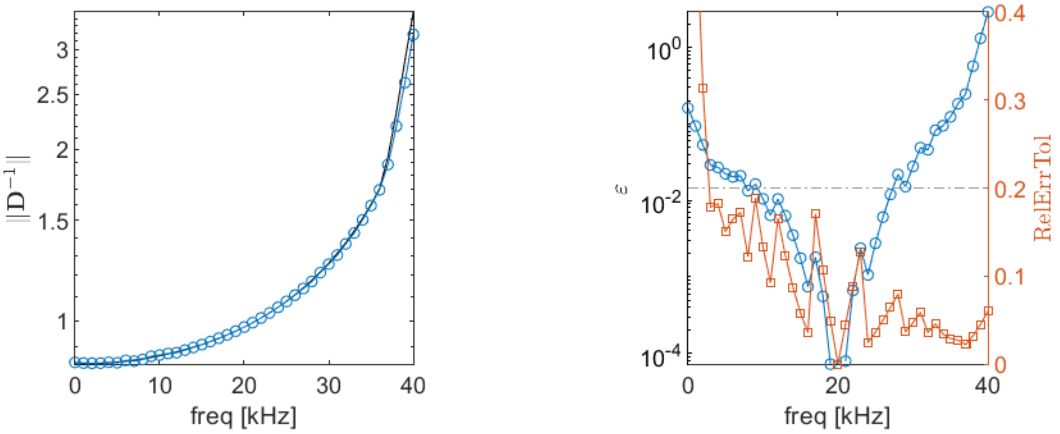

(a) Inverse norm.

(b) Absolute (◯) and relative (□) error.

Figure 5.6: Norms and relative norm comparison for 4500 Dof. Relative Error tolerance 0.2.

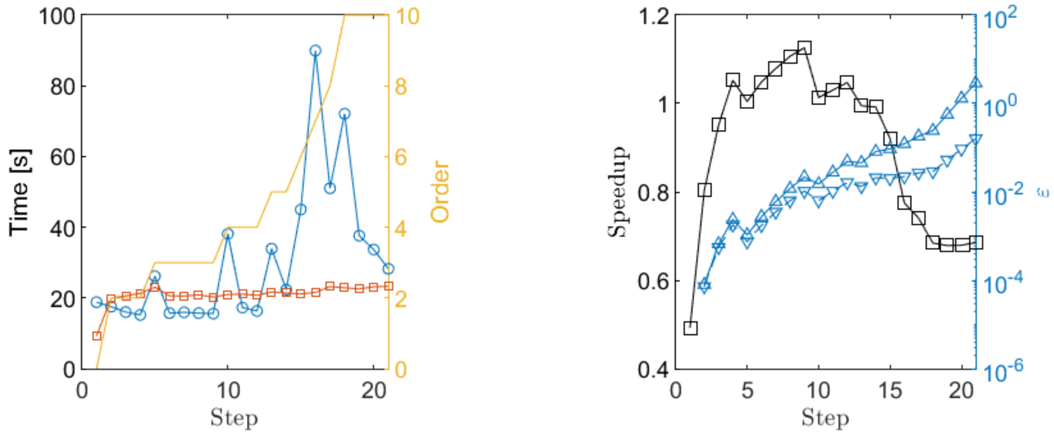

(a) Time and order. (◯) approx., (□) direct calculation.

(b) Relative speed-up (□). Relative error (△) +, (▽) $-\Delta\omega$.

Figure 5.7: Norm and relative speed-up for a shell structure of 4500 Dof. Relative Error tolerance 0.2.

5.6 Conclusions

A solution strategy for harmonic FE problems that require multiple dynamic stiffness matrix inversions dependent on frequency has been discussed. The strategy is based on Neumann series and expands the inverse matrix in a power series. The time complexity of the direct inversion is partially cast onto memory complexity. An index to measure the efficiency of the method has been proposed. The numerical experiments conducted indicate that criteria for the application of the series expansion, with respect to its effectiveness, should be considered. The series approximation approach is effective for relatively small norms of the inverse matrix, and away from singular values.

Our proposed approach evaluates the relative error of the series. The possibility of an error estimator based on the Taylor remainder bound is discussed, but initially rejected, as the computational complexity it requires is higher than the relative computational advantage of the series approximation.

A hybrid approach, with both direct evaluation and series approximation, is commonly used (Liem and McDaniel, 2019). Insofar, criteria for the usage of the solver strategy place gravity onto pre-evaluating the series convergence properties. We suggest placing gravity on the series' effectiveness, as its computational advantage is situational. We suggest further research into the pre-estimation of inverse norms of the dynamic stiffness matrix, as they are a defining factor in the effectiveness of the series approach solution.

Bibliography

Cvetković, L. and Doroslovački, K. Max norm estimation for the inverse of block matrices. *Applied Mathematics and Computation*, 242:694–706, 2014.

Cvetković, L., Kostić, V., Doroslovački, K., and Cvetković, D. L. Euclidean norm estimates of the inverse of some special block matrices. *Applied Mathematics and Computation*, 284:12–23, 2016.

Fan, Y., Collet, M., Ichchou, M. N., Li, L., Bareille, O. A., and Dimitrijevic, Z. Energy flow prediction in built-up structures through a hybrid finite element/wave and finite element approach. *Mechanical Systems and Signal Processing*, 66-67:137–158, 2016.

Lallemand, B., Plessis, G., Tison, T., and Level, P. Neumann expansion for fuzzy finite element analysis. *Engineering Computations*, 16(5):572–583, 1999.

Liem, A. T., Gregory McDaniel, J., and Wixom, A. S. Improving Model Parameters in Vibrating Systems Using Neumann Series. *Journal of Vibration and Acoustics*, 141(1), 2019.

Liem, A. T. and McDaniel, J. G. Convergence estimates for a series approximation of dynamic response of a perturbed system. *Journal of Sound and Vibration*, 459:114855, 2019.

Volkov, Y. S. and Miroshnichenko, V. L. Norm estimates for the inverses of matrices of monotone type and totally positive matrices. *Siberian Mathematical Journal*, 50(6):982–987, 2009.

Waki, Y., Mace, B. R., and Brennan, M. J. Numerical issues concerning the wave and finite element method for free and forced vibrations of waveguides. *Journal of Sound and Vibration*, 327(1-2):92–108, 2009.

Yamazaki, F., Shinozuka, M., and Dasgupta, G. Neumann Expansion for Stochastic Finite Element Analysis. *Journal of Engineering Mechanics*, 114(8):1335–1354, 1988.

Chapter 6

Conclusions

The simulation of damage is an aspect of solid mechanics that attracts research interest. Applications include the design of structures and components and the pre-evaluation of their failure modes, the assessment of residual strength of existing and damaged structures, and the identification of yet-unknown damage state of structures through inverse processes.

Several approaches have been developed to implement damage simulation, pertinent to numerical methods in solid mechanics. Damage can be implemented as a constitutive law and express inherent material properties; this approach is suitable to analyses that attempt to predict the evolution of damage. Discrete modes of damage can be expressed in the material geometrically, such as cracks and voids.

Geometrical introduction of damage is adjoined to several complexities, when damage updating or evolution need be modelled. Remeshing is required by default in crack propagation simulation. Due to uncertainty, in practice, a plethora of scenarios need be analysed, within the space of the uncertain parameters. In damage identification via inverse methods, multiple analyses are required, updating the parameters defining the damage, e.g. crack or inclusion.

Meshing irregular domains is a computationally demanding task. Complexity increases when persistent remeshing is required. Additionally, requirements such as steady mesh quality and detail level ought to be preserved, to maintain a desirable accuracy and avoid computational inflation of the problem. Calculated quantities need to be projected onto the updated mesh, further adding to the computational cost.

The eXtended Finite Element method has been adopted as a suitable solution for the aforementioned problems, due to its ability to construct mesh-independent representations of discontinuities. This is achieved through the incorporation of specialized functions in the so-called approximation space, that extend beyond the conventional polynomials. Examples are discontinuous Heaviside step functions to simulate cracks, and the singular solution of the crack tip displacement and stress field, due to stress infinitely far away. Both those enrichment types are used in the XFEM modelling of cracks.

The capability of efficient crack modelling transcends cracks in certain cases. Cracks can be considered as abstractions that simulate arbitrary forms of damage that are more common in specific materials and components: composite materials for instance suffer from microcracking, matrix-fibre debonding and delaminations. Concerning the linear static and dynamic behaviour of damaged components, cracks represent a local loss of stiffness that can serve as first approximation, i.e. in damage detection problems.

6.1 Development of the eXtended Finite Element

An in-house computational library for the implementation of XFEM has been developed for the purposes of this research.

The code is written in MATLAB. The necessary modules of classical Finite Element simulation are included, i.e. meshing, element integration, assembly of the global stiffness and mass matrices, assembly of load vectors, solution of the linear system and post-processing.

XFEM code requires specialized functions that go beyond classical FE. The evaluation of level set functions of the discontinuity are of cardinal importance, as they convey implicitly the information of the discontinuity's geometry. The choice of enrichment is made on information from the level set, which also provides a local coordinate basis for the evaluation of enrichment functions: crack-tip enrichment is evaluated on polar coordinates emanating from it, and discontinuous enrichment is conveniently taken as the sign of the vertical distance function ϕ.

The integration of element matrices, when those are intersected by discontinuities, require specialized schemes. This is due to the fact that enrichment functions are discontinuous along the cracks, and therefore have singular values. The most common scheme that is also used in this work employs a subdivision of the intersected elements, and Gauss quadrature on the sub-elements produced by said subdivision. This approach is advantageous, as it is relatively easy to extend from classing Gauss quadrature available in FEM codes.

The extended approach introduces additional Degrees of Freedom (DoF) in selected nodes. Consequently, nodes have variable DoFs. This is a source of complexity, and care must be taken to properly map DoFs to nodes. Furthermore, proper mapping can minimize the bandwidth of non-zero elements in the stiffness matrix.

Two levels of post-processing are identified for Fracture Mechanics in general and XFEM in particular. First is the calculation of gradient values, e.g. strains and stresses in the case of Solid Mechanics. The process is directly applied from classical FE, with the addition of the enriched terms, derivatives and DoFs.

The second post-processing level is the application of crack propagation-specific analysis. While several methods and criteria exist, a common ground is the calculation of the energy release rate, and the comparison to a value that is inherent to the material and can be measured experimentally, such that the crack propagates when the calculated value surpasses the intrinsic value. The Stress Intensity Factor (SIF) is a parameter directly connected to the energy release rate and describes the amplitude of the near-tip stress field. The evaluation of any of those parameters requires sufficient resolution of the displacement (and hence stress) fields around the crack. Techniques for the evaluation of fracture parameters include patch recovery and the J-Integral, a contour-independent integral that calculates the un-balance of energy around the crack tip.

The numerical evaluation of the J-Integral requires the evaluation of the displacement and stress fields, and more precisely the partial derivatives of displacements. Evaluation of several contours is required to ensure accuracy. Contours ought to be selected and have values interpolated thereon. The whole procedure is computationally arduous, considering a crack propagation problem where continuous remeshing requires redefinition and re-evaluation of the contours.

The present code implements the approach of the interaction integral, along with a surface transformation of the contour integral, via the divergence theorem (Dolbow et al., 2000). The proposed approach is stable and automable, considering the replication requirement in crack propagation problems. The interaction integral allows for the separation of mixed fracture modes, which is the general case. Calculations are kept to a minimum, as derivatives of the selected domain are retained from the pre-processing stage and evaluated at the post-processing.

In conclusion, the present work provides insights on the inner workings of XFEM, along with a critical view on methods and implementations. An XFEM code is created and validated against analytically derived solutions (Sih, 1974) and computational benchmarks (Tanaka et al., 2017).

6.2 The XFEM in ultrasonic Non-Destructive Evaluation applications

Problems of wave propagation in high frequencies are computationally costly, due to the increased spatial and temporal resolution. Time-transient methods require small spatial discretization to accommodate small wave lengths, which in turn demand proportionally small time steps. Harmonic approaches cast the cost in calculation of high eigenvalues.

The wave approach is adopted in this work, exploiting wave propagation properties in specific structures to drastically decrease the computational cost. Out of a family of wave methods available (Mazzotti et al., 2012; Ichchou et al., 2009), the Wave Finite Element is adopted, as a method that is readily implementable, provided a FE code is available, with minimal additional processing.

The prediction of wave scattering is thus achieved, by few and relatively effortless operations on the available XFEM code mentioned in the previous section.

An ultra-fast computational scheme is created and validated against time-transient simulations. The XFEM allow for a readily parametrized and automable modelling of cracks and other defects.

6.2.1 Computational improvements on matrix inversion for harmonic problems

The frequency-dependent dynamic stiffness matrix requires epxlicit inversion for every discrete frequency evaluated in harmonic problems such as those examined with the WFE and hybrid WFE methods, such as the XFEM/WFE (Waki et al., 2009). The possibility of a Neumann series expansion has been investigated and its performance has been assessed, for applications of such problems.

The method displays computational advantage when it is capable of approximating the results with less computational cost than the conventional explicit inversion of the matrix. The computational advantage reaped from the series approach depends on the capability to accurately estimate the approximation error and use as low order as possible, while maintaining an acceptable absolute error. In the cases studied, namely, the computational advantage is retained for approximations of no more that 4th order. Convergence is assessed on the basis of the relative error, i.e. the relative contribution of each additional higher term of the series: for a well-converged approximation, an additional term of higher order should have very little contribution (Liem and McDaniel, 2020). This approach has been show to be sub-optimal, as the resultant absolute error may be over or under-estimated; the setting of a very conservative relative error is then required to assert a proper absolute error, leading to the loss of computational advantage.

An estimator for the absolute error has been discussed on the basis of the Taylor estimates for remainder bounds. The implementation thereof is, however, directly disadvantageous, as a high-order power of the inverse stiffness matrix need be evaluated. Exact estimate of the norm of the inverse matrix is available only for the 2-norm, which yet defeats the computational advantage. An estimator of the 1-norm, at least in the form of an upper bound, would allow for accurate and fast estimations.

6.3 Directions for future research

6.3.1 Damage identification in arbitrary plates

The wave formulation presented in this work refers to wave propagation in one dimension, while the wave front features are explicitly represented. In most applications, plates and shells extend over 2 dimensions, with waves propagating towards all directions. Excitation from singular points generally produces waves of circular front. The usage of phase arrays (Leleux et al., 2013) is capable of targeting wave packets, creating a linear front. The present formulation of the WFE accommodates for 1-dimensional wave propagation on a bounded waveguide. The usage of absorbent boundaries that emulate infinity conditions, e.g. the so-called perfectly matched layer (Morvaridi and Brun, 2016), is a possible solution to simulate the vanishing energy that is spilled away from the guided waves, as well as the non-bounded wave front.

6.3.2 Computational improvements on wave and hybrid methods

In WFE and hybrid FEM/WFE and XFEM/WFE, several inversions of the dynamic stiffness matrices are required, namely at each discrete evaluated frequency. Computationally efficient schemes have been referenced.

Fan et al. (2016) propose a Craig-Bampton reduction of the internal degrees of freedom of coupling elements. This comprises expressing the system in a discrete number of eigenvalues; the unknown Dof then become the amplitudes of those eigenvalues. Significant system reduction can be thus achieved, as the system's behaviour can usually be adequately expressed with a finite number of significant eigenmodes. It is perceived that the introduction of this technique in the XFEM would yield compound benefits in computational reduction.

We concluded that the Neumann series approach can be improved performance-wise through accurate error estimation. The Taylor remainder estimator provides an upper bound for the error of the approximation. While this bound is directly applicable to scalar quantities, matrices require some norm to be used in accuracy comparisons, which is often costly to compute. In particular, the 2-norm of matrices, albeit an exact estimator of symmetric matrices, requires computational resources potentially equal to an explicit matrix inversion. The 1 and ∞ norms, on the other hand, are trivial to compute, as they are defined as the sums of the absolutes per row or column. The pre-estimation of the 1-norm of the inverse matrix, as given in Morača (2008) for some specific matrices, would be particularly useful in estimating a priori the approximation error of the Neumann series, offering a great advantage to the computation.

Bibliography

Dolbow, J. E., Moës, N., and Belytschko, T. Modeling fracture in Mindlin–Reissner plates with the extended finite element method. *International Journal of Solids and Structures*, 37:7161–7183, 2000.

Fan, Y., Collet, M., Ichchou, M. N., Li, L., Bareille, O. A., and Dimitrijevic, Z. Energy flow prediction in built-up structures through a hybrid finite element/wave and finite element approach. *Mechanical Systems and Signal Processing*, 66-67:137–158, 2016.

Ichchou, M. N., Mencik, J.-M., and Zhou, W. Wave finite elements for low and mid-frequency description of coupled structures with damage. *Computer Methods in Applied Mechanics and Engineering*, 198(15-16):1311–1326, 2009.

Leleux, A., Micheau, P., and Castaings, M. Long range detection of defects in composite plates using lamb waves generated and detected by ultrasonic phased array probes. *Journal of Nondestructive Evaluation*, 32(2):200–214, 2013.

Liem, A. T. and McDaniel, J. G. A novel binomial expansion method for evaluating a Neumann series for the response of a perturbed system. *Journal of Sound and Vibration*, 473:115231, 2020.

Mazzotti, M., Marzani, A., Bartoli, I., and Viola, E. Guided waves dispersion analysis for prestressed viscoelastic waveguides by means of the SAFE method. *International Journal of Solids and Structures*, 49(18):2359–2372, 2012.

Morača, N. Bounds for norms of the matrix inverse and the smallest singular value. *Linear Algebra and its Applications*, 429(10):2589–2601, 2008.

Morvaridi, M. and Brun, M. Perfectly matched layers for flexural waves: An exact analytical model. *International Journal of Solids and Structures*, 102-103:1–9, 2016.

Sih, G. C. Strain-energy-density factor applied to mixed mode crack problems. *International Journal of Fracture*, 10(3):305–321, 1974.

Tanaka, S., Suzuki, H., Sadamoto, S., Okazawa, S., Yu, T. T., and Bui, T. Q. Accurate evaluation of mixed-mode intensity factors of cracked shear-deformable plates by an enriched meshfree Galerkin formulation. *Archive of Applied Mechanics*, 87(2):279–298, 2017.

Waki, Y., Mace, B. R., and Brennan, M. J. Numerical issues concerning the wave and finite element method for free and forced vibrations of waveguides. *Journal of Sound and Vibration*, 327(1-2):92–108, 2009.